Institute of Physics

Polish Academy of Sciences

DOCTORAL THESIS

MOLECULAR BEAM EPITAXIAL (MBE) GROWTH AND ANGLE-RESOLVED PHOTOELECTRON SPECTROSCOPY (ARPES) STUDIES OF PB1-xSNxSE AND α-SN TOPOLOGICAL MATERIALS

Author:
Bartłomiej Turowski

Advisor:
Prof. dr hab. Tomasz Wojtowicz

Auxiliary Advisor:
Dr Valentyn Volobuiev

Warszawa, 2023

I dedicate this thesis to my family.

My loving Wife and Daughter, who are always there for me,

And

My Parents, who supported me and ignited my curiosity about the world

Contents

Abstract

This PhD dissertation focuses on the $Pb_{1-x}Sn_xSe$ and α-Sn (grey tin) thin film topological materials, which belong to the topological crystalline insulators (TCI) and the Luttinger semimetal classes of materials, respectively. The unique property of the topological materials is the presence of the topologically protected gapless surface states, and their behaviour under external perturbation is of great interest. In particular, understanding the band structure at the interface of TCI and magnetic material (MM) holds the potential to realise exotic electronic properties and pave the way for novel spin-orbitronic devices. The topological phases of α-Sn can be tuned by strain or magnetic field, opening the way for possible applications in topological electronics.

In the research for this dissertation, the molecular beam epitaxy (MBE) method was used to produce high-quality thin films of $Pb_{1-x}Sn_xSe$ TCI as well as compressively strained α-Sn in the Dirac semimetal (DSM) phase, grown on hybrid insulating CdTe/GaAs (001) substrates. Structural characterisation of the epilayers was carried out by Reflection High-Energy Electron Diffraction (RHEED), X-ray diffraction (XRD), scanning electron microscopy (SEM) and atomic force microscopy (AFM).

The electronic structure and spin polarization of the surface states of $Pb_{1-x}Sn_xSe$ were investigated using angle-resolved photoelectron spectroscopy (ARPES) and spin-resolved ARPES (SR-ARPES). These studies not only tested the predictions of the band gap opening resulting from the magnetic impurities on the surface of the TCI but also revealed the existence of Rashba-split surface states (RSS) induced by the deposition of a submolayer amount of transition metal (TM) on the surface of the TCI. The results obtained demonstrate the tunability of the Rashba coefficient within the range from 0 to 3.5 eV·Å, along with the absence of a surface states band gap opening of magnetic origin, after TM deposition on the surface of TCI. SR-ARPES investigations conducted at higher photon energies revealed helical spin polarization in both the TCI and normal insulator (NI) phases of $Pb_{1-x}Sn_xSe$, with in-plane spin polarization reaching up to 30%. Remarkably, the TCI-NI transition was observed, triggered by surface compositional changes as a result of TM deposition, rather than surface magnetism from magnetic impurities.

The electronic structure of compressively strained α-Sn was also examined by ARPES. The studies performed revealed the presence of topological Dyakonov-Khaetski states and proved the presence of a DSM phase in compressively strained α-Sn, grown on hybrid insulating CdTe/GaAs (001) substrates.

This work also provided a basis for further optical and transport investigations of topological materials through important contribution to development of the MBE growth technology of such materials and by supplying appropriate structures. Additionally, it proved that α-Sn grown on insulating hybrid substrates is an attractive material for the exploration of relativistic physics, including chiral anomaly.

Acknowledgements

I would like to express my gratitude to Dr V. V. Volobuiev for all the guidance during my PhD studies. He shared his knowledge and expertise in molecular beam epitaxy, angle-resolved photoelectron spectroscopy and x-ray diffraction with me and always had time to explain or discuss the materials we worked on.

I would like to thank Prof. Tomasz Wojtowicz for his expertise in molecular beam epitaxy, guidance in research, time spent, and support in preparation of this dissertation.

I am grateful to Prof. Tomasz Dietl for his kind words and support during my PhD studies.

My deepest appreciation to:

Mgr. Wojtek Zaleszczyk for his help with MBE and for happily sharing his knowledge and helping me whenever I asked.

Dr Alexandr Kazakov for all his insight in physics and great scientific feedback.

Maciej Wiater for sharing his vast knowledge about MBE.

Dr Sergij Chusnutdinow for all discussions and help with understanding the MBE.

Prof. Piotr Wojnar for his kindness and help with MBE.

Dr Tomasz Wojciechowski for teaching me how to operate SEM and for the SEM and EDS measurements.

Dr Marta Aleszkiewicz for her help in understanding AFM and for the AFM measurements.

All my PhD colleagues, especially Ashutos Wadge, Kuba Polaczyński, Rafał Rudniewski, and Piotr Baranowski, for all our scientific and non-scientific discussions.

Staff of the UARPES and PHELIX beamlines at the National Synchrotron Radiation Centre SOLARIS in Kraków for their optimistic attitude and help with gathering ARPES and SR-ARPES data crucial for this dissertation.

Without them, this thesis would not be possible.

Abbreviations

2D	Two-dimensional	MM	Magnetic Metal
2DBZ	2D Brillouin zone	NI	Normal Insulator
2DEG	2D Electron Gas	QCM	Quartz Crystal Microbalance
3D	three-dimensional	QL	Quantum Levels
3DBZ	3D Brillouin zone	QSH	Quantum Spin Hall
AFM	Atomic Force Microscopy	RHEED	Reflection High-Energy
ARPES	Angle-Resolved Photoelectron		Electron Diffraction
	Spectroscopy	RMS	Root Mean Square
BCB	bulk conduction band	RSM	Reciprocal Space Map
BFM	Beam Flux Monitor	RSS	Rashba surface states
BM	Buffer Module	RT	Room Temperature
BS	bulk states	SEM	Scanning Electron Microscope
BVB	bulk valence band	SEDC	Spin Resolved Energy
CB	Conduction Band		Dispersion Curve
CEC	Constant Energy Contours	SR	Spin Resolved
CL	Core Level	SR-ARPES	Spin Resolved Angle-Resolved
DC	Dirac Cone		Photoelectron Spectroscopy
DFT	Density Functional Theory	SOC	Spin-Orbit Coupling
DK	Dyakonov-Khaetski	SOI	Spin-Orbit Interaction
DP	Dirac point	SOT	Spin-Orbit Torque
DSM	Dirac Semimetal	SS	Surface States
EDC	Energy Dispersion Curve	T	Time reversal
EDS	Energy Dispersive	TCI	Topological Crystalline
	Spectroscopy		Insulator
F-D	Fermi-Dirac	TI	Topological Insulator
FWHM	Full width at half maximum	TM	Transition Metals
HH	Heavy Hole	TSS	Topological Surface States
IMFP	Inelastic Mean Free Path	UHV	Ultra-High Vacuum
I	Inversion	VB	Valence Band
KP	Kramer point	VLEED	Very-Low-Energy Electron
LL	Load Lock		Diffraction
MBE	Molecular Beam Epitaxy	VP	Volkov-Pankratov
MDC	Momentum Dispersion Curve	WP	Weyl point
MFP	Mean Free Path	WSM	Weyl semimetal
ML	Monolayer	XRD	X-ray diffraction

Chapter 1

Aim and structure of the thesis

1.1 Motivation and aim of the thesis

The discovery of topological insulators (TI) in 2006 **[1]** started the era of topological materials in the field of condensed matter physics. Various new topologically protected phases of matter were discovered in the following years in one, two, and three dimensions, including, but not limited to, topological crystalline insulators (TCI) and Dirac semimetals (DSM). Topological materials provide new opportunities for superconductivity, information storage and control **[2]**, or spin and charge transport via spin-filtered edge states **[3]**. They can find electronic applications in spintronics and magnetoelectronics, leading to new developments in the field of electronics **[4]**. Of many possible topological phases, the topological insulator / magnetic material (TI / MM) interface is of great interest **[5]**, as the MM can change the efficiency of the spin-charge conversion of the TIs **[6]**, yet this area is relatively unexplored. Even less investigations have been conducted on TCI / MM interfaces, despite the large spin-orbit coupling present in the TCIs **[7]** that can find use in spin-orbitronic devices. Studying the band structure at the said interfaces is critical for understanding and realising new devices based on their exotic electronic properties. On the other hand, studying the evolution of the spin texture of the TCIs when passing through the topological – normal insulator (NI) transition can extend the range of materials suitable for spintronics applications. The helical spin texture of TCI can be preserved in the normal insulator phase, as has been shown experimentally **[8]**. Coupled with the high sensitivity of the TCI to external perturbations that can induce the TCI-NI transition **[9-11]**, it opens the possibility of using lead-tin chalcogenide based TCIs as active elements of spintronic devices. The DSM topological phase can be transformed into a Weyl semimetal (WSM) under breaking of time reversal or inversion symmetry, opening a new field of Weyl topology, with phenomena such as chiral anomaly or chiral magnetic effect **[12]**.

The aim of this work was to grow by molecular beam epitaxy (MBE) epilayers in a form or orientation that is not achievable for the bulk crystals and to study their band and spin structure. The materials of interest were $Pb_{1-x}Sn_xSe$ and α-Sn topological thin film materials. The TCI / TM interface was examined by ARPES in order to provide a better understanding of the band structure evolution dependent on the amount of TM on the surface of the TCI. The TCI-NI transition in $Pb_{1-x}Sn_xSe$ was studied by SR-ARPES to understand the spin texture of the $Pb_{1-x}Sn_xSe$ TCI in both phases, as well as its evolution through the transition. The α-Sn DSM

was studied in a structure design that had not been examined before by ARPES, to complement a larger study of DSM and WSM phases in the α-Sn **[13]**.

The thesis had the following objectives:

- MBE growth of thin and ultra-thin $Pb_{1-x}Sn_xSe$ epilayers on polished and cleaved (111) BaF_2 and thin $Pb_{1-x}Sn_xSe$ epilayers on cleaved (001) KCl;
- Comparison of the MBE growth of $Pb_{1-x}Sn_xSe$ epilayers using both elemental and stoichiometric compound sources;
- MBE growth of α-Sn on insulating hybrid CdTe/GaAs substrates to provide a platform for a wide range of experiments;
- Structural characterization of the epilayers;
- Analysis and understanding of the band structure of $Pb_{1-x}Sn_xSe$ and α-Sn obtained with the use of ARPES;
- Verification of the theoretical predictions of topological band gap opening at (001) and (111) surfaces of $Pb_{1-x}Sn_xSe$ caused by the surface doping of TCI with magnetic impurities;
- Study of the topological transition in $Pb_{1-x}Sn_xSe$ under the deposition of the TM;
- Analysis and understanding of the spin texture of (111)-oriented $Pb_{1-x}Sn_xSe$ obtained with SR-ARPES.

In this thesis, (111) and (001) oriented $Pb_{1-x}Sn_xSe$ TCI, as well as (001) oriented α-Sn (in DSM phase) epilayers were grown using newly installed Veeco MBE multi chamber system. $Pb_{1-x}Sn_xSe$ films were transported either with protective amorphous Se layer or under ultra-high vacuum (UHV) conditions to synchrotron facility in Kraków for in-situ submonolayer thick amount of Fe or Mn transition metal (TM) deposition and further Angle-resolved photoelectron spectroscopy (ARPES) and spin-resolved ARPES (SR-ARPES) measurements. The α-Sn films were transported under ultra-high vacuum (UHV) conditions for ARPES measurements.

1.2   Structure of the thesis

Chapter 1 gives information about the motivation and aim of this thesis.

Chapter 2 introduces the topological class of materials. It provides information on the observed phenomena and provides more detailed information about the TI, TCI, and DSM topological phases. On the basis on that, it introduces the studied materials.

Chapter 3 explains the experimental methods and techniques employed in this work that cover the manufacturing of the studied materials, their structural characterisation, and electronic and spin structure. First, the **Molecular Beam Epitaxy** technique is explained, and the Growth Module #2 (GM#2) VEECO GENxplor MBE System used is described. Since this dissertation is the first one to use this new system, the description of the GM#2 is detailed

because it can be very useful for future users of the system. Next, **Reflection High-Energy Electron Diffraction** (RHEED) analysis technique is introduced and description of the written program for simulation of RHEED patterns is provided. Then, structural characterisation techniques are described. Finally, **ARPES** and **SR-ARPES** experimental methods are described, and information on ARPES data processing method is provided.

Chapter 4 describes the MBE growth process of thin films of the studied materials and their structural characterisation proving, that very high-quality thin layers were grown. **Section 4.1** compares (111) $Pb_{1-x}Sn_xSe$ grown using compound and elemental sources. **Section 4.2** discusses the quality of the $Pb_{1-x}Sn_xSe$ samples further studied by ARPES and SR-ARPES. **Section 4.3** explains the growth method of $Pb_{1-x}Sn_xSe$ epilayers thinner than 120 nm, which differs from the standard MBE growth of 1 µm thick $Pb_{1-x}Sn_xSe$ epilayers. Samples grown by this method are being investigated by the Group of Characterization and Processing of the International Centre for Interfacing Magnetism and Superconductivity with Topological Matter – [MagTop] of the [Institute of Physics PAN] (ON6.3). **Section 4.4** describes the growth process and gives a structural characterisation of α-Sn samples further studied by ARPES. The chapter ends with a summary of the growths and the experience gained.

Chapter 5 presents the main results of this thesis obtained with the use of ARPES and SR-ARPES. First, the influence of transition metal deposition on the surface of (001)- and (111)-oriented $Pb_{1-x}Sn_xSe$ is discussed in **Section 5.1** and **Section 5.2**, respectively. The results presented here are being processed for publication **[14]**. **Section 5.3** shows the first experimental study of the spin-polarized band structure of (111) $Pb_{1-x}Sn_xSe$ across the topological transition **[15]**. **Section 5.4** shows the first experimental ARPES study of (001) α-Sn grown on hybrid (001) GaAs/CdTe substrate. These results were submitted for publication **[13]**. Each section ends with a summary.

In **Chapter 6**, conclusions and the summary of the results obtained is presented, as well as the main scientific achievements of this thesis. The impact of the research on the broader science field is presented.

The results presented in this dissertation were published:

[100] A. Kazakov, W. Brzezicki, T. Hyart, **B. Turowski**, J. Polaczyński, Z. Adamus, M. Aleszkiewicz, T. Wojciechowski, J.Z. Domagala, O. Caha, A. Varykhalov, G. Springholz, T. Wojtowicz, V.V. Volobuev, and T. Dietl, ***Signatures of dephasing by mirror-symmetry breaking in weak-antilocalization magnetoresistance across the topological transition in $Pb_{1-x}Sn_xSe$***. Physical Review B **103**, 24 (2021), [https://doi.org/10.1103/PhysRevB.103.245307], [https://arxiv.org/abs/2002.07622].

[15]   **B. Turowski**, A. Kazakov, R. Rudniewski, T. Sobol, E. Partyka-Jankowska, T. Wojciechowski, M. Aleszkiewicz, W. Zaleszczyk, M. Szczepanik, T. Wojtowicz, and V.V. Volobuev, ***Spin-polarization of topological crystalline and normal insulator $Pb_{1-x}Sn_xSe$ (111) epilayers probed by photoelectron spectroscopy***. Applied Surface Science **610**, (2023), https://doi.org/10.1016/j.apsusc.2022.155434, https://arxiv.org/abs/2212.00816.

Are being processed for publication:

[14]   **B. Turowski**, O. Caha, R. Rudniewski, N. Olszowska, J. Kołodziej, T. Wojtowicz, G. Springholz, and V.V. Volobuev, ***Surface States of Topological Crystalline Insulator $Pb_{1-x}Sn_xSe$ with Ultrathin Transition Metal Adsorbate***. unpublished.

And have been submitted to be published:

[13]   J. Polaczyński, G. Krizman, A. Kazakov, **B. Turowski**, J.B. Ortiz, R. Rudniewski, T. Wojciechowski, P. Dłużewski, M. Aleszkiewicz, W. Zaleszczyk, B. Kurowska, Z. Muhammad, M. Rosmus, N. Olszowska, L.-A. De Vaulchier, Y. Guldner, T. Wojtowicz, and V.V. Volobuev, ***3D Topological Semimetal Phases of Strained α-Sn on Insulating Substrate***. submitted to Advanced Functional Materials, https://doi.org/10.48550/arXiv.2309.03951.

In the **Appendix A**, URANOS ARPES and PHELIX SR-ARPES beamlines that were used to obtain ARPES and SR-ARPES data, are introduced.

In the **Appendix B**, lists of studied samples, list of figures and list of tables are given.

In the **Appendix C**, technical information about the written programs is provided, as well as the code for the RHEED patterns simulations program. The code for the program is available at https://github.com/turobart/RHEED-patterns.git. During my PhD studies, I wrote multiple programs and scripts to automate work in the MBE laboratory and automate data analysis. Improvements to the lab software were made in collaboration with Paweł Ungier, who was responsible for the hardware. I wrote a Python Parameters monitor script for GM#1 and GM#2, which:

- Monitors the flow and temperature of water in water enclosures of the effusion cells;
- Monitors the parameters of turbo pumps;
- Monitors the temperature of cryo pumps;
- Logs Data and displays graph of all monitored parameters.

This program greatly simplifies work in the laboratory.

I also wrote and implemented a password-protected web server on a Raspberry Pi computer to allow automatic and remote control of the flow of liquid nitrogen to GM#1 and GM#2. Custom scripts allow for SMS notifications in the case of the predefined emergency. The server has built in communication with Parameters monitor scripts. It also allows remote

control of the GM#1 RHEED shutter to remotely access RHEED in real time during long growth processes. I wrote the server code using HTML, CSS, JavaScript, php, SQL and Python. The web page is accessible from both personal computers and mobile phones (with different layout of the interface).

I adapted the code of Python Parameters monitor script to make portable temperature logging device, based on Raspberry Pi, for Edwards Cryo-Torr Cryopumps.

I have written a number of Igor and Python scripts for working with data obtained during ARPES measurements. These include procedures for plotting 3D cube maps from 3D data and dynamically fitting the band structure of the studied materials. The scripts are available at https://github.com/turobart/IgorPro-tools-ARPES.git.

Technical note

The abbreviations are provided in a list form at the beginning of the thesis. Each abbreviation is expanded at the first occurrence in every chapter. The layout of this thesis is optimized for reading on electronic devices in PDF form. Each abbreviation has a tooltip. When mouse cursor is placed on the abbreviation, the full name appears after a short time. All internal links to sections, figures, equations, and tables are marked in **desaturated blue bold**. All external links are underlined and marked in blue. The pages at which the references appear, are listed and linked in **bold** at the end of each reference in the bibliography.

Chapter 2

Theoretical introduction

In this chapter, basic information on topological materials is given. First, the theory regarding the observed phenomena is presented. Then, the investigated materials are introduced. Given the highly experimental character of this dissertation, in-depth theoretical formulations have been avoided in favour of more intuitive explanations of the physics behind the discussed topic.

2.1 Topological Materials

The initial theoretical introduction of a new class of materials, topological insulators (TI) **[16, 17]**, based on the quantum spin Hall (QSH) effect **[1]**, has led to extensive research in the search for materials with topological properties. The special characteristics of the topological phases (the topological invariants and the gapless boundary states) rely crucially on the presence of certain symmetries, such as time-reversal or mirror symmetry. In 2D materials, the boundary states are the edge states. In 3D materials, the surface supports the gapless surface states. A topologically non-trivial material cannot be adiabatically deformed to a trivial phase without breaking the respective symmetry **[18]**, thus the term "topological protection". The gapless edge-states in the QSH insulators are protected by the time-reversal symmetry, while the bulk band spectrum remains opened. The QSH effect is characterized by unidirectional edge spin transport: the edge-states with opposite spin polarization propagate in opposite directions at a given edge **[19]**. This type of insulator can be realized in systems with strong spin-orbit interaction (SOI or spin-orbit coupling; SOC), responsible for the band inversion **[20]**, required for the presence of the gapless boundary states. A Z_2 **[16]** topological invariant is used to mathematically characterise the topological properties of the QSH effect **[21]**. The Z_2 index expresses whether the number of times the 1D edge state crosses the Fermi level between 0 and $\frac{\pi}{a}$ is even or odd (in the reciprocal space; a is the lattice constant) **[22]**, defining topologically trivial and non-trivial phases, respectively. In materials with mirror symmetry, such as topological crystalline insulators discussed in **Section 2.1.4**, an integer topological invariant called a mirror Chern number n_M **[23]** dictates the existence of the surface states **[24]**, that is, the non-zero value of n_M is a signature of the topologically protected phase with gapless surface states.

Soon after the initial prediction, the first experimental realisation of the QSH effect was proposed **[25]** and realised **[1]** in HgTe quantum wells. Further investigations led to discoveries on many new topologically protected phases of matter, including 3D TIs **[26-28]**

and Dirac **[29, 30]**, Weyl **[31, 32]** and nodal semimetals **[33]** or higher order TIs **[34]**. Crucially for this thesis, in 2011 the concept of "*topological crystalline insulators*" was introduced by Liang Fu **[35]** to extend the classification of band structures by including crystal point group symmetries.

2.1.1   Spin-orbit interaction

The spin-orbit interaction describes the relationship between the spin of an electron and its orbital momentum. In the atomic physics, a single electron orbiting the nucleus is affected by the following electric field:

$$\vec{E} = -\frac{1}{e}\vec{\nabla}V \tag{2.1}$$

The SOC is significant only in the small area around the atoms **[36]**, as the potential $V(r) = -\frac{Ze^2}{r}$ is spherically symmetrical and thus $V(r) \equiv V(\vec{r})$ and $r = |\vec{r}|$, where Ze is charge of the nucleus. In consequence:

$$\vec{\nabla}V = \frac{dV}{dr}\frac{\vec{r}}{r} \tag{2.2}$$

In its frame of reference, the electron propagating with velocity $\vec{v}$ is affected by magnetic field coming from a positively charged nucleus orbiting the electron:

$$\vec{B} = \frac{\vec{v}}{c^2} \times \vec{E} = \frac{1}{e\,m\,c^2}(\vec{\nabla}V \times \vec{p}) \tag{2.3}$$

where e is the electron charge. Combining **Equations (2.2)** and **(2.3)** reveals that the orbital angular momentum $\vec{L}$ is related to and has the same direction as the magnetic field $\vec{B}$ arising from the movement of the electron:

$$\vec{B} = \frac{1}{e\,m\,c^2}\left(\frac{dV}{dr}\frac{\vec{r}}{r} \times \vec{p}\right) = Z\frac{e}{m\,c\,r^3}\vec{L} \tag{2.4}$$

The spin s of an electron induces spin angular momentum $\vec{S}$ of the electron that creates a spin magnetic dipole moment $\vec{\mu}_s$:

$$\vec{\mu}_s = g_e\frac{\mu_B}{\hbar}\vec{S} \tag{2.5}$$

where $g_e = 2.002318$ is the electron spin g-factor and $\mu_B = \frac{e\hbar}{2m}$ is the Bohr magneton. The spin magnetic dipole moment of the electron experiences a torque due to the magnetic field $\vec{B}$. The torque rotates the spin magnetic dipole moment and, as an effect, it changes the energy of the electron:

$$\Delta E = -\vec{\mu}_s \vec{B} \tag{2.6}$$

Combining **Equations (2.4)** and **(2.5)** with **Equation (2.6)** gives the change in the energy levels of the electrons in the atom due to the spin ($\vec{S}$) – orbit ($\vec{L}$) interaction:

$$\Delta E = \frac{e^2}{2m^2c^2r^3}\vec{S}\cdot\vec{L} \tag{2.7}$$

Since the crystal potential gradient $\vec{\nabla}V$ depends on the charge of the nucleus, the heavier elements exhibit a stronger SOC.

In the crystalline solid, energy bands $E_n(\vec{k})$ are used to describe the motion of the electrons, where n is the band index, and $\vec{k}$ is the wave vector. The band structures of the narrow gap semiconductors can be effectively modelled by $\vec{k}\cdot\vec{p}$ method **[37]** in which $\vec{k}\cdot\vec{p}$ term is produced when the kinetic energy operator in the Schrödinger equation for a single electron in a periodic potential V is applied to a Bloch function Ψ **[37]**:

$$H\Psi = \left(\frac{p^2}{2m} + V(\vec{r})\right)\Psi = E\Psi \tag{2.8}$$

$$\Psi = u_{n\vec{k}}(\vec{r})e^{i\vec{k}\cdot\vec{r}} \tag{2.9}$$

In 1955, Dresselhaus **[38]** extended the $\vec{k}\cdot\vec{p}$ method by introducing the spin-orbit interaction, referred as H_{SO} **[20, 37]**, to the Schrödinger equation for a single electron in a periodic potential, resulting in modification of the **Equation (2.8)**:

$$\left(\frac{p^2}{2m} + V(\vec{r}) + \frac{\hbar}{4m^2c^2}\left(\vec{\nabla}V\times\vec{p}\right)\cdot\vec{\sigma}\right)\Psi = E\Psi \tag{2.10}$$

where $\vec{\sigma} = (\sigma_x, \sigma_y, \sigma_z)$ is the Pauli spin vector, $\hbar$ is reduced Planck constant, $\vec{p}$ is the momentum operator, m is electron mass, and c is the speed of light. The Dresselhaus SOI arises from the lack of inversion symmetry of the material bulk and was initially reported in zinc-blende III-V semiconductors **[38]**. This requirement is not met in the materials studied in this thesis, but a large SOC can result in the Rashba effect, band inversion, and spin-momentum locking, described in **Sections 2.1.2** and **2.1.3**.

2.1.2   Rashba Spin-Orbit Coupling

In 1984 Bychkov and Rashba **[39]** proposed a simple SOC model in which a potential V(z), acting along the surface normal, confines a 2D electron gas (2DEG). The gradient of such potential is $\vec{\nabla}V = \frac{dV}{dz}\vec{z}$, and the resulting Hamiltonian H_R is obtained by substituting this gradient to the SOC Hamiltonian H_{SO} from **Equation (2.10)**:

$$H_R = \alpha_R \vec{\sigma} \cdot (\vec{z} \times \vec{k}) \tag{2.11}$$

where α_R is the Rashba parameter. This parameter is proportional to the gradient of the potential V that confines the 2DEG, and it controls the strength of the SOC [40]. The solution of the Rashba Hamiltonian H_R (**Equation (2.11)**) is the following dispersion relation:

$$E_\pm(\vec{k}_\parallel) = \frac{\hbar^2 k_\parallel^2}{2m} \pm \alpha_R k_\parallel \tag{2.12}$$

where $k_\parallel = |\vec{k}_\parallel|$. Original spin degenerate parabolic band splits into two spin-splitted branches (**Figure 2.1 (a)**), with opposite helical spin texture (**Figure 2.1(b)**). Their energy splitting ΔE directly depends on the Rashba parameter and is expressed by: $\Delta E = \alpha_R \cdot 2k_\parallel$. The Rashba parameter can be expressed as:

$$\alpha_R = \frac{2E_0}{k_0} \tag{2.13}$$

Potential V may be introduced by an external electric field normal to the surface [41] or by surface deposition of donor atoms that induce the potential gradient [42-44].
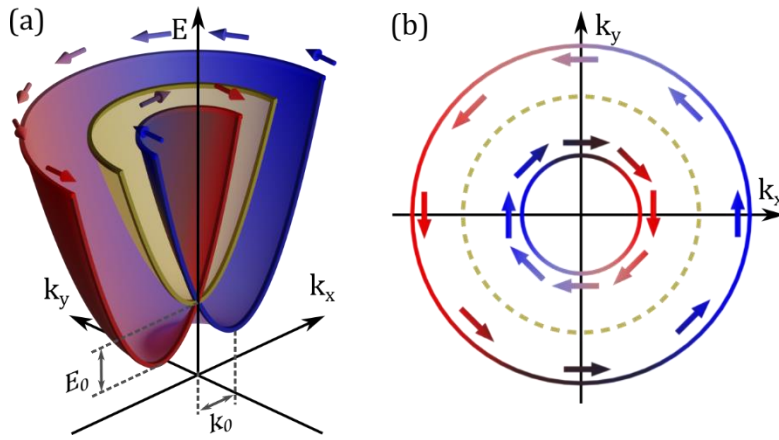
Figure 2.1: Rashba SOC. (a) Schematic band structure with Rashba spin splitting. A spin-degenerate parabolic band (yellow) splitted by SOC into two spin polarized sub-bands (red and blue). **(b)** Constant energy contour of image (a). Band schematic in (a) is obtained using **Equations (3.24)** and **(3.26)**, for the spin-degenerate (yellow) and splitted bands (red and blue), respectively.

Spin splitting by SOC is forbidden in systems with a centre of inversion and does not occur in most solids [45]. The inversion symmetry is broken by the crystal surface, which allows the surface states with the same wave vector $\vec{k}_\parallel$ and opposite spins to be splitted [46]. Breaking of the inversion symmetry on the surface leads to the Rashba SOC [47].

2.1.3   Topological Insulators

The first realization of the TI was performed in HgTe/(Hg,Cd)Te quantum wells [1] and was possible because of the strong SOC in this system. A high charge number of Hg, Cd, and Te atoms requires a relativistic approach, resulting in the following Hamiltonian for an electron in solid:

$$H = H_1 + H_{rel} + H_{SO} \tag{2.14}$$

Where $H_1 = \frac{p^2}{2m} + V(\vec{r})$ is a non-relativistic term, H_{rel} contains the relativistic corrections, and H_{SO} is the Dresselhaus spin-orbit interaction term, since the HgTe/(Hg,Cd)Te has zinc blende crystal structure. These corrections increase in strength with the atomic number [48], as larger charges of the nuclei cause faster movement of the electrons in their orbits.

Figure 2.2 shows the influence of consecutive corrections on the band structure of cadmium telluride (CdTe) (a) and mercury telluride (HgTe) (b) at Γ point. The energy levels derived from the non-relativistic H_1 term are the same for both compounds, but differ when the consecutive corrections are applied. The introduction of the SOC leads to inversion of the valence and conduction bands in the HgTe and, consequently, to a negative bulk band gap.
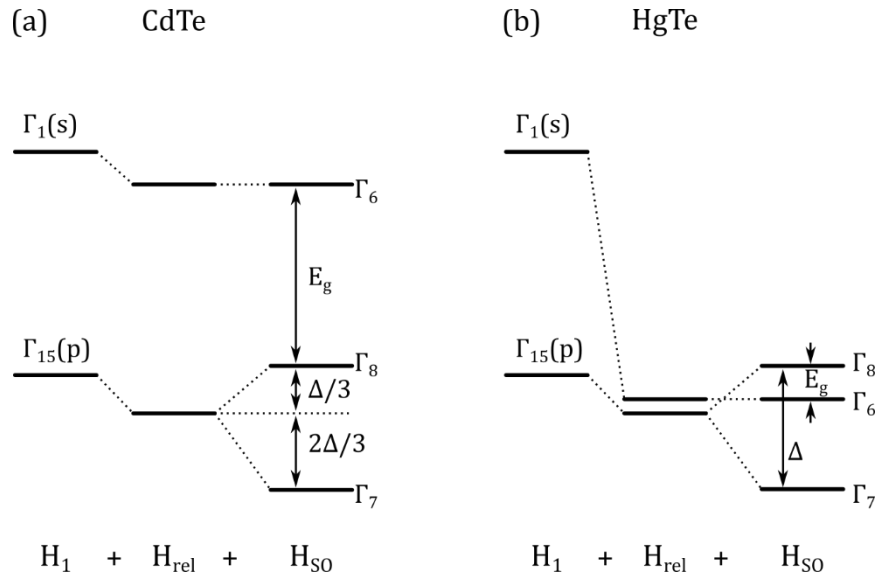
Figure 2.2: **Formation of the energy levels at Γ point in CdTe and HgTe**. Adapted from Ref. [20].

The inversion of Γ_6 and Γ_8 bands, combined with time reversal symmetry, results in the presence of the gapless surface states, while the bulk band gap remains open. The reduction of the size of the TI in one of the dimensions below a certain thickness leads to hybridisation of the surface states. This results in boundary edge states, which can be realised in thin films or quantum wells, as reported for the first time by König et al. [1]. If the band inversion takes place at an uneven number of points in the Brillouin zone, defined by the value of the Z_2 topological invariant, the material is topologically non-trivial. In this case, a pair of two spin

non-degenerate edge states (**Figure 2.3**) cross at the band inversion point at k = 0. This results in the formation of spin-polarized Dirac Cones (DC), characterised by linear dispersion, and a Dirac Point (DP) at the crossing point. The names come from the fact that these cones are described by employing the Dirac equation, with the rest mass set to zero **[49]**.

Figure 2.3: Energy dispersion of the spin non-degenerate edge state of a 2D TI forming a 1D Dirac cone. Adapted from Ref. **[22]**.
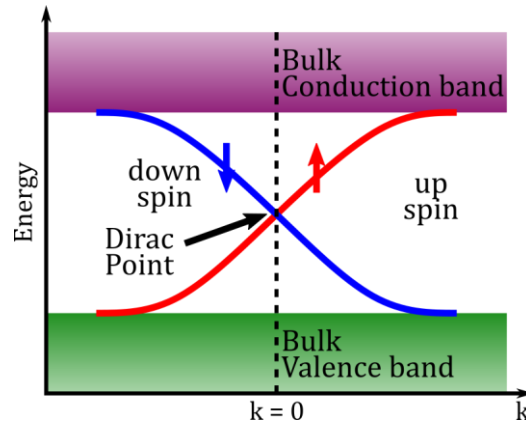
The edge-states are protected from the elastic backscattering, since their spin axis is coupled to the momentum, and remains perpendicular to $\vec{\mathbf{k}}_\parallel$ **[46]**, as shown in **Figure 2.6 (c)**. This effect is called spin-momentum locking and is a result of the SOC. The H_{SO} depends on the vector product of momentum $\vec{\mathbf{p}}$ and potential gradient $\vec{\nabla}V$ (see **Equation (2.10)**). The potential gradient $\vec{\nabla}V$ points along the surface normal and the momentum vector of the surface states lays in the plane of the surface:

$$\vec{\mathbf{p}} = \hbar\vec{\mathbf{k}}_\parallel \tag{2.15}$$

where $\vec{\mathbf{k}}_\parallel$ is wave vector in the surface plane. As a result, the spin axis remains in the plane of the surface, but rotates around, remaining perpendicular to $\vec{\mathbf{k}}_\parallel$ **[46]**.

2.1.4 Topological Crystalline Insulators

The first material realisation of the topological crystalline insulator (TCI) was theoretically predicted in the tin telluride (SnTe) material class **[24]** and was later experimentally confirmed by Angle-Resolved Photoelectron Spectroscopy (ARPES) measurements **[50]**. SnTe has a rock salt crystal structure (see **Figure 2.4 (a)**) and the non-trivial topology in this system is protected by the crystal mirror symmetry of the (110) plane and surface states exist on {001}, {110}, and {111} crystal surfaces. Dirac cones form in high-symmetry surface points of 2D Brillouin zones (2DBZ) situated at the lines of the mirror plane symmetry in the 3D Brillouin zone (3DBZ), as shown in **Figure 2.4 (b)**. The 3DBZ of the (110)-oriented crystal is not shown, since only (001) and (111) samples were studied in the scope of this thesis.

It is convenient to compare the band structure of SnTe with that of a normal insulator lead telluride (PbTe) to explain the origin of the non-trivial topology. For both compounds, a direct band gap is located at the L points of the Bouillon zone. In the case of the trivial PbTe, L_6^+ state is the valence band (VB) edge and state L_6^- is the conduction band (CB) edge, whereas in the case of the non-trivial SnTe the situation is reversed **[51]**, as presented in **Figure 2.5**.
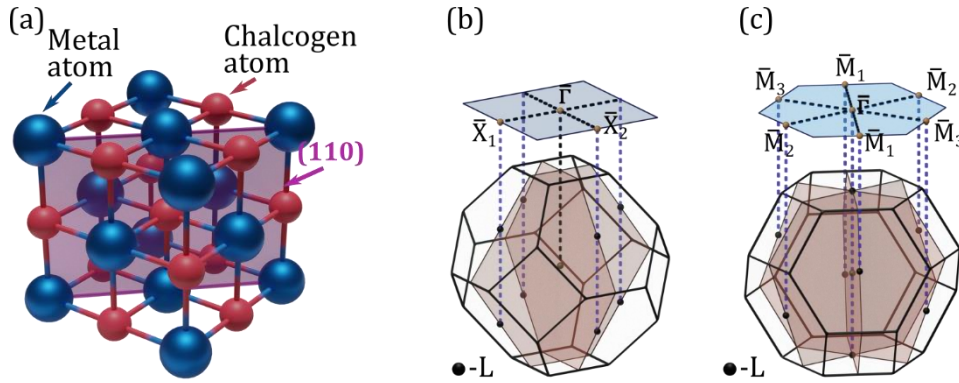

Figure 2.4: Schematic representation of (a) rock salt crystal structure of a chalcogenide with (110) mirror plane marked and 3DBZs for **(b)** (001)-, and **(c)** (111) oriented rock salt crystal, with the corresponding 2DBZs (in blue). {111} mirror planes are marked in dark red. Metal atoms: Pb and/or Sn, chalcogen atoms: Se and Te.

In the initial theoretical model that predicted TCI in SnTe **[24]**, this inversion was explained by deriving VB and CB in PbTe from the p-orbitals of the Te and Pb atoms, respectively, and, by deriving VB and CB in SnTe from the p-orbitals of the Sn and Te, respectively. However, it has recently been reported **[52]** that the CB and VB are primarily composed of the p-orbitals and the molecular orbitals arise from nearest-neighbour s/p-interactions. As a result, SnTe has an inverted band structure and alloying it with PbTe allows for band gap engineering and realisation of the mirror symmetry-protected TCI phase in $Pb_{1-x}Sn_xTe$ **[53]**.
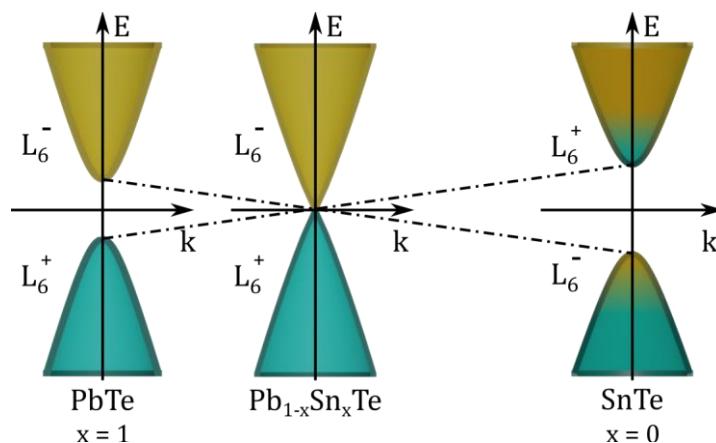

Figure 2.5: Schematic representation of the conduction and valence bands for PbTe and SnTe.

The mirror symmetry of the rock salt structure and the band inversion in SnTe dictate the presence of topological gapless surface states (see **Figure 2.6 (b)**) with linear dispersion,

forming a DC in the bulk band gap, which exhibit helical spin texture due to spin-momentum locking **[54]**, shown in **Figure 2.6 (c)**.

Due to Sn vacancies, SnTe crystals tend to be of a heavy p-type **[55, 56]**. This results in the Fermi energy E_F being below the maximum of the VB, and consequently, in the surface states being unoccupied. SnTe crystals undergo a rhombohedral phase transition **[57]** that leads to breaking of the crystal mirror symmetry of the rock salt structure. These obstacles might be mitigated **[50]**, with ternary substitutional alloy $Pb_{1-x}Se_xTe$ class of materials being one of the ways to realise TCI **[53]**. Another system in which TCI can be realised is $Pb_{1-x}Se_xSe$ **[10]**. This material is discussed in more detail in **Section 2.2.1**, since its study is the focal point of this thesis.
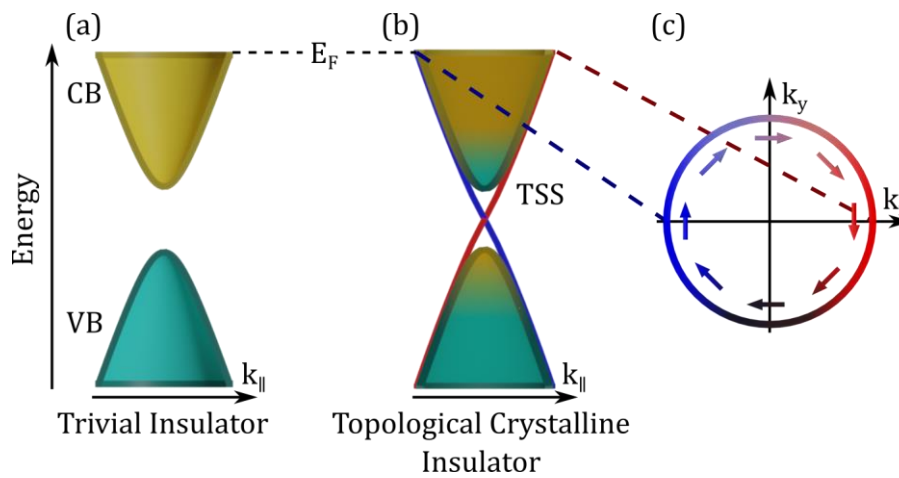

Figure 2.6: Schematic drawing of the band structure of the trivial insulator and the topological crystalline insulator, **(a)** and **(b)** respectively. The blue and red lines mark spin-resolved topological surface states (TSS) forming a Dirac cone (DC). **(c)** Fermi surface of (b) showing helical spin texture of the TSS coming from the spin-momentum locking.

2.1.5 Dirac Semimetals

The Dirac semimetal (DSM) is a material in which the conduction and valence bands touch each other in some points of Brillouin zone (BZ) and the bulk band gap is closed in fourfold degenerate points, called Dirac points (DP; **Figure 2.7 (a)**). Time reversal (T) and inversion (I) symmetry are required for the formation of DPs, but are not sufficient to ensure their topological protection **[58]**. This requires additional space group symmetries that keep DPs intact as symmetry-protected degeneracies **[58]**. This symmetry exists in α-Sn, which is discussed in **Section 2.2.2**. Breaking of either T **[59]** or I **[60]** symmetry results in separation of the DP into a pair of Weyl nodes (or Weyl points, WP) with opposite chirality and a transition of the DSM into a Weyl semimetal (WSM). Objects of opposite chirality are mirror images of each other that cannot be physically superimposed, and are commonly referred to have left or right hand chirality. The chirality index $Z = \hat{k} \cdot (\hat{\sigma} \times \hat{E})$ defines the relation

between wave vector $\vec{\mathbf{k}}$, polarization spin $\vec{\boldsymbol{\sigma}}$ and symmetry-breaking field $\vec{\mathbf{E}}$ [61]. The hat (^) symbol indicates unit vectors. For Z = 1, the chirality is called "right-handed", while for Z = -1, the chirality is called "left-handed". If the band crossing points of the WPs are located at E_F, the Fermi-arc surface states connect the pair of nodes [32]. The dispersion around the WPs is linear and resembles the Weyl equation [62], which is a simplified two-component Dirac equation that gives a dispersion relation for left and right moving (chiral) particles, hence the name '*Weyl semimetal*' [32]. The chirality (or handedness) is an innate property of Weyl fermions, and a pair of Weyl fermions with opposite chirality can be combined into a Dirac fermion [58] when *T* and *I* symmetries are preserved.
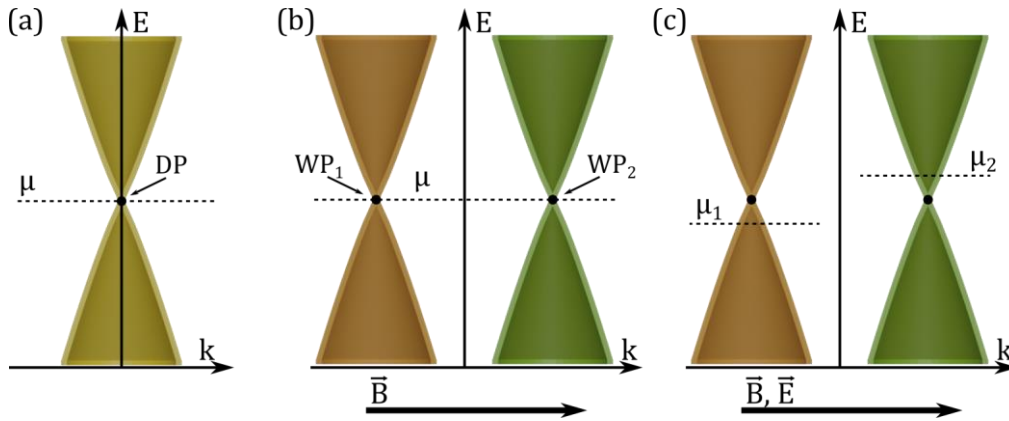

Figure 2.7: Schematic image of the electron spectrum in DSM and WSM. (a) Single Dirac cone in DSM with a Dirac point (DP) labelled. **(b)** Pair of opposite chirality Dirac cones (with Weyl points WP labelling points of band closing) emerging from separation of the DC under *T* symmetry breaking by external magnetic field $\vec{\mathbf{B}}$. **(c)** Presence of parallel magnetic $\vec{\mathbf{B}}$ and electric $\vec{\mathbf{E}}$ fields effects in difference of the chemical potentials µ for left and right handed Dirac cones. Image based on Ref. [63].

Applying magnetic field to DSM breaks the *T* symmetry and splits DP into a pair of WPs, with opposite chirality, along the direction of the field [59], as shown in **Figure 2.7 (b)**. If an electric field, parallel to the direction of the magnetic field, is applied to the WSM, a difference in the chemical potentials µ for the left and right handed cones is created (**Figure 2.7 (c)**) resulting in an electron spectral flow between the cones that balances their electron population [63]. This effect is called the chiral or Adler-Bell-Jackiw anomaly [64] that leads to exotic transport behaviours in condensed matter, such as negative longitudinal magnetoresistance, angular-dependent interlayer resistance, and the planar Hall effect [65]. This makes the WSM and DSM classes of materials interesting for the research of relativistic effects in the solid state, as well as for possible low-power consumption electronic devices [66].

2.2   Topological materials investigated in this thesis

In this section, $Pb_{1-x}Sn_xSe$ TCI and α-Sn Luttinger semimetal are introduced.

2.2.1 $Pb_{1-x}Sn_xSe$

$Pb_{1-x}Sn_xSe$ is a narrow-gap semiconductor and ternary substitutional alloy of PbSe and SnSe. Its band gap ranges from 0.27 eV (PbSe, direct **[67, 68]**) to -0.68 eV (rock salt SnSe, direct **[69]**) with a bulk band gap closing at $x_{Sn} \cong 0.3$ at room temperature. Because of this, both PbSe and $Pb_{1-x}Sn_xSe$ were extensively studied and used for the generation **[70, 71]** and detection **[72, 73]** of infrared radiation, as the 0.27 eV band gap of PbSe corresponds to 4.6 µm wavelength, which can be further increased by decreasing the band gap through alloying with SnSe (see **Figure 2.8**).
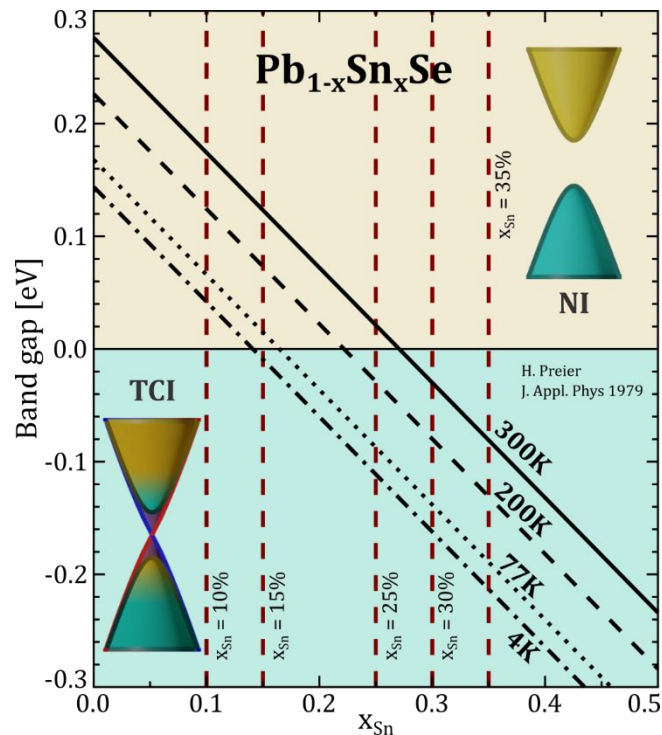

Figure 2.8: Band gap dependence on composition of $Pb_{1-x}Sn_xSe$ in 300 K, 200 K, 77 K and 4 K. Red dashed lines mark average compositions grown samples, discussed in **Chapter 4**. Adapted from Refs. **[67, 68]**.

Furthermore, PbSe has long been known for its good thermoelectric properties **[74]** and SnSe has been more recently shown to be an interesting thermoelectric material **[75]**. Both compounds are promising candidates for the effective use of the Seebeck and Peltier effects **[76]**, due to their low thermal conductivity **[75]** or their ability to increase the Seebeck coefficient **[77]** that influence the figure of merit zT, which quantifies the efficiency of the material to convert heat into electricity **[78]**.

The work of Liang Fu **[35]**, defining the new "*topological crystalline insulator*" class of materials, renewed the interest in the $Pb_{1-x}Sn_xSe$, especially in the single crystal phase **[10, 79]**. It was shown to undergo the topological phase transition from normal insulator (NI) to TCI induced by Sn content increase **[9]**, by cooling down the material **[10]** or applying pressure **[80]**. To conserve the required crystal point symmetries $Pb_{1-x}Sn_xSe$ must retain the

rock salt structure, which is obtained for composition with x_{Sn} in the range of 0 to 0.4 **[67]**. For this reason, the samples presented in this thesis are limited to the Sn content $x_{Sn} \leq 0.35$. The increase in Sn content in $Pb_{1-x}Sn_xSe$, crucial to obtaining the TCI phase, results in high bulk hole concentrations **[81]** due to the intrinsic p-type character of SnSe coming from its tendency to cation vacancy formation **[82]**. To circumvent this and obtain n-type samples, fine bismuth (Bi) doping is employed **[83]**. In the studied samples, Bi doping was kept below 0.016%. If the doping is high enough (more than 1%), the $Pb_{1-x}Sn_xSe$ (111) system transitions from TCI to Z_2 TI and TSS gap opens at $\bar{\Gamma}$ point **[9]**.

The films studied in the scope of this thesis were grown along [001] and [111] directions. **Figure 2.4 (a)** shows rock salt structure of the $Pb_{1-x}Sn_xSe$ with indicated non-polar and polar (001) and (111) atomic planes. Images **(b)** and **(c)** show 3DBZs and 2DBZs for (001) and (111), respectively, oriented rock salt crystal, with positions of DCs at high-symmetry surface points. On the (001) plane, DCs exist at $\bar{X}$ points and correspond to two L points of the 3DBZ projecting to (001) 2DBZ. On the (111) plane, DCs exist at six $\bar{M}$ points at the edge of the 2DBZ, each corresponding to one L point of the 3DBZ, and at $\bar{\Gamma}$.

The initial prediction of topological crystalline insulators **[35]** does not require SOC in order to support gapless surface states but in the real material it is responsible for the band inversion and thus it is necessary for TSS to appear.

Despite the fact that $Pb_{1-x}Sn_xSe$ has been studied for many decades, it still is an interesting platform for basic and application oriented research, as well as research of effects that are important for applications.

2.2.2   α-Sn

Grey tin (α-Sn) is an elemental topological material that belongs to the Luttinger semimetal class of materials. It can undergo phase transitions from zero-gap semiconductor (ZGS) to topological insulator and Dirac semimetal induced by strain engineering **[84]**. The Luttinger semimetal is a general name for semimetals in which the bulk spectrum consists of two double-degenerate quadratic bands with opposite signs at k = 0 **[85]**. The name comes from the model **[86]** derived by Luttinger for a system with full cubic symmetry near Γ point at k = 0. The grey tin has the diamond cubic structure, as presented in **Figure 2.9 (a)**. **Figure 2.9 (b)** shows the BZs corresponding to (001) α-Sn. The Γ point of the 3DBZ projects to the $\bar{\Gamma}$ point of (001) 2DBZ, near which ARPES studies of the electronic structure were carried out. Compared to other group IV materials with the diamond structure, the unstrained α-Sn has an inverted band ordering **[84, 87]**: at Γ point the *s*-orbital-dominated Γ_7^- state is below *p*-orbital-derived Γ_8^+ state, located at the Fermi level (E_F), **Figure 2.9 (c)**, middle. This inversion allows for the existence of topologically non-trivial states. At Γ point heavy-hole (HH) valence band maximum and inverted light-hole (iLH) conduction band minimum touch at fourfold degenerate Γ_8^+ **[88]**. The degeneracy of this band is a consequence of the cubic

symmetry of the diamond structure **[89]**. If a directed perturbation to the lattice structure is applied, such as uniaxial strain, the symmetry of the lattice is reduced and, as a result, the degeneracy at k = 0 is lifted and the degenerate Γ_8^+ band splits into Γ_6^+ and Γ_7^+ bands **[84]**. Under in-plane tensile or compressive strain α-Sn becomes TI or DSM, respectively **[87]**, as presented in **Figure 2.9 (c)** left and right. The tensile strain pushes Γ_6^+ band down and Γ_7^+ band up opening bulk band gap. Because of this and the band inversion in unstrained α-Sn, it becomes TI. The compressive strain pushes Γ_6^+ band up and Γ_7^+ band down and causes two discrete band crossing points, Dirac points, and thus shifts the system to the DSM phase.

As mentioned in **Section 2.1.5,** additional space group symmetries are required to keep Dirac nodes intact. In the case of α-Sn, D_{4h} point group symmetry is responsible for the protection of DP **[85]**.
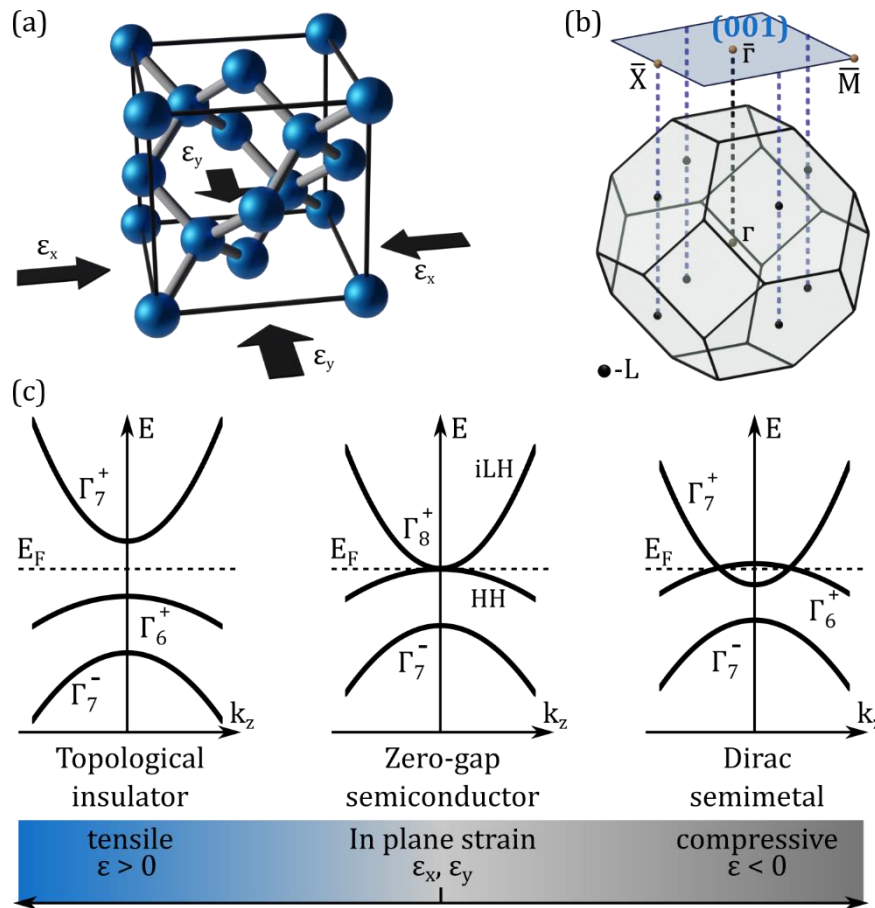
Figure 2.9: Crystal and electronic structure of α-Sn. (a) Unit cell of α-Sn with $Fd\bar{3}m$ space group, with positive (ε < 0) compressive in-plain strain direction marked by black arrows. **(b)** Corresponding bulk and (001) surface BZs with high-symmetry point locations labelled. **(c)** Topological phase diagram in vicinity of $\bar{\Gamma}$ point α-Sn under negative to positive in-plane strain, left to right, respectively. Tensile strain, ε_x, ε_y > 0, causes topological band gap opening and, as a result, the transition to a TI phase; unstrained α-Sn is a ZGS; under compressive strain, ε_x, ε_y < 0, α-Sn becomes a DSM with two Dirac points. iLH stands for inverted light holes and HH for heavy holes. Image (c) adapted from Refs. **[84, 87]**.

The introduction of strain may be achieved by growing thin layers of tin on a substrate with a mismatched lattice constant. The epitaxial growth of thin films also makes it possible to obtain a stable α-Sn phase above room temperature **[90]**, as the grey tin in bulk form is stable only below 13.2 °C **[91, 92]**. Above this temperature, it undergoes a phase transition to white tin (β-Sn) making it difficult to study the α-Sn.

Chapter 3

Experimental methods

In this chapter, the basics of the experimental techniques used are discussed, and the experimental systems used are presented briefly. **Molecular Beam Epitaxy** (MBE) and **Angle-resolved photoelectron spectroscopy** (ARPES) are emphasised since they were the main experimental techniques I used. First, MBE is discussed, followed by a description of the VEECO GENxplor MBE GM#2 system used and the description of the growth and transfer of the grown samples to the ARPES facility. Next, **Reflection High-Energy Electron Diffraction** (RHEED) is described in the context of the results presented in the **Chapter 4**. Then characterisation techniques: **X-ray diffraction** (XRD), **Scanning electron microscope** (SEM), and **Atomic force microscopy** (AFM) are described. Finally, ARPES, **Spin-resolved angle-resolved photoelectron spectroscopy,** and **ARPES data processing** (SR-ARPES) are discussed. Technical information about ARPES and SR-ARES systems is given in **Appendix A**.

3.1   Molecular Beam Epitaxy

Molecular Beam Epitaxy is a well-established method **[9, 83, 93]** of growing high quality thin epitaxial structures made of insulators, semiconductors, or metals. In epitaxial growth, a crystal of a particular crystallographic orientation grows on another crystal. The orientation of the substrate crystal determines the orientation of the grown crystal. In MBE, a molecular beam of elements impinges on a substrate, kept at controlled temperature, and typically crystalizes in a thin film form. It also allows for controlled growth of other 2D structures such as supper-lattices and quantum wells, as well as 1D nanowires and 0D quantum dots, but growth processes of these structures require additional steps and typically are more complicated than growth of thin films. The sources for the beams typically are effusion cells filled with the materials used, which are heated to allow their effective evaporation or sublimation. The ultra-high vacuum (UHV) environment (pressure in the growth chamber less than 10^{-9} mbar) ensures the high purity of the grown epilayer by preserving the molecular beam nature of the mass flow from the sources and limiting the possibility of adsorbing unintentional contaminants from the residual gas in the growth chamber. The former is preserved when the mean free path (MFP) of the molecules of the used material is greater than the distance between the source orifices and the substrate. The MFP is the average distance traversed by the molecules between successive collisions, and can be expressed as:

$$L = \frac{1}{\sqrt{2} \cdot \pi \cdot n \cdot d^2} \tag{3.1}$$

where d is the molecular diameter, n is the concentration of the gas molecules in the vacuum, and is related to the beam pressure p and temperature T by $n = \frac{p}{k_B \cdot T}$ where k_B is the Boltzmann constant. Assuming that the molecules of the beam (d_b) and the residual gas (d_g) create a mixture of two gases ($d_{bg} = \frac{d_b + d_g}{2}$), the maximal pressure of the residual gas in the growth chamber, ensuring no collision between molecules, can be expressed as [94]:

$$p_g = k_B \cdot T \cdot \frac{L_b^{-1} - \sqrt{2} \cdot \pi \cdot n_b \cdot d_b^2}{\pi \cdot d_{bg}^2} \tag{3.2}$$

where L_b is the distance between a source and the substrate, and typically it is less than 0.5 m. For $Pb_{1-x}Sn_xSe$ MBE growth, relevant for this thesis, p_g can be calculated using: $d_b = d_{PbSe} = 6.04 \times 10^{-10}$ m, T = 350 °C (623 K), $d_g = 3.74 \times 10^{-10}$ [94] and cell operating temperature of 525 °C (798 K, used for n_b calculation), and equals $p_g = 6.42 \times 10^{-2}$ Pa = 6.42×10^{-4} mbar. To simplify the calculation, the size of the PbSe molecule is used as d_b, because for the growth of $Pb_{1-x}Sn_xSe$ in Growth Module #2 MBE compound sources (PbSe and SnSe) are used. The d_{PbSe} is calculated as the sum of th radii of the Pb (1.75 Å) and Se (1.20 Å) atoms plus Pb-Se bond length (3.09 Å). The value of p_g obtained shows that the UHV (< 10^{-9} mbar) is more than sufficient to ensure the molecular beam nature of the mass flow.

The composition of films is controlled by the relative rate of molecular beams at the substrate position. This rate also affects the thickness of the epilayer and its doping if additional dopant elements are used. The typical growth rate is maintained at 1 μm/hour (~1 monolayer/s) ensuring a very smooth surface of the grown films. Such a low growth rate leads to more rigorous base pressure limits, needed to achieve negligible levels of unintentional contaminants in epilayers. A clean epilayer is grown if the deposition time of a single monolayer (ML) of contaminants (t_g) is much greater than the deposition time of a single ML from the molecular beams. In the case of $Pb_{1-x}Sn_xSe$ grown in Growth Module #2 MBE, following molecular beam fluxes were used to obtain a growth rate of ~1 ML/s for an epilayer with x_{Sn} = 0.34: PbSe 1.61×10^{-6} mbar, SnSe 4.9×10^{-7} mbar. The base pressure of the chamber is 10^{-10} mbar, however, in Residual Gas Analyser (RGA) scans only H_2 is detected above 10^{-10} mbar. Other prominent vacuum contaminants, namely H_2O, N_2, and CO_2, are below 10^{-11} mbar, with other possible contaminants at levels below 10^{-12} mbar. In these conditions, the deposition time of a single layer of contaminants can be estimated as $t_g \approx 14$ hours when taking into account molecular beam fluxes needed to grow 1 ML of $Pb_{1-x}Sn_xSe$. The t_g obtained is of a similar order as that required for the growth of a clean epilayer defined in Ref. [94]. UHV conditions are needed to ensure minimal contamination of the epilayer coming from residual gas in the growth chamber.

The schematic image of a typical MBE growth chamber is presented in **Figure 3.1**. The chamber is surrounded by a liquid nitrogen (LN_2) shroud (cryopanel) that stabilises the conditions inside when the cells and/or the sample are heated. It prevents reevaporation of

the materials from previous growths that could have been deposited on the inside walls of the chamber. Cryogenic pumps maintain UHV, which is monitored by a dedicated ion gauge. The source materials are placed in heated crucibles located in the effusion cells. The cells are cooled by a constant flow of water in their water enclosures to ensure stable thermal conditions. Molecular beams that come from cells can be blocked by shutters to selectively start or stop a given beam. This allows for precise control over the composition of grown structure, its doping, and growth time, which correlates to its thickness that can be controlled on an atomic level. The beam flux pressure of the materials is controlled by the temperature of the effusion cells and is measured by a flux monitor (BFM), a vacuum gauge moved to a position in front of the substrate, that measures current of ionised beam between two electrodes. The more ions go through the space between the electrodes, the bigger the measured current intensity, which is directly related to the gas molecule density, that is, the gas pressure (given in mbar). The deposition rate is measured in-situ using a quartz crystal microbalance (QCM) **[95]** moved to the same position as the BFM. In this case, the material is deposited on a vibrating quartz crystal resonator. Given parameters for the measured material, the change in the resonator frequency is recalculated to the deposition rate in angstroms per second. The composition and thickness of the film can be directly calculated from the measured material deposition ratio and the deposition rate, respectively. Similarly, the flux ratio may be used to calculate the composition as well as, with prior growth rate calibration, the thickness of the grown film.
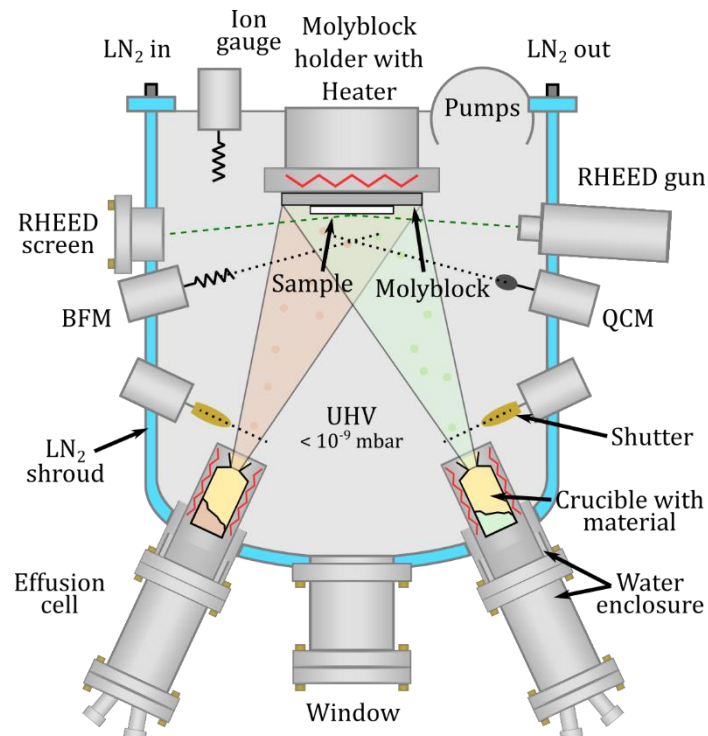

Figure 3.1: Schematic image of a MBE UHV growth chamber with the main elements labelled. Abbreviations: RHEED - Reflection High-Energy Electron Diffraction; BFM – Beam Flux Monitor; QCM - Quartz Crystal Microbalance; LN_2 – liquid nitrogen, UHV – Ultra-High Vacuum.

Additional ports with windows allow for observation of the grown sample, e.g. with a CCD camera of an external pyrometer. Molecular fluxes of materials impinge on a properly prepared crystal substrate of choice, which imposes crystallographic orientation of a film and can induce strains to the grown film in the case of lattice constant mismatch between substrate and grown epilayer. The temperature of the substrate is controlled with high precision, typically using a resistive heater that radiatively heats the molyblock holder to which the sample is attached. In most cases, the growth temperature is kept constant during the process at some predefined value, well above the room temperature (RT). The huge advantage of MBE is that growth mode and growth rate of the grown epilayer are monitored and can be controlled in real time by RHEED technique (see **Section 3.2**).

Taking into account all of the above, the MBE growth method has several key advantages. The UHV environment combined with 7-9N pure elements (see discussion of **Figure 3.10)** provides conditions for the growth of materials with a very small amount of unintentional impurities. It provides possibility of producing non-equilibrium crystalline structures, such as α-Sn stable in RT. Individual shutters provide the possibility of abrupt start and stop of the growth process, fine control over doping, and the possibility of producing thin layer structures with abrupt interfaces. Low growth rates, of less than 1 ML/s, allow for very precise control of thickness of the grown structures, at atomic level. Precise control over growth temperature allows fine-tuning of the growth conditions in order to reduce the interdiffusion and number of defects in the material. The growth process can be controlled in real time by in-situ RHEED. The description of the MBE method presented in this section is based on Ref. **[96]**.

The MBE growth of thin films depends mainly on the kinetics of the surface processes, such as atom adsorption, surface migration, and attachment to the surface. The state of the entire growth system is far from the thermal equilibrium due to the UHV environment, since the temperature of the species (which depends on the temperature of the sources), arriving at the surface is different from the temperature of the substrate **[97]**. Three main growth modes, two of which are shown in **Figure 3.2**, can be distinguished. They depend on interaction strength between atoms and the surface. In the island (Volmer-Weber) growth mode (see **Figure 3.2 (a)**), the adatoms (atoms adsorbed on the surface) bond stronger to each other than to the substrate, which leads to formation of local islands minimizing interaction of the material with the substrate. In the layer-by-layer (Frank-van der Merwe) growth mode (see **Figure 3.2 (b)**), adatoms bound weaker to each other than to the substrate. First, a new layer nucleates at various points on the surface, and then new adatoms attach to the edges of these monolayer islands, forming a complete monolayer. In the layer plus island (Stranski-Krastanov) mode (not shown), both single layers and islands are formed on the substrate, typically because of the lattice mismatch between epilayer and a substrate. Strains present in the initial few grown monolayers are alleviated by the formation of 3D islands on the surface of the film.
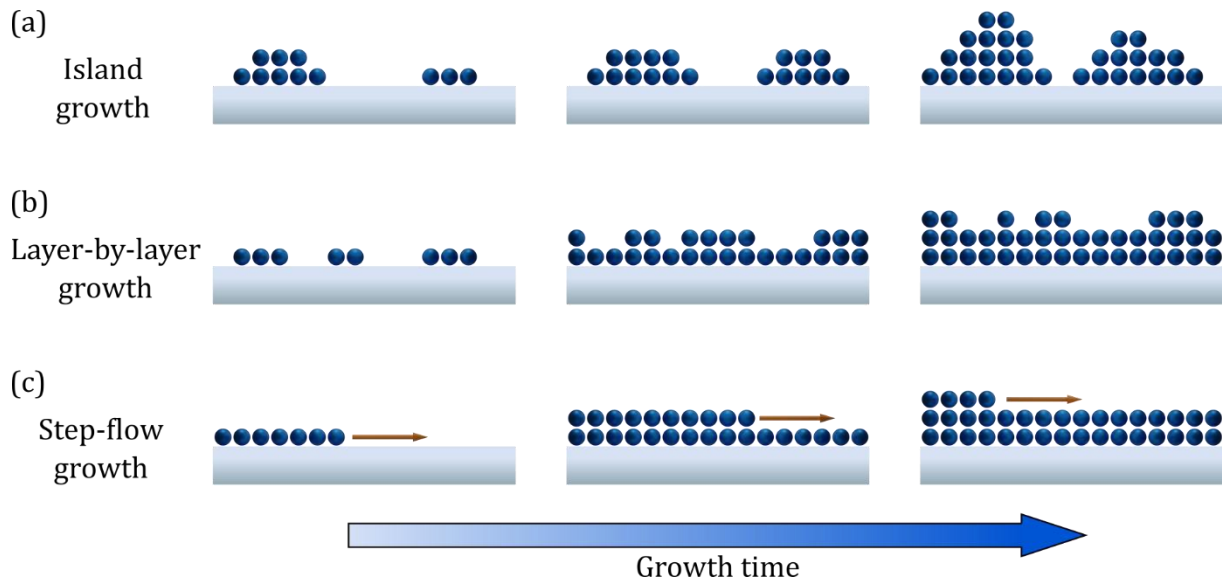
Figure 3.2: MBE growth modes of epilayers relevant for later discussion in **Section 4.2.1**. **(a)** 3D island (Volmer-Weber) growth mode. **(b)** 2D layer-by-layer (Frank-van der Merwe) growth mode. **(c)** 2D step-flow growth mode. For clarity of the image (001) orientation of atoms is presented in the schematics.

The surface migration (diffusion) of an adatom can be modified by the temperature of the substrate. At lower growth temperatures, the mobility of the adatoms on the surface is reduced. With insufficient mobility of the adatoms, they do not diffuse to other adatoms, shifting the growth toward an island mode. A higher substrate temperature increases the mobility of the adatoms. After adsorption to the surface, they are more likely to diffuse and attach to other adatoms, increasing the size of monolayer islands, shifting the growth toward a layer-by-layer mode. A step-flow-mode, shown in **Figure 3.2 (c)**, is a variation of the layer-by-layer growth mode. If the substrate is not perfectly flat, e.g. there are some terraces or steps on the surface, and the growth temperature is sufficiently high, adatoms have sufficient mobility to diffuse to these step edges and kinks without initiation of new monolayer islands by interaction with other adatoms. Attachment of the new adatoms occurs at the steps and results in a step-flow growth mode. If the surface mobility of the adatoms is reduced, the growth mode will change from step-flow to layer-by-layer with multiple layers forming at the same time **[98]**.

3.1.1 Growth Module #2 description

All $Pb_{1-x}Sn_xSe$ samples manufactured by me were grown in the Growth Module #2 (GM#2) VEECO GENxplor MBE System intended for materials in groups IV-VI. In this section, detailed information about GM#2 is given. In the next section, my involvement in upgrades of the GM#2 and PM systems is presented.

GM#2 is connected with the Growth Module #1 (GM#1) VEECO GENxplor MBE System, used for CdTe/GaAs hybrid buffer fabrication, and the Preparation Module (PM) via two UHV buffer modules (BM#1 and BM#2), as shown in **Figure 3.3**.
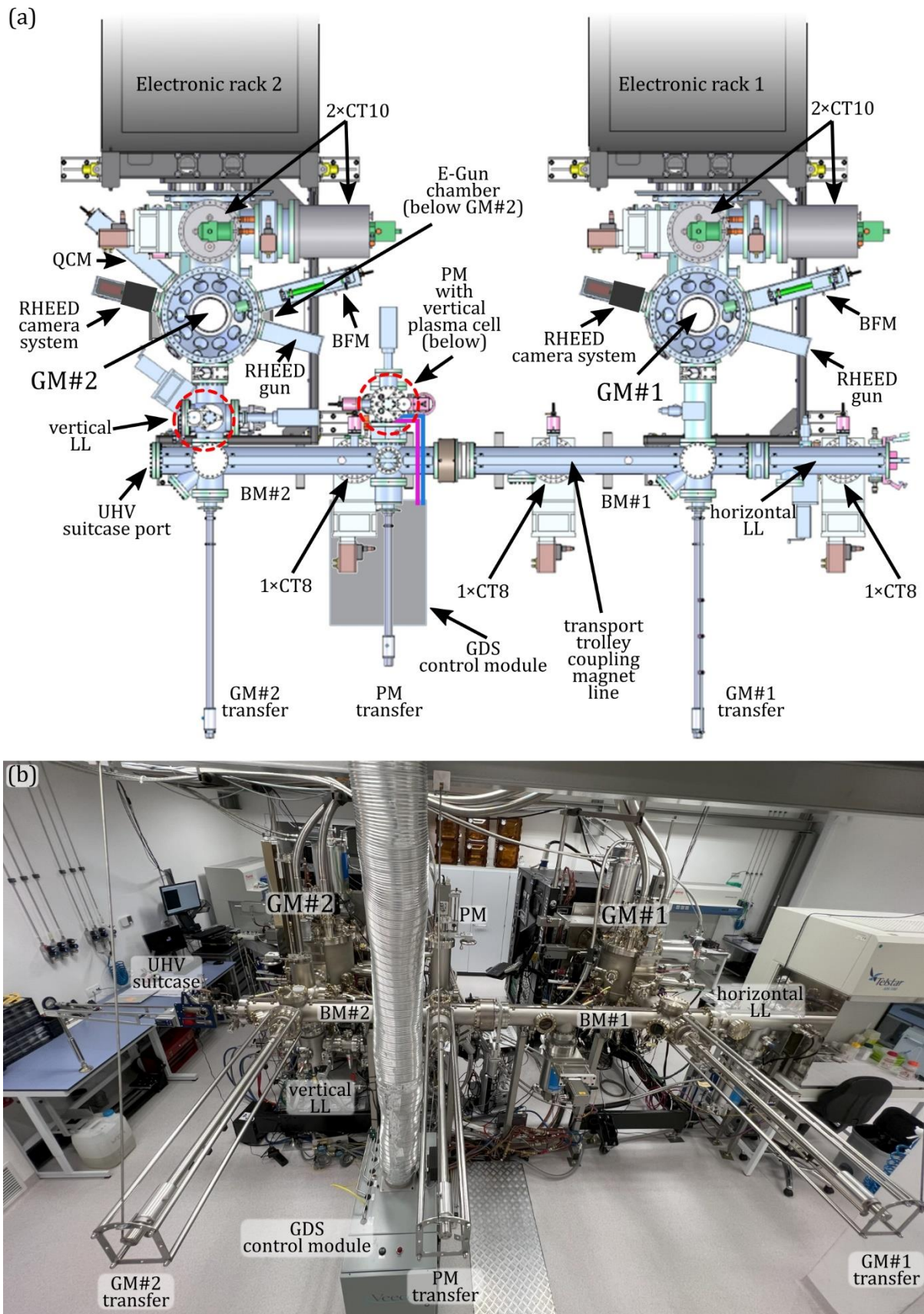
(a)

(b)

Figure 3.3: GM#1, GM#2 and PM manufactured by Veeco. **(a)** Schematic picture of the system by Veeco, with minor image modifications and elements labelling by B. Turowski. **(b)** Photo of the system shown in (a) with main elements labbeled for reference.

PM is a smaller vacuum chamber, without cooling, capable of withstanding a prolonged molyblock bake-out at 550 °C. It is used for the deoxidation of substrates such as GaAs and Si by thermal means or by using a plasma cell supplied with argon (Ar) and hydrogen (H_2) gases through the Gas Delivery System (GDS), shown in **Figure 3.4 (c)**. GM#1 is a twin Growth Module dedicated to materials in groups II-VI. Magnetically coupled trolley (**Figure 3.4 (d)**) and storage lift in the BM#2 (**Figure 3.4 (a)**) allow for transfer of samples between the chambers without air exposure and, consequently, mixed growth of multiple samples in both chambers. The transfer forks of all three modules are similar. In **Figure 3.4 (b)**, the inside of the top part of GM#2 is shown. The ion gauge monitors vacuum in the GM#2 and RGA is used to control composition of the residual gas of the chamber in operating state during and after bake-out. Bake-out is performed after opening the vacuum system for the installation of new components of the system or refilling crucibles of the effusion cells. During opening, the system is pressurized by N_2. During the bake-out, the temperature of the entire chamber is kept at 120 °C to ensure that all possible residual gas contaminants are removed by pumps.
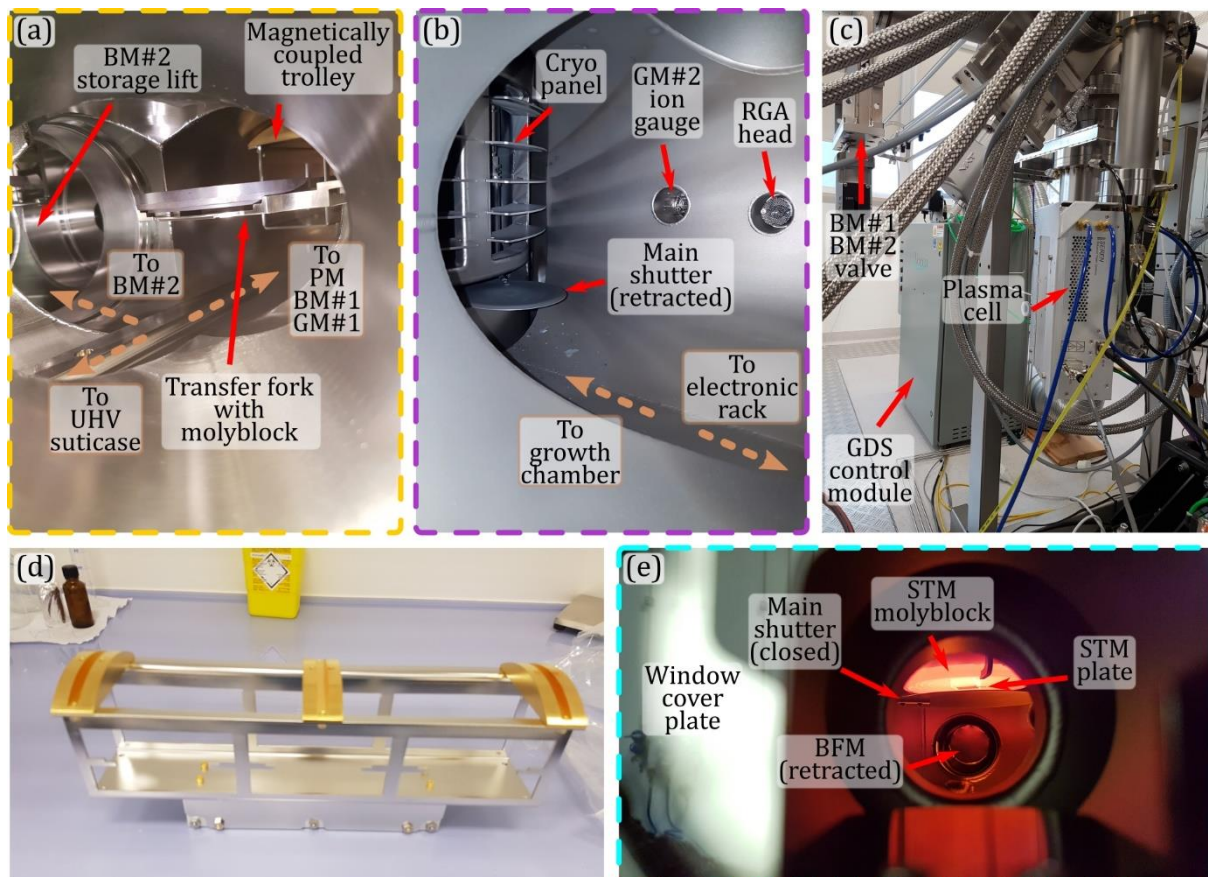

Figure 3.4: UHV components of GM #2 and BM, and bottom view of PM. (a) BM#2 intersection of the magnetically coupled trolley line and the transfer fork line. View through the window marked yellow in **Figure 3.14 (b)**. **(b)** Inside view of the top part of GM#2. Visible cryopanel is above the molyblock holder shown in photo (e). Photo taken through Cryopump port marked purple in **Figure 3.13 (a)**. **(c)** Side view of plasma cell installed in PM. **(d)** Magnetically coupled trolley with space for three substrate holders (molyblocks). **(e)** Photo of the heated STM molyblock at 1000 °C taken through the GM#2 view window (marked light blue in **Figure 3.14 (b)**). Photos by W. Zaleszczyk.

During the growth process, when the substrate holder is kept at elevated temperature, the cryo panel attracts contaminants in the residual gas in the chamber to improve the vacuum conditions. **Figure 3.4 (e)** shows a photo of an STM molyblock heated up to 1000 °C.

Figure 3.5 shows the schematic picture of GM#2. The growth chamber is equipped with ten side and one bottom standard 4.625″ cell ports (numbers 1 to 11 in picture **(a)**) for water enclosures of effusion cells, to which 4.5″ effusion cells are introduced. A bigger port located at the bottom of the growth chamber is housing a vacuum chamber (G1 to G4 in picture **(a)**), custom made by VEECO, to which an additional Telemark E-Beam Multi-Pocket Source with four 15 cm^3 crucibles is mounted.
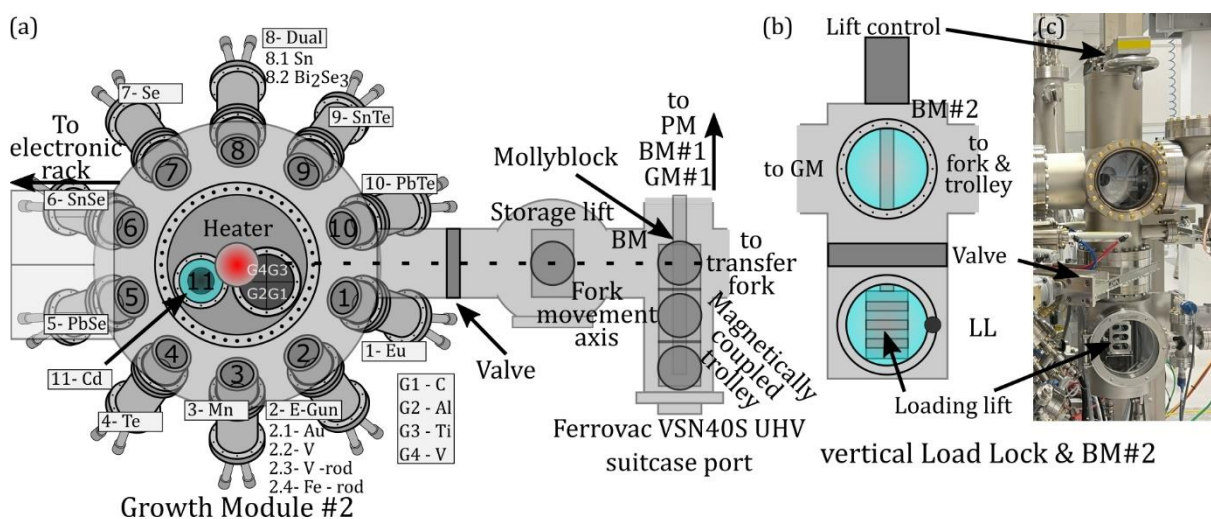

Figure 3.5: Schematic top view of Growth Module #2 and Load Lock (LL). (a) Picture of GM#2 with information on available materials. **(b)** Picture of vertical Load Lock. **(c)** Corresponding photo of vertical Load Lock. Samples are loaded through LL using a removable loading lift with three spots for molyblocks. An additional four molyblocks can be stored in the storage lift in the BM#2. A magnetically coupled trolley is used to transfer samples to and from PM and GM# 1 through BMs.

The growth chamber is equipped with the following effusion cells and crucibles, some of which are presented in **Figure 3.6**.

1. Port 1: EPI-35-LT-DF-DT cell with a 35 cm^3 crucible;
2. Port 2: Mantis QUAD-EV-C Mini e-beam Evaporator –**(d)**;
3. Ports 3-6: VEECO GEN10-400g-SUMO cells with SUMO 400g crucibles - **(a)** and **(c)**;
4. Port 7: GENX-500cc-Se-VC-V Selenium Valved Cracker cell with 500 cm^3 crucible;
5. Port 8: PKG, DUAL 5cc, H2O Dual Dopant Source cell with two 5 cm^3 crucibles –**(b)**;
6. Ports 9 & 10: VEECO GEN10-400g-SUMO cells with SUMO 400g crucibles - **(a)** and **(c)**;
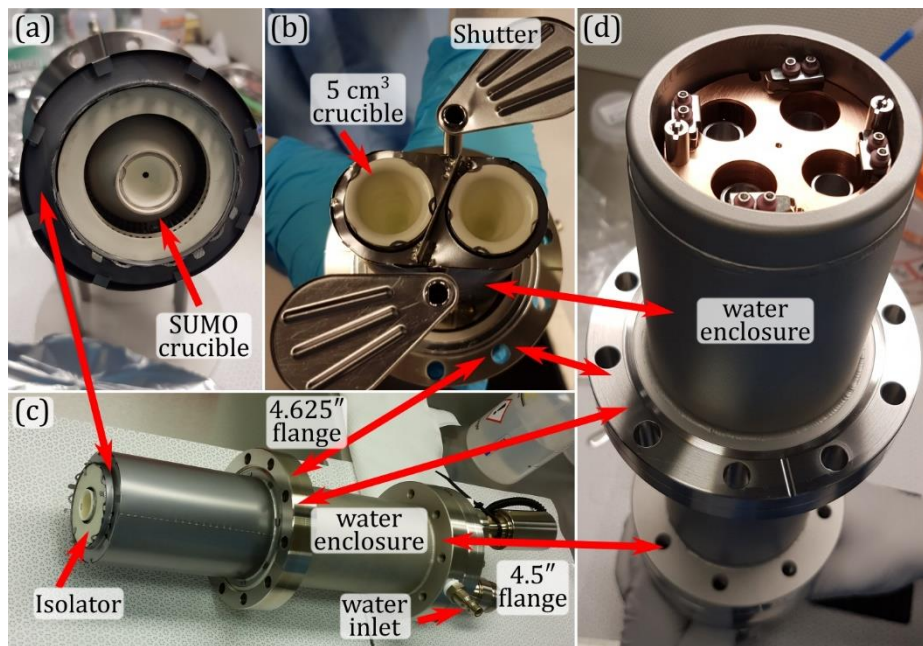7. Port 11: VEECO GENX-35-DF-DT-SP cell with 35 cm^3 crucible.

Figure 3.6: Cells used in the GM #2 system. (a) Front view of the Veeco GEN10-400g-SUMO effusion cell with crucible installed. **(b)** VEECO 5cc Dual Dopant Source cell with crucibles installed. **(c)** Side view of the VEECO GEN10-400g-SUMO effusion cell with flanges of the water enclosure (4.625″) and of the cell (4.5″) marked. **(d)** Top/side view of the Mantis QUAD-EV-C Mini e-beam Evaporator. Common elements indifferent to cell type are marked with blue arrows. Photos are in different scales. Photos by W. Zaleszczyk.

Figure 3.7 shows photos of the crucibles used in GM#2. Conical crucibles (photo **(a)**) are used in the Dual Dopant Source cell, since large volumes of dopant materials are not needed. Because of their higher capacity, cylindrical crucibles (photo **(b)**) are better suited for materials that are used more often. Veeco SUMO crucibles (photo **(c)**) are an alternative for the cylindrical crucibles that provides better long-term flux stability. **Figure 3.8** shows schematic pictures of the crucibles used.
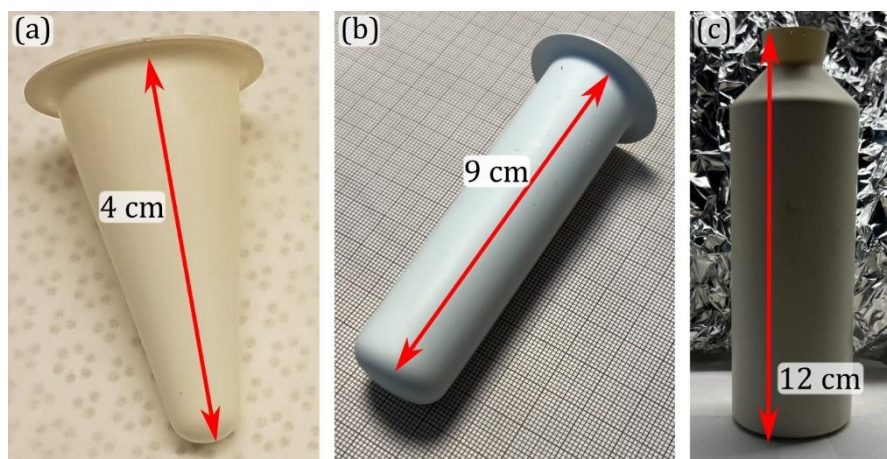

Figure 3.7: Crucibles used in the effusion cells of GM #2 system. (a) Conical 5 cm³ crucible. **(b)** Cylindrical 35 cm³ crucible. (c) Veeco SUMO 400g crucible. Photos are in different scales. Crucibles are made of Pyrolytic Boron Nitride.
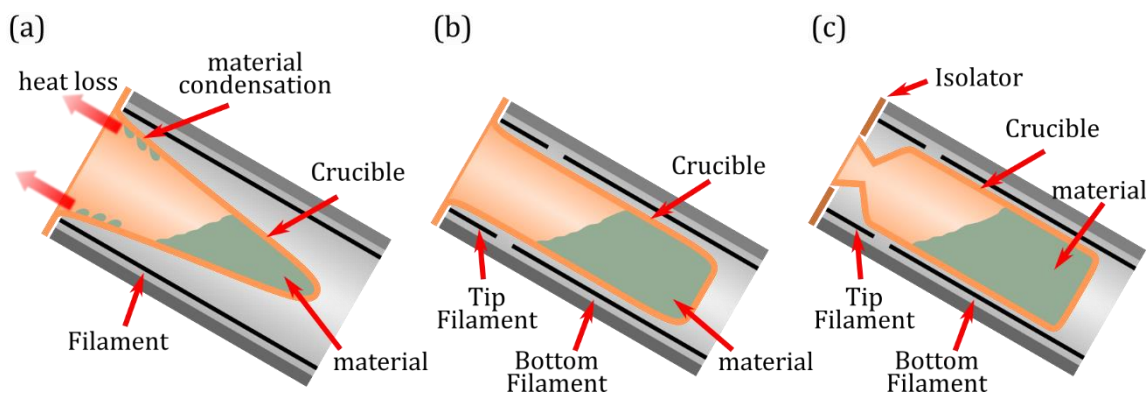
Figure 3.8: Schematic picture of the crucibles used in GM#2. (a) Conical crucible heated by a single filament. The filament uniformly heats the entire crucible. Heat loss in the orifice area causes condensation of the material vapours (see **Figure 3.10 (d)**). **(b)** Cylindrical crucible heated by two filaments. The tip filament keeps the orifice area at elevated temperature, preventing condensation of the vapours of the used material. **(c)** Veeco SUMO crucible heated by two filaments. The reduced orifice ensures stable material flux from the cell. The isolator ensures stable temperature conditions near the orifice.

Conical crucibles are used in the Dual Dopant Source cell mounted to port 8 of the GM#2 (see **Figure 3.5 (a)**). Two conical crucibles heated by separate filaments. This allows for a simpler technical design of the effusion cell, but radiative heat loss near the orifice of the crucible causes condensation of the material vapours; see **Figure 3.10 (d)**. This kind of crucible is also more susceptible to large shutter flux transients. When a shutter blocks the flux from the effusion cell, it reflects some of the heat coming from the cell. When the shutter is opened, the temperature conditions near the orifice area change, affecting the flux stability. Additionally, the flux from such a crucible varies in the long term because of the conical shape of the cell, as different parts of the crucible are in different distance from the filament, and as the active area of evaporation/sublimation of the material changes with time. The active area of the material is constant throughout the use of cylindrical crucibles (**Figure 3.8 (b)**), which corresponds to a better long-term flux stability. To avoid the issue of condensation, an additional filament is used. The bottom filament temperature defines material flux, and the tip filament temperature, 100-200 °C higher than the base temperature, prevents the condensation near the orifice. The cylindrical crucibles also offer greater material capacity. To further improve long-term flux stability, Veeco SUMO crucibles in double filament effusion cells are mainly used in the GM#2; see **Figure 3.8 (c)**. The reduced orifice area, heated by tip filament, ensures stable material flux in the long term, and the isolator near the orifice stabilises temperature in this area to reduce effect of shutter flux transients.

Each port, except for 8, has a pneumatic retractable shutter (see **Figure 3.9 (a)**) that can block the flux and allows independent control of the impingement time of the material onto the substrate. The Dual Dopant Source cell (mounted to port 8) has separate shutters for each of two crucibles (**Figure 3.6 (b)**) that rotate sideways. **Figure 3.9 (b)** shows a photo of a shutter uninstalled for cleaning. During normal operation of the effusion cells, some of the material

deposits on the bottom side of the shutter. It must be removed to prevent it from detaching and falling onto the effusion cell.
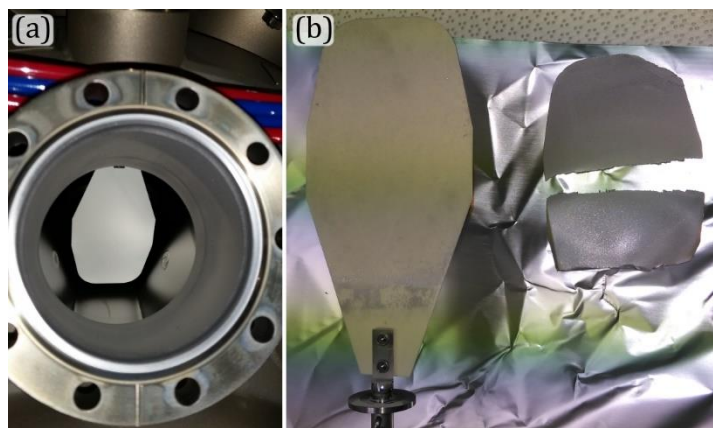

Figure 3.9: Effusion cell shutter. (a) Bottom view of an extended shutter through a cell port. **(b)** Cleaned shutter removed from a growth chamber (left) and cadmium (Cd) deposited on its surface (right) after normal effusion cell usage. The shutter is made of Pyrolytic Boron Nitride. Photos by W. Zaleszczyk.

Effusion cells and shutters are made of Pyrolytic Boron Nitride (PBN). This material has high purity, reaching 99.999% and it does not react with most molten metals, semiconductors, or their compounds. It also has good thermal shock resistance up to 2000 °C and good oxidation resistance below 1000 °C. Additionally, it has a smooth surface with no pores and does not wet with most semiconductor melts.

The following elements and compounds, as shown in **Figure 3.5 (a)** and noted in **Table 3.1**, are available:

Table 3.1: Elements and compounds available in GM #2. M and T stand for Mantis and Telemark e-beam sources, respectively.

Elements	Compounds	E-beam
europium (Eu)	lead selenide (PbSe)	gold (Au) – M
manganese (Mn)	tin selenide (SnSe)	iron (Fe) – M
tellurium (Te)	lead telluride (PbTe)	vanadium (V) – M and T
selenium (Se)	tin telluride (SnTe)	aluminium (Al) - T
tin (Sn)	bismuth selenide (Bi_2Se_3)	titanium (Ti) - T

To ensure high purity of the grown structures, materials of extremely high purity are used in the effusion cells. The purity of a source material is determined by "N number". For example, 6N indicates 99.9999% purity. The materials used in GM#2 are of 4N to 7N purity. **Figure 3.10** shows photos of PnSe (photo **(a)**) and SnSe (photo **(b)**) synthesised directly from 6N Pb, Sn and Se by J. Korczak in IF PAN and used in GM#2. Photo **(c)** shows front view of VEECO GEN10-400g-SUMO cell filled with SnSe shown in photo **(b).** Photo **(d)** shows conical crucible for Sn of Dual Dopant Source Cell after normal use, with condensation of the Sn near the orifice.
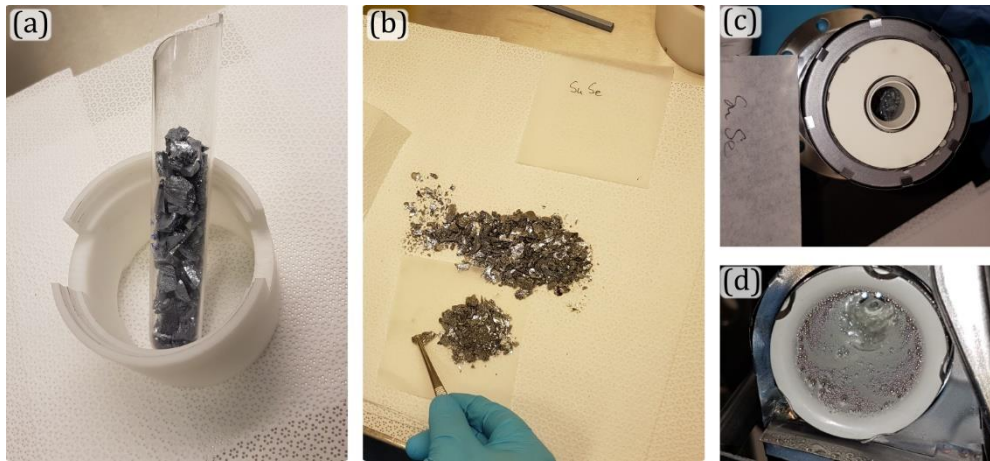
Figure 3.10: Materials in the crucibles. (a) Open ampule with PbSe just before refilling of the crucible.
(b) SnSe in the laminar flow cabinet just before refilling of the crucible. **(c)** Veeco GEN10-400g-SUMO
effusion cell filled with SnSe from photo (b). **(d)** Sn crucible of the Dual Dopant Cell after several months of
operation. Condensation of the Sn near the orifice is visible. The telluride and selenide compounds used in
GM#2 were manufactured by direct synthesis of elements by J. Korczak in IF PAN using 6N Te, Se, Pb and
Sn. Photos by W. Zaleszczyk.

The base pressure in the GM #2 system is better than 10^{-10} mbar and is achieved by the
combination of the liquid N_2 cryo-panel cooling and two Edwards Cryo-Torr 10 (CT10)
Cryopumps, with the pumping speed of 3000 l/s for N_2. Effusion cells are cooled by 16 °C
water passing through water enclosures.

In the MBE, the growth occurs on a substrate attached to a holder that allows for transfer of
the grown sample in the UHV system. Three kinds of 3″ molyblocks are used in the GM#2
setup, as presented in **Figure 3.11**:

1. Hollow (rim) molyblocks **(i)**. These can be used for: growth on 3″ wafers mounted by
   a retainer plate (not shown in the photo) or 2″ wafers with an adapter; growth on
   10×10 mm wafer pieces with **(ii)** molybdenum adapter plate; growth on ¼ of 2″
   wafers with **(iii)** molybdenum adapter plate;
2. Full in-bond molyblocks **(iv)** to which substrates are attached by a sticking agent such
   as In-Ga eutectic;
3. STM molyblocks **(v)** that allow insertion of STM Scienta Omnicron type plates,
   photo **(c)**.

Samples grown on STM plates were transferred to a Ferrovac VSN40S ultra-high vacuum
(UHV) suitcase (with a base pressure of 2×10^{-11} mbar). It allows for transfer of samples
between different setups (in this case, GM #2 in Warsaw and URANOS and PHELIX in SOLARIS
Kraków) without exposing the surface to the air, which is crucial in case of topological
materials. The UHV suitcase has twelve STM plate slots and is capable of maintaining a
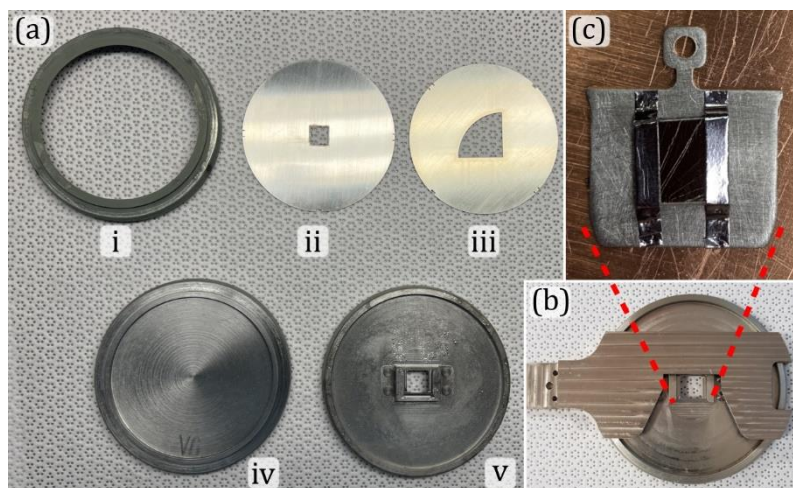10^{-11} mbar vacuum for long periods.

Figure 3.11: Sample handling in the GM #2 system. (a) Used molyblocks: **(i)** hollow molyblock for growths on full 3″ wafers and on 2″ wafers, using the proper adapter; **(ii)** adapter for 10×10 mm pieces; **(iii)** adapter for quarter of 2″ wafer; **(iv)** standard 3″ full molyblock used for growths on substrates attached by sticking agent In-Ga; **(v)** 3″ STM holder used for growths on substrates attached to STM plates. **(b)** Cut-out transfer fork compatible with both standard and STM molyblocks (shown for a size reference). **(c)** Scienta Omnicron Molybdenum STM plate with sample attached by welded tantalum strips. Photos (a) and (b) are in scale. For a size reference of photo (c), see dashed black lines.

The standard preparation procedure before the growth in the GM #2 system consists of the following steps:

1. Substrate attachment to molybdenum holder (molyblock);
2. Placing molyblocks onto removable Loading lift and moving it into Load Lock (LL);
3. LL pumping with optional bake-out;
4. Rising up Loading lift and removal of chosen molyblock by transfer fork;
5. Transfer of the molyblock to the Growth Chamber, at the Heater position.
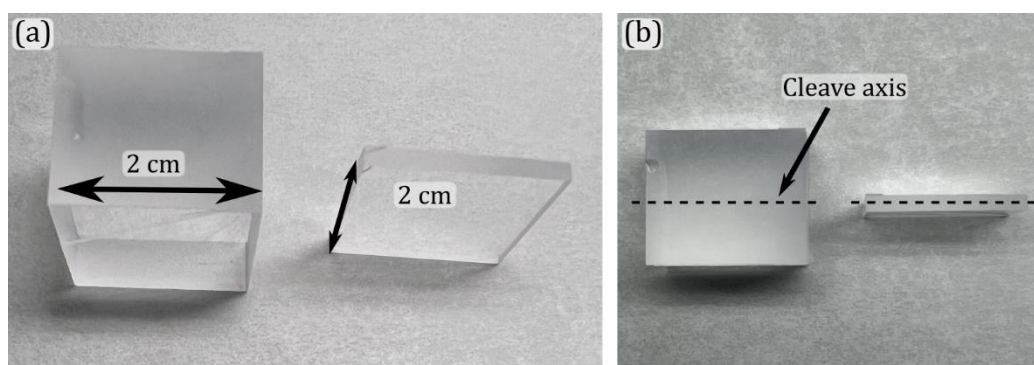

Figure 3.12: BaF$_2$ (111) oriented 2×2 cm bulk crystal from Korth Kristalle GmbH. **(a)** Front view. **(b)** Top view with cleave axis in the middle of the bulk crystal.

Step 1: In the case of BaF$_2$ and KCl substrates, 0.5 mm thick plates are cleaved from the bulk crystal of Korth Kristalle GmbH (see **Figure 3.12** for the BaF$_2$ photo) with a sharp razor blade. Bulk crystals are always cleaved in the middle to obtain two fresh surfaces. The cleaving

procedure of the final, 0.5 mm thin plates requires a great deal of precision and experience. The plates are then attached to the molyblock using In-Ga eutectic for improved heat transfer between the molyblock and substrate.

Step 2: The loading lift is removed from the LL and molyblocks are placed into it. Meanwhile, the LL is kept under a constant flow of room temperature N_2. After moving the lift to LL N_2 flow is shut off and the scroll pump starts pumping LL volume. When the pressure of 10^{-2} mbar is reached, the turbo pump is activated.

Step 3: LL is pumped to up to 10^{-9} mbar. It may also be baked to 250 °C if needed.

Step 4: after reaching a sufficiently high vacuum, the valve between LL and BM is opened, and the loading lift is lifted. Molyblocks can be removed using a transfer fork. They can be placed on a top lift or in a magnetically coupled trolley or be transferred to the growth chamber.

Step 5: The molyblock is moved to the heater position in the growth chamber; the heater is lowered to ensure proper heating of the molyblock and the sample.

GM#2 is equipped with the BFM and the QCM for the precise measurement of the fluxes coming from effusion cells. Both devices are retractable, and during measurement, either of them is placed in front of the substrate position, while the main shutter shields the sample. BFM allows to precisely measure the materials flux ratio used to calculate composition of the grown samples. QCM gives precise information about the deposition rate (in Å/s) and the flux ratio.

3.1.2   Growth Module #2 development

During the PhD studies, I was involved in launching and upgrading the Growth Module #2 MBE system. In 2017, GM#2 was a chamber with only vacuum gauges, pumps, BFM and RHEED gun and screen installed (with custom camera system), as shown in **Figure 3.13 (a)** and **(c)**. During the preparation for the launch of the GM#2 and during the operation of the system, I participated in the following:

- Installation of effusion cells and cell shutters;

- Installation of the Quartz monitor (QCM);

- Installation of CT10 Cryopump (horizontal) and exchange of CT8 Cryopump to CT10 Cryopump (vertical);

- Installation of the base flange, modified to accommodate a smaller vacuum chamber for the Telemark E-Beam Multi-Pocket Source;

- Installation of the vacuum chamber for the Telemark E-Beam Multi-Pocket Source and the respective Telemark Source;

- Exchange of the RHEED screen and installation of the kSA 400 RHEED camera system;

- Installation and adjustments of the BandiT temperature monitoring tool for both GM#1 and GM#2;

- Installation, testing, and operation of Ferrovac VSN40S UHV suitcase;

- Exchange of the GM#2 transfer fork for the cut-out one (see **Figure 3.11 (b)**);

- Installation of the Hydrogen/Nitrogen plasma cell to the PM (**Figure 3.14 (c)**) and subsequent testing and setting of the working conditions.

I was also involved in everyday maintenance of the GM#2 system, as well as I participated in all openings and bake-outs of the system done in order to install new equipment or to refill the depleted sources. **Figure 3.13** shows photos of the GM#2 in 2017, before I started PhD studies (photos **(a)** and **(c)**), and in July 2023 (photos **(b)** and **(d)**).
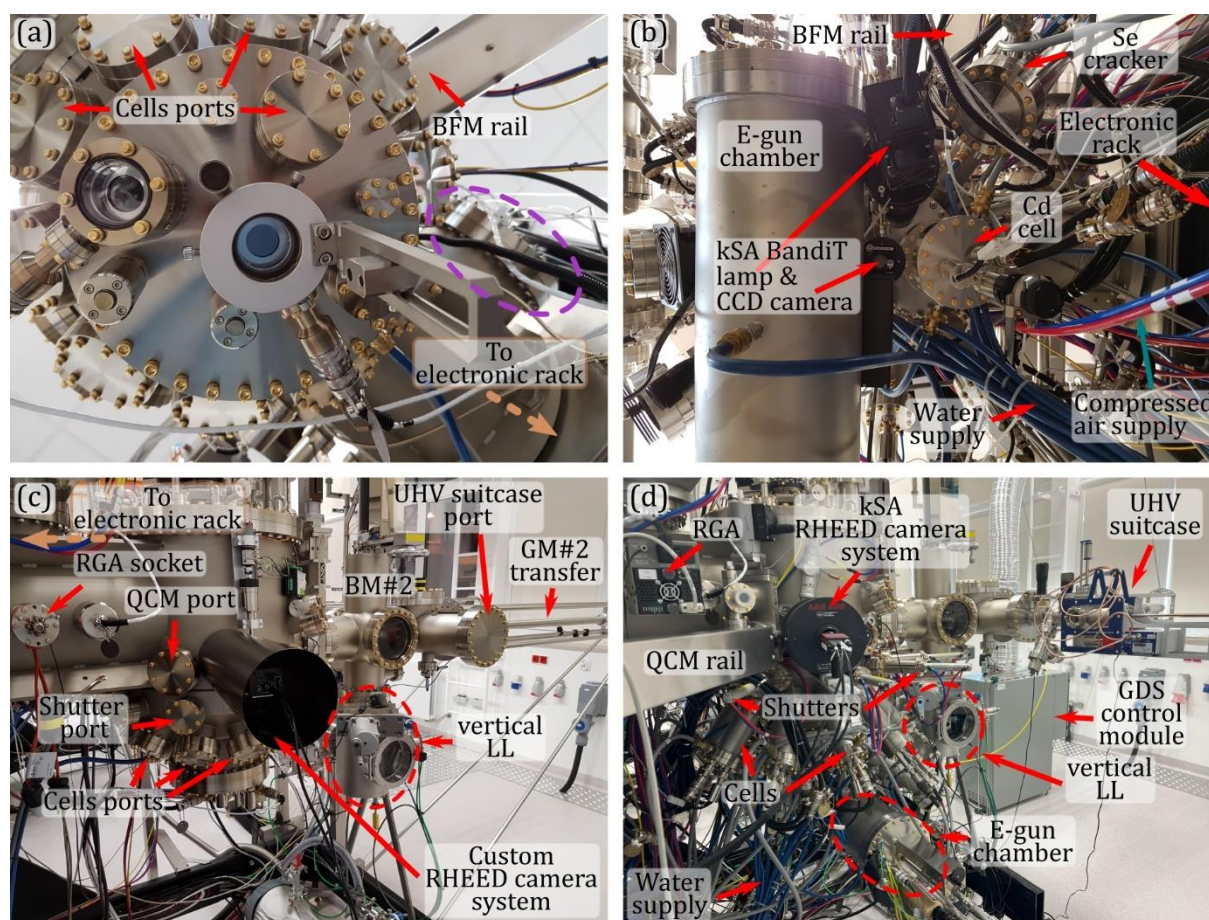

Figure 3.13: Changes of GM#2 over 2017-2023 with main elements labelled. **(a)** bottom view of GM#2 in January 2018. Only vacuum gauges, BFM, RHEED gun, and CT8 pump (last two not visible in the photo) were installed. The purple ellipse marks the port for the CT10 pump installed later. Image **Figure 3.4 (b)** shows the inside of GM#2 visible through this port. **(b)** Bottom view of GM#2 in July 2023. Multiple new elements were installed over 5 years. **(c)** Side view of GM#2 in November 2017. **(d)** Side view of GM#2 in July 2023. Abbreviations are explained in text. Photos by W. Zaleszczyk and B. Turowski.
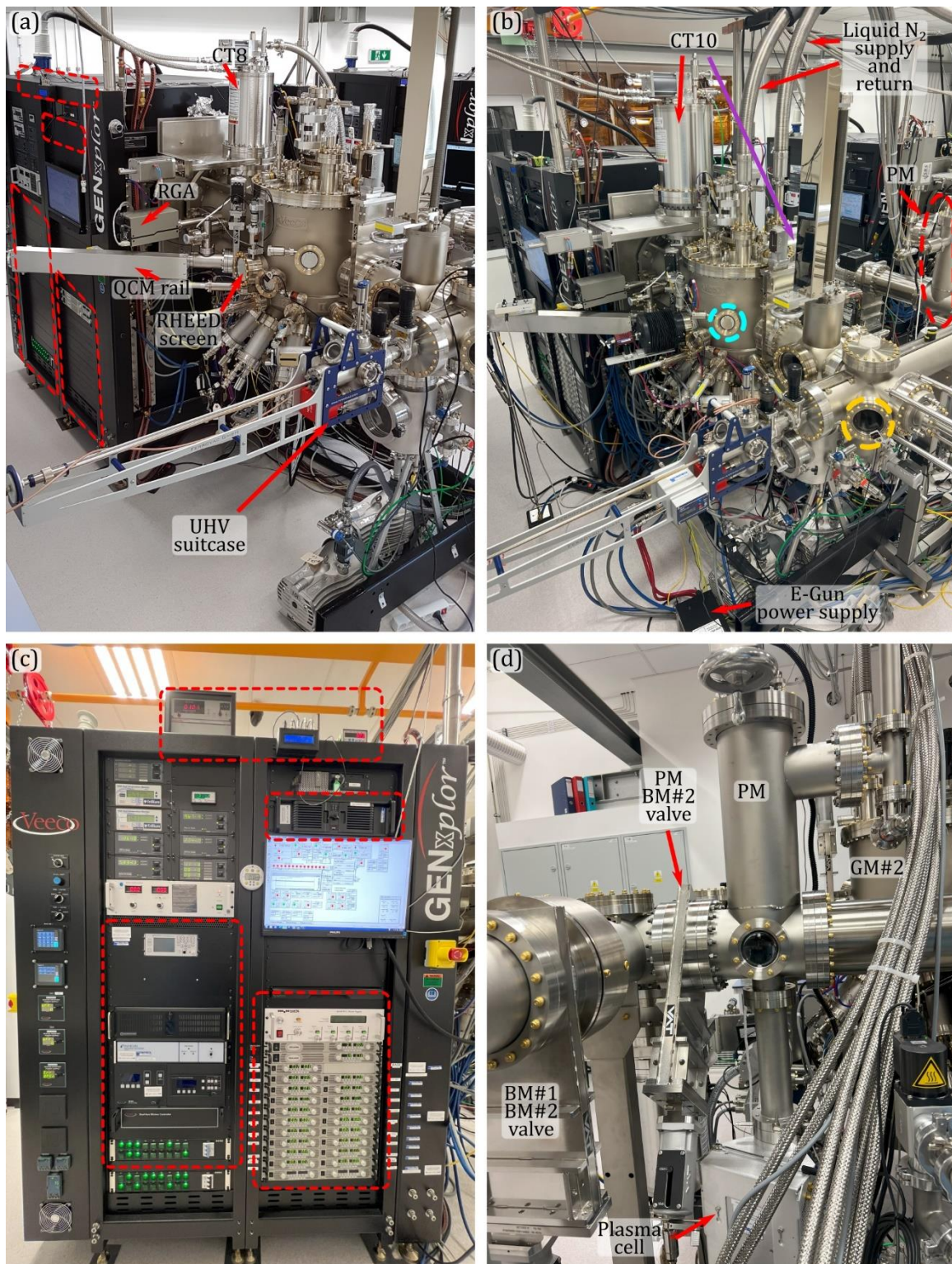
Figure 3.14: Vacuum systems upgrades. (a) Side view of GM#2 in October 2019 during the installation of the effusion cells. Red dashed rectangles mark electrical components that were not yet installed at that time. **(b)** Side view of GM#2 in July 2023. For the clarity of the image, the elements visible in **Figure 3.13** are not labelled. The purple arrow points to the CT10 pump installed in the port marked in **Figure 3.13 (a)** with a purple ellipse. The yellow dashed circle is a view window of BM#2, the light blue dashed circle is a view window of GM#2 growth chamber. **(c)** Electronic rack of GM#2 in in July 2023. Red dashed rectangles correspond to the same rectangles in image (a). **(d)** Side view of the PM. Plasma cell was installed in 2020**.**

Figure 3.14 shows different angle photos of the GM#2 system comparing its current state (photos **(b)** and **(c)**) with its state just before it became operational in October 2019 (photo **(a)**). Red dashed rectangles show, which electronic components were installed in this period: water-cooling monitoring system for Mantis mini E-gun, control unit for kSA BandiT temperature monitoring system, control units for QCM, control unit for plasma source, control unit for Telemark E-Beam Multi-Pocket Source, power supply controllers for all effusion cells. I was involved in all upgrades to the electrical rack. **Figure 3.14 (c)** shows a side view of PM with the plasma source installed below.

In parallel to my research, I wrote multiple scripts and programmes that are being used in the MBE laboratory where I worked. They range from useful to important in everyday work. Details about these are given in **Appendix C**.

3.1.3   MBE growth of $Pb_{1-x}Sn_xSe$ epilayers

Epitaxial growth of $Pb_{1-x}Sn_xSe$ films for ARPES studies was conducted in three MBE systems: Riber 1000, PREVAC 190 and Veeco GENxplor GM#2. In the first one, the samples were grown by V. V. Volobuev on (001) KCl and (111) BaF_2 substrates. In the second one, the samples were grown by V. V. Volobuev and me on (001) KCl and (111) BaF_2 substrates. In the third one, the samples were grown by me, under the supervision of V. V. Volobuev, on (111) BaF_2 substrates. The samples were grown in two technological processes, presented in **Figure 3.15**. In Riber 1000 and PREVAC 190, the samples were grown in steps 1) to 5). In Veeco GENxplor GM#2 the samples were grown in steps 1), 2), 5), since the Ferrovac VSN40S UHV suitcase (see **Section 3.1.5**) allowed for the transport of the samples to the synchrotron facility under UHV conditions. The following technological steps were performed to produce the samples studied:

1) Substrate preparation
2) $Pb_{1-x}Sn_xSe$ growth
3) Amorphous Se cap deposition
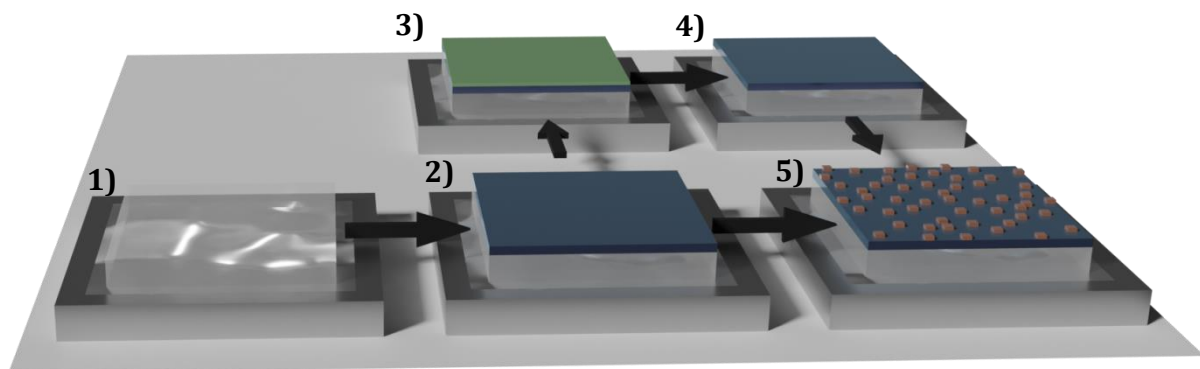4) Amorphous Se decapping
5) Submonolayer transition metal deposition

Figure 3.15: $Pb_{1-x}Sn_xSe$ Sample manufacturing process, with five steps presented.

Step 1: Half millimetre thick square pieces of (111) BaF_2 or (001) KCl (shown as semi-transparent white rectangular right prism) were freshly cleaved from the bulk crystal of Korth Kristalle GmbH to be used as a substrate. They were placed on a molyblock (molybdenum sample holder) or an STM plate with an In-Ga eutectic layer to both improve thermal contact with the molyblock and stick substrate to the holder.

Step 2: 1 µm $Pb_{1-x}Sn_xSe$ films (marked by a dark blue colour) were grown under the conditions given in **Table 3.2**.

Step 3 and 4: Samples grown in the Riber 1000 and PREVAC 190 systems were capped with amorphous Se (marked by green colour) deposited at room temperature to seal the epitaxial film from the air to prevent surface contamination during transport to the synchrotron facility. The selenium cap was then removed in the UHV chamber in the synchrotron facility by heating the sample to 250-330 °C and keeping it at this temperature for 20-60 minutes.

Step 5: Either Mn or Fe (marked by orange colour) transition metals (TM) were deposited on $Pb_{1-x}Sn_xSe$ thin films in 0.075 or 0.15 Å steps.

The comparison of basic technical parameters of growth in the systems discussed is given in **Table 3.2**.

Table 3.2: Comparison of basic technical parameters relevant to the growth of 1 µm thick $Pb_{1-x}Sn_xSe$ epilayers in discussed the MBE systems.

MBE system	Sources	Growth rate	Material flux measurement	Bi doping	MBE growth temperature	UHV [mbar]
Riber 1000 [99]	Stoichiometric PbSe, SnSe	~1 µm/hour	QCM	Bi_2Se_3 effusion cell	380 °C	$<5\times10^{-10}$
PREVAC 190 [100]	Elemental Pb, Sn, Se	~0.1 - 0.3 nm/s (~0.4 - 1 µm/hour)	Flux monitor	-	325 – 365 °C	$< 10^{-9}$
Veeco GENxplor [15]	Stoichiometric PbSe, SnSe	~0.2 nm/s (~0.7 µm/hour)	Flux monitor, QCM	(0.07 - 0.1%) Bi_2Se_3 effusion cell	350-380 °C	$< 10^{-10}$

The material flux ratio was controlled by calibrated BFM or QCM placed in front of the substrate position. The Sn content was in ±1% agreement with the Energy Dispersive Spectroscopy (EDS) and XRD measurements for samples grown in the Veeco GENxplor GM#2 system. In $Pb_{1-x}Sn_xSe$ the native background hole concentration increases strongly with increasing Sn content, resulting in p-type samples. To compensate for this effect and obtain both p-type and n-type thin films, Bi doping was introduced from the Bi_2Se_3 effusion cell in the Riber 1000 and Veeco GENxplor GM#2 systems. The growth temperature varies in different systems due to their specific architecture, but is in a comparable range. In the

Riber 1000 system, the growth temperature was determined by the IRCON IR pyrometer. In the PREVAC 190 system, the growth temperature was determined as a function of the heater temperature, using the heater characteristic (see **Figure 3.16**) created with the use of melting points of indium (In), tin (Sn), lead (Pb) and deoxidation temperature of GaAs. In the GM#2 system, an Ircon 6000 series Modline Plus infrared pyrometer calibrated with the temperature of a molybdenum plate was used.
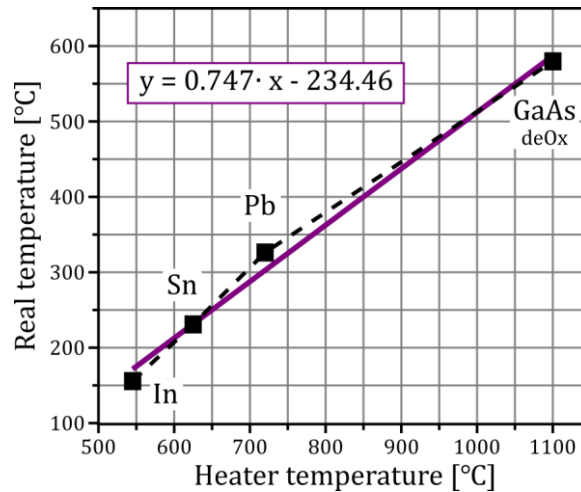

Figure 3.16: PREVAC 190 MBE heater temperature calibration. In, Sn and Pb data points mark melting points of indium, tin, and lead, respectively. GaAs deOx point marks of the GaAs surface oxides desorption temperature observed by RHEED.

$Pb_{1-x}Sn_xSe$ was grown using full 3″ in-bond molyblocks and 3″ STM holders with Scienta Omnicron Molybdenum STM plates (**Figure 3.11 (a) (iv)** and **(v)**, respectively). Full molyblocks were used for samples that were examined by XRD, SEM, and AFM, while STM holders were used for samples that were examined by ARPES and SR-ARPES. The Se cap was also used for samples grown in GM#2 to protect the epilayer surface for XRD measurements.

3.1.4   MBE growth of α-Sn epilayers

The epitaxial growth process of α-Sn thin films was conducted in several steps in the PM, GM#1 and GM#2 systems, on epi ready semi-insulating (001) GaAs substrates from AXT, Inc. with thick CdTe buffers. The growth was performed in ultra-high vacuum, better than 5×10^{-10} mbar. Effusion cells with elemental 7N Cd, Zn and Te in GM#1 and Sn in GM#2 were used as sources. In the GM#1 system calibrated BFM, and in the GM#2 system the calibrated QCM, were used to control the material flux ratio and growth rate. The CdTe (001) buffer was prepared in PM and GM#1 by R. Rudniewski in steps 1) to 3), and α-Sn was grown by V. V. Volobuiev, with my participation, in GM#2 as described below:

1) Thermal deoxidation of GaAs (001) in PM;
2) Epitaxial growth of a thin (several nanometre) layer of zinc telluride (ZnTe) in GM#1;
3) Epitaxial growth of CdTe buffer in GM#1;

4) Epitaxial growth of α-Sn thin film in GM#2.

Step 1: The rectangular piece of semi-insulating GaAs (001) was cut from 2″ wafer and attached to the STM plate (**Figure 3.11 (c)**). It was introduced to PM where it was thermally deoxidized at 590 °C, a few degrees above GaAs oxide desorption temperature of 582 °C **[101]**.

Step 2: Due to the fact, that CdTe can grow on (001) GaAs in both [111] and [001] crystal direction and a significant lattice mismatch between GaAs ($a_0 = 5.654$ Å) and CdTe ($a_0 = 6.482$ Å), several nanometre layer of ZnTe ($a_0 = 6.106$ Å) was grown on the GaAs substrate at CdTe growth temperature. This thin layer determines (001) growth and suppresses growth of the (111) phase **[102]**. It also reduces the compressive stress of the CdTe films caused by the lattice mismatch between GaAs and CdTe **[103]**.

Step 3: The growth of 5 μm thick CdTe buffer with the growth rate of 0.185 nm/s was carried out at the substrate temperature of 295-325 °C, measured by the kSA BandiT temperature monitoring system. A sufficient thickness of the CdTe film results in a fully relaxed layer **[104]**. After CdTe buffer growth, the hybrid substrate was transferred to GM#2 system, through the UHV buffer chambers (BM#1 and BM#2, **Figure 3.3**).

Step 4: The growth of a thin (30 – 200 nm) layer of α-Sn, with the deposition rate of 0.004 nm/s at the substrate temperature of 10 °C, measured by kSA BandiT temperature monitoring system. The temperature characteristics of GaAs and CdTe were provided by kSA company.

The schematic of the grown sample is shown in **Figure 3.17**. The lattice mismatch between α-Sn ($a_0 = 6.490$ Å) and CdTe ($a_0 = 6.482$ Å) causes a compressive in-plane stain of -0.1% that shifts the system toward the Dirac semimetal phase. Details of this are discussed in **Section 4.4.2**.
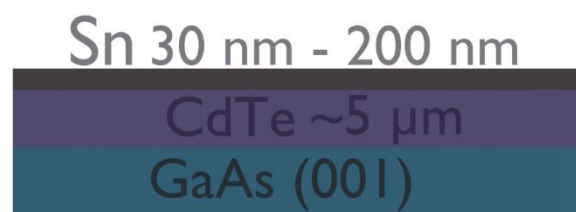

Figure 3.17: Schematic structure of α-Sn thin layer grown on CdTe buffer.

3.1.5   Ultra high vacuum suitcase

The Ferrovac VSN40S UHV suitcase **[105]** was used to transfer the samples from the MBE system to the synchrotron facility while preserving pristine surfaces of the samples **[83]**. The main elements of the suitcase are presented in **Figure 3.18**. The suitcase is equipped with a vertical storage unit capable of holding 12 standard Scienta Omnicron-type STM plates

(**Figure 3.11(c)**) with samples. The samples are moved in and out of the suitcase with a magnetically driven wobble stick manipulator. The manipulator can rotate by 360 degrees along its main axis. It ends with pincers that safely hold the plate by the ring while allowing for small movement of the plate. When combined with vertical and horizontal wobble of the transfer rod (wobble stick), it allows for precise control over the STM plate in different systems.
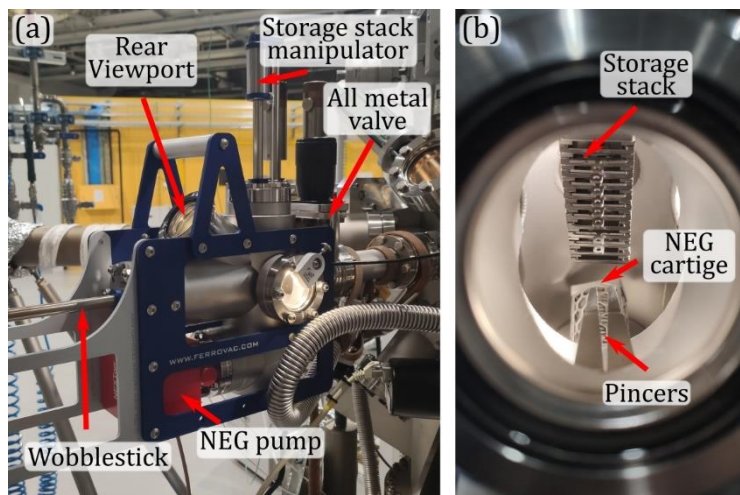

Figure 3.18: UHV suitcase elements. (a) Main elements of the UHV suitcase. **(b)** Rear Viewport view at storage stack. Photos by M. Zięba.
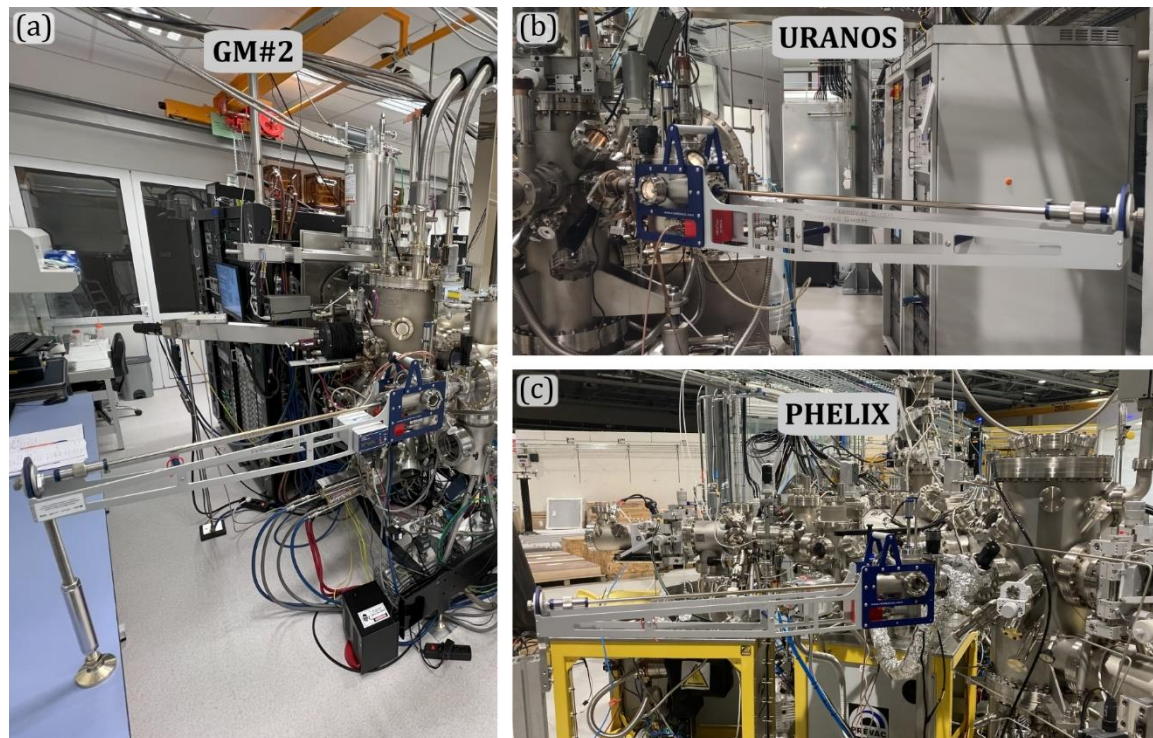

Figure 3.19: Ferrovac VSN40S UHV suitcase attached to **(a)** GM#2 MBE Buffer Module, **(b)** URANOS (former UARPES) beamline Preparation Chamber, **(c)** PHELIX beamline Preparation Chamber.

The UHV suitcase is capable of maintaining 10^{-11} mbar vacuum for long time thanks to the build-in combined NEG/Ion pump technology (NEG-Non Evaporable Getter). A pre-pumped all-metal valve is used to seal the suitcase during the transfer between UHV systems. The suitcase attached to the discussed UHV systems is shown in **Figure 3.19**.

3.2   Reflection High-Energy Electron Diffraction

Reflection High-Energy Electron Diffraction (RHEED) is an analysis technique used in MBE systems for in-situ real-time quality assessment of a structure during the growth process. Shape, intensity and arrangement of features (spots and streaks) present in the RHEED pattern give information about atomic arrangement, flatness of the surface, presence of domains, growth mode, and rate. **Figure 3.20** shows the schematic of a RHEED setup (upside down), with the main elements labelled. A beam of high-energy (in GM#2 accelerating voltage of 15 kV is used) electrons (e⁻), coming from an electron gun, is directed by and adjustable magnetic focusing lens and deflection coils, at a small variable glancing angle θ (1° - 3°), at the surface of the sample where it is diffracted on atoms composing the surface. Diffracted electrons form an interference pattern on a perpendicularly placed luminescent detector (fluorescent screen) **[106]**. The sample can be rotated azimuthally (ϕ) to obtain electron diffraction from different intersections of the crystal lattice of the material and, in turn, to find certain patterns corresponding to the crystallographic orientation of the surface and the azimuthal angle ϕ.
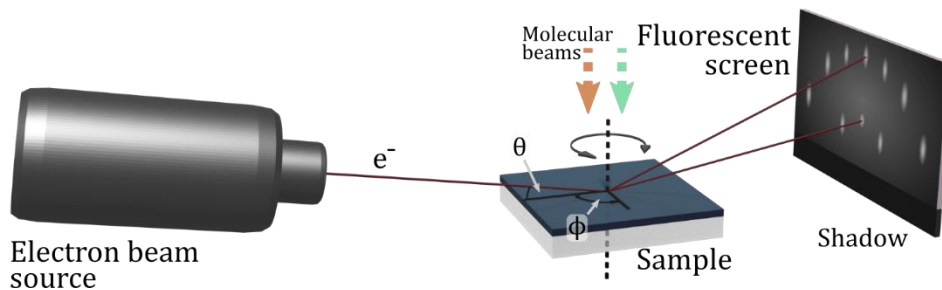

Figure 3.20: Schematic of a RHEED setup (shown upside down)**.**

When diffraction is described, electrons are considered a wave, according to the wave-particle duality. The de Broglie wavelength of electrons accelerated by voltage V (in volts) is given by the following approximation **[96]**:

$$\lambda_B \approx \frac{12.247}{\sqrt{V \cdot (1 + V \cdot 10^{-6})}} \; [\text{Å}] \tag{3.3}$$

Assuming accelerating voltage V = 15 keV, the wavelength of the electrons is approximately 0.1 Å, which is smaller than the lattice constants of crystals grown by MBE (for example, for PbSe a = 6.12 Å, and the interplanar distance is 3.6 Å). This is especially important for the explanation of the origin of the RHEED features. **Figure 3.21** shows the relationship, by the

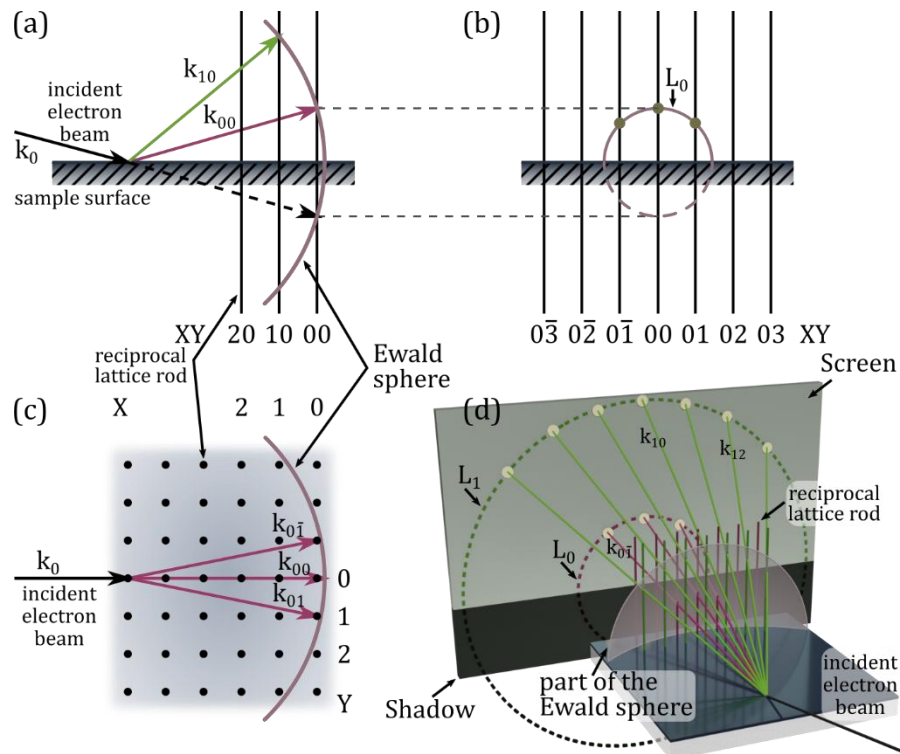Ewald construction formalism, between the RHEED pattern and the reciprocal space of the material studied.

Figure 3.21: Origin of RHEED features. (a) Side and **(c)** top view of the sample surface (shaded dark blue) and its reciprocal space and Ewald construction. **(b)** Intersections of Ewald sphere with 0th reciprocal lattice rods showing formation of 0th Laue circle. **(d)** 3D view of the Ewald construction concept presented in (a), (b), and (c) with wave vectors extended to the screen plane. L_0 and L_1 denote the 0th and 1st Laue circles, k_{XY} denote wave vectors that go through intersections between the Ewald sphere and XY reciprocal rods.

The main assumption of this formalism is a restriction to elastic scattering of the electrons. Under this condition, the magnitudes of all wave vectors of diffracted waves k_{XY} are the same as the wave vector of the incident electron beam k_0:

$$|k_0| = |k_{XY}| \tag{3.4}$$

The Ewald sphere is formed by end-points of the $|k_{XY}|$ drawn from the diffraction origin (see **Figure 3.21 (a)** and **(c)**). The constructive interference of the diffracted waves occurs for the waves, which wave vectors intersect with the reciprocal lattice of the material (i.e. points at which Ewald sphere intersects with the reciprocal lattice). Due to the small grazing angle θ, the beam interacts mainly with topmost layer of atoms. In the simplified approach, the surface of the sample can be assumed to be two-dimensional. Because of that, its reciprocal space is represented by regularly spaced, infinitely thin parallel rods that stand perpendicular to the sample surface (see **Figure 3.21 (a)** and **(d)**). The intersection points of the Ewald sphere with the reciprocal lattice lay on concentric circles, called Laue circles (see **Figure 3.21 (b)**), and appear as diffraction spots on the screen. Because of sample shadowing of the beam, only half-circles are visible. Consequently, the RHEED pattern from a 2D surface is always arranged

on the semicircles. The number of diffraction spots and their spacing depend on the radius of the Ewald sphere and the spacing of the reciprocal lattice rods. For V = 15 keV the radius of the sphere is approximately 63.5 $Å^{-1}$ ($2\pi/\lambda_B$) and for PbSe the distance between the rods is 1.03 $Å^{-1}$ ($2\pi/a_{PbSe}$), which provides a good resolution of observation.

The above description assumes ideal conditions and a perfectly flat surface. During real growth, the Ewald sphere has some finite thickness due to convergence of the beam and the electron energy spread. Similarly, the thickness of the reciprocal lattice rods is finite because of lattice imperfections and thermal vibrations. This results in elongation of the diffraction spots in a direction perpendicular to the shadow edge on the screen and formation of a streaked pattern.
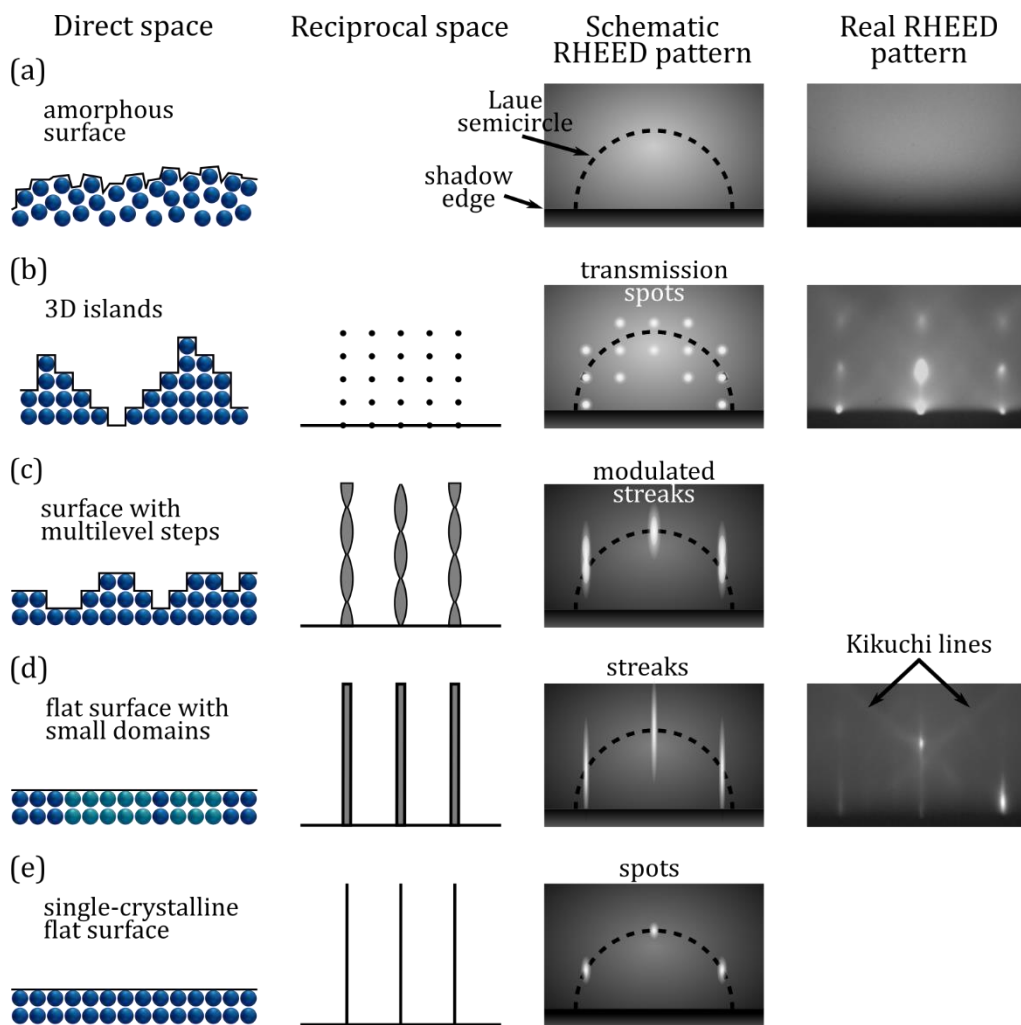

Figure 3.22: Schematics of realistic surfaces relevant for this thesis with corresponding reciprocal space, and schematic and real RHEED patterns. **(a)** Amorphous surface lacking long-range ordering of the atoms. Real RHED image of amorphous Se deposited on (111) $Pb_{1-x}Sn_xSe$. **(b)** 3D islands. Real RHEED image of $Pb_{1-x}Sn_xSe$ deposited on BaF_2 recorded along [112] azimuth. **(c)** Multilevel stepped surface. **(d)** Flat surface with out-of-phase domains smaller than the coherence length of the electron beam. Different colour atoms (blue ● and cyan ●) denote the domains. Real RHEED image of $Pb_{1-x}Sn_xSe$ grown on BaF_2 recorded along [112] azimuth. **(e)** Flat, single-crystalline surface. Image based on Ref. **[107]**.

Figure 3.22 shows some of the possible RHEED patterns with the corresponding schematic images of the surface and its reciprocal space. Image **(a)** shows the RHEED pattern of amorphous Se deposited at RT on $Pb_{1-x}Sn_xSe$. As expected, no spots or streaks are present, as no diffraction can occur from the amorphous surface. Image **(b)** shows a surface with 3D islands and its reciprocal space, which is the same as in case of 3D crystal, i.e. 3D array of reciprocal points. The resulting RHEED pattern is in the form of transmission spots because the electron beam transmits through protruded parts of the islands and it is no longer a reflection diffraction pattern. Image **(c)** shows that the presence of multilevel steps on the surface causes the modulation of the reciprocal rod thickness that depends on the step height **[108]** and results in modulated streaks in the RHEED pattern. Image **(d)** shows most common RHEED pattern obtained for high quality 2D layers. The presence of small out-of-phase domains **[107]** or any disorder on the surface **[109]**, such as the presence of terraces **[108]**, results in increased thickness of the reciprocal rods and broadening of the diffraction spots, which is stronger in the direction of the beam **[109]**, that is, perpendicular to the shadow edge on the fluorescent screen. Image **(e)** shows reciprocal space and schematic RHEED pattern from a single-crystalline flat surface. The diffraction spots in the expected RHEED pattern are slightly broadened because of the finite thickness of the Ewald sphere, as mentioned above.

Observation of the RHEED pattern during growth allows for a qualitative evaluation of the epilayers. If the observed pattern differs from the expected one, the process can be stopped and started anew.

3.2.1   RHEED pattern simulation

Using the Ewald sphere construction explained in the previous section, RHEED patterns can be calculated. However, simulation of realistic looking RHEED patterns requires an approach that simulates non-infinite thickness of the reciprocal space rods (see **Figure 3.22**). In order to do that, RHEED patterns were simulated with custom written Python script using the general structure and transformation proposed in Ref. **[110]**:

$$x = \frac{k_0 x_d}{\sqrt{d^2 + x_d^2 + y_d^2}} \tag{3.5}$$

$$y = k_0 \left(-\frac{d}{\sqrt{d^2 + x_d^2 + y_d^2}} + \cos\theta \right) \tag{3.6}$$

where x and y are coordinates of the reciprocal space of the sample surface, k_0 is the wave vector of the electrons (see **Equation (3.4)**), d is the distance between the sample and the fluorescent screen, x_d and y_d are the coordinates of the RHEED image on the fluorescent screen, and θ is the angle of incidence of the electron beam. The above system of equations is the geometric projection of the 2D x, y image of the reciprocal space rods through a 3D Ewald sphere of radius k_0 (with origin of the sphere shifted by $k_0 \cdot \cos\theta$) to a 2D x, z image (named x_d,

y_d in **Equations (3.5)** and **(3.6)**) on the RHEED screen. For a material with defined orientation and composition, the reciprocal space can be determined, and thus x and y are known. The angle of incidence, distance d and wave vector k_0 are system-dependent. This allows for calculation of x_d and y_d and simulation of the RHEED pattern of a given material. Details about the script are given in **Appendix C.**

Figure 3.23 shows real (**(a)** and **(b)**) and simulated (**(c)** and **(d)**) RHEED patterns of (111) oriented $Pb_{0.69}Sn_{0.31}Se$, with parameters of the script used for the simulation corresponding to the technical parameters of the GM#2 chamber.
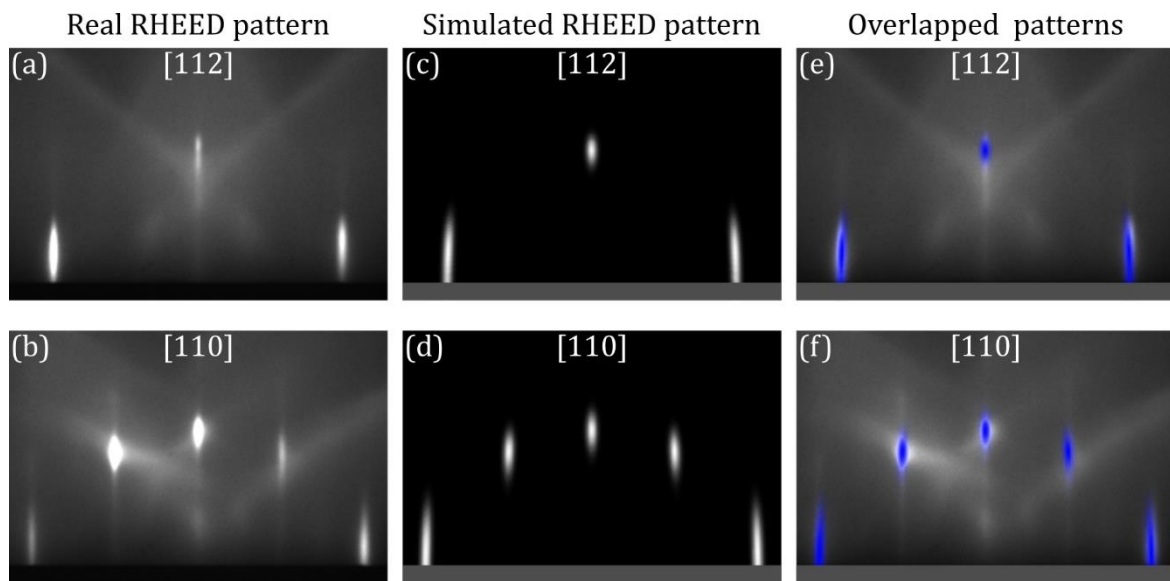

Figure 3.23: RHEED pattern simulation for (111) oriented $Pb_{0.69}Sn_{0.31}Se$. **(a)** and **(b)** RHEED patterns of sample G11 ($Pb_{0.69}Sn_{0.31}Se$, see **Appendix B**) recorded along [112] and [110] azimuths, respectively. **(c)** and **(d)** simulated RHEED patterns of (111) oriented $Pb_{0.69}Sn_{0.31}Se$ along [112] and [110] azimuths, respectively. **(e)** Overlapped image of (a) and (c). **(f)** Overlapped image of (b) and (d). Grey bar at the bottom of the (c)-(f) images corresponds to the shadow edge (black, bottom) visible in images (a) and (b).

The RHEED patterns obtained show very good agreement with the experimental results (see the overlapped patterns in images **(e)** and **(f)**). The patterns can be simulated for any azimuth angle and any material and orientation, with the assumption that the electron beam interacts only with the topmost layer of atoms. Such simulations enable more detailed analysis of RHEED during and after the growth process.

3.2.2 RHEED intensity oscillations

The growth rate of an epilayer formed during the layer-by-layer MBE growth mode can be determined from intensity oscillations of the diffraction spots in the RHEED pattern or intensity oscillations of the specular spot. The specular spot is a reflection of the specular beam, which reflects from the surface at the same exit angle as the angle of incidence of the incident electron beam. One period of oscillation corresponds to the growth of a full

monolayer. Usually, the specular beam spot is observed. Observation of the oscillations allows for a precise determination of the growth rate **[111]**. It also enables the determination of the growth mode by the presence or lack of evident intensity oscillations.

Figure 3.24 (a) and **(b)** shows model of specular spot intensity oscillations (for clarity of the image, a (001) oriented sample schematic is presented) as a function of surface coverage:
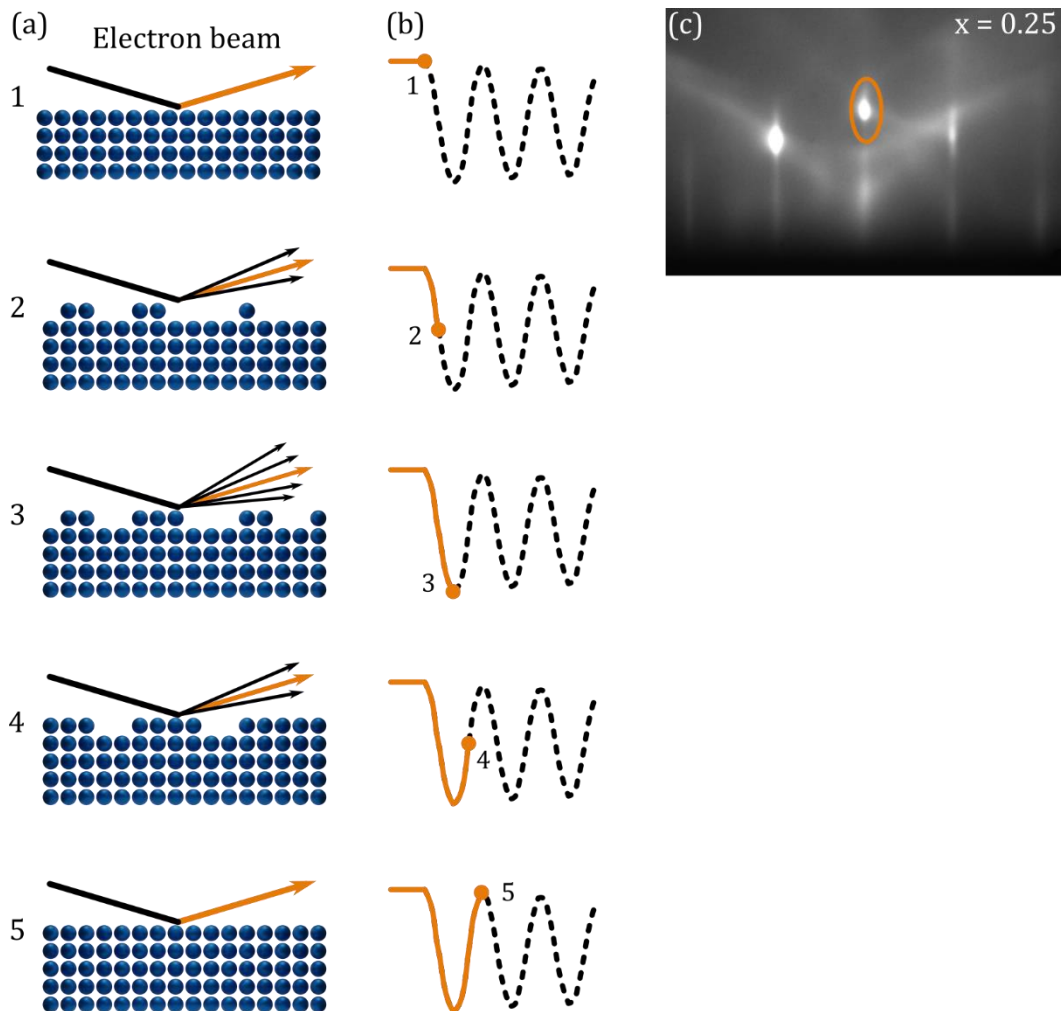

Figure 3.24: RHEED intensity oscillations model. **(a)** Behaviour of diffracted electron beam on different coverage of the surface 1-5. **(b)** Corresponding (1-5) intensity oscillation of specular spot. **(c)** Specular spot reflection (orange ellipse) visible during growth of 1 μm $Pb_{0.75}Sn_{0.25}Se$ film on (111) BaF_2 substrate, recorded along [110] azimuth. For clarity of the image (001) orientation of atoms is presented in the schematics.

1. Initially, the electron beam diffracts on a flat surface resulting in maximum intensity of the specular spot.
2. With increasing coverage, the surface becomes rougher, causing increased beam scattering.
3. When half of the surface is covered by a new layer, the intensity of the spot reaches a minimum.

4. With increasing coverage, the surface smoothness recovers, and the intensity of the spot recovers.
5. When full new layer is grown, the maximum intensity is obtained.

Figure 3.24 (c) shows the location of the specular spot in the RHEED pattern of the 1 μm thick $Pb_{0.75}Sn_{0.25}Se$ film on (111) BaF2 substrate, recorded along [110] azimuth. For smooth layer-by-layer growth of studied Pb1-xSnxSe intensity variations were impossible to observe by naked eye, thus no RHEED images for model discussed above are presented. The oscillations were recorded and analysed by the kSA 400 analytical RHEED system.

3.3   X-ray diffraction

X-ray diffraction (XRD) is a technique used for the structural characterisation of materials. It is used to investigate monocrystalline and polycrystalline materials in the form of powders, bulk crystals, and thin films. In the case of thin films studied in this thesis, the XRD was used to determine the crystal structure, lattice constant, sample composition, presence of strains in the epilayer, its thickness, and to confirm growth of single-phase single-crystalline films.

As the name implies, it is based on diffraction of X-rays on a periodic lattice of atoms composing the studied material. X-ray waves (0.1 – 100 Å) are used because the constructive interference of the waves can occur only when the incident wave has the wavelength in the same range as the interplanar distance between the atoms (several Å). The exact condition of constructive interference is expressed by Bragg's law:

$$n \cdot \lambda = 2d \cdot \sin \theta \qquad\qquad (3.7)$$

where n is the order of reflection equal to the integer number of wavelengths in the path difference of diffracted X-rays between adjacent crystal planes, λ is the wavelength of the incident beam, d is the interplanar distance, and θ is the angle between the incident beam and the diffracting planes, as presented in **Figure 3.25**.
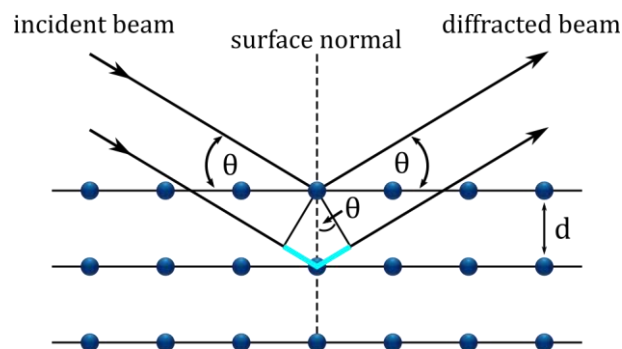

Figure 3.25: Bragg's law. The incident beam reflects from the atomic planes with interplanar distance d. The beams diffracted from the subsequent atomic planes interfere constructively when their beam path difference 2d·sinθ (marked in cyan) is equal to the multiplicity n of the beam wavelength λ.

The incident beam penetrates the material and reflects from more than one atomic plane. Considering constant λ from X-ray source and the constant d of the studied material, the constructive interference occurs at specific angles of incidence θ between all beams reflected from subsequent planes, which beam path difference is equal to integer multiplicity of the wavelength n·λ.

For cubic crystals such as $Pb_{1-x}Sn_xSe$ and α-Sn, relationship between lattice spacing d and lattice constant a has the following form:

$$\frac{1}{d_{hkl}^2} = \frac{h^2 + k^2 + l^2}{a^2} \tag{3.8}$$

where h, k, and l are Miller indices indicating crystallographic planes and d_{hkl} is d of a given plane, used in **Equation (3.7)**. By varying the incident beam angle θ in a measurement, the diffraction maxima, called hkl reflections, are obtained that correspond to possible d_{hkl} values. Knowledge of hkl reflections present as well as correspondent d_{hkl} makes it possible to identify the different phases in the material under study to determine whether the sample is single crystalline and to determine the orientation of the thin film. It is important to note that some of the reflections are not observed due to destructive interference between beams diffracted at certain Bragg angles. Diffraction selection rules, presented in **Table 3.3**, show, from which planes diffraction can or cannot be observed in the case of rock salt and diamond cubic structures.

Table 3.3: Diffraction selection rules for $Pb_{1-x}Sn_xSe$ and α-Sn

Unit cell	Forbidden reflections	Allowed reflections
Rock salt ($Pb_{1-x}Sn_xSe$)	h, k, l mixed (odd and even)	h, k, l all odd h, k, l all even
Diamond cubic (α-Sn)	h, k, l mixed (odd and even) h, k, l all even and h + k + l ≠ 4·n	h, k, l all odd h, k, l all even and h + k + l = 4·n

Combining **Equations (3.7)** and **(3.8)** allows for the calculation of θ for specific crystallographic orientations corresponding to d_{hkl}, when the lattice constant a is known, or, conversely, the calculation of the lattice constant using measured diffraction angles **[112]**.

The intensity of hkl reflections depends on the arrangement of the atoms in a unit cell and is proportional to $\left|F_{hkl}^2\right|$, where F_{hkl} is the structure factor defined as **[112]**:

$$F_{hkl} = \sum_{j=1}^{N} f_j e^{2\pi i\left(hu_j + kv_j + lw_j\right)} \tag{3.9}$$

where N is the total number of atoms in a unit cell, f is the atomic scattering factor of a given atom, and u, v, and w are the coordinates of a given atom normalised by the lattice parameters of the unit cell along the x, y, and z axes, respectively. The atomic scattering factor depends on the atomic number Z.

XRD measurements presented in this thesis were carried out by V. V. Volobuev using PANalytical X'Pert Pro MRD diffractometer with a 1.6 kW X-ray tube using CuKα_1 radiation (λ = 1.5406 Å), a symmetric 2 × Ge (220) monochromator and 2D Pixel detector. I participated in some of the measurements. The measurements were carried out in 2θ–ω schema, where the movements of the sample and the detector are coupled and move by ω and 2θ angles, respectively, where ω is the angle of incidence of the X-ray beam and angle 2θ is related to ω by $\omega = \frac{1}{2} \cdot 2\theta$. Furthermore, Reciprocal space maps (RSM) were measured around symmetric and asymmetric reciprocal lattice points, which can be used to calculate in-plane and out-of-plane lattice constants, $a_{\parallel}$ and $a_{\perp}$, respectively.

$$a_{\parallel} = \frac{2\pi}{Q_{\parallel}} \sqrt{h_1^2 + k_1^2 + l_1^2} \tag{3.10}$$

$$a_{\perp} = \frac{2\pi}{Q_{\perp}} \sqrt{h_2^2 + l_2^2 + l_2^2} \tag{3.11}$$

where $Q_{\parallel}$ and $Q_{\perp}$ are X and Y dimensions of RSM, respectively. The h, k, l indices for a given direction of the lattice constant are obtained by the decomposition of the Q_{hkl} vector, as shown in **Figure 3.26**.
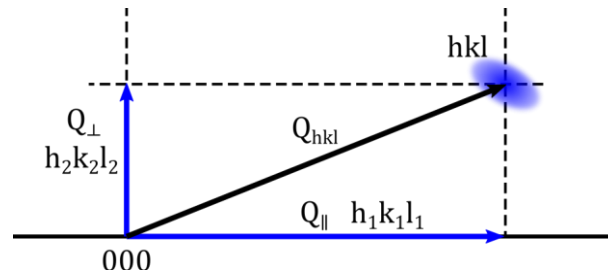

Figure 3.26: Determination of in-plane and out-of-plane lattice constants with reciprocal space maps. Point hkl marks reciprocal lattice point around which RMS is measured. Vector Q_{hkl} is decomposed to two vectors, $Q_{\parallel}$ and $Q_{\perp}$ and h = h$_1$ + h$_2$, k = k$_1$ + k$_2$, l = l$_1$ + l$_2$.

The lattice constant obtained in XRD measurements can be used to determine the composition of an alloy, such as Pb$_{1-x}$Sn$_x$Se, according to the Vegard's law **[113]**. The in-plane and out-of-plane lattice constants can be used to determine strains of the film. Strain calculation is explained in **Section 4.4.2**, since it was relevant in the case of α-Sn epilayers.

3.4   Scanning electron microscope

Scanning electron microscope (SEM) allows for high resolution scanning of the surfaces by a focused beam of electrons. Carl Zeiss Auriga Cross-Beam microscope was used to measure thickness of grown films in order to determine the growth rate of the films and calibrate the BFM and QCM. The electron accelerating voltage in the SEM used is in the range of 0.1 to 30 kV,

which corresponds to the de Broglie wavelength (**Equation (3.3)**) in the range of 122.46 to 6.98 pm (10^{-12} m). The typical imaging resolution in this system at 15 kV is 1 nm.

Figure 3.27 (a) shows a schematic of the internal structure of the SEM column. Electrons, coming from an electron source, such as a Schottky Field Emitter, are formed into a beam by anode aperture and focused by a set of magnetic lenses. The objective lens and scanning coils allow for x and y scanning of the surface of the sample. Electrons ejected from the sample are collected by the respective detectors. The In-Lens detector, primarily used for imaging of the grown films, collects secondary electrons. During operation, the SEM column and the specimen chamber are kept in vacuum. Samples are introduced to the system through a load lock, shown in photo **(b)**, presenting SEM in IF PAN. The SEM image **(c)** shows a cross-section of a PbSe epilayer grown in the PREVAC 190 system for growth rate calibration. Typically, an electron high tension (EHT) voltage of 5 kV was used.
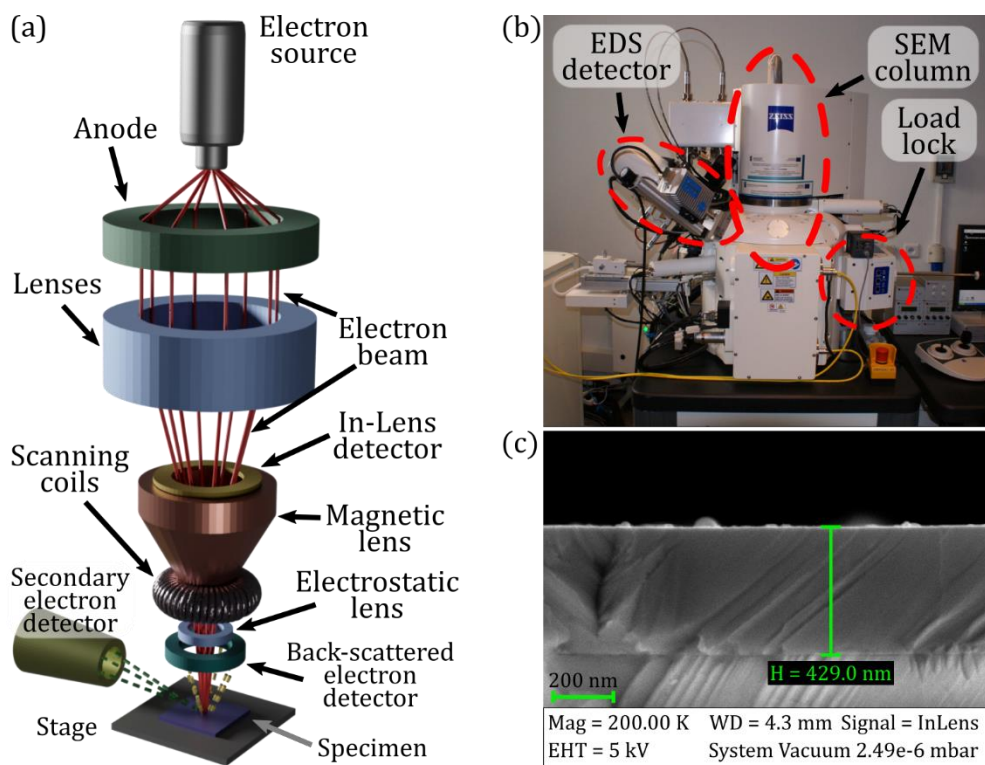

Figure 3.27: Scanning electron microscope. (a) Schematic of the internal structure of the SEM column. Elements are not in scale. **(b)** Photo of the Carl Zeiss Auriga Cross-Beam microscope in IF PAN. **(c)** Cross-sectional SEM image of the PbSe epilayer grown for the calibration of the growth rate in the PREVAC 190 system, with the basic parameters of the SEM, at the time of the measurement, given.

The microscope is equipped with a Bruker XFlash 5030 Energy Dispersive Spectroscopy (EDS) Detector, which was used to determine the composition of the grown films. EDS measurements were made with an accelerating voltage of 20 kV. EDS is based on phenomena in which an incident electron beam excites an electron in an inner shell of an atom. The electron vacancy created by this excitation is then filled by an electron coming from a higher-energy shell in the atom. The energy difference of this process is emitted in the form of X-ray

radiation and recorded by an energy-dispersive detector with its number of occurrences (counts). Because the energy of this transition is unique to the specific element and transition, it allows for the determination of the composition of the studied material **[114]**.

EDS measurements presented in this thesis were carried out by dr T. Wojciechowski. I made the SEM measurements of the PbSe and SnSe epilayers used for the calibration of BFM and QCM in PREVAC 190 and Veeco GENxplor GM#2, respectively.

3.5   Atomic force microscopy

Atomic force microscopy (AFM) is a technique of imaging surface topography by tracing (scanning) the sample with a cantilever probing tip **[115]**. Atomic scale resolution can be reached for fine tips. In the simplest case (contact mode), the cantilever is deflected under the interaction force between the probing tip and the surface. The response of the cantilever as a function of x, y tip position is a value measured as surface topography. The deflection of the cantilever is stabilised to be constant and the vertical (z) response of the piezo scanner is the topography height - **Figure 3.28 (a)**. To avoid drag between probe and sample (which can cause surface damage), an oscillating probe can be used. . In so-called dynamical modes (tapping, intermittent contact, non-contact) the cantilever amplitude changes and/or resonant frequency shifts, depending on the distance between probe and the surface.

AFM images were obtained in Tapping Mode with Bruker MultiMode 8-HR microscope by dr M. Aleszkiewicz. In this mode, the cantilever oscillates with predefined a frequency, causing the tip to have intermittent contact with the surface during measurement. The amplitude of the oscillations is maintained to be constant and the corresponding vertical (z) response of the piezo scanner is the topography height. An exemplary AFM image for the material studied in this thesis, $Pb_{1-x}Sn_xSe$, is presented in **Figure 3.28 (b)**.
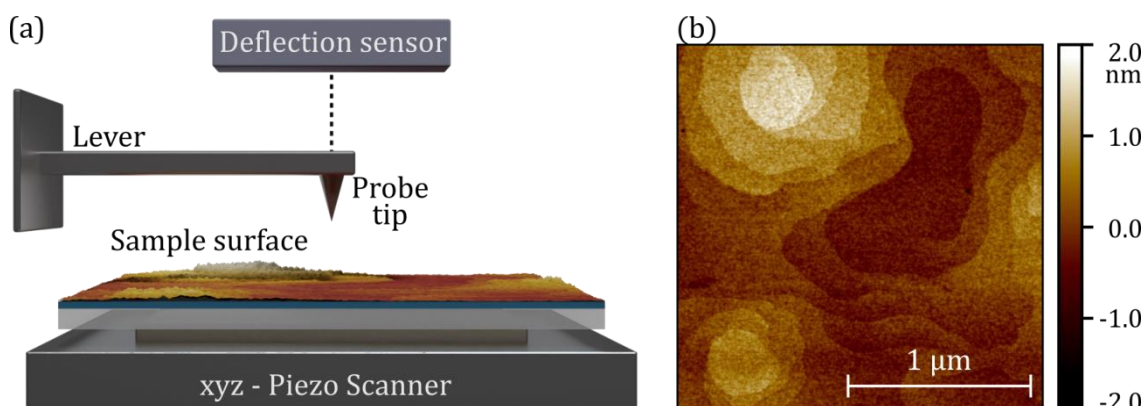

Figure 3.28: Basic principle of AFM. (a) A cantilevered probing tip (exchangeable when worn) scans the sample on the X and Y axes. The deflections of the cantilever and the response of the piezo scanner on the Z axis caused by the force between the tip and the surface of the sample are monitored as a function of x and y position. **(b)** 2 μm × 2 μm AFM image of $Pb_{0.75}Sn_{0.25}Se$ thin film grown on BaF_2 (111). AFM measurements were done by dr M. Aleszkiewicz. Data presentation by B. Turowski.

Measurement data was processed using open source Gwyddion software **[116, 117]**. The main parameter of comparison between AFM images of different samples presented in this thesis is the RMS roughness parameter, extracted using the Gwyddion software with **Equation (3.12) [117]**. The RMS is a root mean square average of the height deviations in the line profile from mean height ($\bar{z}$) of the profile and can be used to determine the quality of the surface of the sample and its flatness.

$$\text{RMS} = \sqrt{\frac{1}{N}\sum_{n=1}^{N}(z_n - \bar{z})^2} \tag{3.12}$$

3.6   Angle-resolved photoelectron spectroscopy

Angle-resolved photoelectron spectroscopy (ARPES) is a widely used method to obtain the band structure including surface states of a material **[10, 83, 118]** and is therefore extremely useful in studying topological materials. The ARPES measurements presented in **Chapter 5** were performed at the National Synchrotron Radiation Centre SOLARIS, Kraków (Poland), at URANOS beamline (formerly UARPES), with incident photon energy hν greater than 17 eV and temperature ranging from 8 K to room temperature (RT) or at PHELIX beamline, with incident photon energy hν 50-90 eV at temperature range 80-300 K.

The basics of the operation of ARPES is the photoelectric effect **[119]**, presented in the bottom right inset in **Figure 3.29**. High-energy photons, in the case of samples studied in this thesis generated by a synchrotron, excite electrons close to the material surface. If the energy of the photon hν is greater than the work function Φ of the studied material, the electrons with binding energy E_B are excited and can escape from the solid as photoelectrons, with kinetic energy E_{kin}:

$$E_{kin} = h\nu - \Phi - E_B \tag{3.13}$$

The photoemission process can be described using the one-electron approximation by Three-Step Model, developed by Berglund and Spicer **[120]**, shown schematically in **Figure 3.30 (a)** and explained in detail in Refs. **[121]** and **[122]**:

1) Excitation of the electron in the solid by photon,
2) Photoelectron propagation to the surface,
3) Emission of the photoelectron into vacuum

Step 1: Excitation of the electron in the solid by photon.

Assuming that the momentum of the incoming photon is much smaller than the momentum of the excited electron, the photon's momentum may be neglected. Under this assumption,

excitation of the electron is a direct transition (with momentum conservation) in the reduced Brillouin zone scheme.
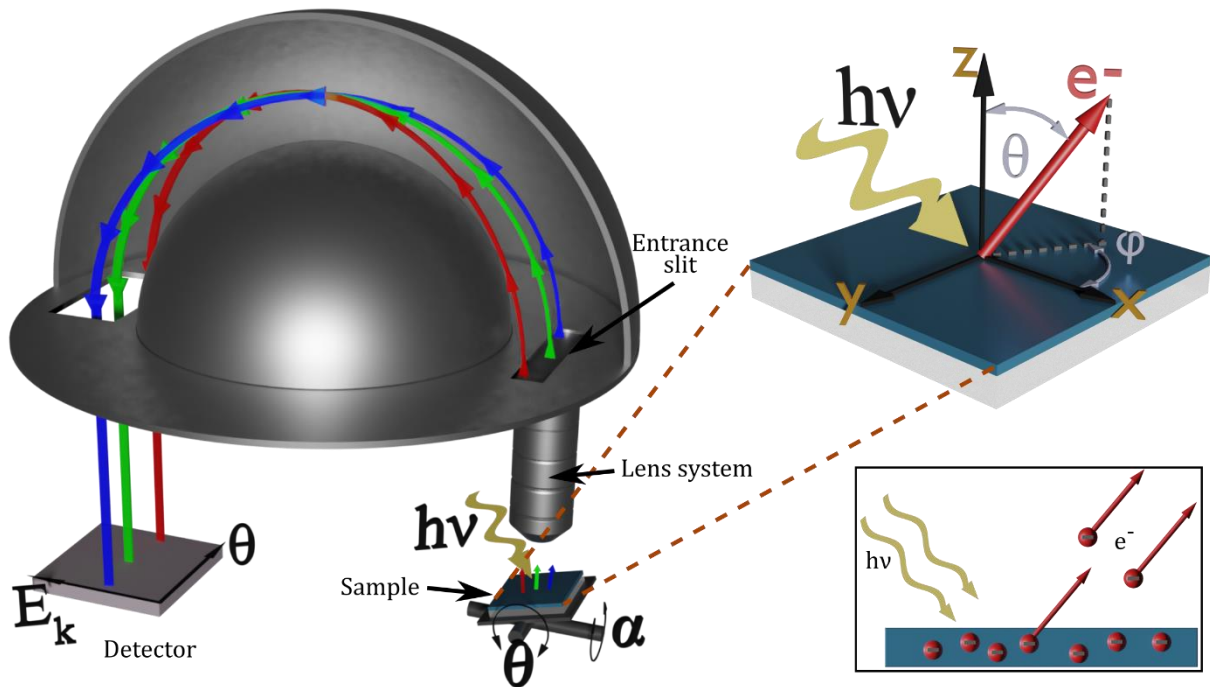

Figure 3.29: Schematics of the ARPES setup. High-energy electromagnetic radiation (hν) hits the sample surface and excites photoelectrons (e⁻). The spherically shaped detector redirects them and records their kinetic energy (E_k) and emission angle (θ). The sample may be tilted by angles α and θ to obtain emission from the chosen part of the Bouillon zone.
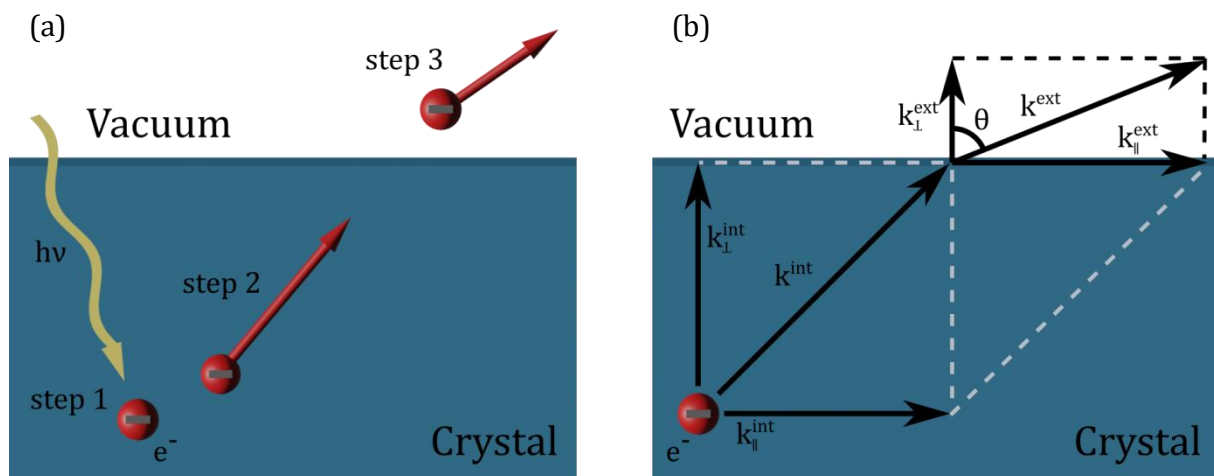

Figure 3.30: Three-step model of the photoexcitation process. (a) Schematics of the three-step model photoemission process. **(b)** Conservation of the momentum vector in step 3; *int* and *ext* denote the internal and external wave vectors of the photoelectron.

Step 2: Photoelectron propagation to the surface

The number of photoelectrons reaching the surface is limited by the electron-electron interaction and depends on the inelastic mean free path (IMFP) of the electrons, which depends mainly on the electron energy. IMFP in angstroms can be described by a semi-empirical formula derived from Ref. **[123]**:

$$\lambda_{IMFP} = \frac{538}{E^2} + 0.41 \cdot \sqrt{a^3 \cdot E} \tag{3.14}$$

where a is the lattice constant of the material in nanometres and E is the kinetic energy of the electron in electron volts (eV). First part of the **Equation (3.14)** describes IMFP for $E \leq 150$ eV and second part for $E > 150$ eV. The shorter the IMPF, the lower the probability that electrons further from the surface will reach the surface. Minimal mean free paths of ~3 - 10 Å are for energy in the 10 eV to 100 eV range **[124]**, which roughly corresponds to lattice constants of $Pb_{1-x}Sn_xSe$ and α-Sn. This means that only electrons from thin region just beneath material surface contribute to the obtained band structure, while electrons coming from deeper parts of the crystal are scattered before they reach sample surface due to limited IMPF.

Step 3: Emission of the photoelectron into vacuum

The potential difference between the bulk of the crystal and the vacuum causes refraction of the escaping electron at the surface, as presented in **Figure 3.30 (b)**.

Wave vector component in the direction parallel to the surface is conserved during the escape (in reduced Brillouin zone scheme):

$$k_{\parallel}^{int} = k_{\parallel}^{ext} \tag{3.15}$$

Since angle of refraction (emission) θ and kinetic energy of the photoelectron E_{kin} are recorded during the ARPES measurement and photoelectrons emitted into the vacuum are treated as free electrons, the parallel component $k_{\parallel}^{int}$ of the electron wave vector inside the crystal can be calculated as:

$$k_{\parallel}^{int} = \sqrt{\frac{2m}{\hbar^2} E_{kin}} \cdot \sin\theta \tag{3.16}$$

As a result, the 2D E_{kin} vs $k_{\parallel}$ image of the photoemission intensity is recorded that shows the band structure close to and at the surface of the studied material.

The wave vector component perpendicular to the surface ($k_{\perp}^{int}$) can be obtained if assumption of nearly free electrons in the solid is made. Under this assumption, an inner potential V_0 is introduced: $V_0 = E_V - E_0$, where E_V vacuum level potential and E_0 is bottom of the valence band (free electron parabola).

$$k_\perp^{int} = \frac{1}{\hbar}\sqrt{2mE_{kin} \cdot \cos^2\theta + V_0} \qquad (3.17)$$

The inner potential V_0 depends on the studied material and needs to be determined beforehand. It may be done by detecting photoelectrons emitted along surface normal ($k_\parallel^{ext} = 0$), while varying energy of incident photons hν and measuring energy of photoelectrons E_{kin}. By identifying the high-symmetry points of the 3D Brillouin zone in $k_\perp$, the inner potential V_0 can be determined [125].

The focus point of the thesis are the topological surface states that exist on the surfaces of the studied materials. Their 2D character reduces the wave vector k to its $k_\parallel^{int}$ component. The study of the $k_\perp^{int}$ component was beyond the scope of this thesis, as the electronic structure of the bulk was not studied in detail.

Measurements were done with help of URANOS beamline staff: dr Natalia Olszowska, prof. Jacek Kołodziej, mgr Marcin Rosmus.

3.7   Spin-resolved angle-resolved photoelectron spectroscopy

Spin-resolved angle-resolved photoemission spectroscopy (SR-ARPES) is similar to ARPES in that photoelectrons with a well-defined energy E_{kin} and emission angle θ are collected and redirected to a spin detector. Main methods that are used for electron spin detection are: Mott detector [126] and Very-low-energy electron diffraction (VLEED) detector [127]. $Pb_{1-x}Sn_xSe$ thin films were studied at the PHELIX end-station at SOLARIS, Kraków (Poland) [128], which is equipped with the FOCUS GmbH FERRUM 2D VLEED spin detector [129]. The detector measures the intensity of electrons reflected by positively and negatively magnetized ferromagnetic target material, I^+ and I^- respectively. The principle of operation is based on the asymmetry of very low energy spin-polarized electrons scattering from a magnetized crystalline solid target. In ferromagnetic materials, the binding energies of majority and minority spin bands can be made unequal by applying an external magnetic field, thus making reflectivity of the incident electrons spin-dependent. The intensity asymmetry A of the reflected electrons is defined as:

$$A = \frac{I^+ - I^-}{I^+ + I^-} \qquad (3.18)$$

Then, the spin polarization P may be calculated as:

$$P = \frac{A}{S} \qquad (3.19)$$

Where S is a Sherman function coefficient [130] determined for a given detector by measuring a fully polarized electron beam [129]. For a detector used at the PHELIX end-station S = 0.275.

In the results presented in **Chapter 5**, intensities I^+ and I^- correspond to energy distribution curves (EDC) measured for a VLEED target magnetized in opposite directions. EDC is a vertical line profile through the band structure - only electrons escaping sample at the predefined emission angle θ are collected. This allows for the calculation of spin-resolved EDCs (SR EDC) [131, 132]:

$$\text{SREDC}_{\uparrow,\downarrow} = \frac{I_+ + I_-}{2} \cdot (1 \pm P) \tag{3.20}$$

To obtain incident beam polarization P, and in turn SR EDC, the two measurements, I^+ and I^-, have to be carried out with short enough time difference to minimise the influence of the intensity drift. Assuming intensity variations to be linear in time, the drift influence may be further minimised by adopting the measurement sequence described in Ref. [133]. Here it was adopted as I^+, I^-, I^-, I^+, with equal time separation and equal durations of the consequent measurements.
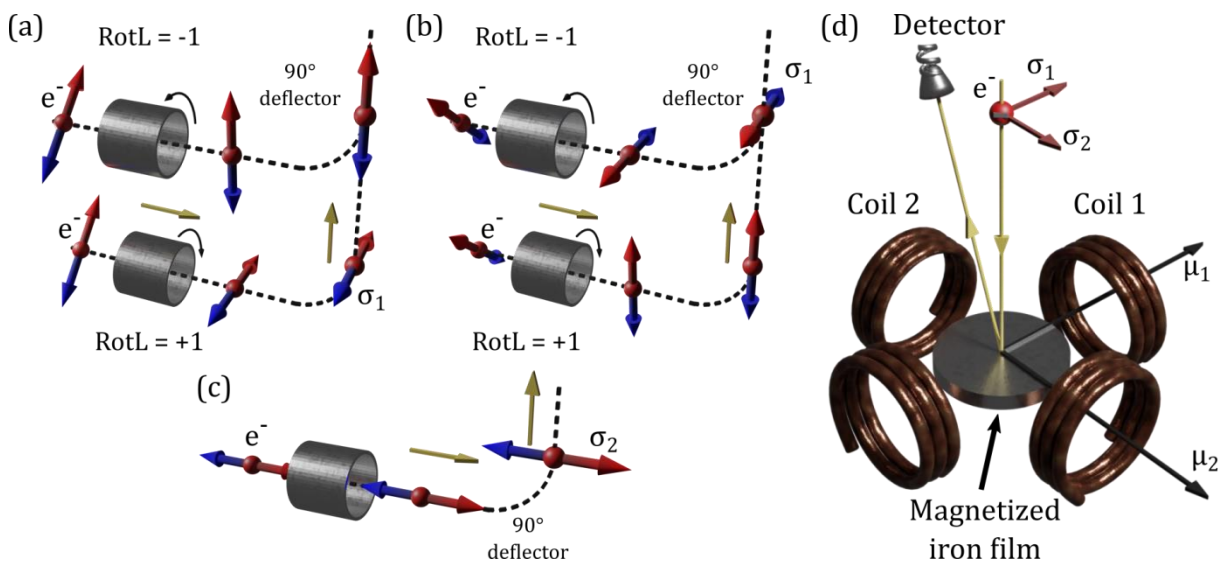

Figure 3.31: Spin polarization detection schematic at the PHELIX end-station of the SOLARIS synchrotron in Kraków, Poland. (a, b) photoelectron in-plane spin components rotation by rotator lens RotL. Rotation is either positive (+45°, RotL = +1) or negative (-45°, RotL = -1). **(c)** Rotation lens does not affect the out-of-plane spin component. Further 90° deflection makes one in-plane spin component perpendicular to magnetisation axes of the target iron film, making it undetectable. **(d)** Scheme of the scattering geometry in the FOCUS GmbH FERRUM 2D VLEED spin detector. Only electrons with spin polarization σ parallel magnetisation direction μ of the Fe film are reflected to the detector. Magnetisation can be switched in four different states by two pairs of coils. Combining the four-coil system (d) with spin rotation and 90° deflection (a, b, c) allows for detection of all three orthogonal spin resolved components of photoelectrons escaping the studied material.

Measurements were done with the help of [PHELIX](#) beamline staff: dr Eng. Magdalena Szczepanik, dr Ewa Partyka-Jankowska, mgr Tomasz Sobol.

3.8 ARPES data processing

All ARPES, SR-ARPES, and Core Level (CL) data collected and presented in this thesis were initially processed with IGOR Pro 8 software by WaveMetrics, Inc. This software is used for scientific data analysis that include, but is not limited to, generating plots and graphs, fitting, data extraction, and presentation. Igor Pro software is available on both beamlines at which ARPES measurements were carried out, with custom procedures written by beamline staff. It allows for visualisation and analysis of large sets of data providing the user with a wide range of functions to simplify the process. However, this results in steep learning curve for the use of this software. All ARPES and SR-ARPES results presented in **Chapter 5** were processed using Igor Pro 8. In addition to the build-in functions and procedures available at the endstations, I wrote custom procedures that were used to significantly shorten the time required to find Fermi level, the band structure, plot constant energy contour (CEC) stacked graphs, and 3D cube maps, which were further processed by Phyton scrips that I wrote. All my custom-written procedures are available on the MagTop data server.

Samples of which spectra were used for the exemplary presentation of the visualisation methods used are listed in **Table 3.4**.

Table 3.4: Pb$_{1-x}$Sn$_x$Se samples used to discuss the presentation of the data.

name	code	Sn content [%]	Thickness	Aim of presentation	Bi [%]
G34	G011422B	15	1 μm	Colour scale	0.079
G36	G011522B	30	1 μm	Curvature **[134]** procedure application	0.1
G37	G011522C	26	1 μm	Finding E$_F$	0.069

3.8.1 Finding Fermi level of the sample

ARPES measurements allow for determination and visualisation of the electronic structure of the studied samples. Raw data consist of the intensity of electrons emitted at the known emission angle θ with the kinetic energy E$_k$. Angle θ is recalculated to the wave vector k$_∥$ according to **Equation (3.16)**. The energy scale is obtained by subtracting the Fermi energy E$_F$ from the kinetic energy of the electrons. This enables a direct comparison of samples with different E$_F$ when the Fermi level is universally labelled zero at the E-E$_k$ energy axis. **Figure 3.32** shows the process of finding the Fermi energy.
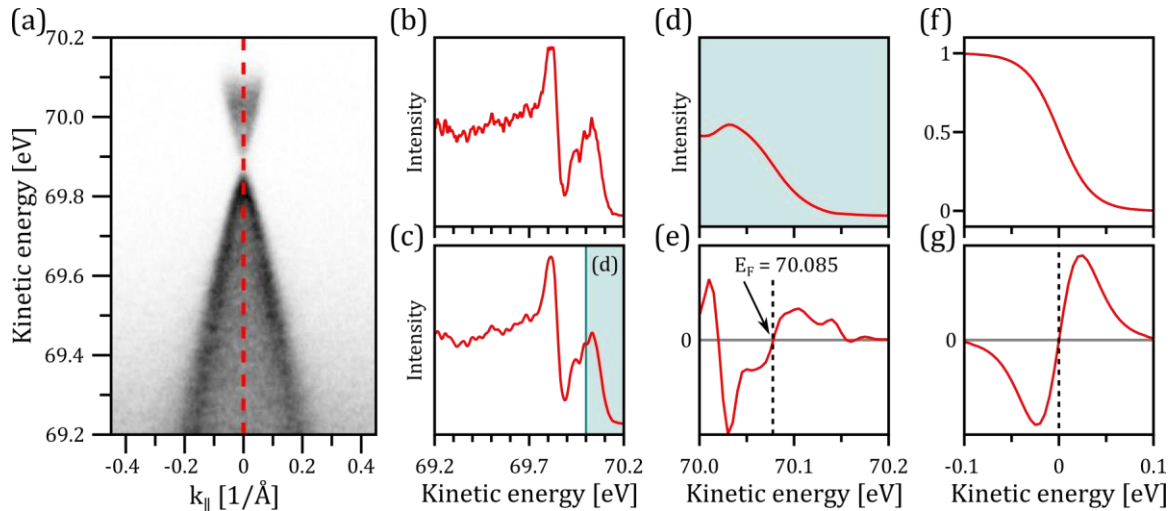
Figure 3.32: Determination of Fermi energy E_F from raw ARPES data. (a) raw ARPES spectrum of
$Pb_{0.74}Sn_{0.26}Se$ near $\bar{\Gamma}$ point collected at 200 K (sample G37) with an exciting photon energy of 70 eV with the
emission angle θ recalculated to the wave vector $k_\parallel$. **(b)** EDC at $k_\parallel$ = 0 marked by the red dashed line in image
(a). **(c)** EDC from image (b) with applied binomial smoothing. **(d)** part of the conduction band in the 70-
70.2 eV range from image (c). **(e)** second-order derivative of (d) with inflection point being E_F. **(f)** Fermi-
Dirac distribution in the -0.1 to 0.1 eV energy range at 200 K. **(g)** second-order derivative of (f).

First, an energy line profile (energy distribution curve (EDC)) of the raw spectrum (image **(a)**)
is taken at $k_\parallel$ = 0 (image **(b)**). Then, a binomial smoothing **[135]**, employing the Smooth
function **[136]** available in the IGOR Pro 8 software, is used. The function is a Gaussian filter
that convolves the data with normalised coefficients derived from Pascal triangle at a level
equal to the smoothing parameter. To streamline the procedure for E_F determination, the
smoothing parameter 3 is used. Finally, a second-order derivative of the conduction band (CB)
tail (image **(d)**) is calculated in order to find the inflection point of the CB tail (image **(e)**). This
procedure relies on the fact that the average number of electrons occupying a single particle
state i near Fermi energy may be described by Fermi-Dirac (F-D) distribution:

$$\bar{n}_i = \frac{1}{e^{\varepsilon_i / k_B T} + 1} \tag{3.21}$$

where ε_i is the energy of the state i, k_B is the Boltzmann constant and T is the temperature in
Kelvins. For simplicity, the total chemical potential (Fermi level) is assumed to be zero.
Image **(f)** shows the F-D distribution in the -0.1 to 0.1 eV energy range at 200 K. The inflection
point of the second derivative of the F-D distribution (image **(g)**) is the Fermi level.
Consequently, the position in the energy of the inflection point in image **(e)** is the Fermi level
of the raw spectra (image **(a)**).

3.8.2   Colour scale and intensity adjustments

In order to facilitate the understanding of ARPES results, further visual processing of the data
is needed. First, a proper pseudo-colour scheme, or colour map, needs to be chosen to

improve readability of the images. Then the colour scale and range need to be adjusted. **Figure 3.33** shows three possible representations of the same ARPES image.
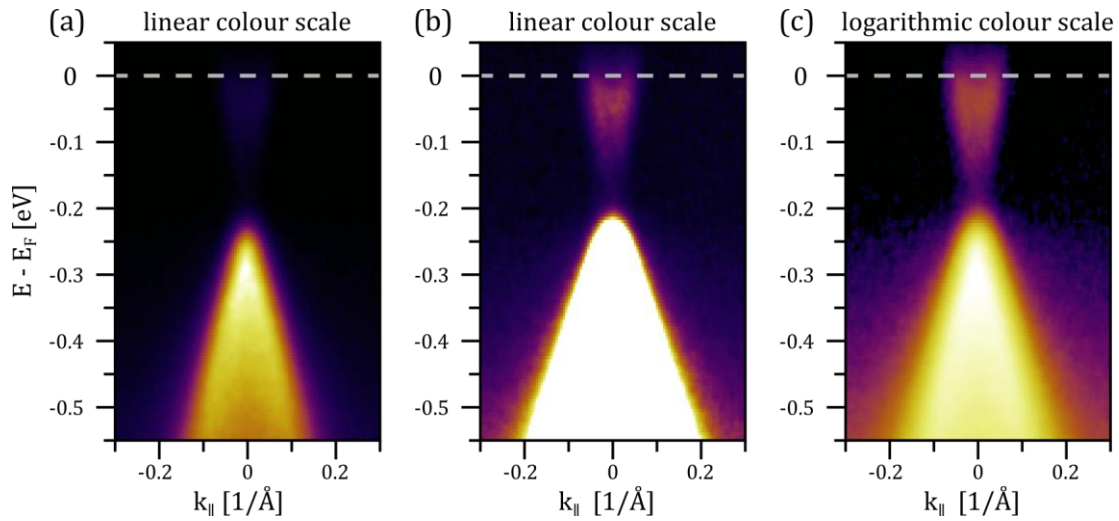

Figure 3.33: ARPES spectra of 1 μm thick Pb$_{0.85}$Sn$_{0.15}$Se layer near $\bar{\Gamma}$ point at 200 K grown on BaF$_2$ (111) with different colour scales applied. (a) linear colour scale of the image, CB is barely visible. **(b)** linear colour scale of the image with reduced colour range, where VB is overexposed. **(c)** logarithmic colour scale of the image, where both CB and VB are well visible. Sample G34.

Due to the difference in the intensity of conduction and valence bands (VB) in the raw data, the linear colour scale of **Figure 3.33 (a)** does not allow for a proper analysis of the band structure. CB is barely visible in the image. Reducing the colour map range of the image with the linear colour scale (**Figure 3.33 (b)**) by decreasing its maximum displayed value allows for better visualisation of the CB. The drawback of this approach is an overexposure of the VB, as most of the information about this band is in higher image intensities that are above the threshold needed to make CB visible. The application of a logarithmic colour scale, presented in **Figure 3.33 (c)**, is the best choice, as CB is well defined and information about VB is retained on the image and the band gap can be estimated.

3.8.3 Finding the band structure

ARPES is used to study the band structure of the materials. In some cases, obtained spectra require further processing in order to find the locations of all the interesting bands. **Figure 3.34** shows the procedure for finding the band structure in such a case. Image **(a)** shows ARPES spectra of 1 μm thick Pb$_{0.7}$Sn$_{0.3}$Se (111) epilayer near $\bar{\Gamma}$ point at 200 K. At this temperature, the sample is expected to be in the topological crystalline insulator (TCI) phase, with Dirac-like surface states crossing in the band gap near $\bar{\Gamma}$ point. Indeed, the very intense Dirac point (DP; crossing of the topological surface states) and topological surface states (TSS) in VB are visible, but the CB is undistinguishable. To improve visualisation of the spectra, edge-finding algorithms are employed.
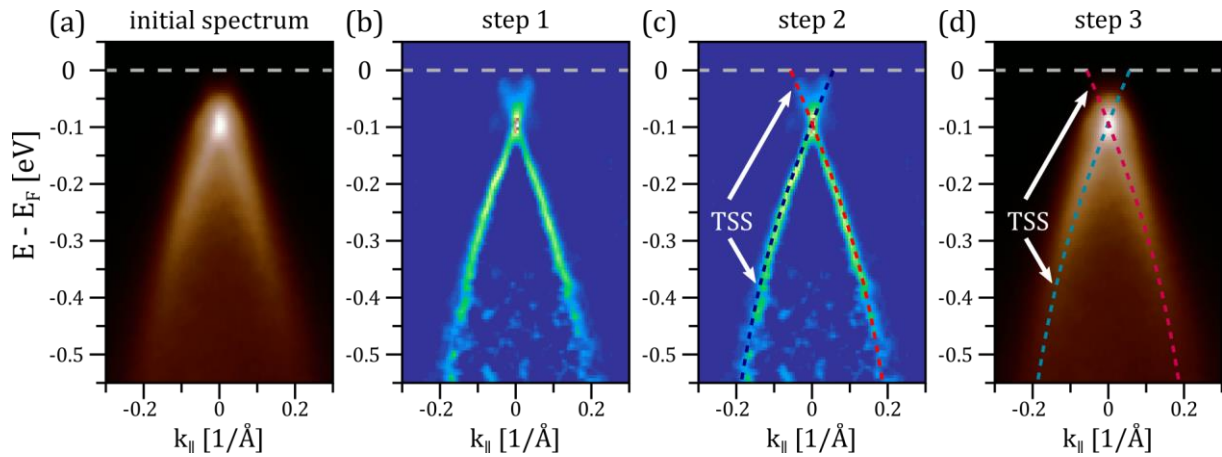
Figure 3.34: Finding positions of surface bands from the raw ARPES spectra of the 1 μm thick Pb$_{0.7}$Sn$_{0.3}$Se (111) epilayer near $\bar{\Gamma}$ point at 200 K. (a) initial spectrum with a linear colour scale. **(b)** 2D curvature **[137]** of the initial spectrum (a). **(c)** Surface states guidelines (blue and red dashed lines) overlapping band structure obtained from (b). **(d)** Surface states guidelines overlapping initial ARPES spectrum. Sample G36.

Most often, a 2D second derivative (the sum of the vertical and horizontal second derivatives of the image) is used for this purpose **[100, 138]**. In 2011, *Zhang et al.* **[137]** proposed the use of the curvature method as a tool for the analysis of experimental curves such as ARPES spectra in order to find the position of the bands. Another commonly used method is to take multiple energy dispersion curves **[50, 139]** or momentum dispersion curves (MDC) **[140, 141]** of the analysed spectra to find the maxima in the obtained line profiles. The maxima are then used to find the position of the bands. In this thesis, the 2D curvature method adapted for IGOR Pro software by Zhang P. **[134]** is used to better visualise the band dispersion and find their positions. **Figure 3.34 (b)** shows the 2D curvature of the image **(a)**. After fine-tuning the procedure parameters, the band structure is much more clearly visible. In the next step (see image **(c)**), the obtained 2D curvature image is used to fit the dispersion relation equation for massless Dirac fermions:

$$E(k_\parallel) = \varepsilon_0 \pm \hbar v_D \cdot k_\parallel \tag{3.22}$$

where ε_0 is an additional energy offset used to compensate for E_F shift due to sample doping. To improve accuracy of the fitting, second-order correction of the Dirac velocity v_D is used **[142]**:

$$v_D = v_0(1 + \alpha \cdot k_\parallel^2) \tag{3.23}$$

where α is the correction term.

Combining **Equations (3.22)** and **(3.23)** results in the fit presented in **Figure 3.34 (c)**. In step 3, the obtained dispersion relation is placed on top of the initial ARPES image to improve direct visualisation of the band dispersion.

In the case of samples in the normal insulator (NI) phase, an ellipsoidal non-parabolic two-band Kane dispersion relation is used, with an additional energy offset ε_0, derived from equation (3.4) from Ref. **[82]**:

$$E = \pm \frac{E_0}{2} \sqrt{\frac{2\hbar^2 \cdot k_\parallel^2}{E_0 \cdot m} + 1} + \varepsilon_0 \tag{3.24}$$

where $m = \frac{m^*}{m_0}$, and m* is the effective mass of an electron in CB or VB and m_0 is the mass of the electron. E_0 is the bulk band gap of $Pb_{1-x}Sn_xSe$ in meV, calculated from the semi-empirical Preier's formula **[68]**, with x being the Sn content and T being the temperature of ARPES measurement:

$$E_0(x, T) = 125 - 1021 \cdot x + \sqrt{400 + 0.256 \cdot T^2} \tag{3.25}$$

In the case of the (001) samples, **Equations (3.24)** and **(3.25)** are used to fit both Dirac cones.

In the case of the (111) samples with Rashba splitting, the dispersion relation that takes the second-order correction into account **[143]** is used to fit the Rashba surface states (RSS):

$$E_\pm = \varepsilon_0 + \frac{\hbar^2 \cdot k_\parallel^2}{2m_\parallel} \pm \alpha_R \cdot \left(1 + \nu \cdot k_\parallel^2\right) \cdot k_\parallel \tag{3.26}$$

where ε_0 is the energy offset, $m_\parallel$ is the effective mass of an electron, $k_\parallel$ is k-space vector, ν is the second-order correction parameter. The Rashba parameter α_R **[144]** is used as a variable in the fit. The determination error of the α_R is assumed 0.1 eV·Å due to manual fitting of the **Equation (3.26)** to the 2D curvature of the ARPES spectrum. The Rashba parameter can be also calculated using **Equation (2.13)**: $\alpha_R = \frac{2E_0}{k_0}$, with calculation error $\Delta\alpha_R$ estimated by Root Sum Square method as:

$$\Delta\alpha_R = \alpha_R \cdot \sqrt{\left(\frac{\Delta k_0}{k_0}\right)^2 + \left(\frac{\Delta E}{E}\right)^2} \tag{3.27}$$

E_0 and k_0 denote the position of the fitted parabolas' minima in energy and k-space, with respect to the Kramers point (KP), as shown in **Figure 2.1**. ΔE and Δk_0 are respective measurement errors. These were estimated as 0.01 eV and 0.0025 Å^{-1}, respectively, based on detector resolution of URANOS beamline (0.0018 eV and 0.1°, respectively) combined with measurement error of manual determination of the positions of the bands.

Both approaches of determining the Rashba parameters give comparable results, within the margin of error of determination. Because of the fact that α_R is calculated from ARPES spectra, **Equation (2.13)** was used for final determination of the Rashba parameter. For details of features of the Dirac-Rashba spectrum, see **Section 5.2.2**.

Chapter 4

MBE growth and structural characterisation of the samples

In this chapter, MBE growth and structural characterisation of $Pb_{1-x}Sn_xSe$ and α-Sn samples will be presented. Samples discussed in a given section are listed in the table at the beginning of this section, with names used in the thesis. The lists of all samples relevant to this thesis are presented in **Appendix B**.

I was involved in the growth of $Pb_{1-x}Sn_xSe$ samples prepared in two MBE setups: PREVAC 190, equipped with elemental Pb, Sn, and Se sources and Veeco GENxplor GM#2, equipped with stoichiometric PbSe and SnSe compound sources. Most of the epilayers discussed were grown by me, under the supervision of dr V. V. Volobuev, in the latter system. Details of the growth procedures are described in **Section 3.1.3 MBE growth of Pb1-xSnxSe epilayers**. I also participated in some of the growths of α-Sn samples in Veeco GENxplor GM#2. Details of the growth procedure are described in **Section 3.1.4 MBE growth of α-Sn epilayers**.

4.1   Comparison of (111) $Pb_{1-x}Sn_xSe$ MBE growth with elemental and compound sources

In this section, a comparison of RHEED, AFM, and XRD measurements for films grown in PREVAC 190 and Veeco GENxplor GM#2 is presented. The systems are equipped with elemental and compound sources, respectively. I participated in growth of the samples in the PREVAC system, carried out by dr V. V. Volobuev. In the GM#2 system, the samples were grown by dr V. V. Volobuev and me. AFM measurements were performed by dr M. Aleszkiewicz. XRD measurements were performed by dr V. V. Volobuev, with my assistance. The purpose of the comparison presented in this section is to establish whether the use of elemental or compound sources influences the properties of $Pb_{1-x}Sn_xSe$ epilayers grown under similar conditions. The growth from compound sources is expected to be less demanding in terms of choosing the proper IV to VI flux ratio, but can suffer from worse purity of materials. In the case of elemental sources, 7N elements are used, while compound sources are produced by direct synthesis of elements from 6N elements (see **Figure 3.10**) and the final purity is worse. The samples discussed are listed in **Table 4.1**. Samples grown in the PREVAC MBE system were studied in Ref. **[100]**.

Table 4.1: List of Pb₁₋ₓSnₓSe samples relevant for comparison of MBE growth with elemental and compound sources.

name	code	substrate	Sn content [%]	Thickness	Growth T [°C]	Studied by	Comments
P1	P121517B	BaF₂	19	1 μm	325	AFM	-
P3	P011118A	BaF₂	24	50 nm	250/440	XRD	Anneal: 5min
P5	P011118C	BaF₂	16	50 nm	250/440	XRD	Anneal: 5min
P7	P032918B	BaF₂	19	1 μm	363	AFM	Se decap
G2	GM2_250220B	BaF₂	34	1 μm	340	AFM, XRD, EDS	-
G9	G102121A	BaF₂	25	1 μm	365	XRD	Se cap
G11	G102621A	BaF₂	31	1 um	350	XRD	Se cap
G12	G102821A	BaF₂	15	1 μm	360	XRD	Se cap

Figure 4.1 shows the RHEED patterns recorded after the growth of 1 μm Pb₁₋ₓSnₓSe using compound sources (stoichiometric PbSe and SnSe) and elemental sources (Pb, Sn, Se), **(a)** and **(b)**, and **(c)** and **(d)**, respectively. In both cases, streaky patterns, with sharp reflections on Laue semicircle and Kikuchi lines are visible, pointing to atomically smooth, flat surfaces.
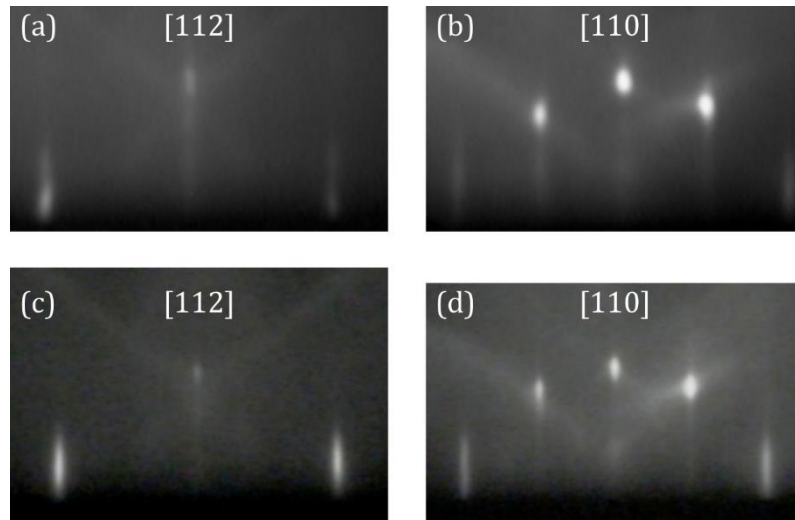
Figure 4.1: RHEED patterns of (111) Pb₁₋ₓSnₓSe epilayers, recorded along [112] and [110] azimuths, grown using compound and elemental sources. **(a)** and **(b)** $x_{Sn} = 0.19$ (sample P7) film grown with elemental sources. **(c)** and **(d)** $x_{Sn} = 0.34$ (sample G2) film grown with compound sources.

Figure 4.2 shows representative AFM images of the 1 μm thick Pb₁₋ₓSnₓSe films grown on cleaved (111) BaF₂ in the PREVAC 190 and Veeco GENxplor GM#2 systems, **(a)** - **(c)** and **(d)** - **(f)**, respectively. In both cases, characteristics spiral step structure **[145]** is present. On the surface of the samples grown with elemental sources, a single spiral is slightly wider on average (see **Figure 4.2 (a)** and **(d)**). The RMS roughness is also greater for the studied films grown with the elemental sources. One also has to keep in mind that the composition of the layers is different. Therefore, the samples are not fully comparable.
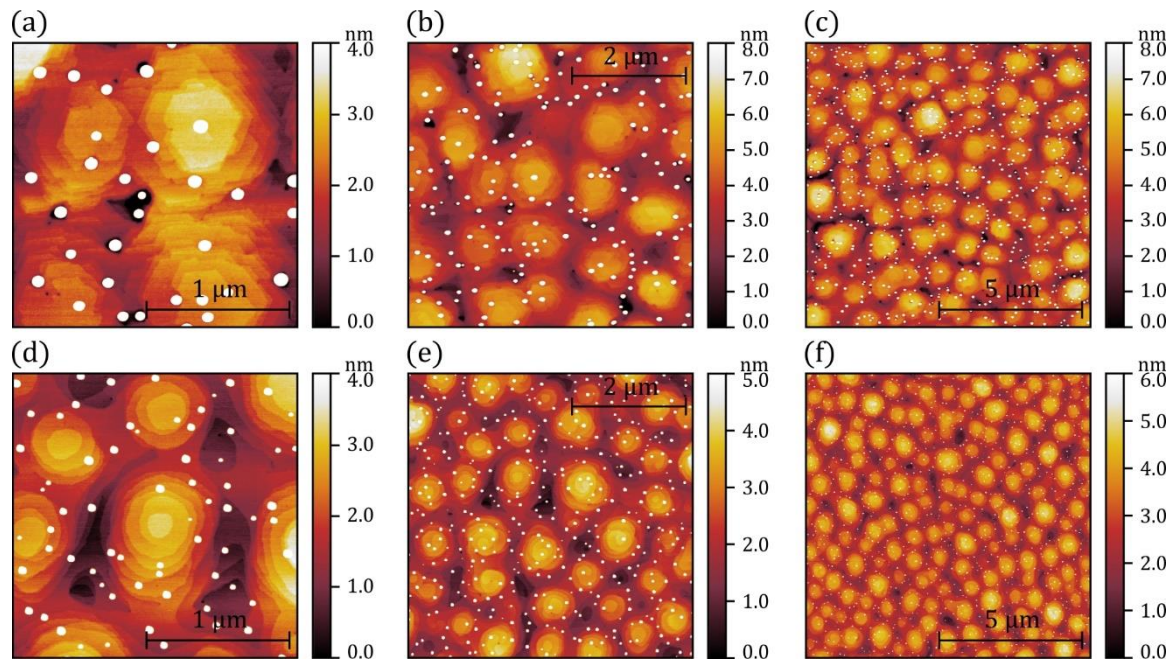
Figure 4.2: AFM images of 1 μm thick Pb$_{1-x}$Sn$_x$Se films grown on (111) BaF2 using compound and elemental sources. (a), (b), (c) x_{Sn} = 0.19 (sample P1) film grown with elemental sources with RMS = 2.42 nm. **(d), (e), (f)** x_{Sn} = 0.34 (sample G2) film grown with compound sources with RMS < 1 nm. Measurements were performed by M. Aleszkiewicz. Data presentation by B. Turowski.

In **Figure 4.3**, a comparison of the XRD measurements of Pb$_{1-x}$Sn$_x$Se films grown in the PREVAC 190 and Veeco GENxplor GM#2 systems is presented. Wide range 2θ-ω scans, presented in **(a)** and **(b)**, for both kinds of epilayers show only the presence of the (111) phase. The samples grown using elemental sources were significantly thinner (50 nm) and because of this, the signal ratio of BaF$_2$ to Pb$_{1-x}$Sn$_x$Se is much higher in this case. The sampling of the scans for the 50 nm epilayers is lower because of the shorter measurement time, as these measurements were carried out at the time of familiarisation with the measurement system. Similarly, reciprocal space maps (RMS) show a stronger signal coming from BaF$_2$ for 50 nm samples.
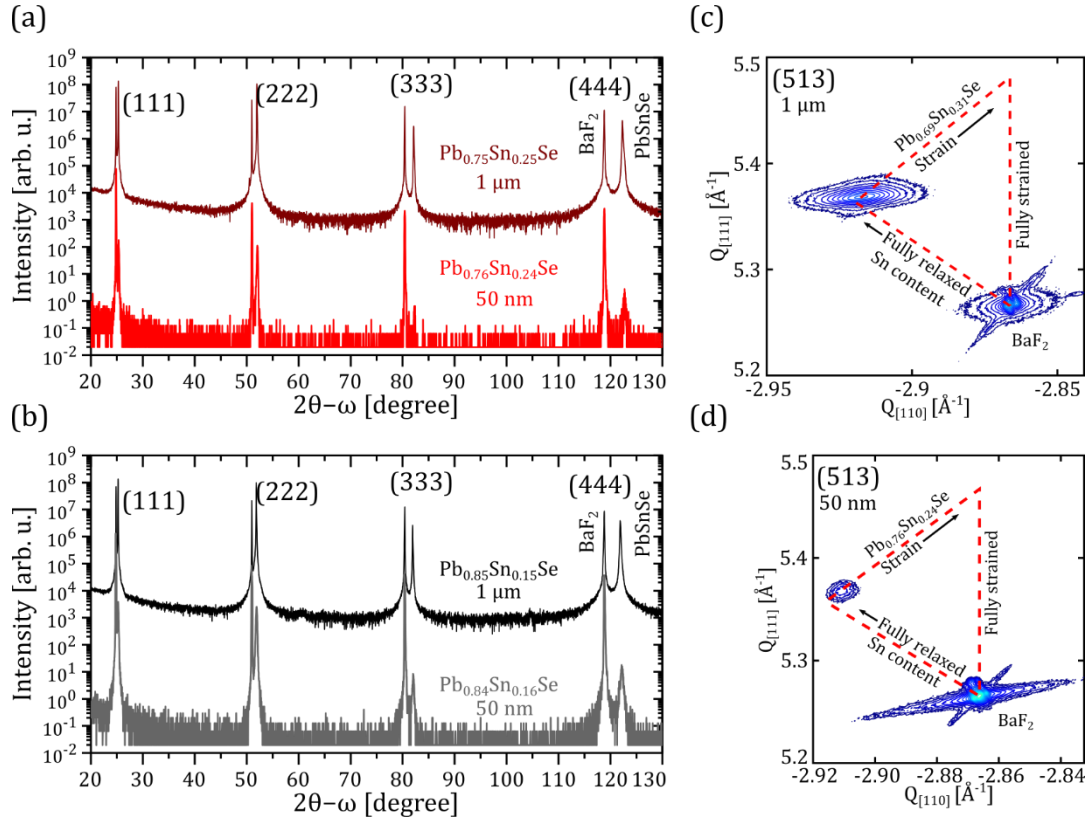
Figure 4.3: XRD investigation of (111) Pb$_{1-x}$Sn$_x$Se epilayers grown using elemental and compound sources. (a) and **(b)** Wide range 2θ-ω scans of samples with Sn content of 15-16% and 24-25%, respectively. Bottom scans (lighter colours) show 50 nm thick films grown with elemental sources (samples P3 and P5 in (a) and (b), respectively). The top scans (darker colours) show 1 μm thick films grown with compound sources (samples G9 and G12 in (a) and (b), respectively). **(c)** and **(d)** RSM around the asymmetric (513) reciprocal lattice point at room temperature (samples G11 and P3 in (c) and (d), respectively) showing strain induced by growth of Pb$_{1-x}$Sn$_x$Se on BaF$_2$. Measurements were performed by dr V. V. Volobuev, with B. Turowski assistance for 1 μm thick samples. Data presentation by dr V. V. Volobuev and B. Turowski.

4.2   Pb$_{1-x}$Sn$_x$Se epilayers for ARPES and SR-ARPES

In this section preparation, by MBE growth, and the characterisation of Pb$_{1-x}$Sn$_x$Se grown on BaF$_2$ (111) in the VEECO GENxplor system are discussed in order to demonstrate the high quality of the epilayers grown that were later studied by ARPES and SR-ARPES. Research of some of the samples prepared in this system was published in Ref. **[15]** and presented in part during the 5th International Conference on Applied Surface Science (ICASS 2022) in the form of a 20 minutes oral presentation. I grew the samples with dr V. V. Volobuev. Structural characterisation of the epilayers was done by XRD, SEM (with EDS), and AFM. I assisted in XRD measurements performed by dr V. V. Volobuev. SEM (EDS) measurements were performed by dr T. Wojciechowski. AFM measurements were performed by dr M. Aleszkiewicz. The samples were grown to observe the influence of transition metal deposition

on the surface of $Pb_{1-x}Sn_xSe$ TCI in normal and topological crystalline insulator phases. The samples discussed are listed in **Table 4.2**.

Table 4.2: List of $Pb_{1-x}Sn_xSe$ samples relevant for structural quality characterization of epilayers studied by ARPES.

name	code	Sn content [%]	Thickness	Studied by	Bi [%]
G1	GM2_120220B	0	1 μm	XRD	-
G2	GM2_250220B	34	1 μm	AFM, XRD, EDS	-
G3	GM2_070920A	26	1 μm	ARPES, CL	0.06
G6	G072621A	24	2.5 μm	XRD	-
G9	G102121A	25	1 μm	XRD	0.067
G11	G102621A	31	1 μm	XRD, RHEED	0.08
G12	G102821A	15	1 μm	XRD	0.08
G13	G102921A	0	260 nm	RHEED	-
G17	G110421A	14	1 μm + 250nm	RHEED	0.082
G20	G110821B	24	1 μm + 250nm	RHEED	0.068
G31	G011322A	12	1 μm	ARPES/SR, RHEED	0.079
G39	G070822Ap	27	1 μm	AFM	-
G40	G070822Ac	27	1 μm	AFM	-
G41	G092922A	27	1 μm	RHEED oscillations (Mn)	-
G42	G102622A	28	10×10nm	RHEED oscillations	-

4.2.1 Samples growth

In order to study topological transition in $Pb_{1-x}Sn_xSe$, samples in both normal insulator and topological crystalline insulator phases were grown in the range of 0% to 35% tin content. During MBE growth, RHEED patterns were recorded in-situ to assess the quality of the films in real time. **Figure 4.4** and **Figure 4.5** show representative patterns observed for $Pb_{1-x}Sn_xSe$ epilayers. Streaky and high contrast patterns, with sharp reflections on Laue semicircle, coming from surface diffraction of the electrons, and intense Kikuch lines, coming from the diffraction within the growing crystal, are observed. Such patterns indicate a two-dimensional growth mode and atomically flat surfaces. Images **(a)** to **(f)** in both **Figure 4.4** and **Figure 4.5** show RHEED images of the corresponding 1 μm thick $Pb_{1-x}Sn_xSe$ films grown on BaF_2 (111) substrates, recorded along [110] and [112] azimuths, respectively. They show that high-quality epilayers were grown over a range of different compositions of $Pb_{1-x}Sn_xSe$ having the rock-salt structure. Images **(c)** , **(d)** and **(e)** show a representative RHEED of samples with compositions similar to those of samples studied with ARPES and SR-ARPES. Images **(f)** show that there is no degradation in sample surface quality, when studied by RHEED, after a one-month storage in the UHV suitcase, used to transfer samples from the GM#2 system to the synchrotron facilities.
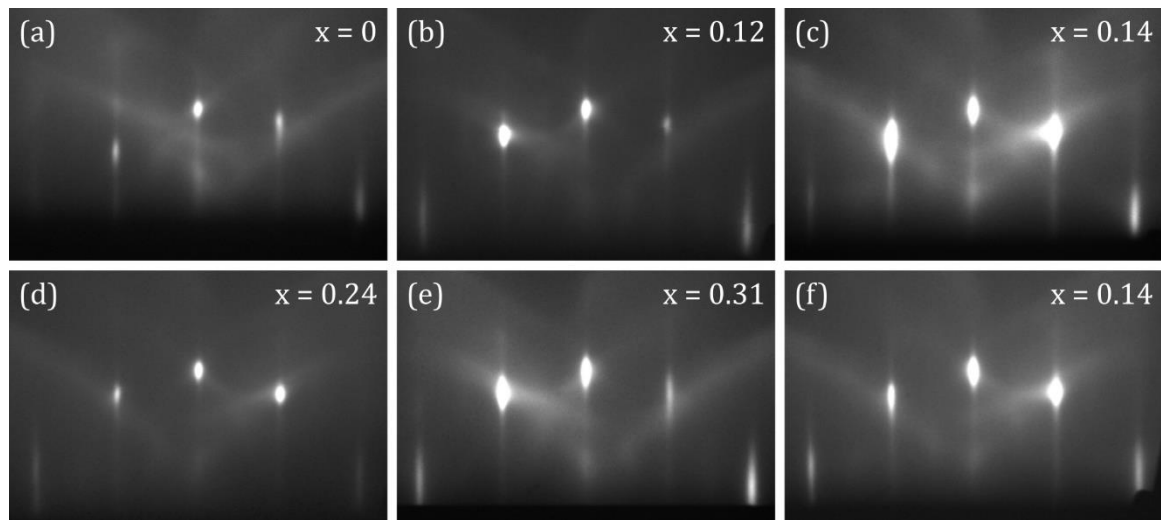
Figure 4.4: RHEED patterns of 1 μm Pb$_{1-x}$Sn$_x$Se epilayers recorded along [110] azimuth grown on BaF$_2$ (111) substrates in the GM#2 system for x = 0, 0.1, 0.15, 0.25 and 0.3, (a) to (e), respectively. (f) RHEED pattern recorded along [110] azimuth of sample (c) after one-month long storage in the UHV suitcase. Samples G13, G31, G17, G20, G11 (a) to (e), respectively.
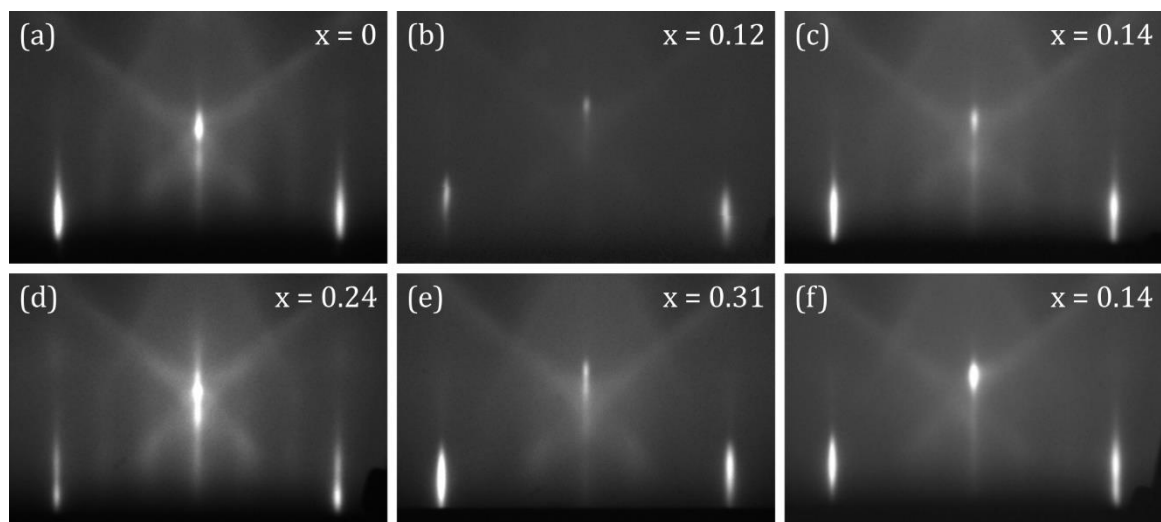

Figure 4.5: RHEED patterns of 1 μm Pb$_{1-x}$Sn$_x$Se epilayers recorded along [112] azimuth grown on BaF$_2$ **(111) substrates** in the GM#2 system for x = 0, 0.1, 0.15, 0.25 and 0.3, **(a)** to **(e),** respectively. **(f)** RHEED pattern recorded along [112] azimuth of sample (c) after one-month long storage in the UHV suitcase. Samples G13, G31, G17, G20, G11 (a) to (e), respectively.

To establish the growth mode of the films grown in the GM#2 system, 80 seconds growth of Pb$_{0.72}$Sn$_{0.28}$Se (sample G42) at various values of substrate temperature was carried out on a refreshed surface of a 1 μm thick Pb$_{0.73}$Sn$_{0.27}$Se layer (sample G41) grown on BaF$_2$ (111), and kept in the UHV chamber. Growths were carried out with a pause after each substrate temperature decrease to allow proper stabilisation of the substrate temperature. Specular spot intensity was recorded for two minutes: 20 seconds before, 80 seconds during, and 20 seconds after the growth. The specular spot intensity oscillations are presented in **Figure 4.6**, as recorded by the kSA 400 analytical RHEED system software, which was also used for the

damped sine wave fit of the oscillations. The fits were used to calculate the growth rate of $Pb_{0.72}Sn_{0.28}Se$, shown in **Table 4.3**, at the corresponding temperatures.
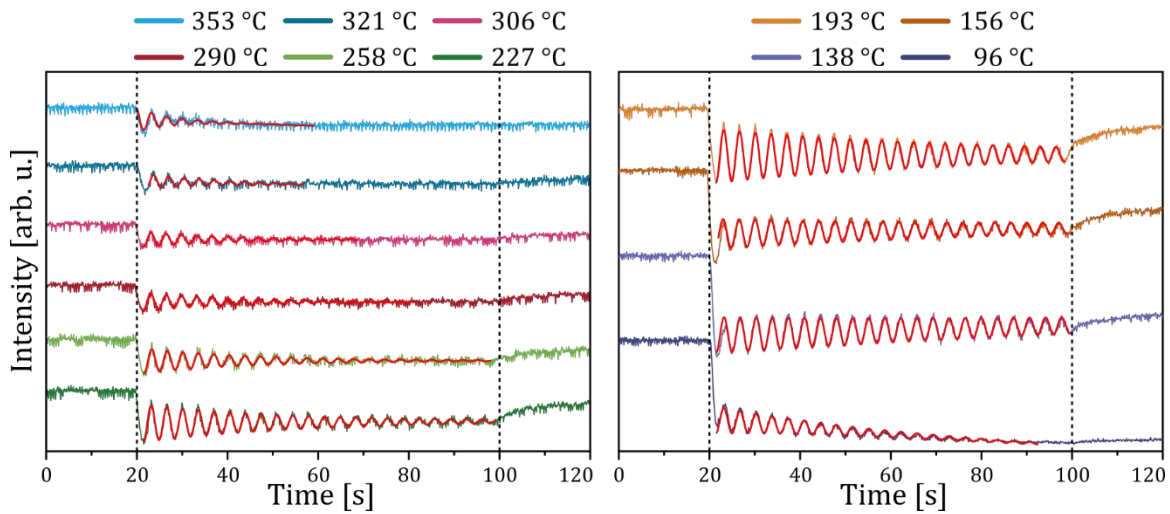

Figure 4.6: Specular spot intensity oscillations as a function of $Pb_{0.72}Sn_{0.28}Se$ growth time for different substrate temperatures. The damped sine wave fit (in red) for all film deposition temperatures was done in the kSA 400 analytical Reflection High-Energy Electron Diffraction (RHEED) system software. Black dashed lines mark the beginning (left) and end (right) points of growth. Sample G42.

For a substrate temperature above 290 °C, the specular spot intensity oscillations disappear after ~10 periods. Initial few monolayers grow in layer-by-layer mode, but due to high surface mobility and presence of surface steps, the growth shifts to step-flow mode and the oscillations disappear. Interpreting the growth mode as the step-flow mode is supported by the presence of fine streaks in RHEED patterns coming from the presence of terraces on the sample surface **[108]**. Reduction of the growth temperature induces a layer-by-layer growth mode with persisting oscillations of the specular spot intensity. For growths in the temperature range of 277 – 138 °C, oscillations were present for the entire 80 seconds of deposition, with 193 °C being the most pronounced. Growth temperature below 100 °C reduced the surface mobility of adatoms and resulted in 3D island growth.

Table 4.3: Growth rate of $Pb_{0.72}Sn_{0.28}Se$ calculated from the damped sine wave fits shown in **Figure 4.6** using the kSA 400 analytical RHEED system software. Sample G42.

Temperature [°C]	353	321	306	290	258	227	193	156	138	96
Growth rate [Å/s]	1.054	1.057	1.041	1.031	1.026	1.012	1.008	0.997	0.992	0.989

The growth rates are determined by the software used from the period of recorded oscillations and the lattice plane distance of the grown material. The decrease of the growth rate with decreasing temperature is counterintuitive. The lower substrate temperature should decrease the desorption of the molecules from the surface, resulting in a higher growth rate. Observed phenomena can be explained by a model suggested by A.I. Nikiforov et al. **[146]** in which one RHEED oscillation period does not necessarily correspond to growth of

one full monolayer. At the temperatures of transition from 2D to step-flow growth mode, which is the case here, the maximal derivation of thickness of the film grown during one oscillation period was found to be as high as 25%. In the case of growth of $Pb_{0.72}Sn_{0.28}Se$, the growth rate decrease is 6%. The growth rate determined by QCM was 1.207 Å/s, measured before the start of the experiment.

4.2.2   Structural and compositional characterization

AFM images support the conclusion from RHEED patters of smooth 2D growth of the films. **Figure 4.7 (a)**, **(b)** and **(d)** show a characteristic spiral step structure for films grown on cleaved BaF_2 **[145]**. The origin of such structure is in the 1.2% - 2% lattice mismatch between $Pb_{1-x}Sn_xSe$ and BaF_2. The mismatch causes a screw type threading dislocations that pin the surface steps. The root mean square (RMS) roughness is below 1 nm and the step size is ~1 nm. Spiral step structure is absent for $Pb_{0.73}Sn_{0.27}Se$ grown on polished BaF_2 (Crystal GmbH BaF_2 substrate (111)K<0.5°), as shown in **Figure 4.7 (c)**.
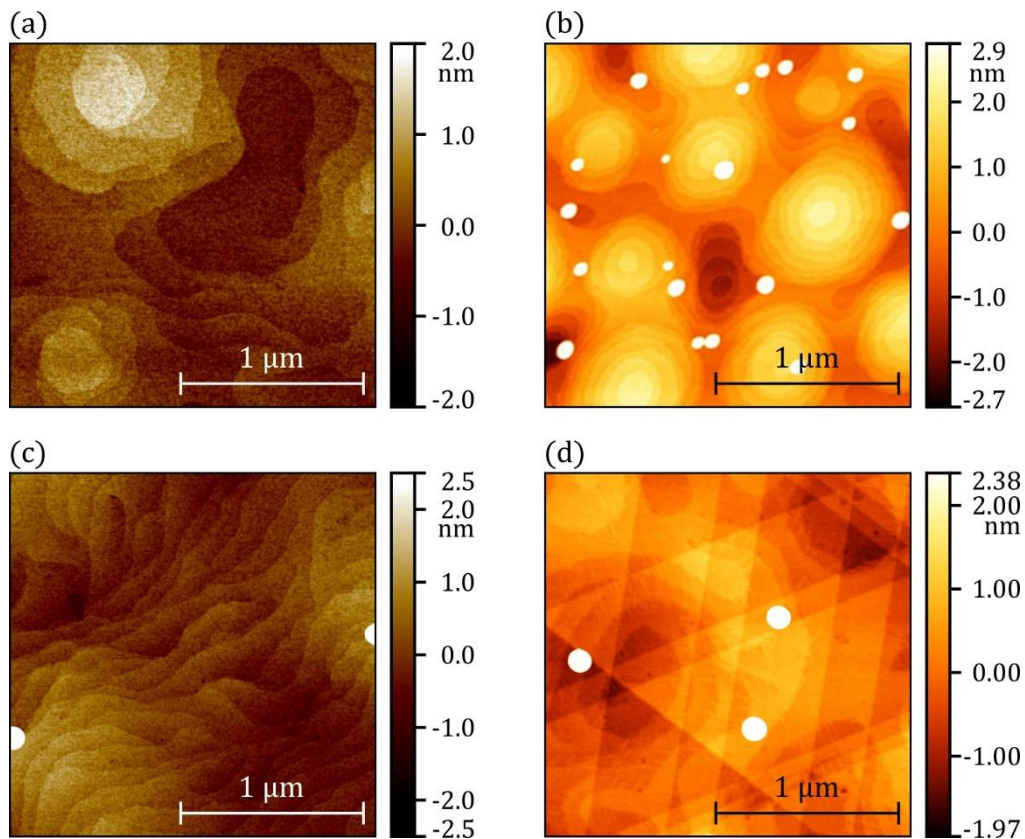
Figure 4.7: AFM 2 μm × 2 μm images of $Pb_{1-x}Sn_xSe$ films grown on (111) BaF_2. (a), (c) x_{Sn} = 0.27, (b) x_{Sn} = 0.34, (d) x_{Sn} = 0.26. (a), (b), (d) grown on cleaved BaF_2, (c) grown on polished BaF_2. (d) 0.3 ML Fe deposited on the surface. Image (a) adapted from Ref. **[15]**. Samples G39, G2, G40, G3 (a) to (d), respectively. Measurements were performed by dr M. Aleszkiewicz. Data presentation by B. Turowski.

Due to a slight polishing off angle of less than 0.5° the steps on the substrate have preferred orientation. In the step-flow growth mode, the $Pb_{1-x}Sn_xSe$ film growth follows the initial

orientation of the steps, resulting in semi-parallel orientation of the steps on the surface of the grown film. Similarly, the RMS roughness is below 1 nm and the step size is ~1 nm.

White spots are present in the AFM images for each measured $Pb_{1-x}Sn_xSe$ film to a greater or lesser extent. The deposition of a sub-monolayer (ML) amount of TM (Fe in this case) causes the emergence of an additional triangular pattern in AFM images.

Single-phase single-crystalline film growth was confirmed by XRD measurements. **Figure 4.8 (a)** and **(c)** show that only {111}-type reflections of the substrate and the film are present.
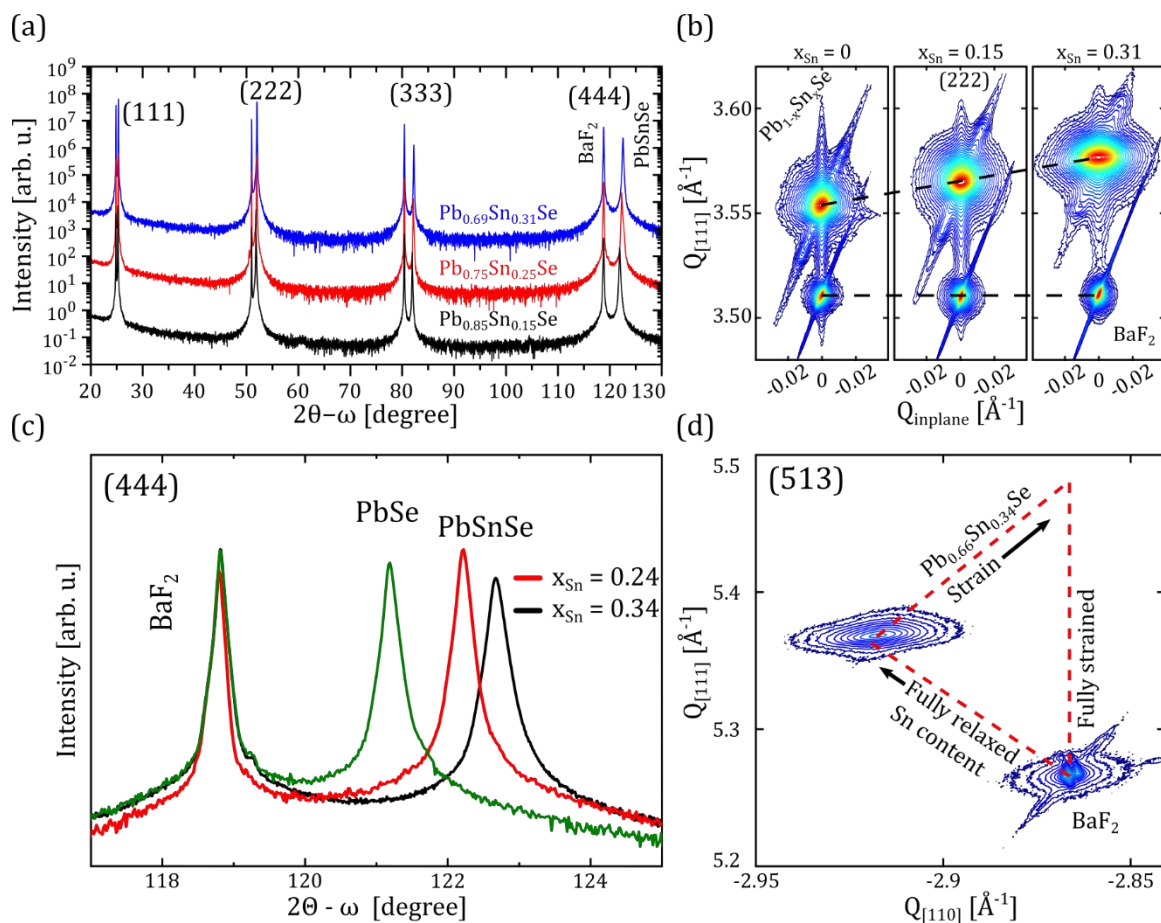
Figure 4.8: Structural investigation of (111) Pb₁₋ₓSnₓSe epilayers by XRD. (a) Wide range 2θ-ω scans of samples with Sn content of 15%, 25% and 31% (G12, G9 and G11). **(b)** Reciprocal space maps (RSM) of symmetric (222) reflection of samples with Sn content 0%, 15% and 31%, respectively, left to right (G1, G12, G11). **(c)** High resolution 2θ-ω scans of samples with nominal Sn content of 0%, 24% and 34% (G1, G6, G2). **(d)** RSM around the asymmetric (513) reciprocal lattice point showing the strain induced by growth on BaF₂ for sample G2. Images (a) and (b) adapted from Ref. **[15]**. Measurements performed by V.V. Volobuev with B. Turowski assistance. Data presentation by B. Turowski.

The typical FWHM value of ω-rocking curve extracted from (222) RSM (**Figure 4.8 (b)**) was 40 - 70 arcsec for BaF₂ substrates and 200 - 500 arcsec for 1 µm thick $Pb_{1-x}Sn_xSe$ films. This FWHM value gives information on the existence of defects such as dislocations and mosaicity

in the grown film – ω-rocking broadens due to their presence. The smaller the FWHM, the closer the film is to the perfect epitaxial layer. The position of $Pb_{1-x}Sn_xSe$ in (222) RSM is a linear function of the Sn content. Similarly, there is an x_{Sn} dependent shift of the diffraction peaks to larger diffraction angles, as shown in **Figure 4.8 (c)**. Both of these correspond to a decrease of the $Pb_{1-x}Sn_xSe$ lattice constant a_{PbSnSe}, which is related to the Sn content x_{Sn} by the following equation **[147]**:

$$x_{Sn} = \frac{6.1240 - a_{PbSnSe}}{0.1246} \qquad (4.1)$$

With increasing x_{Sn}, the lattice constant of $Pb_{1-x}Sn_xSe$ decreases and the strains in the grown film increase. The a_{PbSnSe} was calculated in accordance to **Section 3.3 X-ray diffraction**. **Figure 4.8 (d)** shows that 1 μm thick $Pb_{0.7}Sn_{0.3}Se$ is indeed slightly strained when grown on BaF_2, as the position of the $Pb_{0.7}Sn_{0.3}Se$ maxima moves along the red dashed line corresponding to the expected position of the strained $Pb_{0.66}Sn_{0.34}Se$ maxima.

In addition to the above, a sample with x_{Sn} = 0.34 was analysed by EDS to characterize its composition and verify the nominal Sn content calculated from deposition rate measurements with QCM. It was found to be 32% and within 2% agreement with the composition obtained by XRD and EDS **(Figure 4.9)**.
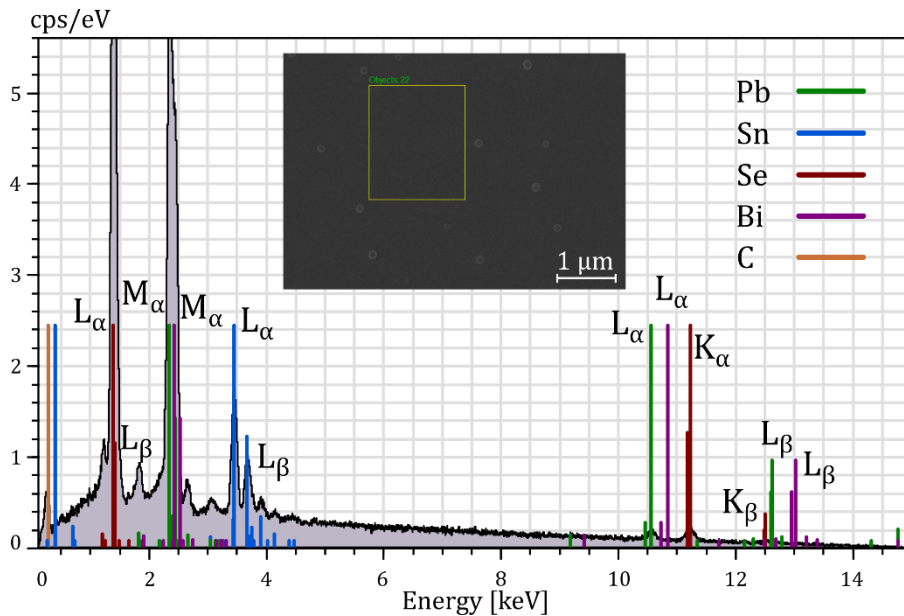

Figure 4.9: EDS of 1 μm thick $Pb_{1-x}Sn_xSe$ film with x_{Sn} = 0.32. Operating voltage 15 keV. Inset: SEM image of the scanned sample fragment. Sample G2. Measurements performed by dr T. Wojciechowski with B. Turowski assistance. Data presentation by B. Turowski.

Table 4.4 shows the detailed results of the EDS measurement of 1 μm $Pb_{1-x}Sn_xSe$ film with Sn content estimated from the deposition rate as 30%. Small traces of carbon (C) are usually present for every sample measured in the used setup. Due to the fact that bismuth (Bi) doping

is less than 1%, it is below the detection limit of EDS. The tin content x_{Sn} is calculated as follows:

$$x_{Sn} = \frac{at.\,\%_{Sn}}{at.\,\%_{Sn} + at.\,\%_{Pb}} \qquad\qquad (4.2)$$

and equals to 32%.

Table 4.4: Composition of 1 μm Pb$_{1-x}$Sn$_x$Se film with x$_{Sn}$ = 0.32 obtained from the EDS data presented in **Figure 4.9**. Sample G2. The nominal Sn content was 34%, estimated by QCM deposition rate measurement.

Element	wt. %	at. %	at. % C norm.
Pb	50.77	21.16	32.79
Sn	13.82	10.05	15.57
Se	30.48	33.32	51.64
C	4.93	35.47	-

Some of the samples studied in the scope of this thesis were covered by an amorphous Se cap to protect Pb$_{1-x}$Sn$_x$Se surface from exposition to the air atmosphere. Prior to the ARPES studies, the Se layer was re-evaporated in the UHV chamber to recover the original clean epilayer surface. **Figure 4.10** shows that no significant decrease in the quality of the Pb$_{1-x}$Sn$_x$Se film is observed in AFM after Se decapping. The characteristic spiral step structure is still present, albeit it is not as sharp as in samples that have not been capped with Se.
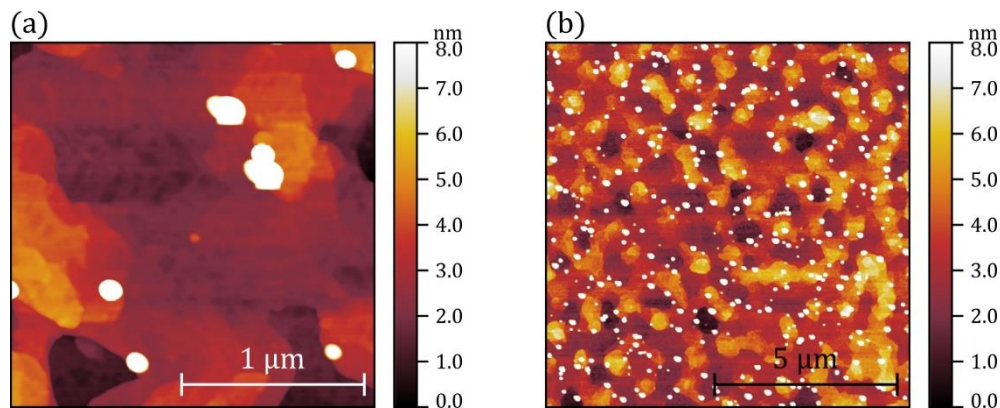
Figure 4.10: AFM images of Pb$_{0.81}$Sn$_{0.19}$Se film grown on (111) BaF2 after 100 nm Se decapping. (a) 2 μm × 2 μm image. **(b)** 10 μm × 10 μm image. Measurements done by dr M. Aleszkiewicz. Data presentation by B. Turowski.

4.2.3 Transition metals

In this thesis, Fe and Mn Transition metals (TM) were deposited in submonolayer thickness on a surface of Pb$_{1-}$Sn$_x$Se TCI in order to verify whether a magnetic impurity on the surface would induce ferromagnetism that would lead to spontaneous breaking of a crystalline symmetry and result in gap opening in surface spectrum **[148, 149]**.

Transition metals belong to groups 3 to 12 of the periodic table. The term 'transition' comes from their transitional position between metals of groups 1 and 2 and predominantly non-metals of groups 13 to 18. The first row of the TM, which encompasses iron (Fe) and manganese (Mn) used in this thesis, coincides with the filling of the 3d orbitals. The TM can be defined as an element possessing filled or partially filled valence d orbitals in one or more of its oxidation states [150]. The d electrons are responsible for the interaction with the bonding electrons, which are described by crystal-field theory [151]. The occupation of the d subshell by electrons is responsible for the magnetic properties of a given material. The possible occupation is restricted by the Pauli Exclusion Principle and the Hound's rule. According to the Pauli Exclusion Principle, no two electrons can occupy the same quantum state at the same time. According to the Hound's rule, every orbital in a subshell must be singly occupied before any orbital can be doubly occupied, and all electrons in singly occupied orbitals must have the same spin. Therefore, a TM with partially filled d orbital has unpaired electrons, which causes a non-zero magnetic moment and magnetic properties of the given element. Transition metals are discussed in great detail in the book titled *Transition Metal Chemistry* by M. Gerloch and E. C. Constable [152].

4.2.4 Deposition of TM

Manganese (Mn) and iron (Fe) transition metals were deposited at RT on the surface of epilayers with Sn content ranging from 25% to 30%. Fe depositions were performed in the preparation chambers of the URANOS and PHELIX beamline end-stations, using available electron beam evaporators. Mn depositions were performed in the preparation chamber of the URANOS beamline end-station, for samples grown in the Riber 1000 system, using a quadruple Knudsen effusion cell. Additional experiments of Mn depositions were performed in the growth chamber of the GM#2 system using a Knudsen effusion cell [153, 154]. The evolution of the RHEED patter for such Mn deposition is presented in **Figure 4.11**. In all systems, calibrated QCMs were used to control the thickness of the deposited TM. The deposition steps are presented in **Table 4.5** and **Table 4.6** for epilayers studied at URANOS and PHELIX beamlines, respectively.

Table 4.5: Transition metal deposition (thickness in ML) on the surface of 1 μm thick $Pb_{1-x}Sn_xSe$ epilayers studied by ARPES.

Sample	Code	% Sn	TM	1st dep.	2nd dep.	3rd dep.	4th dep.	5th dep.	Sum
R1	MBE_3431B	26	Mn	0.1	0.1	0.1	0.1	0.2	0.6
R2	MBE_3440A	30	Mn	0.1	0.1	0.1	0.1	-	0.4
R3	MBE_3440B	30	Mn	0.1	0.1	0.1	0.1	-	0.4
R4	MBE_3426A	25	Fe	0.05	0.05	0.1	-	-	0.2
R5	MBE_3426B	25	Fe	0.05	0.05	0.1	-	-	0.2
G3	GM2_070920A	26	Fe	0.1	0.1	0.1	-	-	0.3
G5	GM2_140920A	30	Fe	0.2	0.2	0.2	-	-	0.6

The samples grown in the Riber 1000 MBE system were covered in-situ with an amorphous Se layer in order to protect the sample surface from air exposure. The samples were annealed in the preparation chamber of the URANOS end-station for 15-40 minutes at 200-330 °C. Details are given in **Appendix Table B.5**.

Table 4.6: Transition metal deposition (thickness in ML) on the surface of 1 μm thick $Pb_{1-x}Sn_xSe$ epilayers studied by SR-ARPES.

Sample	Code	% Sn	TM	1st dep.	2nd dep.	Sum
G35	G011522A	24	Fe	0.3	-	0.3
G36	G011522B	30	Fe	0.2	0.4	0.6
G37	G011522C	26	Mn + Fe	0.4 Mn	0.2 Fe	0.4 Mn + 0.2 Fe

Samples grown in the Veeco GENxplor GM#2 MBE system were transported to the SOLARIS Synchrotron facility in a UHV suitcase and transferred to the preparation chambers of the URANOS and PHELIX end-stations without air exposure. Samples G3, G4 and G5 had some initial in-situ deposition of TM performed (0.1 – 0.4 ML of Fe or Mn) in GM#2. These depositions were performed after the initial characterisation of the E-gun and in different conditions (sample temperature below 0 °C) than other TM depositions. Due to this fact, it is difficult to define the exact amount of TM on the surfaces of the samples. This point is later referenced in the discussion of ARPES spectra.

In order to study behaviour of the TM adsorbate on the surface, the intensity of the specular spot, along [110] azimuth, was observed during the deposition of 1 ML Mn on the surface of 1 μm thick $Pb_{0.73}Sn_{0.27}Se$ film.
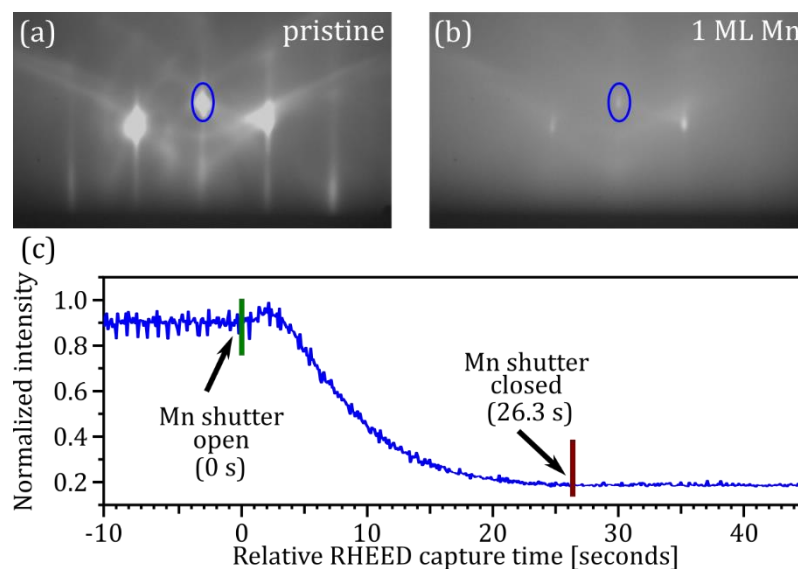
Figure 4.11: Influence of Mn deposition on the RHEED pattern of $Pb_{1-x}Sn_xSe$. (a) RHEED pattern of 1 μm $Pb_{0.73}Sn_{0.27}Se$ epilayer recorded along [110] azimuth. **(b)** RHEED pattern of the same sample after deposition of 1 ML Mn. **(c)** Specular spot (blue ellipse in images (a) and (b)) intensity of the same sample as a function of Mn deposition. Adapted from Ref. **[15]**. Sample G41.

Figure 4.11 (a) and **(b)** show RHEED patterns before and after 1 ML Mn deposition, respectively. An increase in background noise is observed, as well as a decrease in the intensity of the specular spot (**Figure 4.11 (c)**). There are no additional features, such as spots or rings, in the RHEED pattern after Mn deposition (**Figure 4.11 (b)**). This reveals that the TM forms a disordered, amorphous, or nanocrystalline, phase on the surface of $Pb_{1-x}Sn_xSe$.

4.3   Ultra-thin $Pb_{1-x}Sn_xSe$ layers MBE growth

Ultra-thin (30 to 120 nm) $Pb_{1-x}Sn_xSe$ epilayers were grown in PREVAC and GM#2 systems. Samples grown in the PREVAC 190 system (P3-P6) were studied in Ref. **[100]**. The samples I grew in the GM#2 system are being studied by the MagTop Group of Characterisation and Processing (ON6.3). The permalloy (NiFe) is deposited on the samples via magnetron sputtering **[155]** in order to study magnetodynamic properties of the $Pb_{1-x}Sn_xSe$/NiFe bilayers using inverse spin hall effect voltage measurements. The full list of ultra-thin epilayers grown in GM#2 is presented in **Appendix Table B.3**. Samples relevant to the discussion presented in this subchapter are given in **Table 4.7**.

Table 4.7: List of $Pb_{1-x}Sn_xSe$ samples used to discuss the growth of ultra-thin epilayers.

name	code	Sn content [%]	Thickness	Growth T [°C]	Annealing T [°C]
P1	P121517B	19	1 μm	325	-
P4	P011118B	32	50 nm	250	440
G47	G121021A	26	30 nm	200	380

The ultra-thin $Pb_{1-x}Sn_xSe$ film growth procedure is different from the one described in **Section 3.1.3 MBE growth of Pb1-xSnxSe**. The substrate temperature is set to allow for an island growth mode of $Pb_{1-x}Sn_xSe$ on bare BaF_2. In the PREVAC 190 system, growth was carried out at 250 °C. In the GM#2 system, the growth was carried out at 180-225 °C. After deposition of the desired thickness, controlled by BFM or QCM, the substrate temperature was increased to 440 °C or 340-390°C in the PREVAC and GM#2 systems, respectively. Then, the sample was annealed for 5-10 minutes, while the evolution of the RHEED pattern was observed. **Figure 4.12** shows the RHEED images recorded along [110] and [112] azimuths of sample G47, before ((a) and (c)) and after ((b) and (d)) annealing at 380 °C. Initially, after deposition of 30 nm $Pb_{0.74}Sn_{0.26}Se$, spots coming from 3D islands on the surface are visible. After annealing, high contrast, streaky patterns are visible, with reflections on the Laue semicircle and intense Kikuch lines. The streaks are sharper than in the case of 1 μm layers, suggesting a smoother surface. After the growth, samples that were later examined by different methods were covered with amorphous Se at RT to protect the surface when the samples are removed from the UHV.
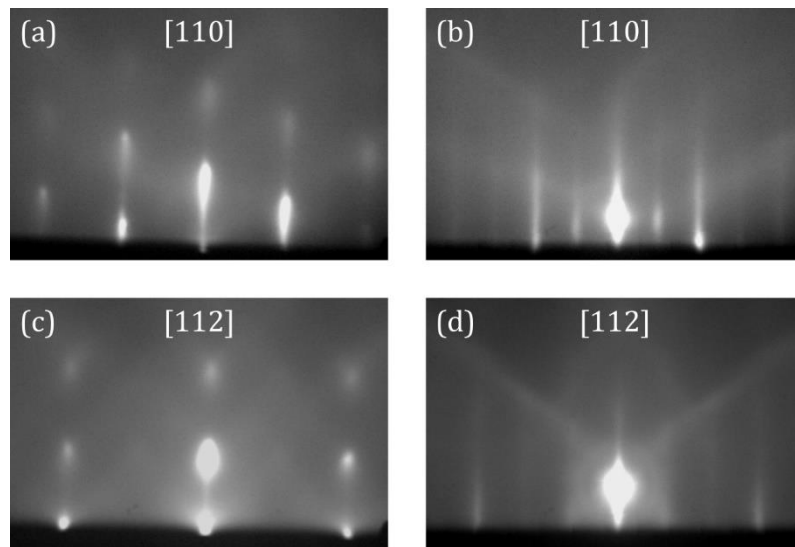
Figure 4.12: RHEED patterns of 30 nm Pb$_{0.74}$Sn$_{0.26}$Se film. **(a), (b)** along [110] azimuth. **(c), (d)** along [112] azimuth. Images (a) and (c) show RHEED after initial deposition of the material. Images (b) and (d) show RHEED annealing. Sample G47.

AFM images of 1 μm and 50 nm thick Pb$_{1-x}$Sn$_x$Se films, grown in the PREVAC 190 system, presented in **Figure 4.13 (a)** and **(b)**, respectively, show that the above conclusion was correct. The RMS roughness of 50 nm films is significantly smaller (0.345 nm for 50 nm vs 2.32 nm for 1 μm thick film), meaning a smoother surface. It is also consistent with an elevation level difference of 1 monolayer (1 atomic layer of metal + 1 atomic layer of Se). The spiral step structure, characteristic for thicker layers of Pb$_{1-x}$Sn$_x$Se grown on cleaved (111) BaF$_2$, is absent for 50 nm layers grown on a similar substrate.
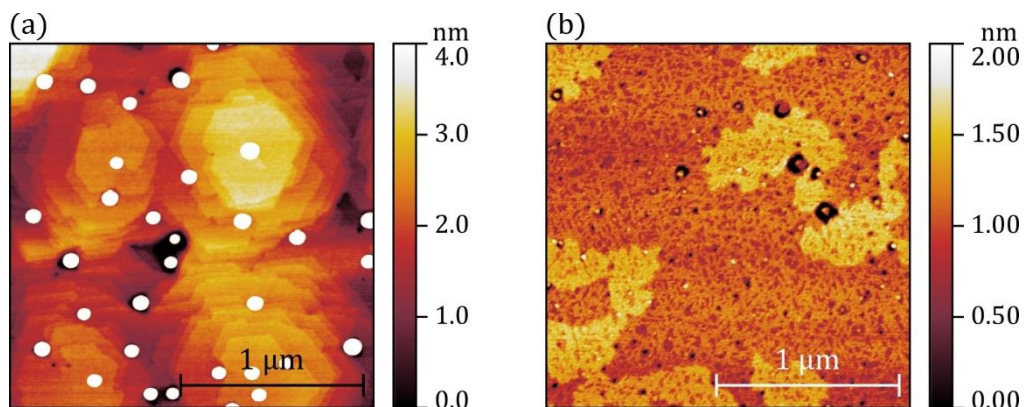
Figure 4.13: AFM 2 μm × 2 μm images comparison of Pb$_{1-x}$Sn$_x$Se thin and ultra-thin films grown on (111) BaF$_2$. (a) 1 μm thick x$_{Sn}$ = 0.19 film (sample P1) with RMS = 2.42 nm. **(b)** 50 nm thick x$_{Sn}$ = 0.32 film (sample P4) with RMS = 0.345 nm. Measurements performed by M. Aleszkiewicz. Data presentation by B. Turowski.

4.4 α-Sn epilayers for ARPES

In this section, preparation by MBE growth and characterisation of α-Sn grown on CdTe (001) are discussed. Results shown in this subchapter were resented in a poster titled *Growth of Gray Tin epilayers on insulating (001)-CdTe/GaAs substrates and its Angular Resolved Photoemission Spectroscopy studies* during the online 49th International School & Conference on the Physics of Semiconductors "Jaszowiec 2021". The samples were grown by R. Rudniewski (hybrid CdTe/GaAs substrate) and dr V. V. Volobuev (α-Sn epilayers). I participated in some of the α-Sn growths. AFM measurements were done by dr M. Aleszkiewicz. XRD measurements were done by dr V. V. Volobuev. Transport studies of samples α-Sn with a similar thickness (50-200 nm) are being done by J. Polaczyński and are the focus point of his PhD thesis. The obtained results are submitted for a publication **[13]**. The discussed samples are listed in **Table 4.8**.

Table 4.8: List of Sn samples used for structural characterisation.

name	code	phase	Thickness [nm]	Studied by
V1	GM2_290320A	α-Sn	50	XRD
V2	GM2_290320C	β-Sn	50	XRD
V3	GM2_200420A	α-Sn	30	XRD (fringes), RHEED
V13	GM2_180221A	α-Sn	150	XRD (wide range)
V14	G061521A	α-Sn	50	AFM

4.4.1 Samples growth

In order to study the Dirac semimetal phase in grey tin, epilayers with thickness varying from 30 nm to 200 nm were grown on (001) GaAs substrates with CdTe (001) buffers. The complete MBE growth procedure is described in detail in **Section 3.1.4 MBE growth of α-Sn**. **Figure 4.14 (a)** shows that high quality hybrid CdTe/GaAs buffers were prepared as a substrate. **Figure 4.14 (b)** shows the 2D growth of thin α-Sn epilayers.
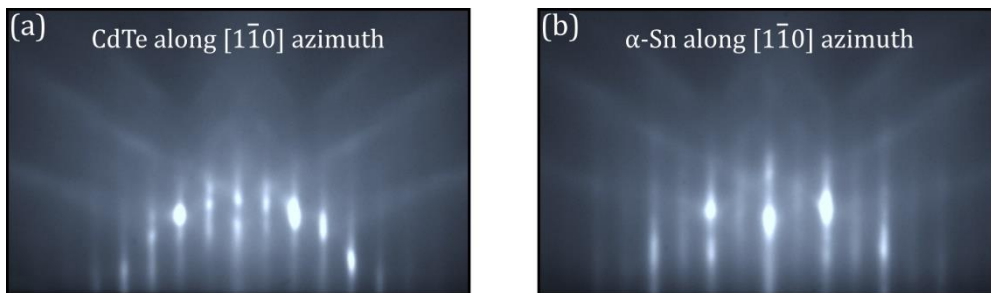
Figure 4.14: RHEED patterns of **(a)** CdTe buffer before grey tin epitaxial growth and **(b)** 30 nm α-Sn epilayer recorded along [1̄10] azimuth. CdTe buffer growth by R. Rudniewski, α-Sn growth by V. V. Volobuev. Data presentation by B. Turowski. Sample V3.

Half order reconstruction maxima are observed, similar to reports of high quality (001) α-Sn grown on InSb **[90, 156, 157]**. In both cases, sharp reflections on the Laue semicircle and intense Kikuch lines are visible in the RHEED patters. In Refs. **[90, 156, 157]** the formation of α-Sn is determined by (2x2) reconstruction observed during the film growth. In order to verify the RHEED pattern obtained (see **Figure 4.14 (b)**), the simulation of the patterns for α-Sn with (2x1) reconstruction and (2x2) reconstruction, **Figure 4.15 (a)** and **(b)**, respectively, was performed with the script described in **Section 3.2.1**.
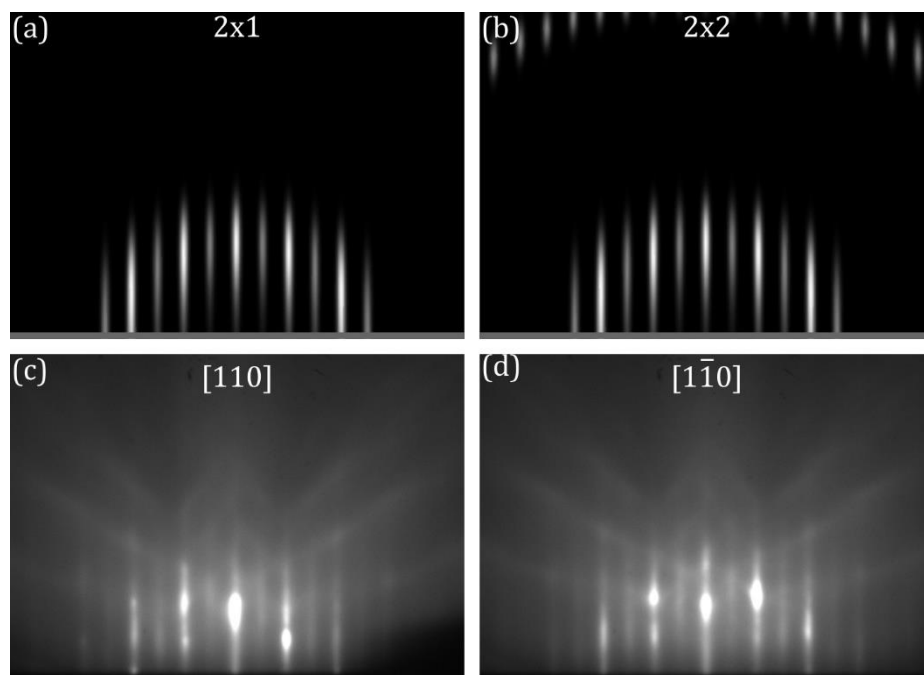
Figure 4.15: Surface reconstructions of α-Sn. **(a)** Simulated RHEED pattern of α-Sn with 2x1 reconstruction. **(b)** Simulated RHEED pattern of α-Sn with 2x2 reconstruction. **(c)** Real RHEED pattern along **[110]** azimuth of 30 nm thick α-Sn. **(d)** Real RHEED pattern along **[1$\bar{1}$0]** azimuth of 30 nm thick α-Sn. Sample V3.

The positions of the diffraction streaks and spots in the simulated RHEED patterns are in good agreement with the experimental results. The reconstruction between main streaks is present in both RHEED patterns recorded along [110] and along [1$\bar{1}$0], images **(a)** and **(b)**, respectively. However, in the simulated image **(b)** of (2x2) reconstruction, additional diffraction spots from another Laue ring are visible near the top of the image. These spots are absent in the simulated image **(a)** of the (2x1) reconstruction and are absent in the real RHEED pattern (images **(c)** and **(d)**). This suggests that the manufactured sample is α-Sn-(2x1). This conclusion is supported by the RHEED study of α-Sn grown by MBE on InSb (100), presented in Ref. **[158]**. The authors report that for 20 nm thick films the surface reconstruction is predominantly two-domain (2x1) with small amount of (2x2). The number of (2x2) structures increases for thickness greater than 50 nm **[158]**. It is important to note, that the presented RHEED simulation is a simplification and does not take into account all possible factors. The diffraction spots absent in **Figure 4.15 (c)** and **(d)** might be visible at higher accelerating voltage.

4.4.2   Structural and compositional characterization

Figure 4.16 shows the AFM image of a 30 nm thick α-Sn epilayer. The Root Mean Square (RMS) is of the order of 2 nm proving smooth surface of the films and confirming conclusions from RHEED patterns presented in **Figure 4.14**. The main source of Sn layer roughness seems to be the CdTe buffer, demonstrating a similar surface pattern and RMS.
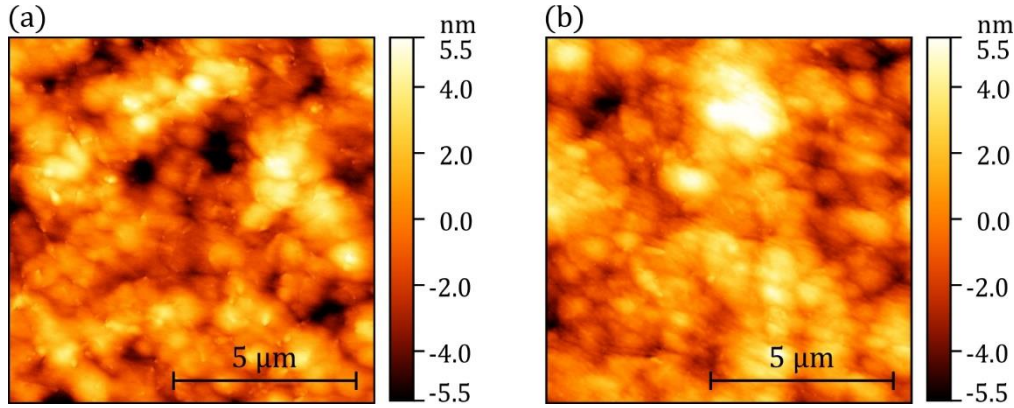

Figure 4.16: AFM 10 μm × 10 μm images of **(a)** CdTe grown on GaAs (001) substrate and **(b)** 50 nm thick α-Sn film grown on (001) CdTe buffer. Measurements done by M. Aleszkiewicz. Data presentation by B. Turowski. Samples V15 and V14, (a) and (b) respectively.

XRD measurements confirm that the grown films are α-Sn. Since grey tin has a diamond cubic structure, and the epilayers were grown on (001) substrate, the expected XRD reflections of high quality (001) epilayer are (00X), where X is multiplicity of four, due to diffraction selection rules presented in **Table 3.3**. **Figure 4.17** shows the comparison of XRD 2θ-ω scans of 50 nm thick α and β Sn epilayers grown on (001) CdTe/GaAs, marked with purple and turquoise colours, respectively. Both CdTe and GaAs have the zinc blende crystal structure with allowed reflections for h, k and l all being odd or even. Due to the (001) orientation of the growth, h and k are always even (equal to zero), thus reflections only from planes with even l are observed.
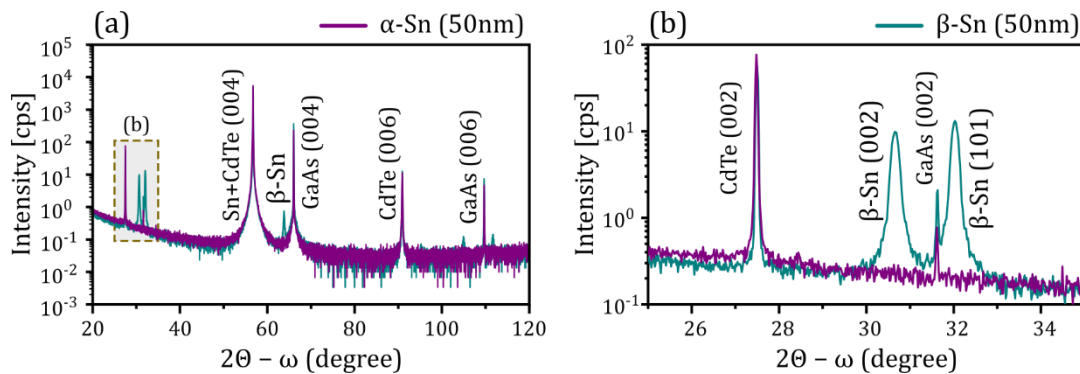
Figure 4.17: 2θ-ω scans of α and β Sn/CdTe/GaAs (001) 50 nm films. (a) Wide range scan; dashed rectangle shown in (b). **(b)** Zoom-in to (002) reflection. Samples V1 and V2, α and β Sn respectively.

Figure 4.17 (a) shows that indeed, only even-l reflections are present for the CdTe/GaAs substrate and only (004) reflection for α-Sn is present, confirming the diamond cubic structure. The β-Sn has a tetragonal unit cell, for which $h^2 + k^2 + l^2$ needs to be even. In the range presented in **Figure 4.17 (b),** the allowed reflections of β-Sn are (002) and (101). Indeed, two β-Sn maxima are visible, and no reflections from α-Sn are present, as expected.

Greater Bragg reflection angles provide better separation of close situated peaks. **Figure 4.18** shows more detailed XRD measurements of the 150 nm thick α-Sn epilayer. In image **(a),** a wide-range 2θ-ω scan, including (008) reflection, is presented. Image **(b)** shows high resolution XRD in the vicinity of (004) reflection. The presence of thickness fringes proves the high quality of the α-Sn, that is, the epilayer grown on the CdTe is flat and has a uniform thickness. The XRD spectrum (purple) is also in agreement with a simulated spectrum (green). Image **(c)** shows (008) reflection of α-Sn and CdTe, which is better resolved than at (004) reflection. **Figure 4.18 (d)** and **(e)** show (206) asymmetric RSM in full and zoom-in range, respectively, with labelled position of CdTe (green triangle) as well as real strained (pink square) and expected relaxed (grey circle) α-Sn maxima. From the XRD asymmetric RSM shown in **Figure 4.18 (e)**, the in-plane ($a_\parallel$) and out-of-plane ($a_\perp$) lattice constants can be determined using **Equations (3.10)** and **(3.11)**, respectively, as described in **Section 3.3 X-ray diffraction**. Using known values of elastic constants, the values of strains, as well as the unstrained lattice constant a_0 can be determined. The elastic constants are measured by applying strain to a material in a controlled manner and are known with high precision for most materials. For the diamond cubic structure, there are three constants: C_{11}, C_{12}, and C_{44} **[159]** and for α-Sn these are equal: C_{11} = 69 GPa, C_{12} = 29.3 GPa, C_{44} = 36.2 GPa **[160]**. These elastic constants were used to calculate Poisson's ratio $\nu = \frac{C_{12}}{C_{11}+C_{12}} = 0.298$, as well as parameter $k = \frac{2 \cdot C_{12}}{C_{11}} = 0.849$, which is used in calculation of the unstrained lattice constant a_0 (see **Equation (4.3)**). The Poisson's ratio and the parameter k are related by: $k = \frac{2 \cdot \nu}{1-\nu}$.

$$a_0 = \frac{a_\perp + k \cdot a_\parallel}{k + 1} \tag{4.3}$$

The in-plane ($\varepsilon_\parallel$) and out-of-plane ($\varepsilon_\perp$) strains are calculated using:

$$\varepsilon_\parallel = \frac{a_\parallel - a_0}{a_0} \tag{4.4}$$

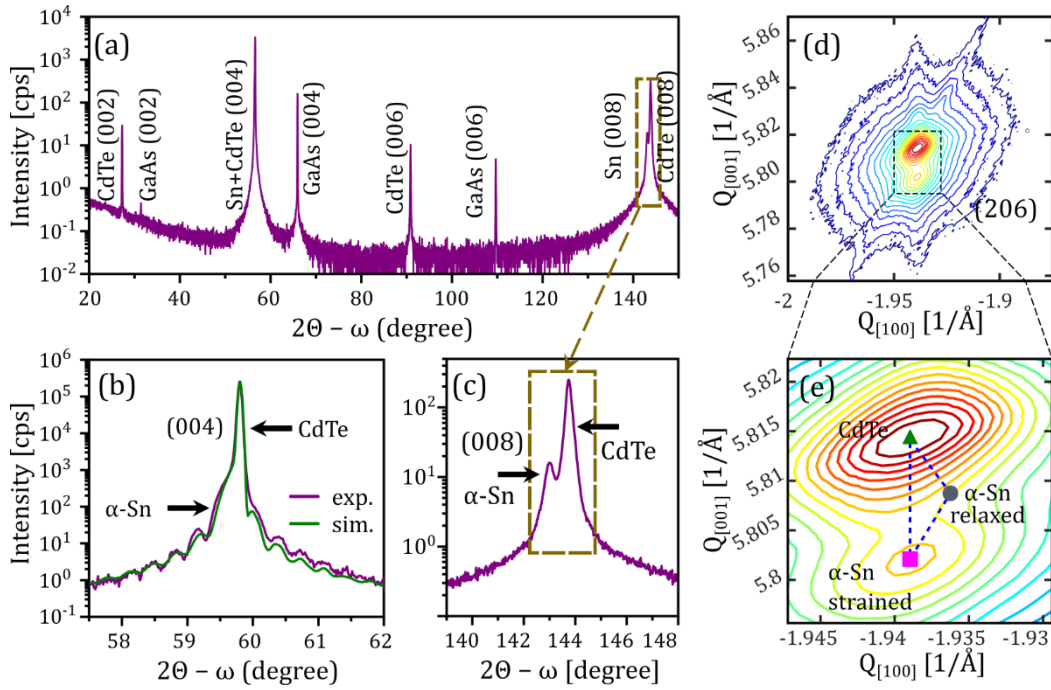$$\varepsilon_\perp = \frac{a_\perp - a_0}{a_0} \tag{4.5}$$

Figure 4.18: Structural investigation of α-Sn epilayers by XRD. (a) Wide range 2θ-ω scan of a 150 nm Sn/CdTe/GaAs (001) film. **(b)** (004) reflection HR-XRD pattern of 30 nm Sn film with thickness fringes, experimental and simulated curves are marked with purple and green lines, respectively. **(c)** (008) XRD patter for the same film as (a) showing resolved grey-Sn and CdTe peaks. **(d, e)** (206) asymmetric RSM for (a) film, in (e) dark blue dashed relaxation triangle, calculated with Poisson's ratio ν=0.298, is shown, positions of CdTe and fully relaxed and fully strained α-Sn are represented with green triangle, grey circle and pink square, respectively. Measurements performed by V.V. Volobuev. Data presentation by V. V. Volobuev and B. Turowski. Samples V13 (a, c, d, e), V3 (b).

Lattice constants and strains calculated using equations described above are shown in **Table 4.9** below.

Table 4.9: Grey tin 150 nm film parameters from XRD measurements shown in **Figure 4.18 (d, e)**. Sample V13

Material	Reflection	Q_x [1/Å]	Q_z [1/Å]	$a_\parallel$ [Å]	$a_\perp$ [Å]	a_0 [Å]	$\varepsilon_\parallel$ [%]	$\varepsilon_\perp$ [%]
CdTe	(206)	1.938925	5.8144242	6.481	6.484	6.482	-0.02	0.02
Sn	(206)	1.939120	5.8022105	6.481	6.497	6.490	-0.14	0.12

Obtained a_0 = 6.490 Å and is in close agreement with the unstrained lattice constant of α-Sn previously reported in the literature **[90]**, namely a_0 = 6.4897 Å. Calculated strains show that α-Sn layer grown on CdTe is compressively strained in-plane by -0.14% The in-plane strains induce tetragonal distortions, which are prerequisite for the DSM phase **[87]** (see **Figure 2.9 (c)**).

4.5   Epilayers growth summary

$Pb_{1-x}Sn_xSe$ (111) epilayers grown on cleaved BaF_2 in two different MBE systems equipped with elemental and compound sources were compared. RHEED patters recorded during growth show high quality of the layers, regardless of the MBE system. The AFM shows that the obtained epilayers are qualitatively and quantitatively similar, as the same spiral step structure is present and the spiral size is comparable. The XRD investigation reveals the presence of only the (111) phase in both cases. The results obtained allow for a conclusion, that both elemental and stoichiometric compound sources can be used for epitaxial growth of high structural quality (111) $Pb_{1-x}Sn_xSe$ epilayers. This result is important because it paves the way to nanostructures grown with elemental sources that have higher purity as compared to those grown from binary sources. This, in turn, should allow for better control of carrier concentration in the IV-IV TCI, since background doping due to the residual dopants could be reduced.

The experience I gained when participating in the growth of the epilayers in the PREVAC 190 system was used for further growths in the Veeco GENxplor GM#2 system. Multiple growths were carried out in the newly launched MBE system to obtain epilayers of very high quality, allowing for ARPES studies. The quality of the thin films was confirmed by RHEED, AFM, XRD and EDS measurements, proving that I can grow $Pb_{1-x}Sn_xSe$ epilayers by MBE on both cleaved and polished (111) BaF_2 substrates. I made an important contribution to the launch of this new GENxplor MBE system. The culmination of the acquired skills was the growth of ultra-thin $Pb_{1-x}Sn_xSe$ epilayers that are currently studied in the MagTop Group of Characterisation and Processing (ON6.3).

I also participated in growth of grey tin thin films on hybrid CdTe/GaAs (001) substrates. Structural characterisation of the samples proves their high quality and the presence of the intended in-plane compressive strain. Such strain is the prerequisite of the Dirac semimetal phase, which was studied later by ARPES, as discussed in **Section 5.4**.

In addition, I have written a Python script (see **Section 3.2.1**) that makes the understanding of the RHEED of the grown films easier by facilitating the analysis of the recorded patterns both in real time and after growth.

Chapter 5

ARPES studies of Pb$_{1-x}$Sn$_x$Se and α-Sn epilayers

In this chapter, Angle-Resolved Photoelectron Spectroscopy (ARPES) and Core Levels (CL) studies of Pb$_{1-x}$Sn$_x$Se and α-Sn, as well as Spin Resolved ARPES (SR-ARPES) studies of Pb$_{1-x}$Sn$_x$Se samples will be presented. First, the deposition of transition metal on the surface of (001) and (111) Pb$_{1-x}$Sn$_x$Se is discussed. Next, a spin polarized study of (111) Pb$_{1-x}$Sn$_x$Se is presented. Finally, the band structure of compressively strained α-Sn grown on hybrid insulating CdTe/GaAs (001) substrates is presented. The samples discussed in a given section are listed in a table at the beginning of the section, with names used in the thesis. The lists of all samples relevant to this thesis are presented in **Appendix B**.

ARPRES and CL studies of Pb$_{1-x}$Sn$_x$Se samples were conducted during two <u>URANOS</u> (former UARPES) beamtimes at the SOLARIS Synchrotron Centre:

1) "2D Ferromagnetism Induced by Topological Surface States" by V.V. Volobuiev and T. Hyart;
2) "Strain induced phase transition from topological insulator to Dirac semimetal in grey tin epilayers grown on insulating substrates" by V.V. Volobuiev and T. Wojtowicz. During this beamtime, additional Pb$_{1-x}$Sn$_x$Se samples were measured in spare time.

ARPES and SR-ARPRES studies of Pb$_{1-x}$Sn$_x$Se samples were conducted during two <u>PHELIX</u> beamtimes at the SOLARIS Synchrotron Centre:

3) "Spin resolved ARPES through topological transition in PbSnSe (111) epilayers" by V.V. Volobuiev;
4) "Spin texture in topological crystalline insulators with Dirac-Rashba energy spectrum" by V.V. Volobuiev, T. Wojtowicz and G. Springholz.

ARPRES and CL studies of α-Sn were the main research topic of **2)** beamtime.

I participated in all ARPES and CL measurements and data analysis of Pb$_{1-x}$Sn$_x$Se and α-Sn epilayers during **1)** and **2)** beamtimes, as well as in initial ARPES and SR-ARPES measurements during **3)** beamtime, which were conducted to familiarise with the PHELIX system. Samples G7, G15, G16, G20, and G28 were studied during these sessions. I was involved in the data analysis of all samples studied at the PHELIX end-station, including samples studied during **4)** beamtime. I prepared all the data for the presentation.

V. V. Volobuiev, R. Rudniewski, and A. Kazakov were involved in ARPES and SR-ARPES measurements. The ARPES and PHELIX end-stations staff helped with data acquisition. Details about these two end-stations are provided in **Appendix A: URANOS beamline**.

5.1   Deposition of TM on (001) Pb$_{1-x}$Sn$_x$Se

Surface states (SS) were predicted to exist on the (001) surface of Topological Crystalline Insulator (TCI) **[35]**. Their presence was studied by ARPES in the SnTe **[50]**, Pb$_{1-x}$Sn$_x$Te **[53]**, and Pb$_{1-x}$Sn$_x$Se **[10]** systems. The bulk gap of Pb$_{1-x}$Sn$_x$Se is located at four equivalent L (111) points on the hexagonal faces of the 3D Brillouin zone (3DBZ) **[82]**. The topological surface states on the (001) surface come from two L points, at the top and bottom of the 3DBZ (see **Figure 2.4 (b)**), that project to $\overline{X}$ point of 2D Brillouin zone (2DBZ). The band structure consists of double Dirac cones (DC), which are located next to each other and their Dirac points (DP), formed by Topological Surface States (TSS), are separated in the k-space by Δk **[161]**. Another possible description of the band structure assumes the separation of double DCs in energy with the DPs separated by ΔE **[162, 163]** and located at $\overline{X}$ point at $k_\parallel$ = 0. Here, the first approach is used. **Figure 5.1** shows the schematic band structure near the $\overline{X}$ point of the (001) surface of Pb$_{1-x}$Sn$_x$Se. In image **(a)**, double DCs at $\overline{X}$ point are shown. The DPs are located along $\overline{\Gamma} - \overline{X} - \overline{\Gamma}$ direction and are protected by the mirror symmetry of the {110} plane. In image **(b)**, (001) 2DBZ is shown, with Fermi surface of four double DCs in high-symmetry $\overline{X}_1$ and $\overline{X}_2$ surface points.
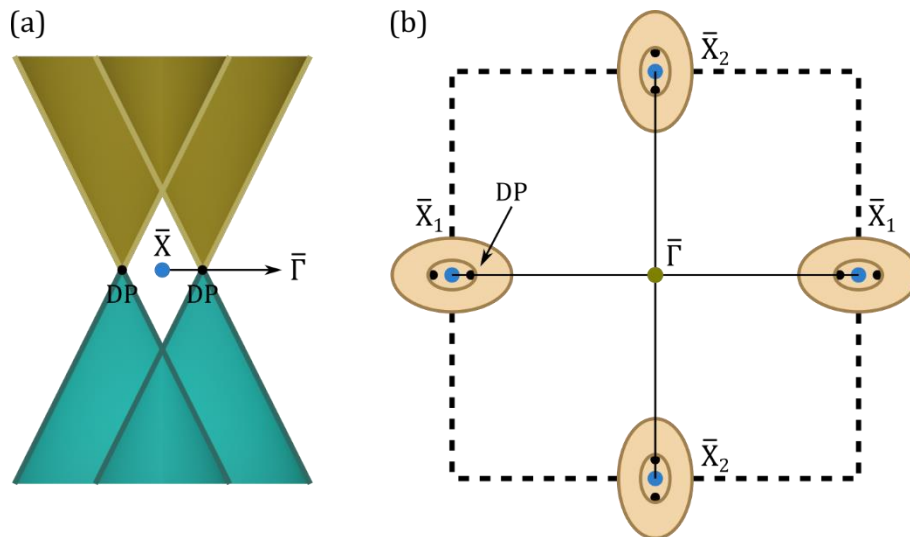
Figure 5.1: Schematic picture of the TSS at (001) surface of Pb$_{1-x}$Sn$_x$Se. (a) Two Dirac cones located at $\overline{X}$ point of 2DBZ separated in k-space in $\overline{\Gamma} - \overline{X} - \overline{\Gamma}$ direction. **(b)** Fermi surface of (001) 2DBZ with {110} mirror symmetry lines (solid black), and $\overline{\Gamma}$ and $\overline{X}$ surface points depicted; Dirac points (DP) are not located at the Fermi surface and are shown for reference.

Since both TCI and Topological Insulators (TI) are predicted to host TSS on some of their surfaces, it is important to verify the existence of similar effects in both classes of topological

materials. The presence of the helical spin texture of the TSS in TIs **[164, 165]** makes them interesting in terms of applications in spintronics, such as spin-to-charge conversion **[166]** and magnetisation switching via spin–orbit torque **[167]**. More detailed discussion about this topic is provided in Ref. **[168]**. These effects are observed in systems with magnetically doped TIs **[169, 170]** and in TIs interfaced with magnetic materials **[171]**. Given this fact, the band structure at the interface of TI and magnetic metal (MM) is of particular interest not only from the point of view of fundamental research, but also for possible applications in spin-orbitronic devices **[172]**. The (001) surface of $Pb_{1-x}Sn_xSe$ was shown to host spin-polarized TSS **[8]**, and thus a study of MM surface doping would broaden general knowledge in this regard. To date, research on trivial/topological heterostructures of TCI has focused on evolution of the band structure near $\overline{X}$ surface point of (001) $Pb_{1-x}Sn_xSe$ **[163]** or $Pb_{1-x}Sn_xSe$ quantum well systems grown in the (111) direction **[173, 174]**. Here, transition metal (TM) was deposited in a submonolayer (ML) amount on the surface of (001) $Pb_{0.74}Sn_{0.26}Se$ TCI in order to study the evolution of the band structure at the TCI/TM interface, which was previously explored in (111)-oriented TIs **[43, 44, 118]**. Another goal was to verify the theoretical predictions of topological band gap opening at (001) surface due to the surface doping of TCI with magnetic impurities **[148]**. Such doping was theorised to induce 2D ferromagnetism resulting from the lowering of electronic energy by spontaneous breaking of a crystalline symmetry **[148, 175]**. Breaking this symmetry results in the opening of the TSS gap **[24, 176]**.

As the (001) plane is the natural cleavage plane of the bulk $Pb_{1-x}Sn_xSe$ crystals, the presence of TSS was extensively studied on this surface **[8, 10, 161, 177]**, but very little research was done on thin films. Given the fact that modern electronic devices are heavily dependent on thin layer heterostructures **[3, 167]**, the study of (001) $Pb_{1-x}Sn_xSe$ thin films provides valuable insight that could lead to possible device applications of this material. For this reason, $Pb_{1-x}Sn_xSe$ grown by Molecular Beam Epitaxy (MBE) was studied here.

5.1.1 Manganese deposition

The depositions of manganese (Mn) TM were performed on the (001) surface of $Pb_{0.74}Sn_{0.26}Se$, according to the deposition schema described in **Section 4.2.4**. After each deposition, ARPES spectra near $\overline{X}$ point were recorded. Details of the sample studied are given in **Table 5.1**. **Figure 5.2** shows the evolution of ARPES spectra of the (001) $Pb_{0.74}Sn_{0.26}Se$ epilayer (sample R1) near the $\overline{X}$ point, caused by the deposition of various amounts of Mn.

Table 5.1: (001) Pb1-xSnxSe sample studied under Mn deposition.

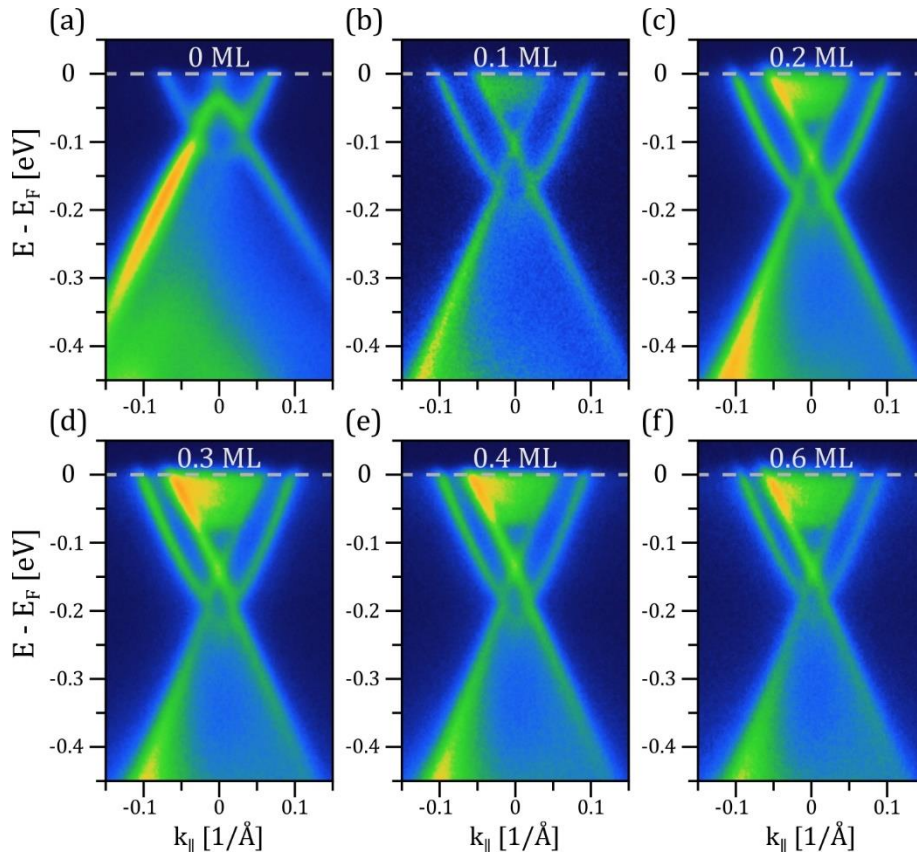| name	code	substrate	Sn content [%]	Thickness [nm]	Studied by	Aim of presentation
R1	MBE_3431B	KCl	26	50	ARPES, Mn deposition	Decrease in $k_\parallel$ distance of double DC

Figure 5.2: Evolution of the ARPES spectra of the (001) Pb$_{0.74}$Sn$_{0.26}$Se epilayer near the $\overline{X}$ point with Mn deposition. The decrease in the k$_\parallel$ distance of double DC caused by Mn deposition is clearly visible. Photon energy E$_{ph}$ = 17.2 eV, measurement temperature 8 K. Sample R1.

The initial deposition of 0.1 ML Mn (**Figure 5.2 (b)**) causes a significant change in the Fermi energy, visible by the downward shift of the energetic position of the Dirac points (E$_D$). Further deposition of Mn, as given in **Table 5.2** and shown in **Figure 5.2 (c)-(f)**, results in a smaller upward shift of Fermi energy (E$_F$). The change of the Fermi level occurs due to the electron doping of the surface and was also observed in TI systems **[43, 44]**. Another noticeable effect is a change in the distance in the k-space between two DPs. Initial deposition of 0.1 ML Mn effects in the most pronounced change in the separation of DCs. A further increase of the Mn thickness leads to a further decrease of the k-space DCs distance, but to a lesser degree. The separation of DPs in the k-space (Δk) and the position in energy in relation to the Fermi energy, E$_F$ – E$_D$, are presented in **Figure 5.3** and **Table 5.2**. In 2018, Polley et al. **[163]** reported a similar effect in (001) Pb$_{0.7}$Sn$_{0.3}$Se covered with an increasing amount of PbSe. Their conclusion was that the wave functions of the double DCs are dephasing, which causes a decrease in their separation in the energy. Another possible explanation is a change in the surface composition of the sample due to surface doping. In 2013, Tanaka et al. **[178]** reported a decrease in the k-space separation of double DCs near the $\overline{X}$ point of (001) Pb$_{1-x}$Sn$_x$Te with the decrease in x$_{Sn}$ content, which is equivalent to shifting the sample towards less topological composition. We interpret our data that by the deposition of Mn on the surface of the sample, the surface composition changes toward a trivial phase. This

explanation is consistent with our recent publication **[15]** and is discussed in more detail in **Section 5.3.5**.
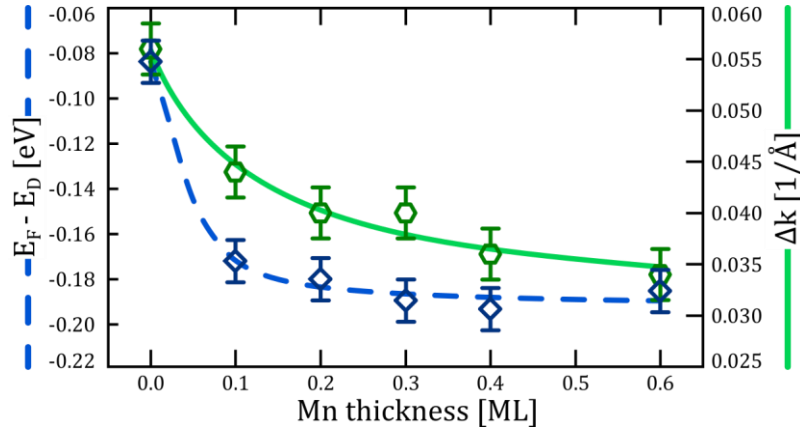
Figure 5.3: Influence of submonolayer TM deposition on the band structure of (001) Pb$_{0.74}$Sn$_{0.26}$Se, with applied eye guidelines. Data details are given in **Table 5.2**. Sample R1.

Table 5.2: Influence of submonolayer Mn deposition on the (001) surface of Pb$_{0.74}$Sn$_{0.26}$Se. The values were obtained from band fits of the ARPES spectra. The estimated Mn thickness deposition error is 0.01 ML.

Mn deposition [ML]	0	0.1	0.2	0.3	0.4	0.6
$E_F - E_D$ [eV]	-0.084	-0.173	-0.181	-0.191	-0.194	-0.186
Δk [1/Å]	0.056	0.044	0.040	0.040	0.036	0.034
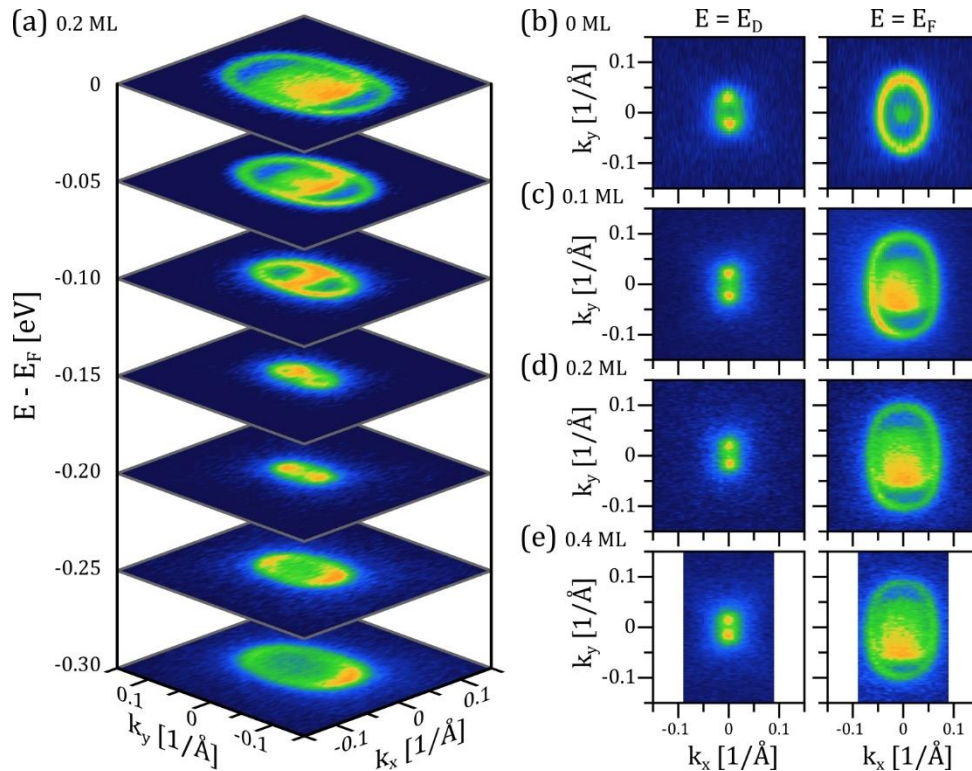
Figure 5.4: Constant energy contours of (001) Pb$_{0.74}$Sn$_{0.26}$Se (sample R1) epilayer near $\overline{X}$ point. (a) Stacked CEC after 0.2 ML Mn deposition. **(b, c, d, e)** Evolution of Dirac points (left) and Fermi surface (right) with 0, 0.1, 0.2, 0.4 ML Fe, respectively, deposited on the surface of the sample. Photon energy E_{ph} = 17.2 eV, measurement temperature 8 K. Sample R1.

Figure 5.4 shows the constant energy contours (CEC) extracted from the 3D ARPES maps recorded after consecutive 0 - 0.4 ML Mn depositions. A quantitative change in the ARPES spectra is observed in the E_D shift and the decrease of the k-space separation Δk of the DPs (**Figure 5.4 (b)-(e)**, left), as discussed above, but the band structure remains qualitatively the same **Figure 5.4 (c)-(e)**). The constant energy contours presented in image **(a)** show a change in the band structure that evolves from a pair of adjacent, overlapping rings to two DPs separated in k-space in $\bar{\Gamma} - \bar{X} - \bar{\Gamma}$ direction. Such change of the band structure that occurs at the Fermi surface by lowering the E_F **[162, 179, 180]** is called a Lifshitz transition **[181]**. Image (**(b)**, right) of the pristine sample shows the Lifshitz transition point **[182]** close to E_F. Initial deposition of the Mn (image (**(c)**, right)) moves the Fermi energy upward, above the transition point, and pair of adjacent rings with centres at the same distance from the $\bar{X}$ point forms the Fermi surface **[162]**.

5.1.2   Summary

ARPES measurements of high quality n-type (001) $Pb_{0.74}Sn_{0.26}Se$, evidenced by sharp features of the ARPES spectra, were carried out at the URANOS beamline at SOLARIS Synchrotron, Kraków, Poland. During the experiments, band structure near $\bar{X}$ surface point was studied with exciting photon energy of 17.2 eV at a temperature of 8 K. The deposition of a submonolayer amount of Mn leads to a change in the separation of double DCs, which can be attributed to the dephasing of their wave functions **[163]** or a change in the surface composition of the sample toward more trivial. Based on additional experiments presented in **Section 5.3.4** we believe that the second interpretation is correct. The Lifshitz transition point **[182]** close to E_F was observed for the pristine sample.

5.2   Deposition of TM on (111) Pb$_{1-x}$Sn$_x$Se

The (111) surface of the TCI is another one on which TSS exist **[24]**. Their presence was predicted in $Pb_{1-x}Sn_xTe$ **[54, 180]** and studied in the SnTe **[139]** and $Pb_{1-x}Sn_xSe$ **[79]** systems. The DPs correspond to the projection of the bulk L (111) points onto a different, time-reversal invariant, momentum at $\bar{\Gamma}$ and each of $\bar{M}$ high-symmetry surface points of (111) 2DBZ (see **Figure 2.4 (c)**). The band structure consists of a DC with TSS crossing at the DP, as presented in **Figure 5.5 (a)**. Image **(b)** shows a schematic of the Fermi surface of the (111) surface, with the positions of all DCs in high-symmetry surface points, and the {110} mirror plane, responsible for mirror-symmetry protection of the surface states.

The effect of surface doping with transition metals (TM) was studied in TI **[43, 44, 118]**, but this field is still unexplored in TCI, as mentioned in **Section 5.1**. Theoretical predictions report that magnetic impurities on the TCI surface effect in opening of the band gap **[148, 149]** on (111) surface. Similarly to the (001) surface study, the (111) surface of $Pb_{1-x}Sn_xSe$ was examined here to verify these predictions. Another goal was to study the evolution of the band

structure of (111)-oriented TCI near $\bar{\Gamma}$ surface point, as Rashba effect **[39]** was reported on the (111) surface of TI **[43, 44, 118]**. Additionally, the band structure near $\bar{M}$ surface point was initially examined, but was not further investigated because of technical difficulties.
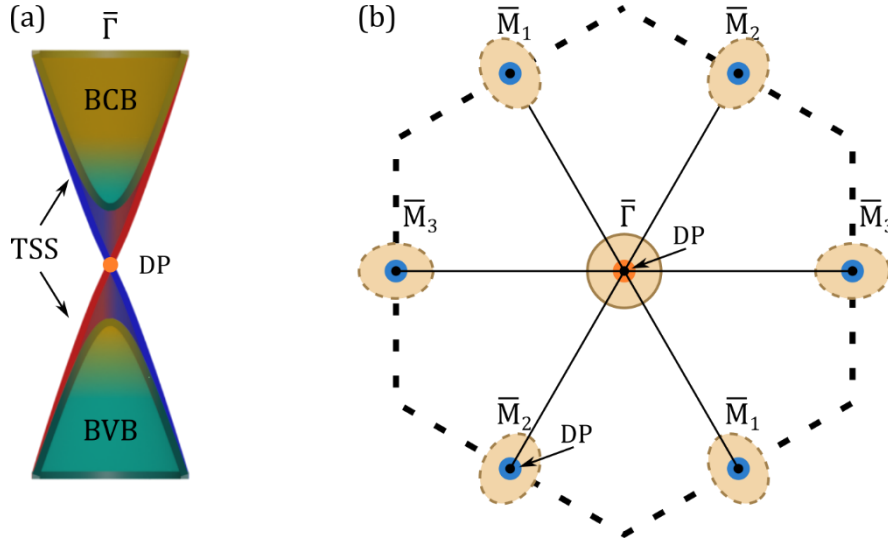

Figure 5.5: Schematic picture of TSS at (111) surface of Pb$_{1-x}$Sn$_x$Se. (a) Dirac cone consisting of TSS (red and blue lines) is located at $\bar{\Gamma}$ and each $\bar{M}$ point of 2DBZ. **(b)** Fermi surface of (111) 2DBZ with {110} mirror symmetry lines (solid black), Dirac points (DP), and $\bar{\Gamma}$ and $\bar{M}$ surface points depicted.

The (111) surface is most often obtained by the MBE growth **[9, 99, 147]**, but it is challenging to cleave rock-salt bulk crystals along the {111} plane **[139, 183]**. Here, the MBE grown (111) Pb$_{1-x}$Sn$_x$Se was studied under the influence of the deposition of Mn and Fe on the surface. The details of the samples studied are given in **Table 5.3**. First, the temperature-dependent topological transition and band structure of (111) Pb$_{1-x}$Sn$_x$Se near $\bar{\Gamma}$ point is presented. Then, features of the band structure near $\bar{\Gamma}$ surface point are described to facilitate understanding of the presented ARPES spectra. Next, the deposition of Mn and Fe at room temperature (RT) on the surface of the Pb$_{1-x}$Sn$_x$Se is discussed. Finally, the core level data of samples with deposited Fe are presented. The chapter ends with a summary of all the work done.

Table 5.3: Discussed Pb$_{1-x}$Sn$_x$Se (111) epilayers studied at the URANOS beamline.

name	code	substrate	Sn content [%]	Thickness [μm]	Deposited TM	Sample type
R2	MBE_3440A	BaF$_2$	30	1	Mn	n-type
R3	MBE_3440B	BaF$_2$	30	1	Mn	p-type
R4	MBE_3426A	BaF$_2$	25	1	Fe	n-type
R5	MBE_3426B	BaF$_2$	25	1	Fe	p-type
G3	GM2_070920A	BaF$_2$	26	1	Fe	n-type
G4	GM2_110920A	BaF$_2$	30	1	Mn	n-type
G5	GM2_140920A	BaF$_2$	30	1	Mn+Fe	n-type

5.2.1   Band structure near $\bar{\Gamma}$ point

In order to verify the topological properties of the studied samples, ARPES spectra were recorded at three different temperatures. **Figure 5.6** shows the temperature-dependent topological transition in pristine $Pb_{0.7}Sn_{0.3}Se$. In image **(a)**, the normal insulator (NI) phase is shown, with well-resolved conduction and valence bands, separated by the 68 meV gap.
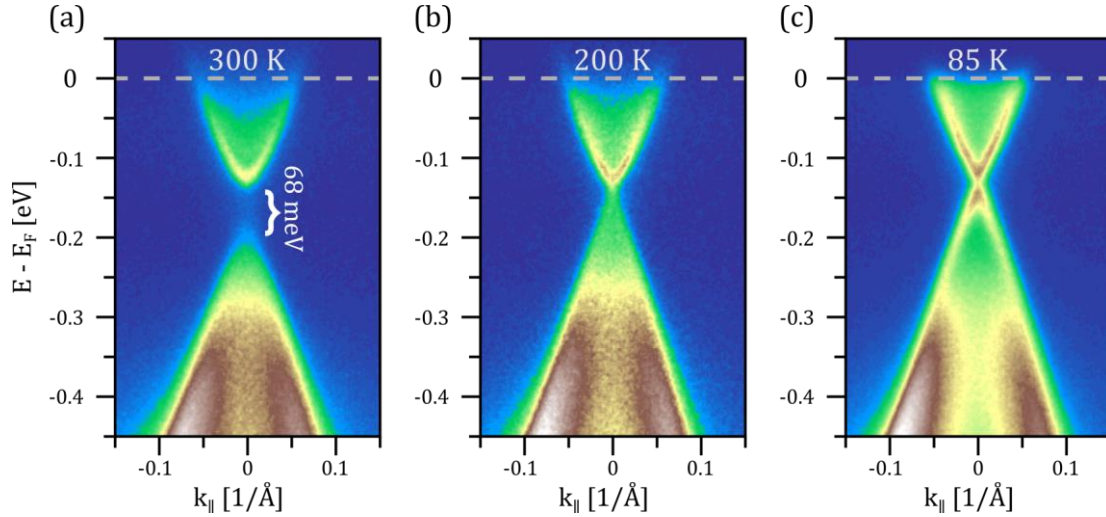
Figure 5.6: Topological transition in pristine (111) Pb$_{0.70}$Sn$_{0.30}$Se recorded near $\bar{\Gamma}$ point. (a) Trivial phase. **(b)** and **(c)** Topological phase. Photon energy E_{ph} = 18 eV. Sample G4.

As the temperature is decreased, the sample undergoes the transition to the TCI phase (images **(b)** and **(c)**) with TSS crossing in the bulk band gap. The result that at 300 K the sample is in the NI phase is quite unexpected, since at this temperature, according to semi-empirical Preier's formula **[68]**, $Pb_{1-x}Sn_xSe$ with x_{Sn} = 0.30 should already be in the TCI phase; see **Figure 2.8** for the band gap dependence. The presence of the band gap (image **(a)**) is most likely connected to a small amount of Mn deposited in GM#2 prior to ARPES measurements (see **Section 4.2.4**). An explanation of this phenomenon is proposed in **Section 5.3.4**.

5.2.2   Dirac-Rashba states near the $\bar{\Gamma}$ point

The conduction band of the (111) $Pb_{1-x}Sn_xSe$ near $\bar{\Gamma}$ point after deposition of Fe on the sample surface undergoes splitting in momentum space (see **Figure 5.7 (d)**). This effect is called Rashba splitting **[39]** and was previously reported in other TCI system, namely in the valence band of bismuth bulk doped $Pb_{1-x}Sn_xTe$ **[83]**. To facilitate discussion of the obtained ARPES spectra, the following procedure is employed, shown in **Figure 5.7 (a)-(c)** and described below. This figure (**Figure 5.7**) shows the band structure of (111) $Pb_{0.74}Sn_{0.26}Se$ epilayer near $\bar{\Gamma}$ point after deposition of 0.4 ML Fe. First, the 2D curvature of the raw spectra is calculated (image **(b)**). Background noise is removed only for the purpose of presentation of the spectra (images **(a)** and **(c)**). Then, TSS are fitted according to **Equation (3.22)**. The Rashba spectrum (RSS – Rashba surface states) is fitted according to **Equation (3.26)**. The described fitting

procedure does not take into account the hybridisation of the TSS and RSS. Hybridisation between surface states manifests itself in decreased energy distance or in the overlap of the Kramer point (KP) and the DP, which are crossing points of RSS and TSS, respectively, as shown in **Figure 5.7 (b)** and **(c)**.
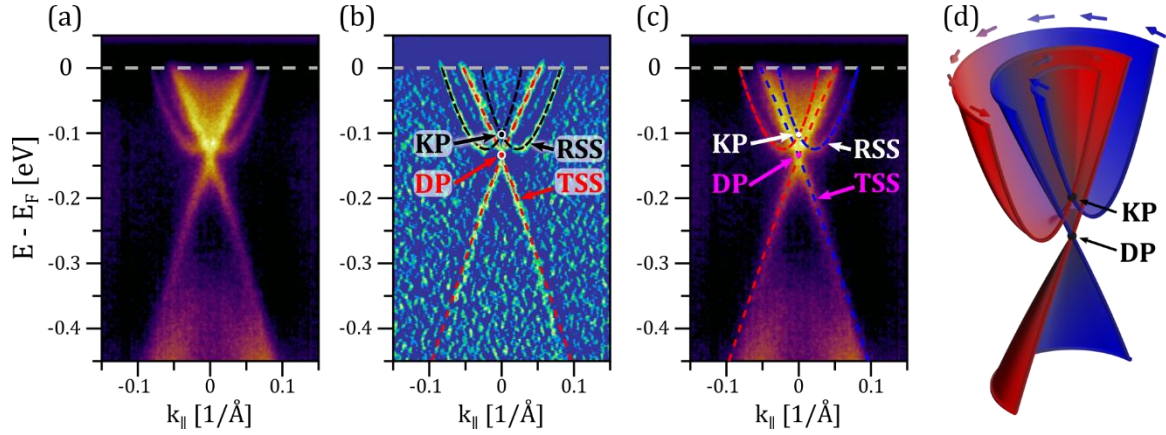

Figure 5.7: ARPES spectra of Pb$_{0.74}$Sn$_{0.26}$Se near $\bar{\Gamma}$ point with 0.4 ML Fe deposited on the surface. The Kramer (KP) and Dirac (DP) points, as well as Rashba (RSS) and topological (TSS) surface states, are labelled. **(a)** ARPES spectra with background noise removed. **(b)** 2D curvature of raw (a) spectrum. **(c)** Spectrum (a) with overlapped TSS and RSS guidelines. **(d)** Schematic image of Rashba splitting with KP and DP labelled. Sample G5.

5.2.3   Manganese deposition

Mn deposition was performed on (111)-oriented Pb$_{1-x}$Sn$_x$Se to verify theoretical predictions **[148]** of the TSS gap opening on both (001), presented in **Section 5.1**, and (111) surfaces to broaden the understanding of the proposed effect.

Figure 5.8 and **Figure 5.9** show the evolution of the electronic structure of n-type and p-type (111) Pb$_{0.70}$Sn$_{0.30}$Se (samples R2 and R3, respectively) after Mn deposition. Both samples demonstrate TCI spectra in pristine condition (images **(a)** and **(a)**). The Fermi energy lies in the conduction band (CB) for n-type samples and in the valence band (VB) for p-type samples. The broad bands from the bulk states, labelled BS, are present inside the TSS cone. The pristine n-type sample (**Figure 5.8 (a)**) shows Rashba splitting in VB. This may be caused by the presence of residual gas adsorbate on the sample surface **[184-186]** or bulk bismuth (Bi) doping used to tune the Fermi level and obtain an n-type sample. Bulk Bi doping was shown to induce Rashba splitting in VB of (111) PbSnTe **[83]**. Another possible explanation is excessive Se on the sample surface **[174]**. Considering the fact that samples R2 and R3 were covered by amorphous Se re-evaporated in the preparation chamber of the URANOS end-station, the latter case is most probable. The deposition of 0.1 ML (image **(b)**) Mn results in an upward shift of E$_F$ in both samples **[43, 44]**, consistent with the results for (001) surface and the results for (111) surface near $\bar{M}$ point after of Fe deposition (see **Figure 5.19** and relevant discussion). Further deposition of Mn leads to the separation of states in momentum

in CB, which is evidence of Rashba splitting. With increasing Mn deposition, the splitting increases and finally saturates.
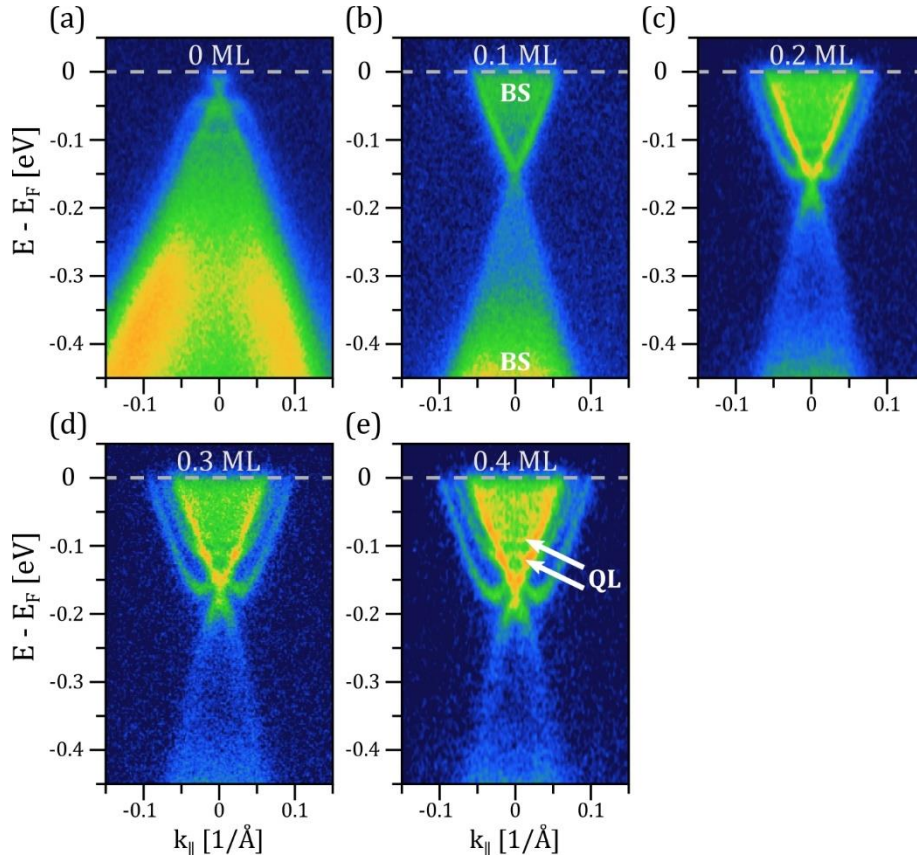
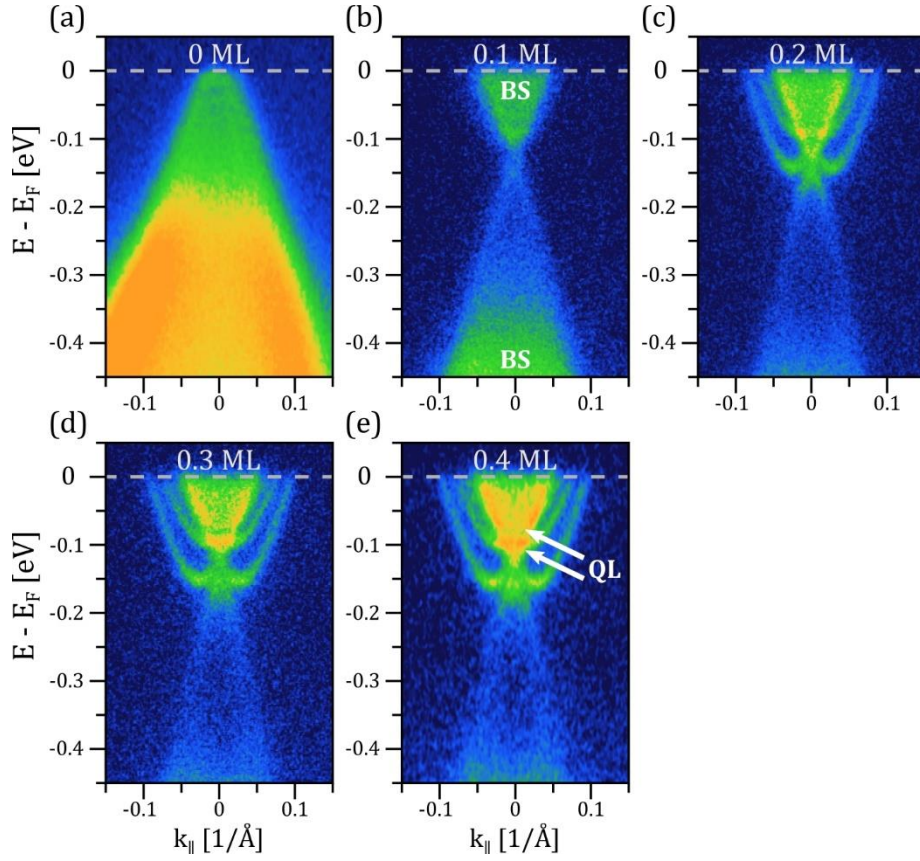**Figure 5.8: ARPES spectra of the n-type (111) $Pb_{0.70}Sn_{0.30}Se$ epilayer near the $\bar{\Gamma}$ point with increasing Mn deposition.** Sample R2. Photon energy E_{ph} = 17.2 eV, measurement temperature 80 K. Sample R2.

Additionally, well-resolved quantum levels (QL) from the 2D electron gas (2DEG), appear after 0.2 ML total Mn deposition (image **(c)**) and become increasingly visible with the amount of TM on the surface of the sample, as presented in images **(d)-(f)**. The 2DEG state undergoes a splitting in momentum **[44, 187]**, giving rise to bands visible between TSS and RSS in images **(d)-(f)**.

The Rashba splitting saturation effect is presented in **Figure 5.10** with a solid eye guideline (circle marker). Similarly, the upward E_F shift also saturates (see the dashed eye guideline, square marker).

Figure 5.9: ARPES spectra of the p-type (111) Pb$_{0.70}$Sn$_{0.30}$Se epilayer near the $\bar{\Gamma}$ point with increasing Mn deposition. Photon energy E_{ph} = 17.2 eV, measurement temperature 80 K. Sample R3.

The Rashba coefficient α_R obtained from band fitting using **Equation (3.26)**, as well as the E_F shift defined as the change of the position of DP in energy in relation to the Fermi energy, $E_F - E_D$, are presented in **Table 5.4**.
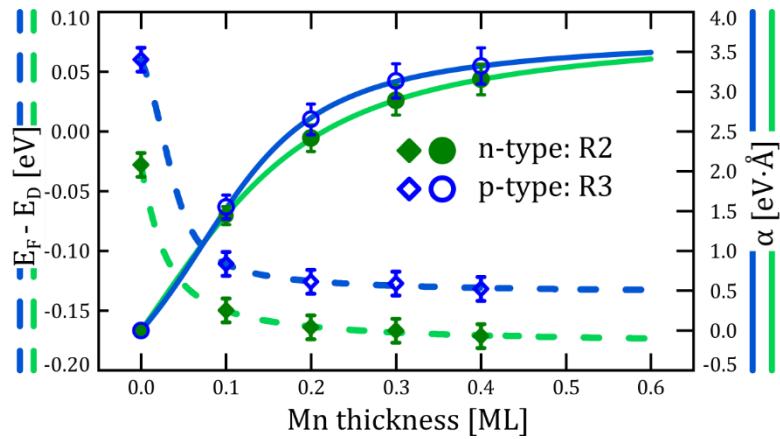
Figure 5.10: Influence of submonolayer Mn deposition on the (111) surface of Pb$_{0.70}$Sn$_{0.30}$Se, with eye guidelines applied. Data details are given in **Table 5.4**.

Table 5.4: Influence of submonolayer Mn deposition on the (111) surface of $Pb_{0.70}Sn_{0.30}Se$. Rashba coefficient α is obtained using **Equation (3.26)**. The estimated Mn thickness deposition error is 0.01 ML.

Mn deposition [ML]	R2		R3	
	$E_F – E_D$ [eV]	α [eV·Å]	$E_F – E_D$ [eV]	α [eV·Å]
0	-0.028	0	0.060	0
0.1	-0.150	1.46	-0.111	1.56
0.2	-0.164	2.52	-0.126	2.75
0.3	-0.167	3.05	-0.128	3.36
0.4	-0.172	3.36	-0.132	3.51

5.2.4   Iron deposition

In order to check the influence of the deposition of other TM on the surface of (111) $Pb_{1-x}Sn_xSe$, Fe deposition was performed. It was done to check, if the obtained effect is Mn-specific or if it may be generalised to the deposition of a TM on the surface of $Pb_{1-x}Sn_xSe$. The first experiment was done during the same beamtime as Mn evaporations (samples R4 and R5 in **Figure 5.11** and **Figure 5.12**, respectively). The samples were covered with amorphous Se re-evaporated in the preparation chamber of the URANOS end-station. The influence of Se on ARPES spectra is visible in **Figure 5.11 (a)** in the form of RSS in VB and was explained in **Section 5.2.3** discussing Mn deposition on (111) surface.

The results obtained for Fe deposition are consistent with those obtained for Mn deposition. The spectra of n-type and p-type samples are qualitatively similar both in the pristine state (images (a) in **Figure 5.8** to **Figure 5.12**) and after the TM deposition. BS are well visible in the TSS cones. For the n-type sample (**Figure 5.11**) RSS in VB, whose origins are proposed in the previous section, disappear after the initial deposition of the TM.
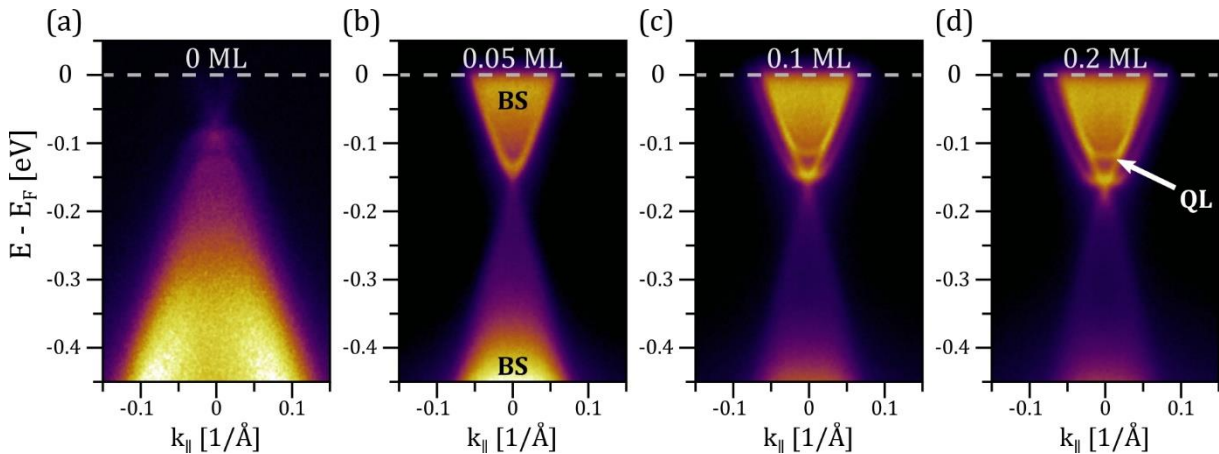
Figure 5.11: ARPES spectra of the n-type (111) $Pb_{0.75}Sn_{0.25}Se$ epilayer recorded near $\bar{\Gamma}$ point, with increasing Fe deposition. Photon energy E_{ph} = 17.2 eV, measurement temperature 80 K. Sample R4.

A further increase in Fe thickness leads to an upward shift of the E_F and emergence of RSS and QL in CB, with momentum splitted 2DEG state between TSS and RSS. It is important to note

that contrary to the n-type sample (**Figure 5.11**), the initial amount of 0.05 ML Fe is enough to cause Rashba splitting in the p-type sample (**Figure 5.12 (b)**).
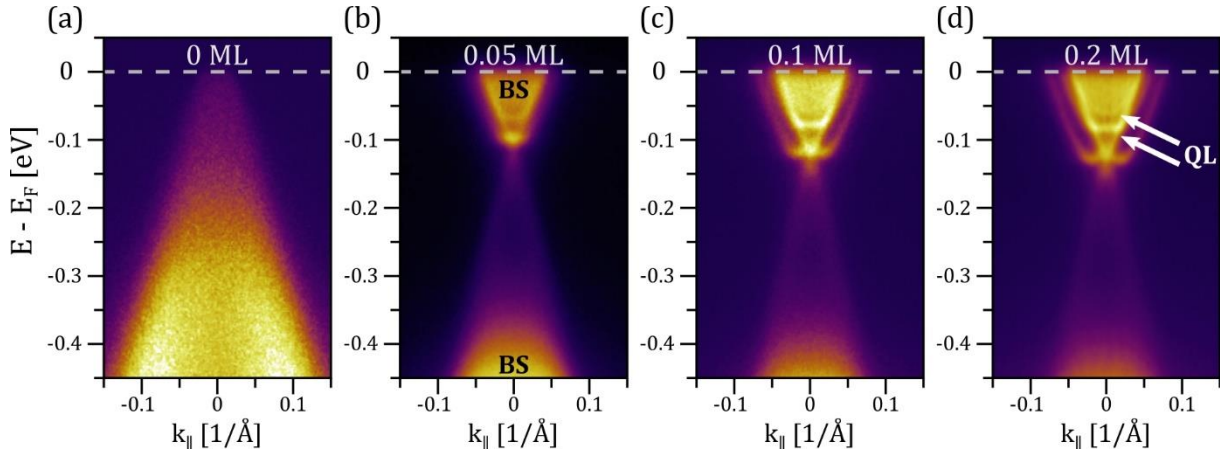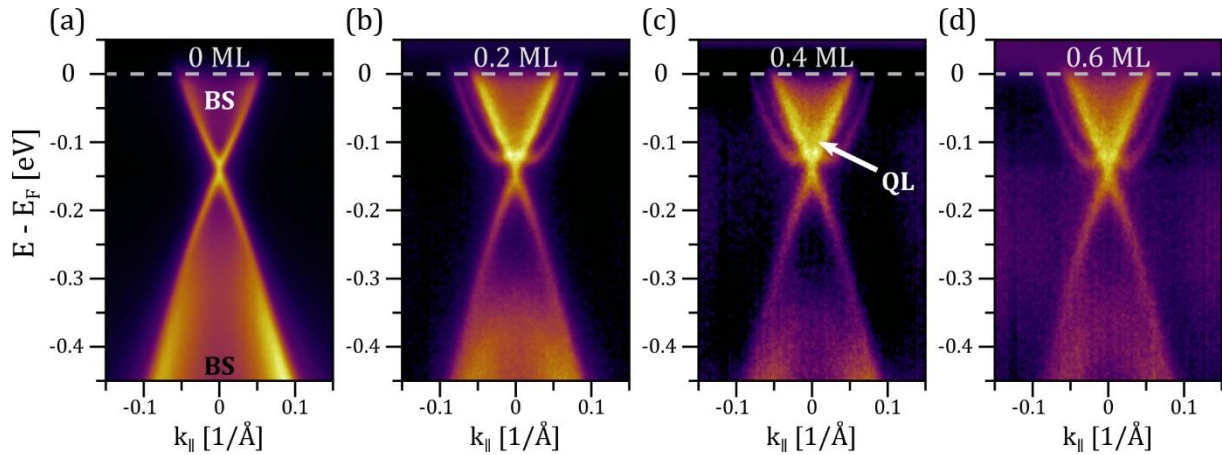

Figure 5.12: ARPES spectra of the p-type (111) Pb$_{0.75}$Sn$_{0.25}$Se epilayer recorded near $\bar{\Gamma}$ point, with increasing Fe deposition. Photon energy E_{ph} = 17.2 eV, measurement temperature 80 K. Sample R5.

The second experiment was carried out during **2)** beamtime at the URANOS beamline at the SOLARIS Synchrotron. The samples were transported to the preparation chamber of the end-station in an ultra-high vacuum (UHV) suitcase, without air exposure. A small amount of TM was deposited in-situ MBE on the surface of these samples; see **Section 4.2.4 Deposition of TM** for the details. The samples presented were doped with Bi in the 0.03-0.09% range to tune E_F and shift it upwards to CB. The depositions were carried out in steps of greater thickness to study the influence of greater amounts of TM deposited on the surface of Pb$_{1-x}$Sn$_x$Se. They also allowed a comparison of the surface quality of the Pb$_{1-x}$Sn$_x$Se with and without an amorphous Se cap. Samples G5 and G3 do not show a significant change of E_F after the initial deposition of Fe (**Figure 5.13 (b)** and **Figure 5.14 (b)**, respectively). This is likely connected to high amount of Bi used for n-type doping, as E_F is already so high that carriers provided by the TM do not affect it and further doping by TM surface deposition **[43]** is limited. A further increase of the amount of deposited Fe leads to similar effects of the Rashba splitting and the E_F change saturation, as well as QL formation and momentum splitted 2DEG. Deposition of 0.3 ML and more of Fe causes a significant increase in background noise signal. This can be caused by deterioration of the surface quality of the examined epilayer. Other possible explanation of this effect is discussed in more detail in **Sections 4.2.4** and **5.3.4**, as it is more relevant in that case.

Figure 5.13: ARPES spectra of the n-type (111) Pb$_{0.70}$Sn$_{0.30}$Se epilayer recorded near $\bar{\Gamma}$ point, with increasing Fe deposition. Spectra (c) and (d) are presented with the background signal subtracted. Photon energy E_{ph} = 18 eV, measurement temperature 80 K. Sample G5.
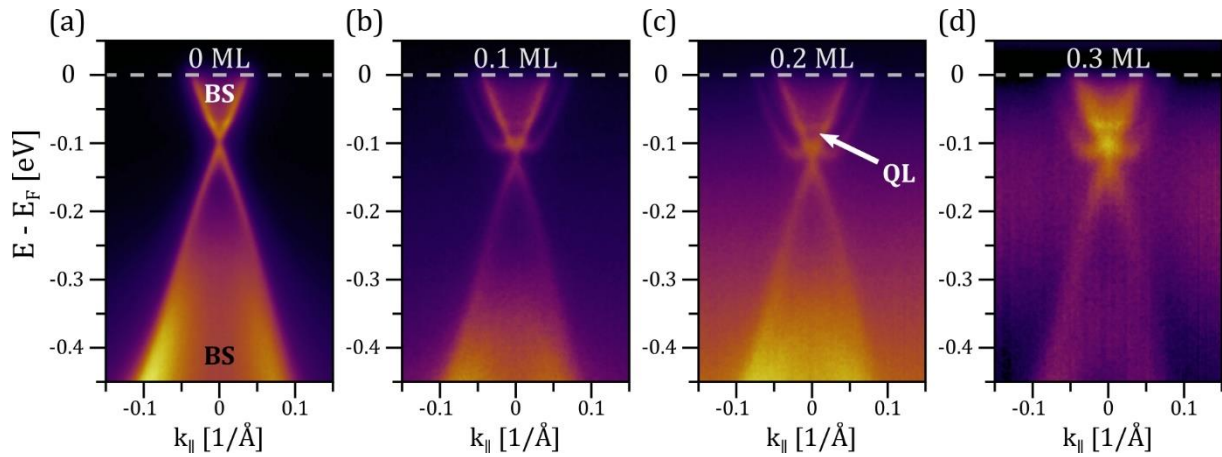

Figure 5.14: ARPES spectra of the n-type (111) Pb$_{0.74}$Sn$_{0.26}$Se epilayer recorded near $\bar{\Gamma}$ point, with increasing Fe deposition. Spectrum (d) is presented with the background signal subtracted. Photon energy E_{ph} = 18 eV, measurement temperature 80 K. Sample G3.

Figure 5.15 shows the Rashba coefficient (α, solid lines, circles) and the Fermi energy shift (E_F-E_D, dashed lines, squares) for samples with Fe deposited on the surface. Although sample G3 (**magenta**) had E_F in CB prior to Fe deposition at the URANOS end-station (was n-type; **Figure 5.14 (a)**), it follows trends similar to the p-type R5 sample (**dark purple**). Its zero Fe thickness points (**magenta** square and circle) are shifted slightly left with respect to the **purple** guidelines (dashed and solid, respectively). This suggests that there was a small amount of Fe (less than 0.05 ML, estimated from the shift) on the surface of the sample. This leads to the conclusion, that sample G3 was initially p–type but Fe deposition in the GM#2 system (see **Section 4.2.4**) shifted E_F upwards to CB. In n-type samples, namely R4 and G5, the change of α with the Fe thickness is similar (**light** and **dark** yellow, respectively), as it increases and saturates. The lack of an initial upward shift of the Fermi energy (equivalent to a downward shift of E_F-E_D) in the case of sample G5 can be caused by the high amount of Bi used for n-type doping since further deposition of TM does not cause further E_F change.
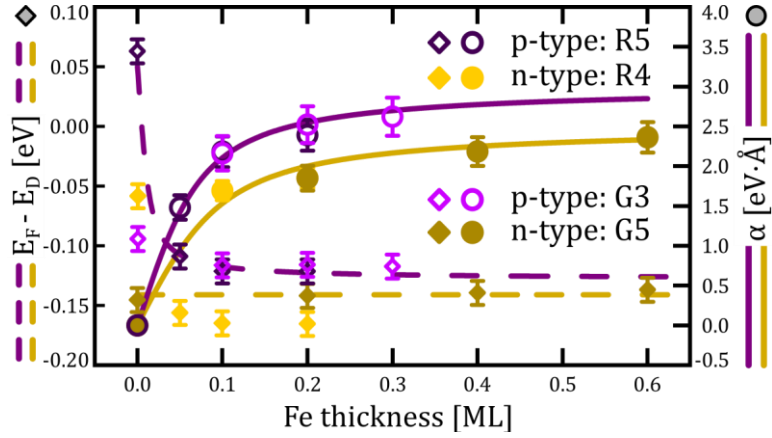
Figure 5.15: Influence of submonolayer Fe deposition on (111) surface of Pb$_{1-x}$Sn$_x$Se, with eye guidelines applied. Data details are given in **Table 5.5** and **Table 5.6.**

Table 5.5: Influence of submonolayer Fe deposition on the (111) surface of Pb$_{0.75}$Sn$_{0.25}$Se with Se cap re-evaporated. Rashba coefficient α is obtained using **Equation (3.26)**. The estimated Fe thickness deposition error is 0.01 ML.

	R4		R5	
Fe deposition [ML]	E$_F$ – E$_D$ [eV]	α [eV·Å]	E$_F$ – E$_D$ [eV]	α [eV·Å]
0	-0.058	-	0.063	-
0.05	-0.157	-	-0.109	1.51
0.1	-0.165	1.74	-0.122	2.28
0.2	-0.166	1.90	-0.122	2.47

Table 5.6: Influence of submonolayer Fe deposition on the (111) surface of Pb$_{1-x}$Sn$_x$Se. Rashba coefficient α is obtained using **Equation (2.13)**. The estimated Fe thickness deposition error is 0.01 ML.

	G3 – 26% Sn		G5 – 30% Sn	
Fe deposition [ML]	E$_F$ – E$_D$ [eV]	α [eV·Å]	E$_F$ – E$_D$ [eV]	α [eV·Å]
0	-0.097	1.16	-0.146	-
0.1	-0.117	2.24	-	-
0.2	-0.116	2.65	-0.142	1.95
0.3	-0.118	2.75	-	-
0.4	-	-	-0.140	2.33
0.6	-	-	-0.137	2.43

Figure 5.16 (a) shows the CECs extracted from the 3D ARPES map recorded after 0.2 ML Fe deposition. The surface states are arranged in concentric circles, which is consistent with the aforementioned claim of RSS emergence. There is no change in CECs bands shape. **Figure 5.16 (b)-(d)** and **Figure 5.17** show the evolution of Fermi surfaces with Fe deposition.
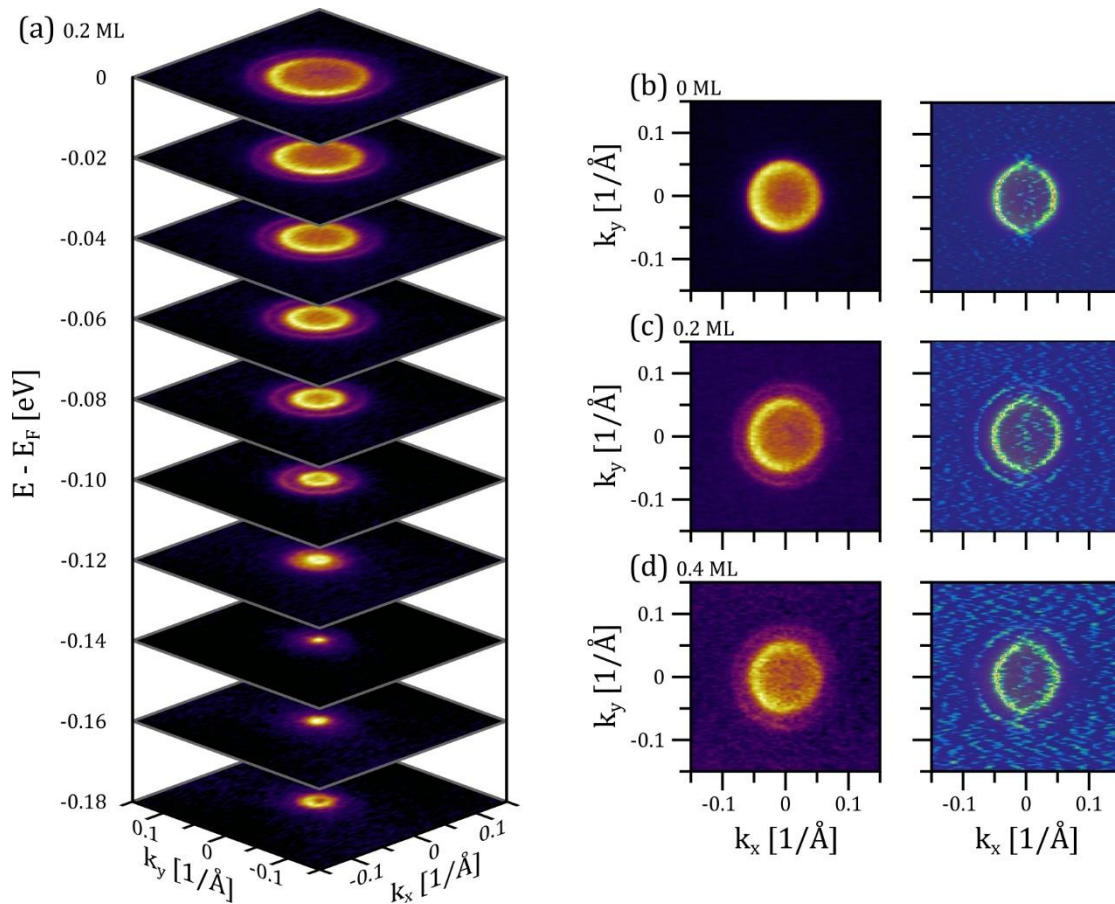
Figure 5.16: Constant energy contours maps of (111) Pb$_{0.70}$Sn$_{0.30}$Se (sample G5). **(a)** Stacked CECs after deposition of 0.2 ML Fe. **(b, c, d)** Fermi surface maps with 0, 0.2, 0.4 ML Fe, respectively, deposited on the surface of the sample. (c) and (d) images on the right show 2D curvature of the respective CEC. Photon energy E$_{ph}$ = 18 eV, measurement temperature 80 K. Sample G5.
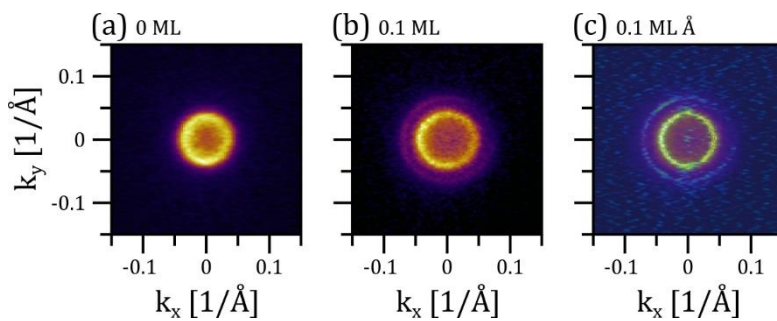

Figure 5.17: Fermi surface maps of (111) Pb$_{0.74}$Sn$_{0.26}$Se with 0 and 0.1 ML Fe, **(a)** and **(b)**, respectively, deposited on the surface. **(c)** 2D curvature of (b). Photon energy E$_{ph}$ = 18 eV, measurement temperature 80 K. Sample G3.

To establish the nature of the states visible in the recorded spectra, the exciting photon energy (E$_{ph}$) dependent measurements were carried out in the range of 17 to 26 eV on the sample with 0.2 ML deposited on the surface (**Figure 5.18**). Varying E$_{ph}$ is equivalent to varying the k$_\perp$ momentum component of the electrons, perpendicular to the sample surface (see **Section 3.6 Angle-resolved photoelectron spectroscopy** for an explanation). If states do

not disperse with E_{ph} change, they are two-dimensional; if they do disperse, they are three-dimensional. The bulk conduction band (BCB) and the bulk valence band (BVB) are most pronounced at 18 eV (see image **(b)**). Significant dispersion is observed for bulk bands and no change in the position of TSS and RSS is observed, proving their surface nature. The observed dependence of the photoemission intensity of surface states comes from transition matrix element effects **[188]** that cause oscillations of their intensity. The apparent lack of the RSS in the spectrum taken with E_{ph} = 26 eV is due to removal of the background noise combined with matrix element effects. Purple arrows (images **(d)** and **(h)**) point to a higher intensity part of RSS present in both highlighted images.
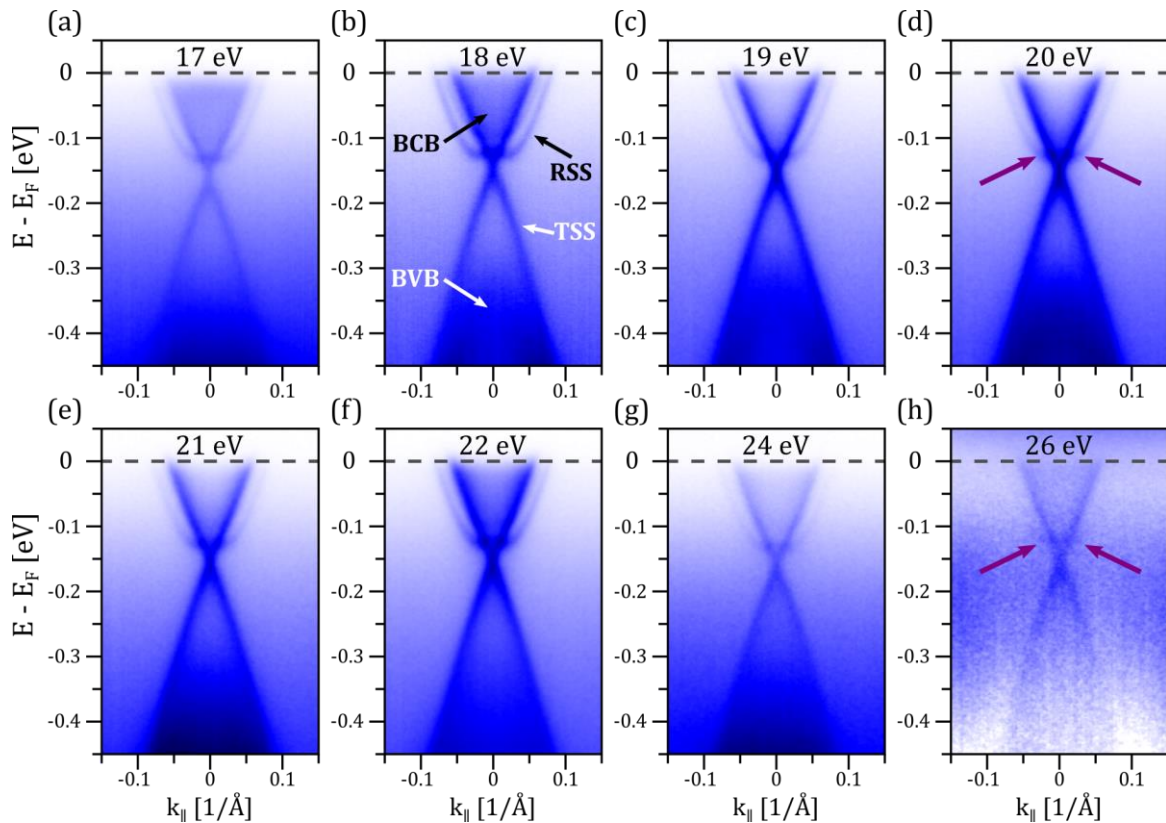
Figure 5.18: Photon energy dependence of Pb$_{0.70}$Sn$_{0.30}$Se with 0.2 ML Fe deposited on the surface, with BCB, BVB, RSS and TSS labelled. The purple arrows in images (d) and (h) point to the highest intensity parts of RSS. Measurement temperature 80 K. Sample G5.

In addition to measurements of (111) Pb$_{1-x}$Sn$_x$Se near $\overline{\Gamma}$ point, spectra near $\overline{M}$ point were also collected for sample R5 after Fe deposition and are presented in **Figure 5.19**. As expected, a single Dirac cone, with TSS crossing in the bulk band gap, is observed (image **(a)**). Increasing the amount of TM leads to a noticeable shift of the DP towards lower energies **[43, 44]**, similar to the results obtained for (001)-oriented samples after Mn deposition. The deposition seems to give rise to a two-dimensional electron gas (2DEG) state that increases in prominence with the amount of Fe on the surface of the sample. Such evolution of the spectra suggests that Fe atoms first donate electrons to the sample, causing an E_F change, and then they form the 2DEG state **[44]** on the surface.
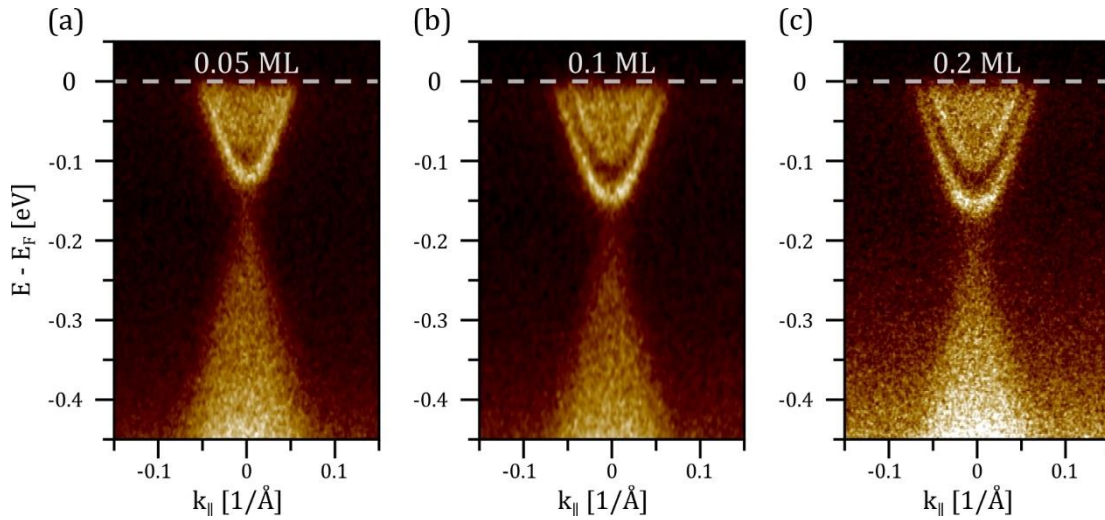
Figure 5.19: ARPES spectra of the p-type (111) $Pb_{0.75}Sn_{0.25}Se$ near $\bar{M}$ point, with Fe deposited on the surface. Photon energy E_{ph} = 17.2 eV, measurement temperature 80 K. Sample R5.

A similar effect has been reported in (001) Bi_2Se_3 TI near $\bar{\Gamma}$ point **[189]** due to the adsorption of impurities on the surface. However, the Fermi surface near $\bar{M}$ point is highly anisotropic and proposed explanation and description of the obtained band structure would require studies that are more detailed. The URANOS beam-line end station did not have azimuthal rotation available at the time of **1)** and **2)** beamtimes, which would have been crucial for proper orientation of the sample in the case of anisotropic dispersion. Because of this and of a relatively weak spectral density, no further measurements of $Pb_{1-x}Sn_xSe$ near $\bar{M}$ point were carried out during **2)** beamtime.

5.2.5   Initial theoretical model of Rashba splitting

To provide a better understanding of the observed effects, an initial model of Rashba splitting on the (111) surface of TCI PbSe using density functional theory (DFT) **[190]** calculations was developed by C. Autieri, G. Cuono, and R. Islam from the Group of Physics of Majoranas (ON6.5) of International Centre for Interfacing Magnetism and Superconductivity with Topological Matter – MagTop of the Institute of Physics PAN. The model assumes compressively strained (by 2%) PbSe (111) in TCI phase **[24]** with Se terminated top surface. The simulated slab had the thickness of 106 Å (31 layers of Se and 31 layers of Pb) with 20 Å of vacuum on top and was asymmetric (Pb at the bottom layer, Se at the top layer) to introduce inversion symmetry breaking that splits DPs at $\bar{\Gamma}$ point coming from opposite simulated surfaces. Sufficient film thickness is crucial to avoid overlap of the wave functions of the TSS at the opposite film boundaries, which would result in energy gap opening **[174]**. A 3d metal (with d-orbital electrons being chemically active) was used to reproduce the experimental coverage by TM. It was found that the experimentally observed DP comes from the Se terminated surface, and the observed Rashba effect comes mainly from the Pb layers close to the surface but also form the deeper ones. Reproduction of Rashba splitting magnitude

comparable to the experimental values was obtained for 3d metal coverage at top position (TM atom located above Se atom; see **Figure 5.20 (a)**). The studied effect in PbSe is influenced by the symmetry of the slab, by the surface termination, and by the structural and electronic properties of the coverage. **Figure 5.20 (b)** shows the obtained surface resolved band structure with the contribution of the bulk filled in red. The dark blue bands are not visible in the experimental results, because they come from the bottom simulated surfaces. The theoretical results obtained are qualitatively comparable with the ARPES spectra obtained during the experiments (**Figure 5.20 (c)**).
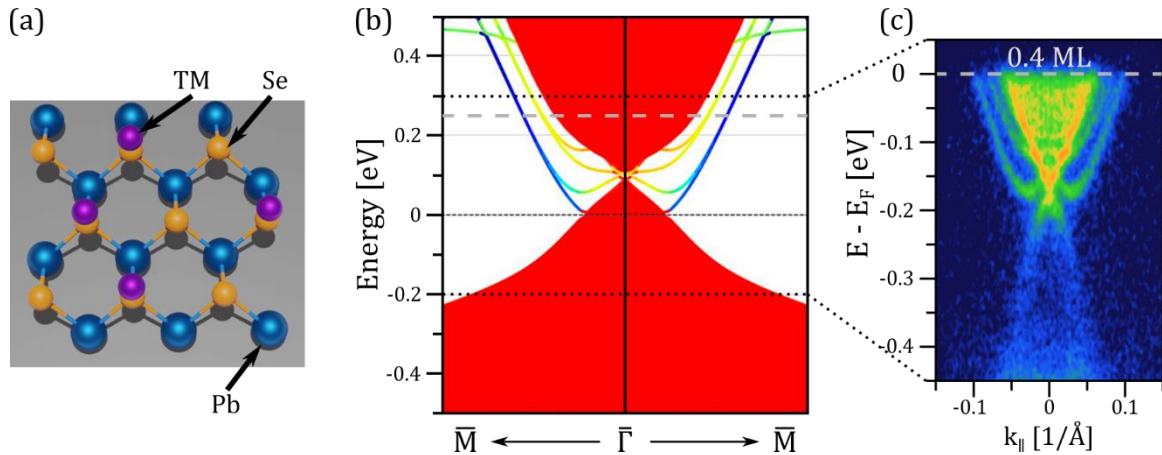
Figure 5.20: Initial Rashba splitting DFT model conclusions. (a) Se terminated (111) PbSe with TM in the top position, i.e. above the Se atom. **(b)** Surface resolved band structure of an asymmetric slab covered by the 3d metal in the top position; contribution of the bulk filled in red. **(c)** ARPES spectra of sample R2 with 0.4 ML Mn deposited on the surface. Dashed lines indicate the approximate energy range correspondence between images (b) and (c). Initial (b) image by R. Islam with minor modifications by B. Turowski.

5.2.6 Core level spectroscopy of (111) Pb$_{1-x}$Sn$_x$Se

Core level spectroscopy is a method accompanying ARPES studies **[83, 138, 191]** widely used in order to determine the atomic composition of a sample. During **2)** beamtime at the URANOS beamline, core level studies on samples G3, G4, G5 were carried out with exciting photon energy E_{ph} of 90 eV at 80 K, with resolution of 0.05 eV. This excitation energy corresponds energy of collected photons $E_{kin} = E_{ph} - E_B$, where E_B is the binding energy of the electrons. In the presented Binding energy range the inelastic mean free path (IMFP) of electrons is less than 10 Å **[124]**, with shorter IMFP at lower E_B. As a result, the recorded signal comes mostly from the surface of the sample, which is important in the case of submonolayer deposition of Fe on the sample.

Figure 5.21 shows CL spectra of Pb$_{0.70}$Sn$_{0.30}$Se (G5) and Pb$_{0.74}$Sn$_{0.26}$Se (G3), images **(a)** and **(b),** respectively. The red spectrum at the bottom of image **(b)** corresponds to pristine Pb$_{0.74}$Sn$_{0.26}$Se. CL signals of only Pb, Sn, and Se are present in this case, proving high surface purity.
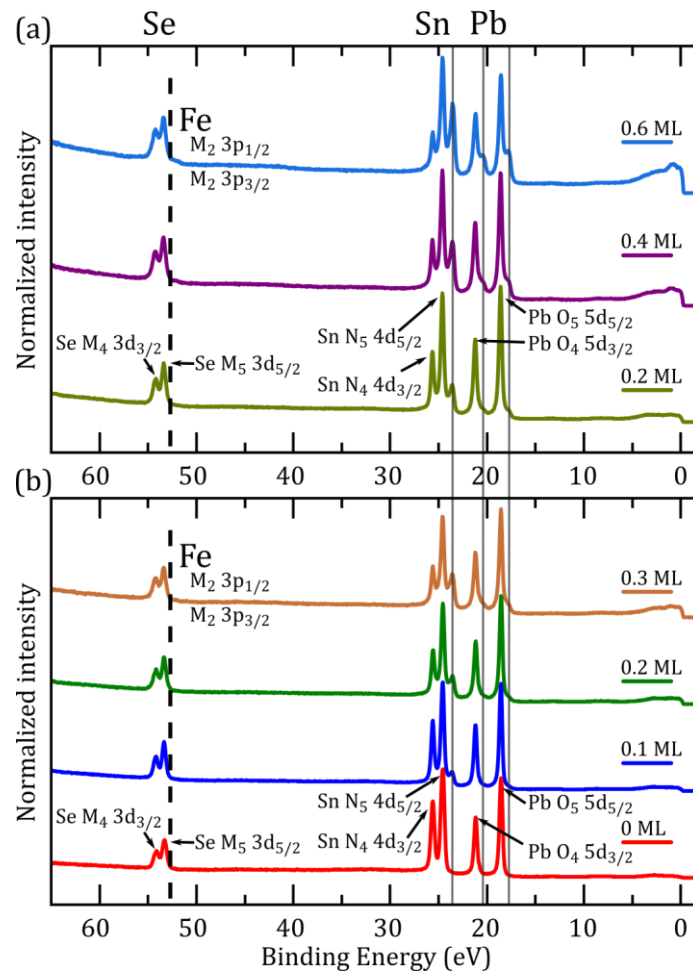
Figure 5.21: Core level spectra obtained with photon energy of 90 eV at 80 K for an increasing amount of Fe on the surface of (a) Pb$_{0.70}$Sn$_{0.30}$Se and (b) Pb$_{0.74}$Sn$_{0.26}$Se. A strong shift of surface Sn and Pb levels is observed by 1 eV and 0.74 eV, respectively. The black vertical dashed line indicates the expected position of the metallic Fe peak. The solid grey lines indicate the positions of additional peaks emerging as a result of Fe deposition. Samples G5 and G3, (a) and (b), respectively.

Table 5.7: Core level binding energies of Pb$_{1-x}$Sn$_x$Se and Fe. Values from the spectra presented in **Figure 5.21**. Samples G5 and G3.

Level	Binding energy [eV] **Figure 5.21**	Binding energy [eV] **[192]**	Chemical shift [eV]	Binding energy [eV] **[193]**
Pb 5d 3/2	21.17	20.7	0.47	21.2
Pb 5d 5/2	18.56	18.1	0.46	18.6
Sn 4d 3/2	25.61	24.9	0.71	25.6
Sn 4d 5/2	24.61	23.9	0.71	24.7
Se 3d 3/2	54.20	55.5	-1.3	Se 3d in SnSe: 53.7
Se 3d 5/2	53.36	54.6	-1.24	Se 3d in PbSe: 53.4
Fe 3p 1/2	-	52.7	-	-
Fe 3p 3/2	-	52.7	-	-

Table 5.7 shows the binding energies of the peaks of individual elements (including metallic Fe 3p) obtained from the measurements compared to their binding energies reported in the

X-ray data booklet by Lawrence Berkeley National Laboratory, University of California [192] (see columns 2 and 3 of **Table 5.7**). Double peak structure is the effect of spin-orbit interaction in a given element. The higher the Z number of an element, the greater the split between the core levels of an atomic subshell.

The measured binging energies of elements in $Pb_{1-x}Sn_xSe$ differ from their elemental values because they depend on the chemical environment of the given element. This shift is called the chemical shift and occurs when the oxidation state of an atom changes by several elementary charges [194] (column 4 of **Table 5.7**). The CL energy of an electron is determined by its repulsive core Coulomb interactions with other electrons and the attractive potential of the nuclei. If an atom is placed in a different chemical environment, its valence charges undergo a spatial rearrangement and it is affected by different potential created by the nuclear and electronic charges of all other atoms in the compound [194]. This leads to a change of its CL energies. The obtained values of the binding energies agree quite well with the values reported for Pb, Sn, and Se in PbSe and SnSe compounds [193] (see column 5 of **Table 5.7**).

The initial deposition of 0.1 ML Fe (image **(b)**, dark blue) does not result in the appearance of expected Fe 3p peaks. Instead, an additional peak appears next to the Sn 4d peaks. Further increase of total amount of Fe on the surface of the samples reinforces the new peak. Simultaneously, the intensity of Sn $4d_{5/2}$ decreases. A similar effect is observed for Pb 5d peaks. At 0.2 ML total Fe thickness (image **(a)** and **(b)** green), two new peaks in lower binding energies start to emerge (position of which is marked by vertical grey lines) and gain in intensity with the increase of deposited Fe amount. At the same time, no signal at binding energy corresponding to Fe 3p is observed (as marked by the black dashed vertical line), but it can overlap with Se 3d peak due to chemical shift. This interpretation is supported by the fact that the relative intensity of the Se peak, with respect to the Sn and Pb peaks, increases with Fe deposition. In 2012 Scholz et al. [43] reported that in the case of small amounts of Fe deposited on the surface of Bi_2Se_3 TI, the Fe core level 3p overlaps with the Se 3d peak. Additionally, new peaks at lower binding energies were attributed to newly formed bonds between Bi and Fe; thus, it was proposed that in the case of Se termination, new bonds between Fe and Se could weaken the interlayer bonding of Se and Bi. In the case of Fe deposited on the surface of $Pb_{1-x}Sn_xSe$, such bonds could be created between Sn and Fe and Pb and Fe. If Se termination is assumed, the bonds between Pb and Se, and Sn and Se could be weakened by new bonds between Se and Fe. Both situations result in a shift of CL peaks of Pb and Se located at the surface, which occurs because of a change in their chemical environment due to Fe deposition. The reported surface shift of Bi CL in Bi_2Se_3 was ~1 eV [43] for both Bi 5d levels. Similarly, both additional Pb 5d levels, appearing after Fe deposition, are shifted by similar energy (0.74 eV), and the additional Sn $4d_{5/2}$ level is shifted by 1.03 eV. Since the spin-orbit splitting of Sn $4d_{3/2}$ and $4d_{5/2}$ levels is 1 eV (see columns 2 and 3 of **Table 5.7)**, it stands to reason that an additional Sn CL appears after Fe deposition (shifted from $4d_{3/2}$) that overlaps with the $4d_{5/2}$ level. It is supported by the fact that the intensity of $4d_{5/2}$ CL does not

change with subsequent Fe deposition, while the intensity of Sn $4d_{3/2}$ and Pb 5d levels decrease with the increase of the intensity of the additional CL. The binding energy values of the Pb 5d and Sn 4d peaks, and additional peaks caused by Fe deposition, are given in **Table 5.8**.

Table 5.8: Core level binding energies of surface levels of Pb and Sn after deposition of Fe on Pb$_{1-x}$Sn$_x$Se surface form Figure 5.21.

Level	Binding energy [eV] of Pb$_{1-x}$Sn$_x$Se CLs in initial state (before Fe deposition)	Binding energy [eV] of additional CL appearing after Fe deposition	Δ Binding energy [eV]
Pb 5d 3/2	21.17	20.43	0.74
Pb 5d 5/2	18.56	17.82	0.74
Sn 4d 3/2	25.61	24.61	1.00
Sn 4d 5/2	24.61	23.58	1.03

5.2.7 Summary

ARPES measurements of high quality (111) Pb$_{1-x}$Sn$_x$Se epilayers, evidenced by sharp features of the ARPES spectra, were conducted in two separate beamtimes at the URANOS beamline at SOLARIS Synchrotron, Kraków, Poland. During the experiments, the samples were studied in photon energy close to 20 and 90 eV and temperature in the range of 80 to 300 K. The temperature-dependent topological transition was proved in the studied samples. The deposition of Fe and Mn in the preparation chamber of the end-station was carried out to verify whether magnetic impurity on the surface of the TCI would break the crystal symmetry and lead to gap opening in the surface states. To date, no such research has been conducted on (111) Pb$_{1-x}$Sn$_x$Se. Contrary to theoretical predictions **[148, 149]**, no band gap opening of the magnetic origin was observed, which is consistent with similar research focused on the deposition of magnetic elements on the surface of the Bi$_2$Se$_3$ TI system **[43, 44, 118]**. Such a gap opening would require fine-tuning of the Fermi energy close to DP **[149]**, which is difficult to achieve.

The deposition of both Fe and Mn transition metals on the (111) surface of Pb$_{1-x}$Sn$_x$Se resulted in the emergence of momentum-splitted, concentrically arranged states in CB attributed to Rashba splitting. The observed Rashba parameter α_R reached 2.5 - 3.5 eV·Å, which is close to the value reported for materials with giant Rashba splitting **[195, 196]**. Initial APRES measurements of samples G3, G4, and G5 did not show Rashba splitting, although some small submonolayer amount of Mn was deposited in-situ MBE in the GM#2 system. The samples were stored in a UHV suitcase, with a base pressure of 10^{-11} mbar, for more than several days. It is very likely that some contaminants present in the residual gas in the suitcase adsorbed on the surface of the epilayers (see **Section 3.1** for the explanation) influencing the purity of the deposited Mn. Deposition of Fe in the preparation chamber of the URANOS beamline resulted in Rashba splitting as described above. This interpretation is corroborated by the

apparent shift in Fermi energy of the G3 sample, visible in **Figure 5.14 (a)**, which follows trends similar as p-type R5 sample, as shown in **Figure 5.15**.

The experimental results motivated theoretical calculations performed by the members of the MagTop ON6.5 Group of Physics of Majoranas at IF PAN that qualitatively explain the obtained data.

Core level spectroscopy proved the high purity of the grown epilayers, with only Pb, Sn, and Se levels visible for the pristine sample. Deposition of Fe on the surface of $Pb_{1-x}Sn_xSe$ leads to the emergence of additional peaks. The result obtained is consistent with previous literature reports on Fe deposition on the surface of Bi_2Se_3 TI in Ref. **[43]**. It broadens the understanding of the TCI / metal interface.

5.3   Spin polarization in (111) $Pb_{1-x}Sn_xSe$

Helical spin polarization of surface states in 3D TIs makes them promising candidates for efficient spin-charge converters **[197, 198]**. It has been demonstrated that a spin-orbit torque (SOT) induced by spin polarized TSS can control magnetisation switching in TI/ferromagnet heterostructures **[5, 167, 199]**. Since TCIs and TIs have similar topological surface states with helical spin structure **[8, 54]**, investigating their spin structure can lead to further developments in the field of spintronics, such as finding new materials suitable for device applications. One possible candidate are TI and TCI in the normal insulator phase. Their helical spin texture, characteristic of the topological phase, has been shown to persist even for the NI phase, **[200]** and **[8]** for (001) orientation, respectively. To date, no research of spin polarization on both sides of the topological transition point has been done in (111) TCI. Because topological protection in TCI comes from crystal symmetry **[35]**, external perturbations, such as manipulation of their crystal structure or lattice parameters, can be used to induce the NI-TCI transition **[9, 10, 99]**.

Taking into account the above, the aim of the research presented in this section was to study the spin-polarized structure of (111) $Pb_{1-x}Sn_xSe$ by SR-ARPES across the topological transition to verify, if spin polarization of the TSS would persist in the NI phase in this material. Another objective was to study the spin polarization of the Dirac-Rashba energy spectrum emerging after the submonolayer deposition of TM on the surface of (111) $Pb_{1-x}Sn_xSe$, as discussed in **Section 5.2**. Surprisingly, no Rashba splitting was observed. Instead, a topological transition, i.e. gap opening in $Pb_{1-x}Sn_xSe$ in the TCI phase, induced by TM deposition, was revealed.

In this section, ARPES and SR-ARPES measurements, performed with p–polarized light (electric field parallel to the plane of incidence) near $\bar{\Gamma}$ point in $\bar{\Gamma} - \bar{M}$ direction, across the topological transition in $Pb_{1-x}Sn_xSe$ grown on BaF_2 (111) are presented for both pristine samples and those with TM deposited on the surface. First, the in-plane and out-of-plane spin polarization in the topological phase $Pb_{1-x}Sn_xSe$ is discussed. Then, the in-plane spin

polarization of TCI and NI $Pb_{1-x}Sn_xSe$ is compared. Next, the influence of annealing of a sample on the ARPES and SR-ARPES spectra is presented. Then, the deposition of Fe on the surface on the ARPES and SR-ARPES spectra is discussed. Finally, a topological transition induced by the deposition of TM is shown. The chapter ends with a summary of all the results.

The results presented here were published in **[15]** and presented in part during the 5th International Conference on Applied Surface Science (ICASS 2022) in the form of a 20-minute oral presentation. I did SR and normal ARPES measurements, as well as compiled and prepared the data for presentation. The data presented were obtained during **3)** and **4)** beamtimes at the SOLAIRS Synchrotron PHELIX end-station under the supervision of V. V. Volobuev and with the help of A. Kazakov and R. Rudniewski, as well as PHELIX beamline staff. Most of the measurements were conducted at 200 K with the exciting photon energy of 70 eV. Details of the sample studied are given in **Table 5.9**.

Table 5.9: Discussed $Pb_{1-x}Sn_xSe$ (111) epilayers studied at the PHELIX beamline.

name	code	substrate	Sn content [%]	Thickness [μm]	Deposited TM
G34	G011422B	BaF_2	15	1	Fe
G35	G011522A	BaF_2	24	1	Fe
G36	G011522B	BaF_2	30	1	Fe
G37	G011522C	BaF_2	26	1	Mn

5.3.1 In-plane and out-of-plane spin polarization

Due to the expected helical in-plane spin texture of the TCIs, spin of the TSS electrons is supposed to be tangential to the Fermi surface **[46]** and, consequently, only one in-plane spin component should be non-zero (see **Figure 2.6 (c)**) at $k_y = 0$ and $k_\parallel = k_x$. **Figure 5.22** shows the spin resolved energy distribution curves (SR EDC) for the (111) oriented $Pb_{0.7}Sn_{0.3}Se$ sample for two measured spin components, one in-plane and one out-of-plane.
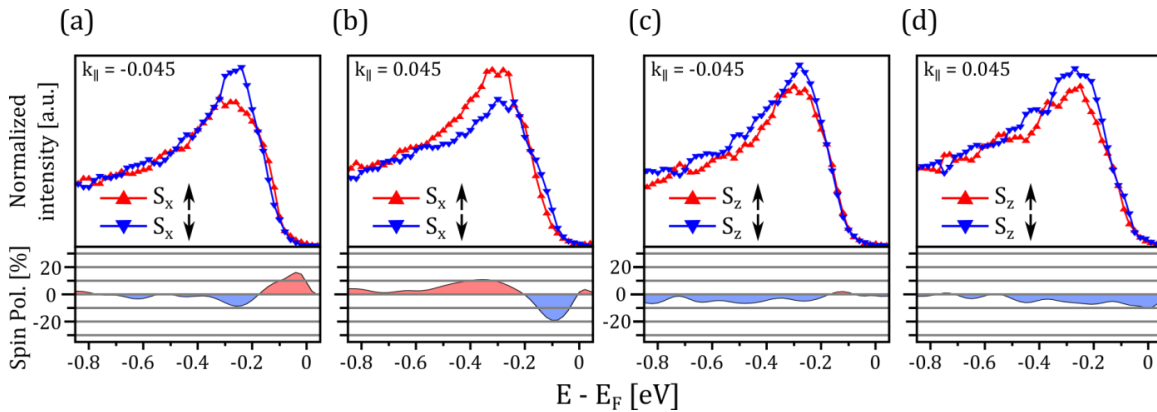
Figure 5.22: Spin resolved energy distribution curves of the $Pb_{0.7}Sn_{0.3}Se$ (111) epilayer recorded at two opposite values of wave vector $|k_\parallel| = 0.045$ Å^{-1} for **(a)**, **(b)** one in-plane (S_x) and for **(c)**, **(d)** out-of-plane (S_z) spin components, with corresponding spin polarization shown below. Sample G36 before annealing.

The second in-plane component is not presented here because at the time of the experiment there were technical problems with a rotator lens, which switches between the S_x and S_y spin components. **Figure 5.22 (a)** and **(b)** shows that, as expected, the opposite in-plane spin polarization for S_x for the negative and positive $k_\parallel$ is detected. At the same wave vector values the SR EDCs for S_z spin component normal to the sample surface (**Figure 5.22 (c)** and **(d)**) show negligible non-opposite out-of-plane spin polarization.

5.3.2   Spin-polarization of $Pb_{1-x}Sn_xSe$ in topological crystalline and normal insulator phases

Spin polarization of pristine $Pb_{1-x}Sn_xSe$ was studied at 200 K for 1 µm thick epilayers with tin content of 30% and 15%. At this temperature, the samples were expected to be in the TCI and NI phases **[67, 68]**, respectively, as marked by dashed vertical lines in **Figure 2.8**. **Figure 5.23** shows that this is indeed the case. For the sample with $x_{Sn} = 0.30$ (**Figure 5.23 (a)**) TSS cross at the DP, a clear indication of the TCI phase. The ARPES spectra of the NI phase sample, with $x_{Sn} = 0.15$, in **Figure 5.23 (b)** shows a band gap of 78 meV that is in close agreement with the semi-empirical Preier's formula **[68]**. The corresponding SR measurements are presented in **Figure 5.23 (c)** and **(d)**. The opposite spin polarization obtained from the SR EDC, extracted at $k_\parallel$ positions indicated by grey vertical dashed lines in **Figure 5.23 (a)**, shows that the helical spin texture is present in the TCI phase. The conduction and valence bands manifest opposite helicity, but spin polarization differs and reaches values of up to 30% and 10%, respectively. The smaller spin polarization of VB is attributed to the overlap of VB TSS with bulk states, which are spin-degenerate. A similar spin polarization of 10% for one of the in-plane spin components was previously reported **[53]** in same class of materials, namely (100) oriented PbSnTe. The DFT calculations for prototypical Bi_2Se and Bi_2Te TIs **[201]** have shown, that the values of the spin polarization is reduced to ~50% due to spin-orbit coupling (SOC). A similar effect of reduction of measured spin polarization is expected here, as strong SOC, responsible for band inversion, is present in $Pb_{1-x}Sn_xSe$. The same magnitude of helical spin polarization is visible in **Figure 5.23 (d)**. It was not previously reported in the trivial phase of $Pb_{1-x}Sn_xSe$, but a similar effect was shown in systems with TI-NI **[200]** or TCI-NI **[8]** transition. Its occurrence may be explained by the presence of Rashba splitting of the surface states, resulting in the presence of helical spin texture in SS, as proposed in Ref. **[202]**. The effect was modelled using tight binding calculations for Bi_2Se_3 TI by taking into account the Rashba term and electrostatic surface potential, in addition to the TI Hamiltonian. The Rashba effect was previously reported in PbSnTe(Se) (111) TCIs **[83, 174]**. The prerequisites for its occurrence are broken inversion symmetry and the presence of an electric field gradient. These are fulfilled in the case of (111) surface, because of its polar nature, i.e. only one kind of atoms, chalcogenide or metal, terminates the surface. In connection with the latter, it may be the reason for the helical spin texture observed in the $x_{Sn} = 0.15$ sample. However, no Rashba split states were detected for this epilayer, even after changing the incident photon energy. Similarly, it was absent for

(001)-oriented $Pb_{0.73}Sn_{0.27}Se$ in the NI phase studied in Ref. [8] that showed spin polarization of SS. The absence of Rashba splitting in the presence of helical spin texture can result from the splitting being so small that it cannot be resolved by ARPES, but it is detected by spin-resolved measurements. Additionally, the electrostatic band bending effect observed in (111)-oriented PbSnTe(Se) [83, 174] can be the reason for the spin-polarized surface resonances, even when the Rashba splitting is absent, as shown in Ref. [202].
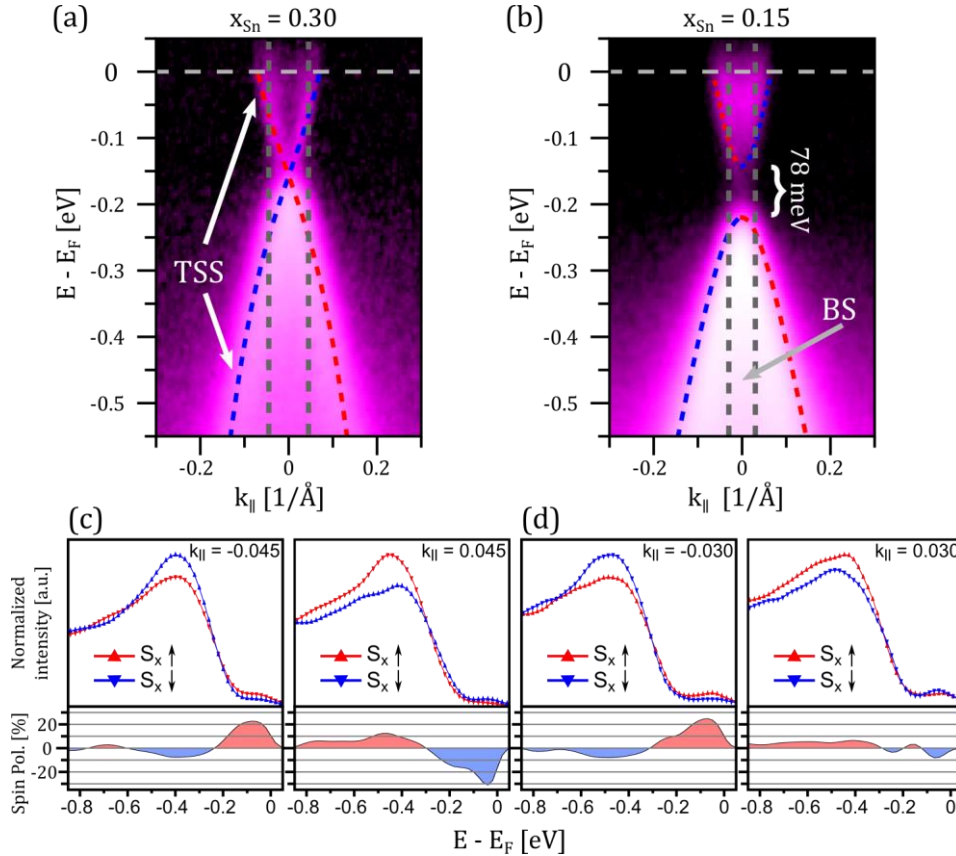
Figure 5.23: (a), (b) ARPES spectra of (111) oriented Pb₁-ₓSnₓSe epilayers and (c), (d) corresponding SR measurements performed at 200 K with a photon energy of 70 eV near the $\bar{\Gamma}$ point. Colour is scaled logarithmically in the image. **(a)** corresponds to the topological composition of x_{Sn} = 0.30 with gapless TSS and **(b)** to the trivial composition of x_{Sn} = 0.15 with a band gap of 78 meV and high intensity of the bulk states. On both (a) and (b) images, the red and blue dashed lines are guidelines of the surface states, whereas the grey vertical dashed lines indicate negative and positive momentum positions where the SR measurements are taken. **(c)**, **(d)** corresponding to (a) and (b) SR EDC of spin-up (red) and spin-down (blue) in-plane spin component and spin polarization is depicted at the bottom. Binomial smoothing with smoothing parameter 3 was applied to SR EDCs; see **Section 3.8**. Image adapted from Ref. [15]. Samples G36 and G34 after annealing, (a) and (b), respectively.

Furthermore, the helical spin texture in the trivial phase $Pb_{1-x}Sn_xSe$ epilayers is further supported by transport measurements and theoretical calculations published in Ref. [100]. The pair of counter-propagating charge contours at the Fermi surface experience π Berry phase shift, caused by spin momentum locking in the TCI TSS. Because the inversion symmetry is broken at the sample surface, the Berry phase quantized to π occurs in both the

TCI and NI phases. It was confirmed by weak-antilocalization measurements and it was shown that it is not the topological order, but the symmetries present in the $Pb_{1-x}Sn_xSe$ system, that lead to Berry phase effects **[100]** described briefly above.

5.3.3   Influence of sample annealing on ARPES and SR ARPES spectra

Some of the samples needed to be annealed before ARPES measurements. Because of the fact that this experimental method is very sensitive to state of the surface, any impurity present there negatively affects the measurements. The samples were annealed at 300 °C for 20 minutes in the preparation chamber of the PHELIX beamline end station. Comparison of ARPES spectra and SR EDCs with corresponding in-plane spin polarization is shown in **Figure 5.24** and **Figure 5.25**.
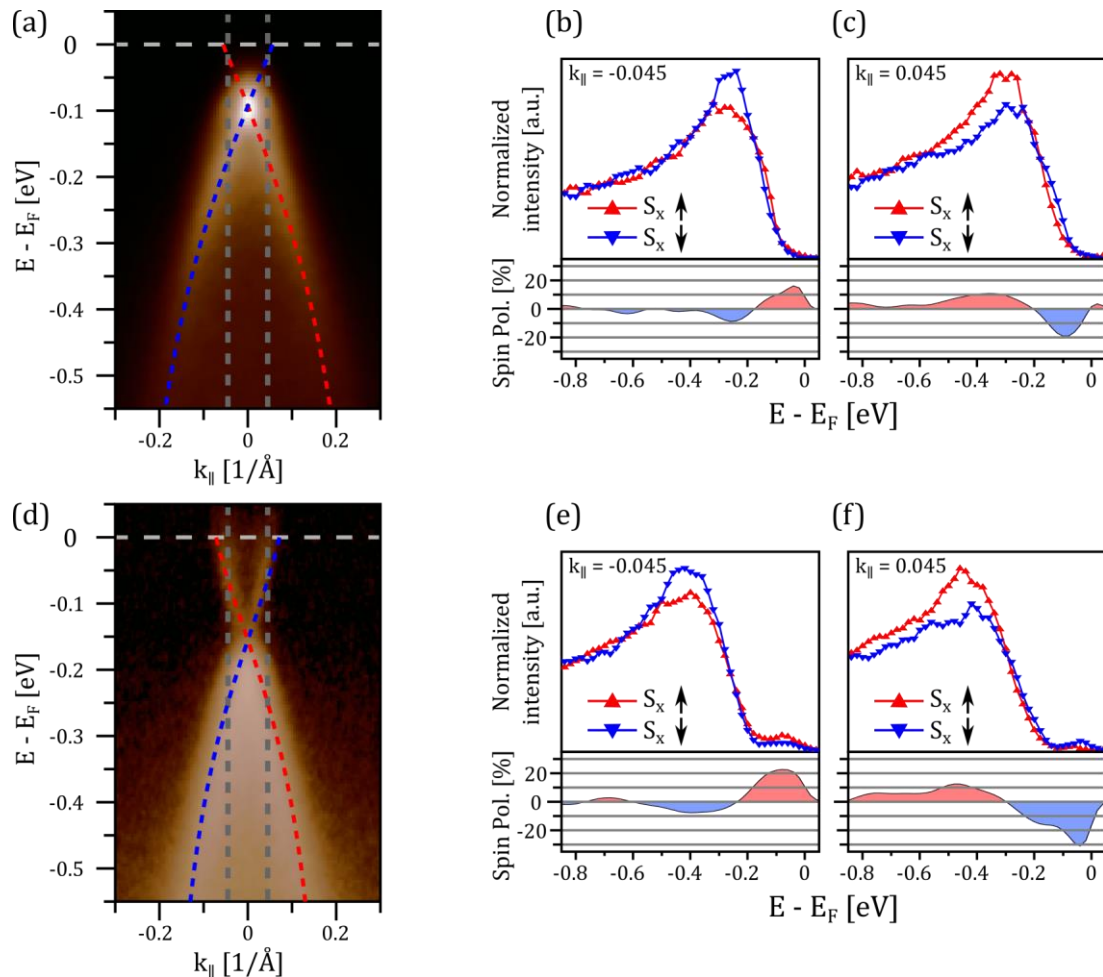
Figure 5.24: Influence of sample annealing on ARPES and SR ARPES spectra of the Pb₀.₇Sn₀.₃Se (111) epilayer. (a) and **(d)** ARPES spectra of the sample before and after annealing, respectively. The blue and red dashed lines are TSS guidelines. The grey vertical dashed lines indicate momentum positions of SR measurements. **(b)**, **(c)** and **(e)**, **(f)** corresponding SR EDC and spin polarizations. The spectra are shown with a logarithmic colour scale. Sample G36.

Annealing of the pristine samples has two main effects visible in the ARPES measurements. It shifts E_F upwards, further to CB, allowing for more complete visualisation of the band structure (overlapped with red and blue dashed lines for better understanding) by making the sample more n-type, as visible in **Figure 5.24** and **Figure 5.25**, (a) and (d). It also improves the spin polarization of the epilayers from up to 20% (**Figure 5.24 (b)** and **(c)**) to up to 30% (**Figure 5.24 (e)** and **(f)**) in the case of $Pb_{0.7}Sn_{0.3}Se$ and from up to 10% (**Figure 5.25 (b)** and **(c)**) to up to 25% (**Figure 5.25 (e)** and **(f)**) in the case of $Pb_{0.85}Sn_{0.15}Se$. The improvement is most likely due to thermal removal of unwanted adatoms that could adsorb on the surface of the sample in transfer and transport, despite UHV, which would give an unpolarised contribution to recorded SR EDCs.
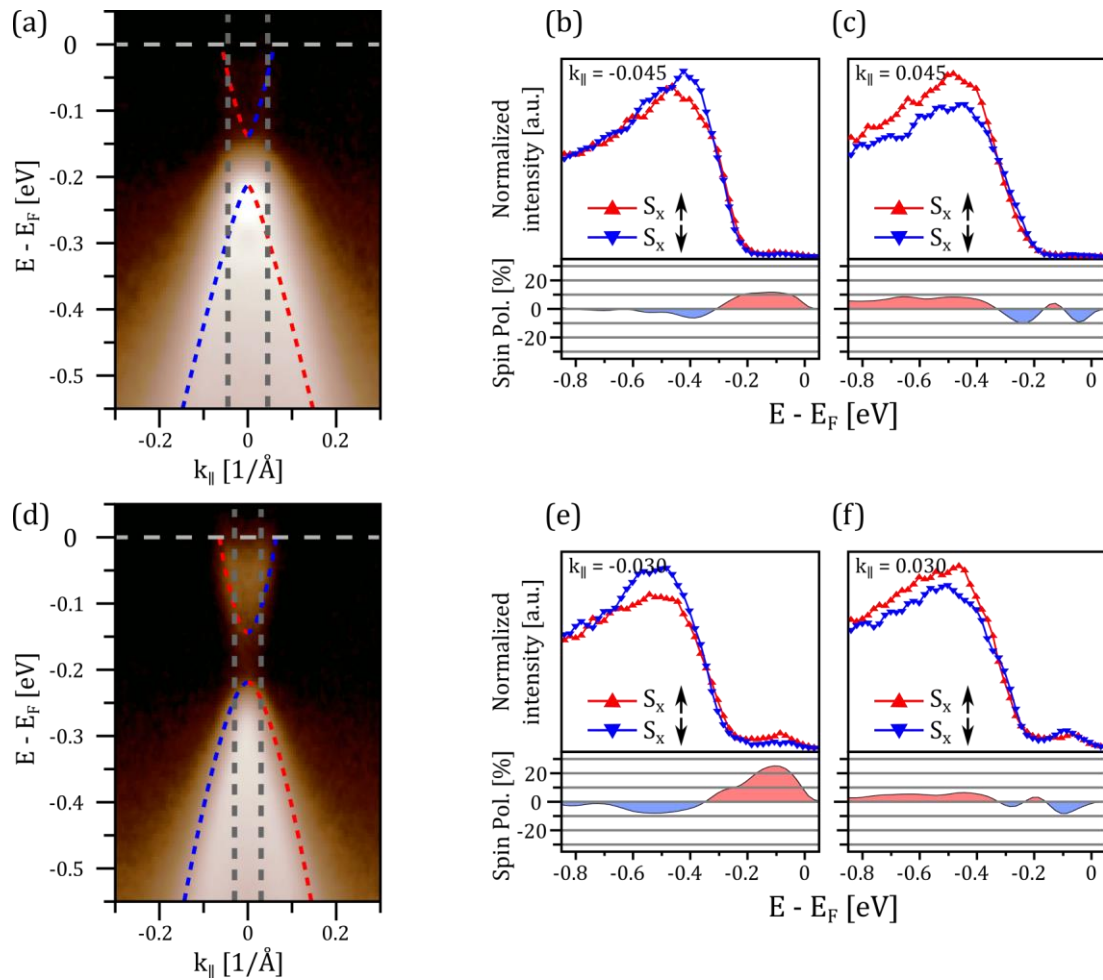
Figure 5.25: Influence of sample annealing on ARPES and SR ARPES spectra of the $Pb_{0.85}Sn_{0.15}Se$ (111) epilayer. (a) and **(d)** ARPES spectra of the sample before and after annealing, respectively. The blue and red dashed lines are surface states guidelines. The grey vertical dashed lines indicate momentum positions of SR measurements. **(b)**, **(c)** and **(e)**, **(f)** corresponding SR EDC and spin polarizations. The spectra are shown with a logarithmic colour scale. Sample G34.

5.3.4   Effect of TM deposition on electronic and spin structure of TCI

The transition from TCI to NI was observed under the deposition of less than 1 ML of Fe and Mn transition metals on the surface of $Pb_{1-x}Sn_xSe$ in the TCI phase, namely with x_{Sn} = 0.30 and x_{Sn} = 0.26, respectively, at 200 K. Details of the deposition process are described in **Section 4.2.4 Deposition of TM**. **Figure 5.26** shows how the electronic structure and spin texture of the $Pb_{0.70}Sn_{0.30}Se$ epilayer change with the deposition of Fe.
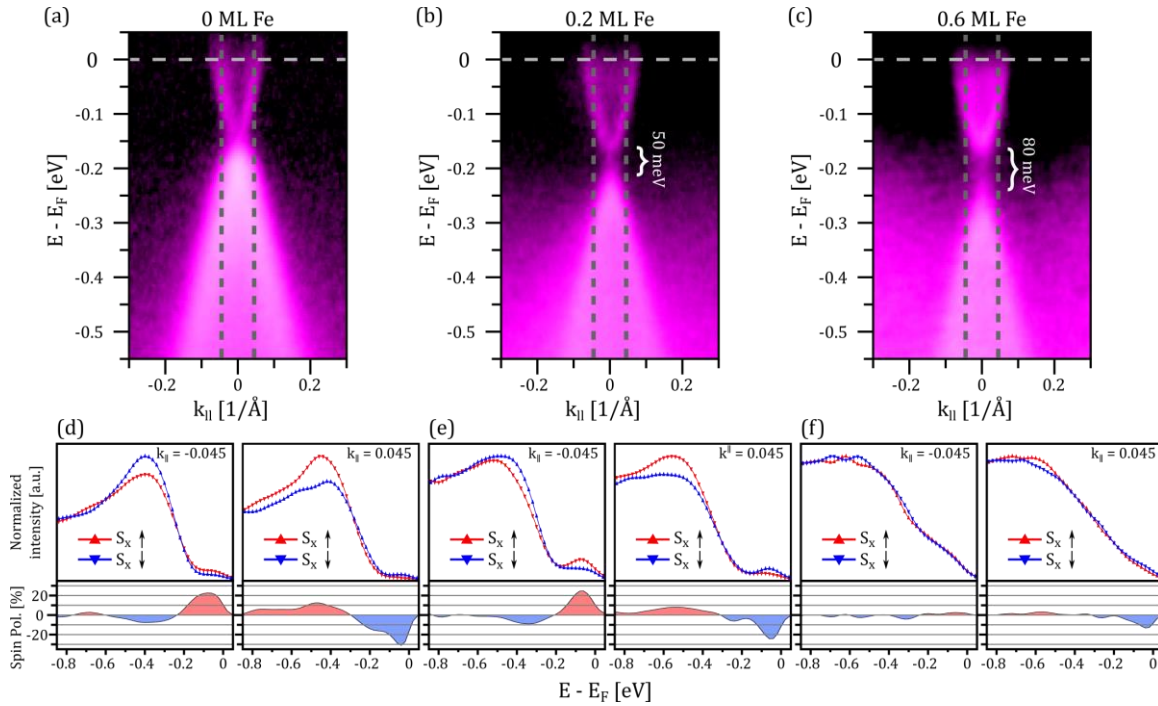
Figure 5.26: (a)–(c) Electronic structure of $Pb_{0.7}Sn_{0.3}Se$ taken at the same conditions as that presented in **Figure 5.23** with an increasing iron thickness from 0 to 0.2 ML and then to 0.6 ML deposited on the surface of the epilayer. Colour is scaled logarithmically on the images; for **(c)**, strong background noise is removed. Grey vertical dashed lines indicate negative and positive positions of momentum for SR measurements. **(d)–(f)** Corresponding smoothed SR EDCs and spin polarization at $|k_{||}|$ = 0.045 1/Å. Binomial smoothing with smoothing parameter 3 was applied to SR EDCs; see **Section 3.8**. Image adapted from Ref. **[15]**. Sample G36.

Pristine sample, **Figure 5.26 (a),** is in the topological phase, as TSS close the band gap. **Figure 5.26 (b)** shows that the deposition of 0.2 ML Fe results in band bending (change of the shape of the bands and their separation) and n-type doping of the sample surface. There is noticeable upward shift of the Fermi level, as well as appearance of 50 meV band gap. With the addition of 0.4 ML Fe (**Figure 5.26 (c)**), bringing the total deposited amount of Fe to 0.6 ML, the surface band gap widens to 80 meV, and the E_F increases slightly even more. The emergence of the band gap does not influence the presence of surface states or so-called precursor states **[200, 203]**. Their surface nature is evidenced by the fact that they do not disperse with varying photon energy (see **Figure 5.28**). Strong background noise coming from the TM deposition is removed from the spectra in **Figure 5.26 (c)**. This effect is

discussed later in this section. In **Figure 5.26 (d)**, **(e)**, and **(f),** SR EDCs and corresponding spin polarization at the same wave vector $|k_\parallel|$ value are presented. Although the deposition of 0.2 ML opened the gap in the surface spectra, the helicity of the surface states does not vanish. Spin polarization reaches up to 25%, while reaching up to 30% for the pristine sample (**Figure 5.26 (e)** and **(d)** respectively). At 0.6 ML of the total deposited Fe the spin polarization drops to ~5% due to the presence of unpolarised disordered Fe states, that overlap with polarized SS and increase the background noise, causing an overall drop in detected spin polarization. A similar effect, under the deposition of another TM, was observed in sample with x_{Sn} = 0.26, which is also expected to be in the TCI phase at measurement conditions, that is, 200 K. Deposition of 0.4 ML of Mn caused 40 meV SS band gap opening and helical spin texture with polarization of up to 30%, **Figure 5.27 (a)** and **(b)**, respectively.
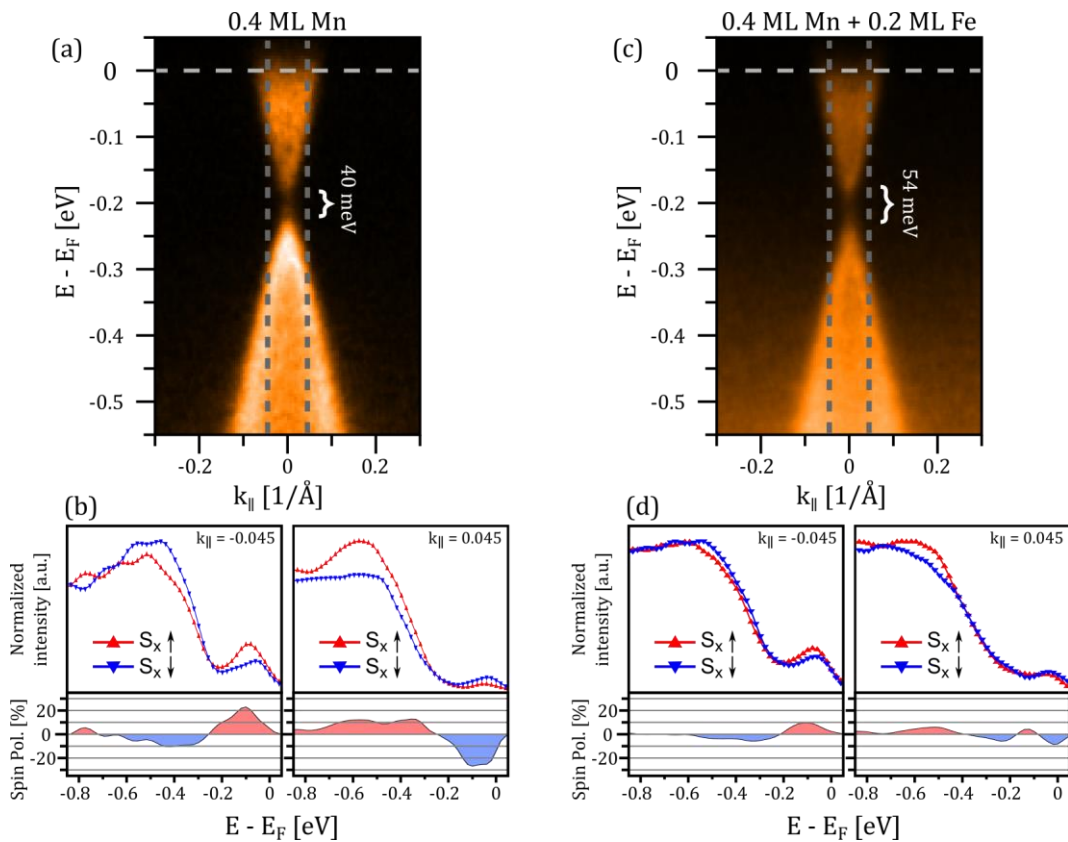
Figure 5.27: (a) Electronic structure of Pb0.74Sn0.26Se and (b) corresponding smoothed SR measurements taken at 200 K with a photon energy of 70 eV near the $\bar{\Gamma}$ point with 0.4 ML of Mn deposited on the surface. The grey vertical dashed lines indicate the negative and positive momentum of the SR measurements. The spectra are shown with a linear colour scale. Adapted from Ref. **[15]**. **(c)** ARPES spectra of the same sample at the same conditions with additional deposition of 0.2 ML Fe on the surface and **(d)** corresponding SR measurements. Binomial smoothing with smoothing parameter 3 was applied to SR EDCs; see **Section 3.8**. Sample G37.

Due to the fact that Mn was not available in the PHELIX beamline preparation chamber, 0.2 ML of Fe was used for further deposition of TM on the surface of the sample. Again, an increase in background noise and a wider opening of the SS band gap was observed (**Figure 5.27 (c)**).

The recorded band structure consists of both bulk and surface states or so-called precursor states **[200, 203]**, despite a band gap opening. The nature of the states was studied by varying the incident photon energy from 66 eV to 74 eV, as presented in **Figure 5.28 (a)-(i)**.
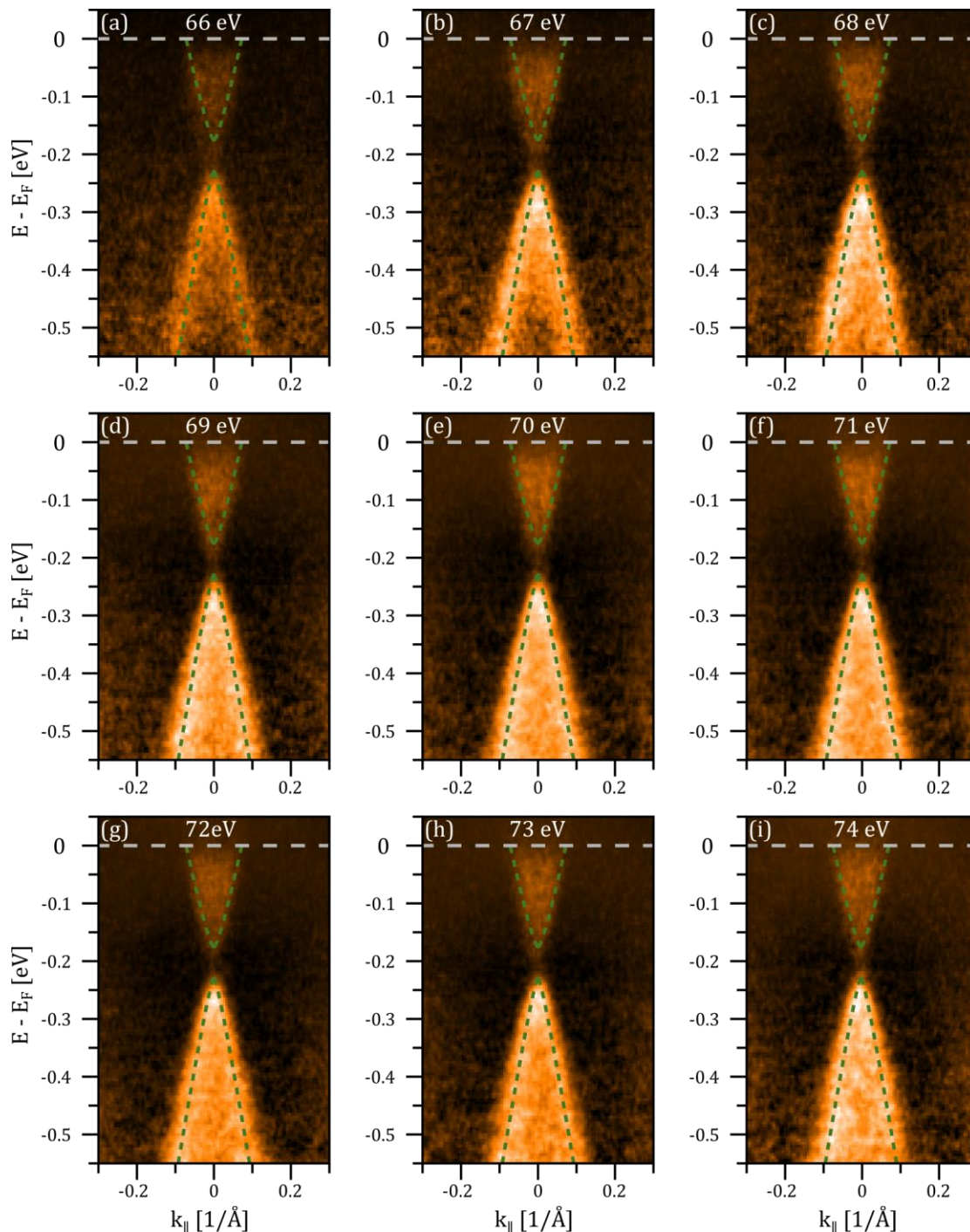
Figure 5.28: Photon energy dependence of Pb$_{0.75}$Sn$_{0.26}$Se with a total of 0.6 ML TM (0.4 ML Mn + 0.2 ML Fe) deposited on the surface. All measurements were taken at 200 K. Green dashed line is a guideline of the surface states; it is the same for every spectrum presented. Strong background noise is removed for all spectra. The spectra are shown with a linear colour scale. Sample G37.

This type of measurement allows scanning through the 3DBZ, along the k_z wave vector component normal to the sample surface. In the case of bulk states, band dispersion is observed. The surface states positions are insensitive to the change of the incident photon energy, and thus no band dispersion should be observed. Indeed, the spectra in **Figure 5.28 (a)** to **(i)** show a very similar band structure. The green dashed line was used as an eye guideline for the SS. Parameters for the equation used for band structure fitting (for details see **Section 3.8.3**) are the same for every spectra. This proves the surface nature of the states, for which spin polarization was measured.

In order to obtain more information about the band structure and better visualise the ARPES spectra, in **Figure 5.29 (a)** and **(b)** the same spectra as in **Figure 5.26 (c)** (with different pseudo-colour maps applied) are shown before and after background noise removal, respectively. Background noise is removed for some of the presented spectra for the purpose of better visualisation of the band structure. The removal procedure employs tools available in Igor Pro software, namely the "ImageRemoveBackground" procedure that removes a general background level, described by a polynomial of a specified order **[136]**. Degree 3 polynomial was used for all presented spectra with the background removed. The appearance, and the increase, with further Fe deposition (**Figure 5.26** and **Figure 5.27**), of the background noise corroborate the conclusion of TM adsorbate forming in disordered state on the surface of the film, as stated in **Section 4.2.4 Deposition of TM**.
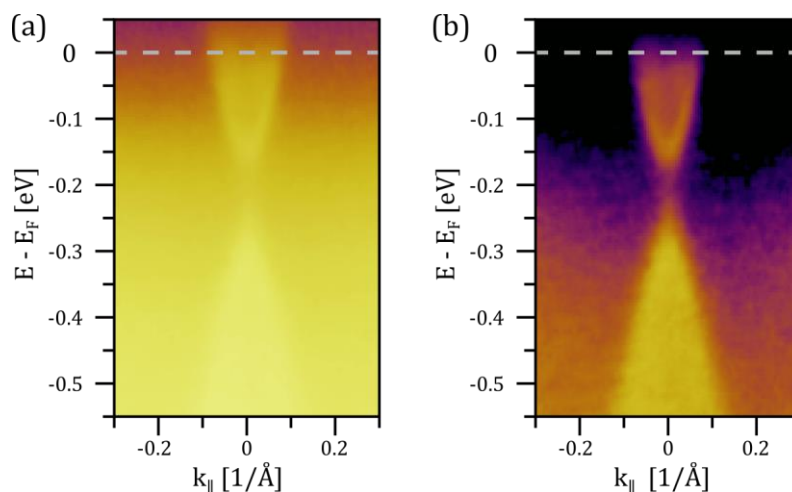
Figure 5.29: **Background noise subtraction in the ARPES spectra of Pb$_{0.7}$Sn$_{0.3}$Se at 200 K with 0.45 Å deposited on the surface. (a)** raw ARPES spectra. **(b)** ARPES spectra with background noise subtracted. The spectra are shown with a logarithmic colour scale, with the same colour map and intensity range applied. Sample G36.

5.3.5   Gap opening induced by TM deposition

The deposition of magnetic atoms on the surface of the TCI may lead to a gap opening due to the breaking of time reversal or mirror symmetries **[100, 176, 204]**, or the creation of a 2D ferromagnetic state **[148, 205]**. Of these two, the creation of a 2D ferromagnetic state is ruled out, as it would require the E_F to be in the band gap, which is not the case in the samples studied. The magnetic origin of the gap opening, which relates to the arrangement of the magnetic moments, would require some critical temperature, below which the gap would always remain open. Another possible explanation is the change of the band inversion point or resonant doping **[206]**.

Temperature-dependent ARPES measurements, presented in **Figure 5.30**, were conducted to establish the origin of the TCI SS gap opening caused by TM deposition. The sample of choice was $Pb_{0.76}Sn_{0.24}Se$ with 0.3 ML Fe deposited on the surface. According to the semi-empirical Preier's relation **[68]** and band gap dependence on the composition of $Pb_{1-x}Sn_xSe$ (see **Figure 2.8**) the topological transition point for a pristine epilayer of this composition is at 254.5 K, that is, below this temperature the SS band gap should be closed.
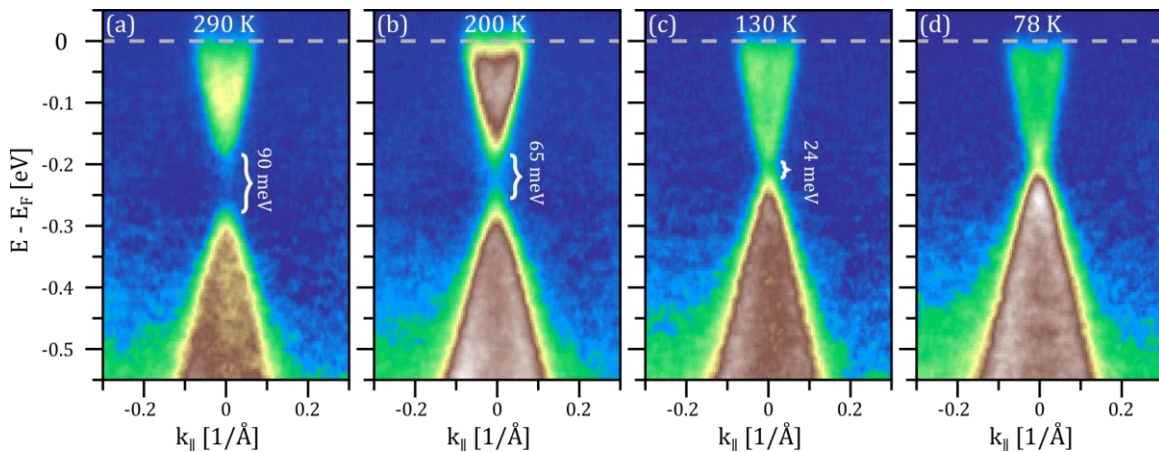
Figure 5.30: Temperature-dependent electronic structure of $Pb_{0.75}Sn_{0.25}Se$ with 0.3 ML of Fe deposited on the surface. $E(k_\parallel)$ spectra taken with a photon energy of 70 eV near the $\bar{\Gamma}$ point. The spectra are shown with a linear colour scale. Image from Ref. **[15]**. Sample G35.

In **Figure 5.30 (b)**, spectrum taken at 200 K is presented. It shows a band gap of 65 meV. With decreasing temperature, the gap gradually closes. At 130 K it reaches 24 meV and at 78 K no gap is observed, **Figure 5.30 (c)** and **(d)**, respectively. This proves that a constant gap was not observed when the temperature was decreased. Instead, the band gap closing point was reached. This rules out the scenario in which the gap would have a magnetic origin. The resonant doping origin of the gap is also excluded, as in this case the gap should also be temperature independent **[206]**.

The opening of the gap in $Pb_{1-x}Sn_xSe$ in the TCI phase by the deposition of TM must therefore have another reason. It is well known that in this system the band gap is composition and

temperature dependent **[67, 68]** (see **Figure 2.8**). Considering this fact, it is reasonable to assert that with the deposition of TM on the surface, the composition-dependent band inversion point changes. Indeed, when the band gap data extracted from **Figure 5.30** are compared with the band gap temperature dependence calculated according to Preier's relation **[68]** and the magneto-optic experiments in Ref. **[147]** it reproduces the band gap energy (E_g) dependence of $Pb_{1-x}Sn_xSe$ with Sn content of 17.5% (**Figure 5.31**). TM deposition seems to change the surface composition of the epilayers and shift it toward a trivial phase by reducing the percentage content of Sn on the surface. TM deposition may be considered as a way of changing surface composition, as the used TM are relatively light elements, and decrease in spin-orbit strength is expected.
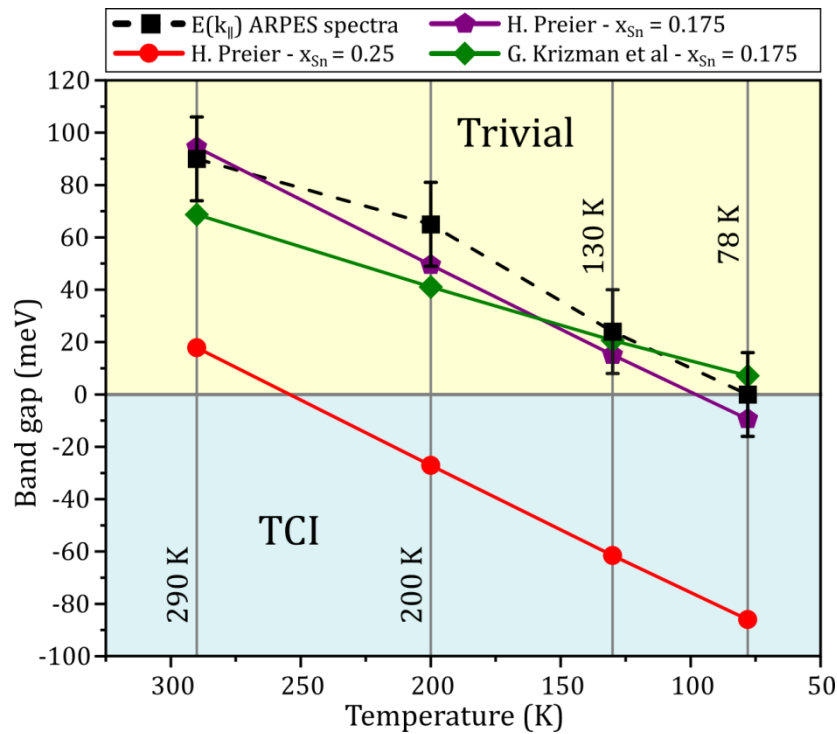
Figure 5.31: Temperature and Sn content dependent band gap energy in $Pb_{1-x}Sn_xSe$. Comparison between E_g extracted from **Figure 5.30** for $x_{Sn} = 0.25$ with 0.3 ML of Fe deposited (black dashed curve) and E_g calculated following Ref. **[68]** for $x_{Sn} = 0.25$ (red line), for $x_{Sn} = 0.175$ (purple line) and following Ref. **[147]** for $x_{Sn} = 0.175$ (green line). Image from Ref. **[15]**.

5.3.6 Summary

The electronic and spin texture of high quality $Pb_{1-x}Sn_xSe$ epilayers grown on (111) BaF_2 was investigated. It was shown that helical spin-polarization of the surface states exists in samples of both topological and trivial phases and has the same order of magnitude. To date, little research has been done to study the spin texture of topological insulators in both the TI and NI phases **[8, 200, 203]** and no such research has been done for (111) $Pb_{1-x}Sn_xSe$. Therefore, the reported results deepen the understanding of the spin structure of $Pb_{1-x}Sn_xSe$ across the topological transition.

The deposition of TM on the surface of (111) $Pb_{1-x}Sn_xSe$ revealed the opening of the band gap, forcing the TCI-NI transition. Reasoning was given to support the conclusion that band opening comes from a change in surface composition and not due to ferromagnetism or crystal symmetry breaking. Demonstrated modification of the band structure at the interface between TCI and TM is an important factor that needs to be considered when designing functional spintronic devices incorporating TCI and TM-based magnetic materials. The results obtained demonstrate an additional method of inducing TCI-NI transition in TCI.

5.4   ARPES measurements of α-Sn epilayers

The inverted band ordering at Γ point of 3DBZ in the unstrained α-Sn allows for nontrivial topology properties of this material. The degeneracy of the light and heavy holes bands **[84]** at the Γ point is a consequence of the cubic symmetry of the diamond structure **[89]**. If this symmetry is broken by external strains, as was done here, the effect is either energy gap opening **[89]** or valence and conduction bands crossing **[87]**. A detailed description of these effects is given in **Section 2.2.2 α-Sn**. The employed compressive in-plane strain results in the formation of Dirac semimetal (DSM) phase in grey tin with two bulk 3D Dirac cones formed near the band touching points along Γ-Z direction perpendicular to (001) surface (**Figure 5.32 (a)**). This direction is $k_\perp$ in terms of ARPES measurement. **Figure 5.32 (b)** shows schematic of bands in direction laying in plane of the (001) surface, along $k_\parallel$ in terms of ARPES measurement, which is the direction of the carried out measurements. A band structure similar to that obtained in ARPES measurements of in-plane strained α-Sn grown on InSb **[207, 208]** is expected. **Figure 5.32 (c)** shows the 3D and (001) 2D Brillouin zones in this system. Red colour denotes high-symmetry points of interest, namely bulk Γ and Z, and $\bar{\Gamma}$ and $\bar{X}$, defining direction of band structures presented in images (a) and (b), respectively.
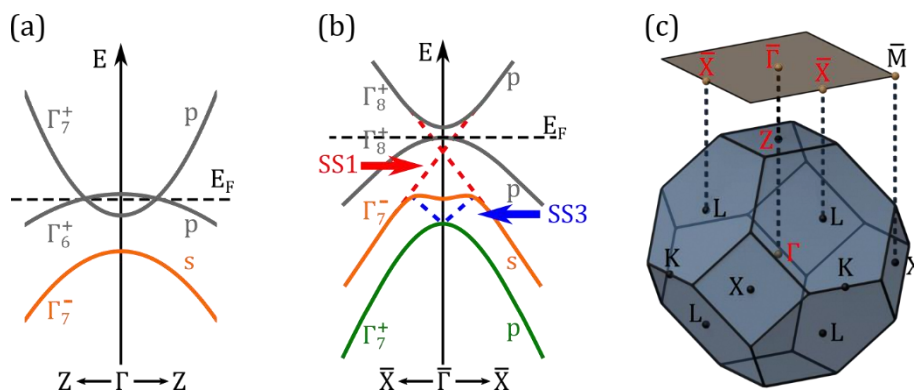
Figure 5.32: Schematic electronic structure and Brillouin zone of α-Sn in the DSM phase. (a) Schematic of the band structure of α-Sn near Γ point along $Z - \Gamma - Z$ direction perpendicular to the (001) surface. **(b)** Schematic of the band structure of α-Sn near $\bar{\Gamma}$ point along $\bar{X} - \bar{\Gamma} - \bar{X}$ direction. **(c)** 3D and 2D (001) Brillouin zones with high-symmetry points labelled. Schematic (a) based on Refs. **[84, 87]**, schematic (b) based on Refs. **[207, 208]**. For the correlation between Γ_8^+ band and Γ_7^+ and Γ_6^+ bands, see **Section 2.2.2**

The DSM phase in α-Sn can further transform to the Weyl semimetal (WSM) phase by application of external magnetic field that breaks the time reversal symmetry **[84]**. Breaking of this symmetry leads to the splitting of each of the DC into a pair of Weyl cones. Considering all of the above, grey tin is a very interesting system that allows study of different topological phases. The goal of the research presented in this chapter was to study by ARPES the DSM phase of α-Sn grown on a (001) CdTe/GaAs hybrid substrate. To date, ARPES studies of α-Sn were carried out only for grey tin grown on InSb **[209-211]** and not on relaxed CdTe buffer. The results obtained broaden the general understanding of the electronic structure of α-Sn in the DMS phase.

The results shown in this subchapter were presented online in a poster titled *Growth of Gray Tin epilayers on insulating (001)-CdTe/GaAs substrates and its Angular Resolved Photoemission Spectroscopy studies* during the 49th International School & Conference on the Physics of Semiconductors "Jaszowiec 2021". The measurements were done by V. V. Volobuev, R. Rudniewski, and me at the SOLAIRS Synchrotron URANOS (former UARPES) end-station in Kraków. The samples have been delivered to the synchrotron facility in a UHV suitcase. Experiments were performed with photon energies ranging from 16 eV to 120 eV. If not stated otherwise, the measurements were carried out at RT. Details about the sample studied are given in **Table 5.10**.

Table 5.10: Discussed α-Sn/CdTe (001) epilayers studied at the URANOS beamline.

name	code	phase	Thickness [nm]	Studied by
V9	GM2_220920A	α-Sn	46	ARPES, CL
V10	GM2_240920A	α-Sn	34	ARPES, CL
V11	GM2_240920B	α-Sn	150	ARPES, CL, E_{ph}, 3D maps
V12	GM2_260920A	α-Sn	100	ARPES, 3D maps

5.4.1 Effect of α-Sn thickness on the band structure

ARPES measurements of four 30-200 nm thick (001) α-Sn/CdTe samples are presented in **Figure 5.33**. The same band structure is observed regardless of the thickness of the epilayer, which confirms the presence of only one topological phase near the surface in this thickness range. Core level spectroscopy measured for the samples shown in **Figure 5.33**, presented in **Figure 5.34**, proves that all of the detected states come from Sn, as only two peaks coming from the $4d_{3/2}$ and $4d_{5/2}$ levels are visible. Additional Te $4d_{3/2}$ and $4d_{5/2}$ levels, originating from the CdTe buffer, are detected for the thinnest 34 nm and 46 nm epilayers (**Figure 5.34 (c)**). Cadmium 4d peaks, with smaller intensity than Te 4d peaks, would be expected close to binding energy 10 eV **[212]**, but are not detected. It was reported in Ref. **[208]** that Te is visible in the CL of α-Sn grown on (001) InSb with a Te buffer layer added before Sn growth. Tellurium acts as a surfactant **[213]** and is present on the top of the thinner films.
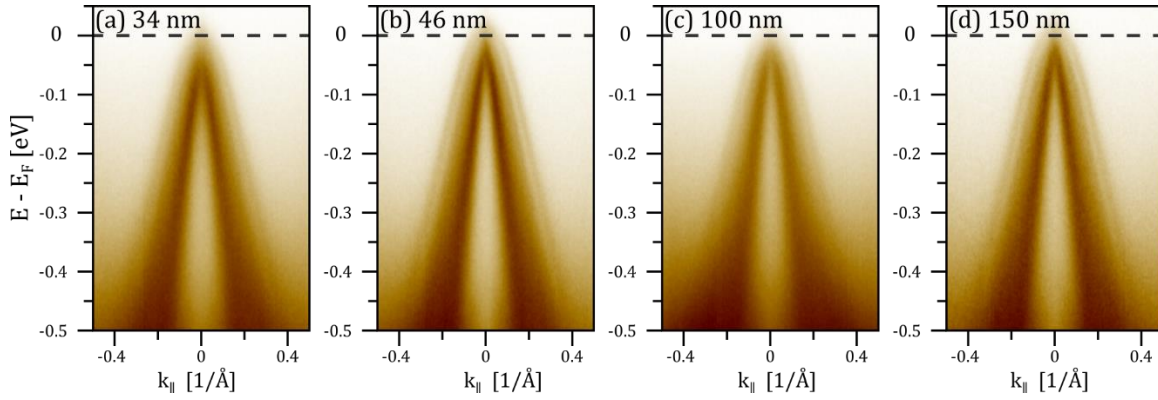
Figure 5.33: α-Sn ARPES spectra near the $\bar{\Gamma}$ point for 34 nm, 46 nm, 100 nm and 150 nm, (a) to (d) respectively. (a), (b) and (d) spectra taken at RT with the photon energy of 20 eV. (c) Spectrum taken at 210 K with the photon energy of 18 eV. Samples V10, V9, V12 and V11, respectively.
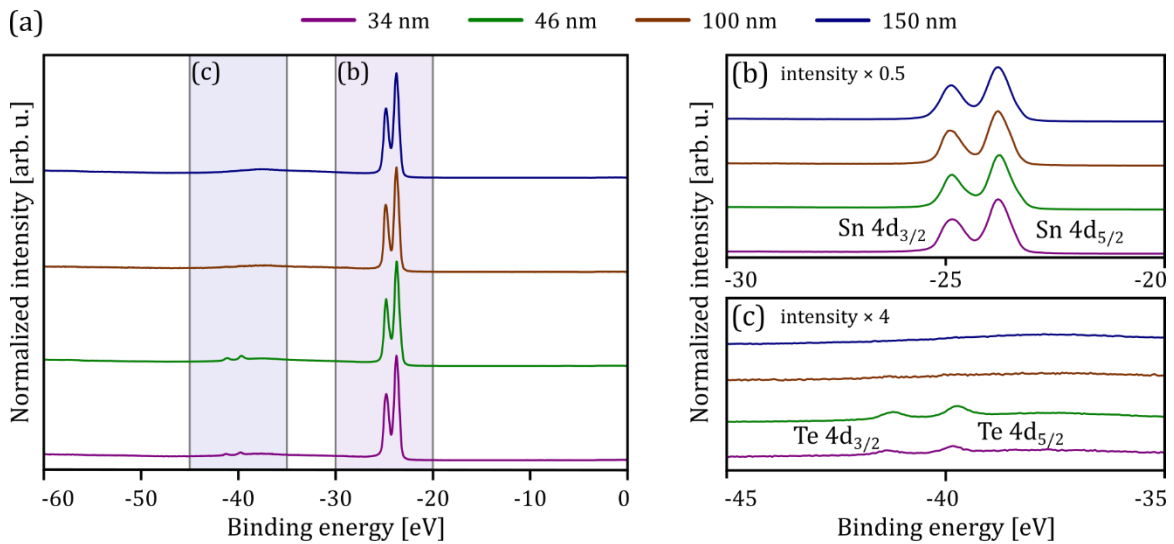
Figure 5.34: Core levels spectra of α-Sn thin epilayers with varying thickness obtained with the photon energy of 90 eV. 100 nm spectrum (brown) measurement taken at 80 K. **(a)** full range measurement. **(b)** -20 eV to -30 eV zoom-in to Sn peaks. **(c)** -35 eV to -45 eV zoom-in to Te peaks present for very thin epilayers.

5.4.2   Band structure of α-Sn in DSM phase

The most important bands near the $\bar{\Gamma}$ point along $\bar{\Gamma} - \bar{X}$ direction (see **Figure 5.32**) are presented in **Figure 5.35** for three values of the exciting photon energies. The most pronounced spectral weight in the spectrum is marked in black, and the locations of other bands that are present are marked in red. In **Figure 5.35 (a)**, at 18 eV two different surface states (SS) are visible: SS1 are more pronounced, whereas SS2 have smaller intensity. In between these two there are heavy hole (HH) broad bulk states, best visible at 26 eV in **Figure 5.35 (b)**. SS1 and SS2 are not visible in this spectrum due to overlap with the intense broad bulk band. At 90 eV, **Figure 5.35 (c)**, SS2 are the most pronounced, while SS1 and HH have a lower spectral weight. At this photon energy, the bulk s-band becomes visible and is

separated in energy from the HH band by 0.40 ± 0.02 eV at $k_\parallel = 0$. This value is consistent with reported infrared ellipsometry **[214]** and magnetooptics measurements **[13]** **Figure 5.35 (e-g)** shows spectra from **Figure 5.35 (a-c)** with the 2D curvature method applied **[134, 137]** and overlapped with the original image to better visualise and reveal all the bands present. In **Figure 5.36 (a)**, the 3D ARPES map of a 150 nm sample (V11) is presented. Cuts along $\bar{\Gamma} - \bar{X}$ and $\bar{\Gamma} - \bar{M}$ directions clearly reveal both SS1 and SS2, together with the bulk HH states. Full cuts along both directions are presented in images **(b)** and **(c)**. The anisotropic dispersion of the SS2 and HH states is consistent with the ARPES studies of α-Sn/InSb (001) **[208, 210]**. The anisotropic character of SS2 and HH, and the isotropic character of SS1 are more clearly visible in constant energy contours (CEC) shown in **Figure 5.37**. The longer energy range ARPES image, presented in **Figure 5.38**, reveals presence of SS3 and Γ_7^+ states (p) deeper in VB (see **Figure 5.32 (b)**). They were reported in compressively strained (001) α-Sn/InSb **[207, 210]**. The distance between the p and HH bands obtained from ARPES is a subject to bigger measurement error due to the broad character of the p band at $k_\parallel = 0$ and is determined as 0.66 ± 0.20 eV, which differs significantly form ellipsometry and magnetooptics measurements **[13]**.
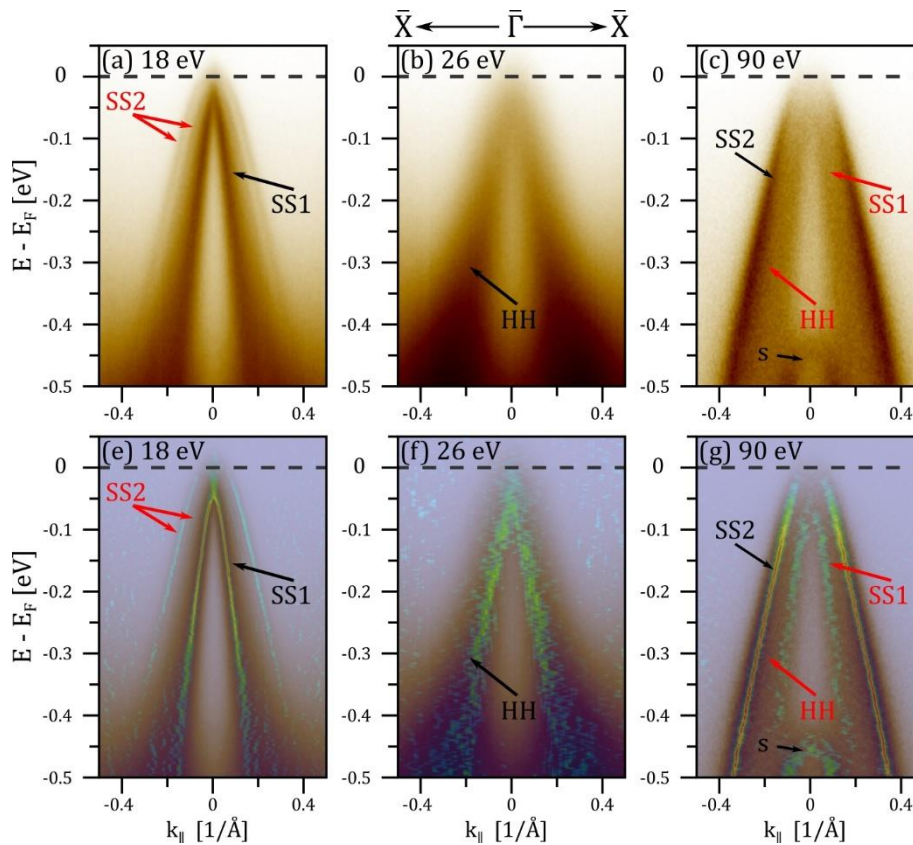
Figure 5.35: Band structure of α-Sn near $\bar{\Gamma}$ point along $\bar{\Gamma} - \bar{X}$ direction with surface states (SS), heavy holes (HH) and s band (s) marked. Measurements taken with the photon energy of **(a)** 18 eV **(b)** 26 eV and **(c)** 90 eV. **(e-g)** spectra from (a-c) with their curvature **[134, 137]** overlapped for a more precise visualisation of the band structure. Sample V11.
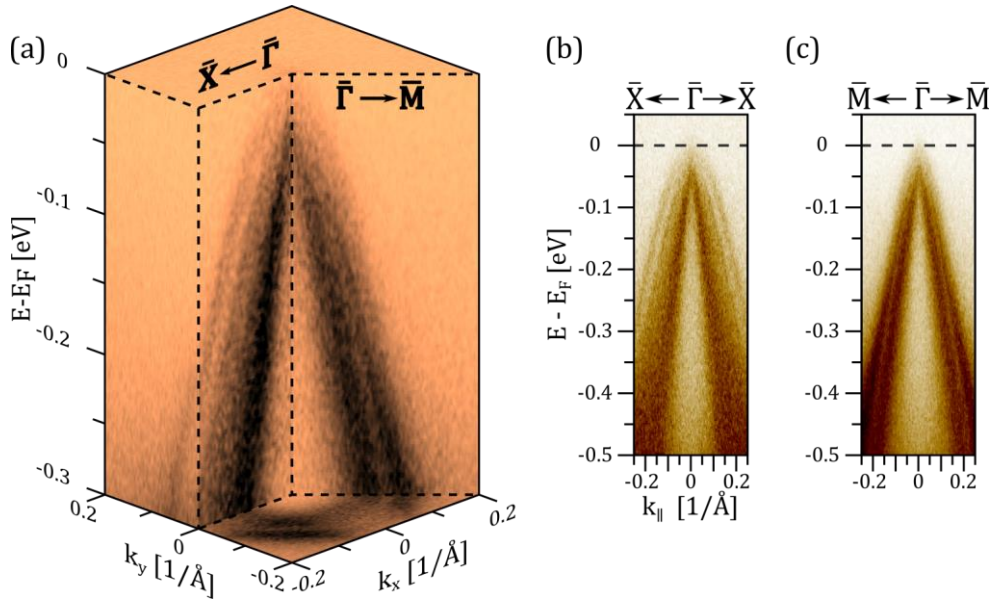
Figure 5.36: α-Sn $\bar{\Gamma} - \bar{X}$ and $\bar{\Gamma} - \bar{M}$ ARPES cuts near $\bar{\Gamma}$ point. (a) ARPES 3D map. **(b)** ARPES image along $\bar{\Gamma} - \bar{X}$ direction. **(c)** ARPES image along $\bar{\Gamma} - \bar{M}$ direction. Measurements taken with photon energy of 20 eV for 150 nm thick epilayer. Data extracted from the 3D map are presented in **Figure 5.37**, with different colour map applied. Initial data handling with procedures written for the IGOR Pro 8 software by M. Rosmus (SOLARIS, URANOS). Data analysis and presentation by B. Turowski. Sample V11.
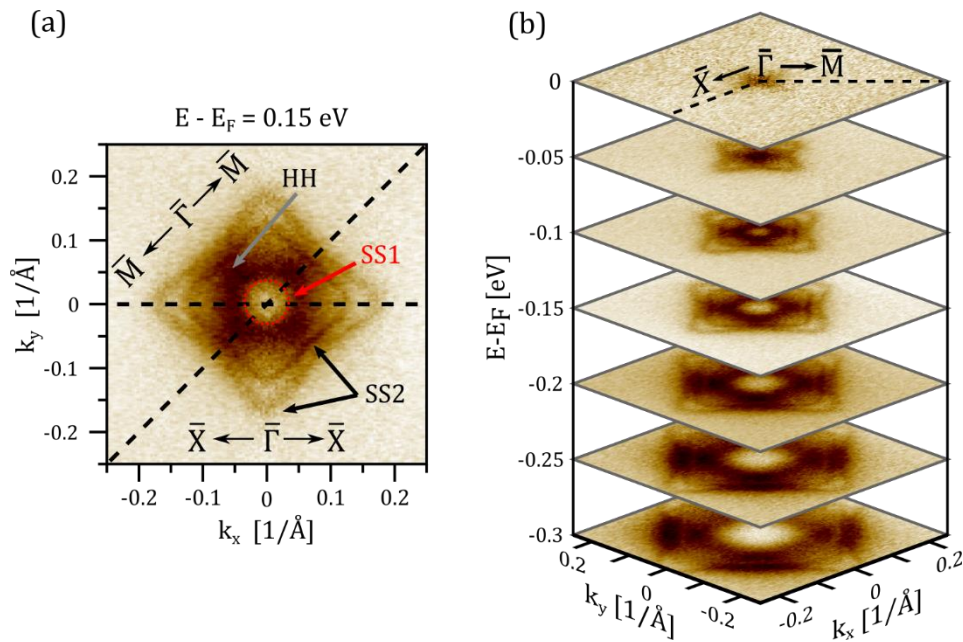
Figure 5.37: Constant energy contours (CECs) of α-Sn near $\bar{\Gamma}$ point. (a) CEC for E - E$_F$ = -0.15 eV, with direction of $\bar{\Gamma} - \bar{X}$ and $\bar{\Gamma} - \bar{M}$ cuts marked with black dashed lines, and the SS1, SS2, and HH bands labelled. **(b)** constant energy surface map (extracted from the 3D map presented in **Figure 5.36 (a)**) of 150 nm thick epilayer. Measurements taken with the photon energy of 20 eV. Initial data handling with procedures for 3D maps written for the IGOR Pro 8 software by M. Rosmus (SOLARIS, URANOS). Data analysis and presentation by B. Turowski. Sample V11.
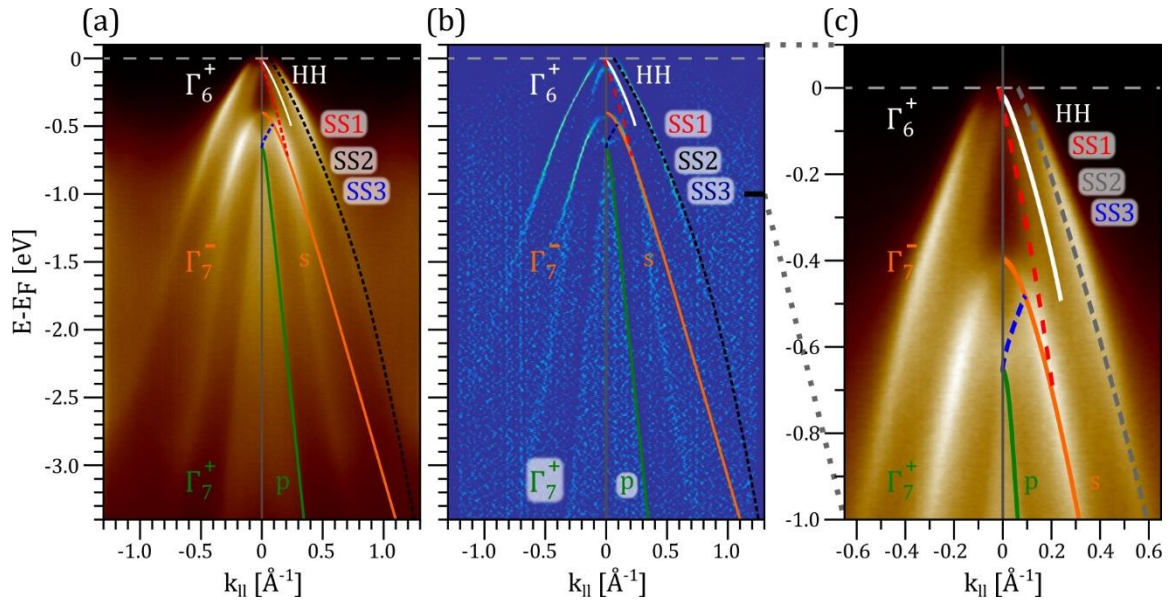
Figure 5.38: Deeper band structure of α-Sn near the $\bar{\Gamma}$ along $\bar{\Gamma} - \bar{X}$ direction. (a) Wide energy range ARPES spectrum. **(b)** Curvature 2D of (a). **(c)** Zoom in of (a) to narrower energy and momentum range. The colours used for the bands guidelines correspond to those in **Figure 5.32 (b)**. Sample V9.

DSM phase in previously studied α-Sn grown on InSb is caused by relatively large tetragonal distortions **[208, 210, 215]**. Similar distortions, equal to $\varepsilon_t = \varepsilon_\perp - \varepsilon_\parallel = 0.26\%$ (see **Table 4.9**), coming from a lattice mismatch between grey tin and CdTe buffer (see **Section 4.4.2** for details) are present in α-Sn presented here. Varying the incident photon energy should result in dispersion of the bulk HH states. In order to verify that, photon energy dependence measurements on sample V11 were carried out (**Figure 5.39**). The energy dispersion curve (EDC) profiles extracted at $k_\parallel = 0$ (**Figure 5.40**) indeed show a weak dispersion. Another possible reason for the dispersion in the spectra shown in **Figure 5.40** can be the suppression of SS2 because of the change of the matrix element **[188]**, which, in the case of a one-electron approximation, depends on the momentum of the exciting photon and affects visibility of the bands in the ARPES spectrum. Detailed explanations of the matrix element in ARPES are given in Ref. **[216]** and, more generally, in Ref. **[217]**. However, the presence of SS1, SS2, and SS3 as well as the point-like Fermi surface (**Figure 5.37 (b)**) were theoretically predicted **[84, 87, 207, 214]** for the DMS phase. The presence of these features in the presented ARPES spectra demonstrates that the DSM phase is present in the studied (001) α-Sn/CdTe/GaAs heterostructures. This interpretation is strongly supported by theoretical calculations of the model that accurately determine the band structure of α-Sn DSM, as well as by magneto-optical measurements **[13]** performed on (001) α-Sn/CdTe/GaAs.
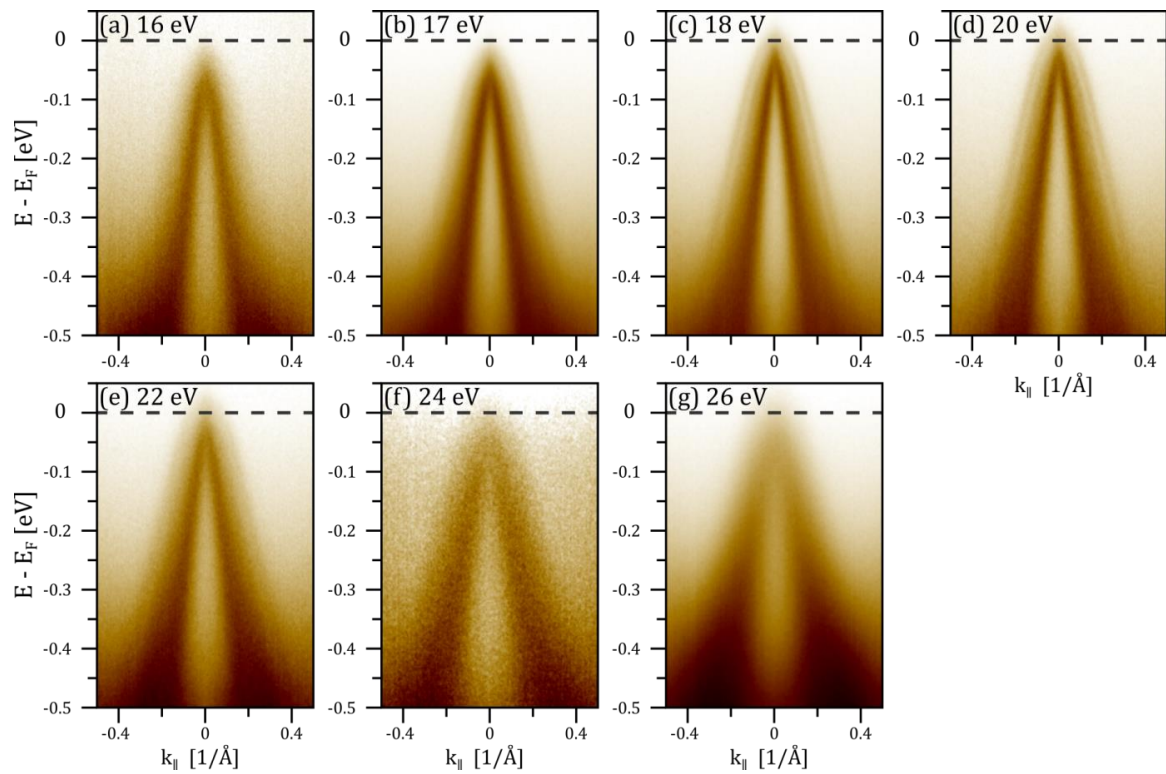
Figure 5.39: Photon energy dependence of 150 nm thick α-Sn epilayer. With increasing photon energy **(a)** to **(g)** the main features of the spectra do not change and a weak dispersion with change of the photon energy is observed. Sample V11.
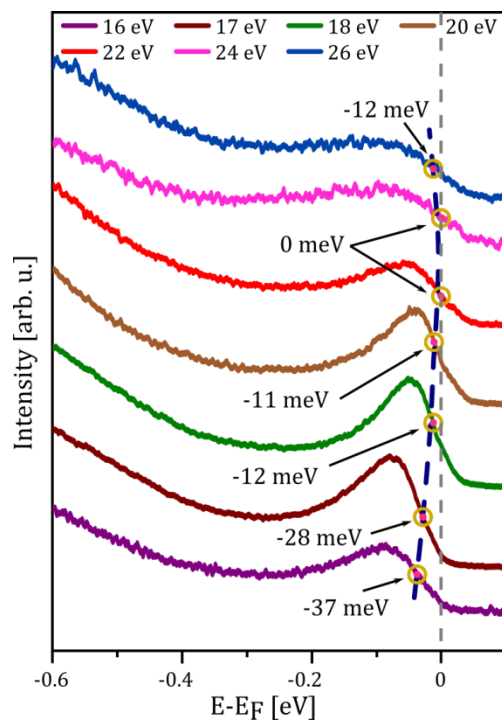
Figure 5.40: Energy dispersion curve profiles of α-Sn ARPES spectra presented in **Figure 5.39** extracted at normal emission ($k_\parallel = 0$). A weak dispersion with change of the photon energy is observed. Sample V11.

5.4.3   New type of surface states in strained α-Sn

The grey tin in the DSM phase hosts three different types of surface states: SS1, SS2, and SS3 (see **Figure 5.38**). Band inversion between Γ_8^+ and Γ_7^-, and Γ_7^- and Γ_7^+ gives rise to SS1 and SS3 (see **Figure 5.32 (b)**), respectively **[207]**. SS1 were reported to have a helical spin texture in SR-ARPES measurements **[218]**, proving their topological nature. On the other hand, the presence of SS2 in the α-Sn DSM phase has only recently been experimentally shown **[210]** and was attributed to the Rashba effect that results from the breaking of the inversion symmetry on the surface. This finding is disputed in Ref. **[13]**, as no beating pattern in Shubnikov–de Haas (SdH) oscillations in magnetotransport measurements was detected, which would be a signature of Rashba splitting. Another possible explanation for the presence of SS2 are the topologically trivial massive surface states (Volkov-Pankratov (VP) or Dyakonov-Khaetski (DK) states) theoretically predicted **[219, 220]** at the interface of a normal insulator and a Luttinger semimetal **[85, 86]**, such as α-Sn or HgTe, near touching point of the CB and VB. VP or DK states were recently predicted **[85, 221]** in strained Luttinger semimetals, and VP states were demonstrated in HgTe **[222]** and PbSnSe **[223]** by transport experiments and magneto-optical spectroscopy, respectively. Conducted ARPES measurements, backed by recent developments in the field of Luttinger semimetals, support the conclusion that SS2 can indeed be massive DK or VP states.

5.4.4   Summary

The electronic structure of high quality α-Sn/CdTe/GaAs (001) heterostructures was investigated. To date, no ARPES research of strained α-Sn grown on insulating hybrid CdTe/GaAs (001) substrates has been reported in the literature. The results presented in this chapter broaden the understanding of the band structure of grey tin by providing ARPES spectra of α-Sn grown on the substrate that is insulating and does not lead to any parallel conductance in magnetotransport studies. This in turn allows for comprehensive studies with the use of a number of various techniques on the same structures, which was not previously possible.

The band structure obtained from ARPES agrees with reports for strained α-Sn grown on InSb (001) **[207, 210, 215]**. The presence of previously reported **[207]** surface states (SS1 and SS3) was confirmed and a new explanation for the existence of recently experimentally revealed **[210]** SS2 in the DSM phase of α-Sn was proposed based on recent studies of Luttinger semimetals **[85, 221-223]** and performed magnetotransport measurements **[13]**.

Chapter 6

Conclusions

In this thesis, two main goals were achieved:

1) The growth technology of thin and ultra-thin $Pb_{1-x}Sn_xSe$ topological crystalline insulator (TCI) and compressively strained α-Sn epilayers has been developed in a newly installed molecular beam epitaxy (MBE) at IF PAN, and high-quality epilayers of this type have been successfully grown by MBE.
2) The band structure and the spin texture of $Pb_{1-x}Sn_xSe$ with and without a submonolayer amount of TM deposited on the surface of the epilayer, as well as the band structure of compressively strained α-Sn have been studied using Angle-Resolved Photoelectron Spectroscopy (ARPES) and spin-resolved ARPES (SR-ARPES) to examine the behaviour of the gapless surface states under external perturbation.

Conclusions and Summary

I presented the developed MBE growth process of $Pb_{1-x}Sn_xSe$ on (001)-oriented KCl and (111)-oriented BaF_2. The 1 μm thick (111)-oriented films were grown using elemental and stoichiometric compound sources. The AFM and XRD characterisation methods were used to show that both types of sources can be used to grow high quality $Pb_{1-x}Sn_xSe$ thin films. This proves that elemental sources, which are of higher purity, can be successfully used to grow nanostructures with better control of carrier concentration in the IV-IV TCI. I also presented the developed procedure for growth of ultra-thin (less than 120 nm) $Pb_{1-x}Sn_xSe$ epilayers, which differs from the standard MBE growth of thin films. Furthermore, I presented the developed process for the growth of grey tin thin films on hybrid CdTe/GaAs (001) substrates, which allows for a comprehensive study of the α-Sn with different techniques taking advantage of the insulating character of the substrate. The growth of $Pb_{1-x}Sn_xSe$ with compound sources, as well as the growth of α-Sn epilayers was carried out in a new MBE system. I was involved in the launch and upgrades of the GM#2 system and worked on the development of growth processes that yield high-quality epilayers. In addition, I wrote a Python script that facilitates the analysis of RHEED patterns. The script uses open source modules (the code is attached in the Appendices), which makes it possible to deploy it on any computer. With minimal adjustments, the programme can be applied to other materials and is not limited to the analysis of the RHEED patterns of $Pb_{1-x}Sn_xSe$ and α-Sn.

In the scope of this thesis, ARPES and spin resolved APRES (SR-ARPES) measurements were performed during four beamtimes, focused on the band structure of $Pb_{1-x}Sn_xSe$, the band structure of α-Sn and the spin texture of $Pb_{1-x}Sn_xSe$.

First, the theoretical prediction of band gap opening of the surface states caused by the magnetic impurity (Fe and Mn transition metals (TM) were used) on the surface of the TCI was tested experimentally. No band gap opening of the magnetic origin was observed, neither on (001) nor on (111) surfaces of $Pb_{1-x}Sn_xSe$ TCI. It was shown that deposition of TM on the surface of $Pb_{1-x}Sn_xSe$ leads to a change in the separation of the double Dirac cones (DC) near $\overline{X}$ surface point, in the case of (001)-oriented epilayers, which was attributed to a change in the surface composition of the sample toward more trivial. In the case of (111)-oriented epilayers, deposition of TM on the surface of thin films resulted in the emergence of momentum-splitted, concentrically arranged states in the conduction band attributed to Rashba splitting, with the value of the Rashba parameter close to the values observed in materials with giant Rashba splitting. The above experiments motivated theoretical calculations of the Rashba splitting effect in $Pb_{1-x}Sn_xSe$. The first ARPES studies were carried out almost exclusively at a temperature of 80 K or lower. These temperatures are below the characteristic temperature of the topological transition for $Pb_{1-x}Sn_xSe$, with x_{Sn} in the range of 20% to 30%.

Next, the spin texture of (111) $Pb_{1-x}Sn_xSe$ in both the TCI and normal insulator (NI) phases was reported and published for the first time **[15]**, as a result of SR-ARPES measurements carried out as a part of this dissertation. It was shown that helical spin-polarization of the surface states, with the same order of magnitude, exists in both the TCI and the NI phases. Additional ARPES studies of the deposition of TM on the surface of (111) $Pb_{1-x}Sn_xSe$ revealed the opening of the surface states band gap, which forces the TCI-NI transition. The band gap opening was attributed to a change in surface composition, and reasoning was given to exclude ferromagnetism or crystal symmetry breaking as a source of this effect. It also demonstrated an additional method of inducing the TCI-NI transition in TCI and provided information about the modification of the band structure at the interface between TCI and TM, which needs to be taken into account when designing functional spintronic devices incorporating TCI and TM-based magnetic materials. Temperature dependent ARPES measurements of $Pb_{1-x}Sn_xSe$ near the temperature of topological transition were performed to complement previous ARPES study at lower temperatures, below the topological transition temperature. Because of that, the gap opening due to TM deposition and subsequent surface composition change could be observed. These studies support earlier conclusions of non-magnetic origin of the surface states gap opening.

Surprisingly, Rashba splitting was not observed in ARPES spectra gathered during spin-resolved measurements. Apparently, the splitting was so small that it could not have been resolved by ARPES, but the detection of the splitting with spin was possible. In addition, the photoemission intensity of surface states is influenced by matrix element effects, which cause

oscillations of their intensity when the energy of the exciting photons is varied. These effects can reduce the visibility of the split surface states. Initial ARPES measurements were performed with exciting photon energy of 18 eV, while spin-resolved measurements were performed with exciting photon energy of 70 eV, due to the available energy range of the SR-ARPES beamline starting at 50 eV.

Finally, for the first time ARPES study of compressively strained α-Sn grown on insulating CdTe/GaAs (001) hybrid substrates was presented. The results obtained complement the understanding of the band structure of grey tin. The presence of bulk and surface states previously reported in compressively strained α-Sn grown on (001) InSb was confirmed. Furthermore, a new explanation for the existence of recently experimentally revealed surface states was proposed – the Dyakonov-Khaetski states. The explanation was based on recent studies of Luttinger semimetals and performed magnetotransport measurements **[13]**. The results presented prove the presence of DSM phase in strained α-Sn grown on hybrid (001) CdTe/GaAs substrates and were part of a larger comprehensive study of the α-Sn, the results of which were submitted for publication **[13]**.

Open questions

The research provided a new way to induce the surface states gap opening in $Pb_{1-x}Sn_xSe$ TCI by changing the surface composition, but did not confirm the theoretically predicted opening of the gap due to surface ferromagnetism. Verification of the latter effect would require growth of $Pb_{1-x}Sn_xSe$ with fine-tuning of the Fermi energy close to DP. To this end, the developed growth technology using elemental sources **[100]** might provide possible way of accomplishing such $Pb_{1-x}Sn_xSe$ epilayers.

APRES measurements of the TCI / TM interface at higher temperatures, close to the temperature of the topological transition, could provide information on the interplay of the Rashba effect and surface states band gap opening due to a change in the surface composition.

Combined ARPES and SR-ARPES measurements carried out with lower photon energies could provide more detailed information on spin polarization and Rashba splitting. During the ARPES studies, it was established that an exciting photon energy of 18 eV provides the best quality ARPES spectra of $Pb_{1-x}Sn_xSe$. This energy is available at the URANOS beamline in SOLARIS, and the installation of spin filters in this system (scheduled for 2023) could provide such an opportunity.

Impact

This thesis provides evidence that both elemental and stoichiometric compound sources can be used for the MBE growth of high quality $Pb_{1-x}Sn_xSe$ thin films, as demonstrated by the results published in Ref. **[100]** and Ref. **[15]**, respectively.

The developed Python RHEED script can be used for pattern simulation that can complement the analysis of real patterns, recorded during the growth, with commercial software such as the kSA 400 analytical RHEED system, available in the GM#1 and GM#2 MBE systems. The script can also be used for educational purposes, and in the future could be expanded to include Kikuchi line patterns, which would greatly increase its usefulness. The use of the Python programming language combined with the use of open-source modules makes it accessible to everyone.

The thesis presents important information on the band structure and spin texture of $Pb_{1-x}Sn_xSe$ and the band structure of α-Sn. The results obtained have been published **[15, 100]** or submitted for publication **[13]** in high impact journals. Some of the results presented are currently being processed for publication **[14]**. Understanding the band structure of the materials discussed provides crucial knowledge that can be applied in the design and manufacture of functional spintronic and electronic devices.

As part of this thesis, growth technology of topological materials in a new MBE system was developed, which can be used in future studies of topological matter.

Appendices

Appendix A   Measurement setups

URANOS beamline

The Ultra Resolved ANgular phOtoelectron Spectroscopy beamline (URANOS, former UARPES) in SOLARIS National Synchrotron Radiation Centre is an installation for the experimental studies of the electronic structure of the solid surfaces by Angle-Resolved PhotoElectron Spectroscopy (ARPES). It was used to obtain band structure of (001) and (111) oriented $Pb_{1-x}Sn_xSe$ and (001) oriented compressively strained α-Sn. **Appendix Figures A.1** and **A.2** show photos and layout of the beamline.
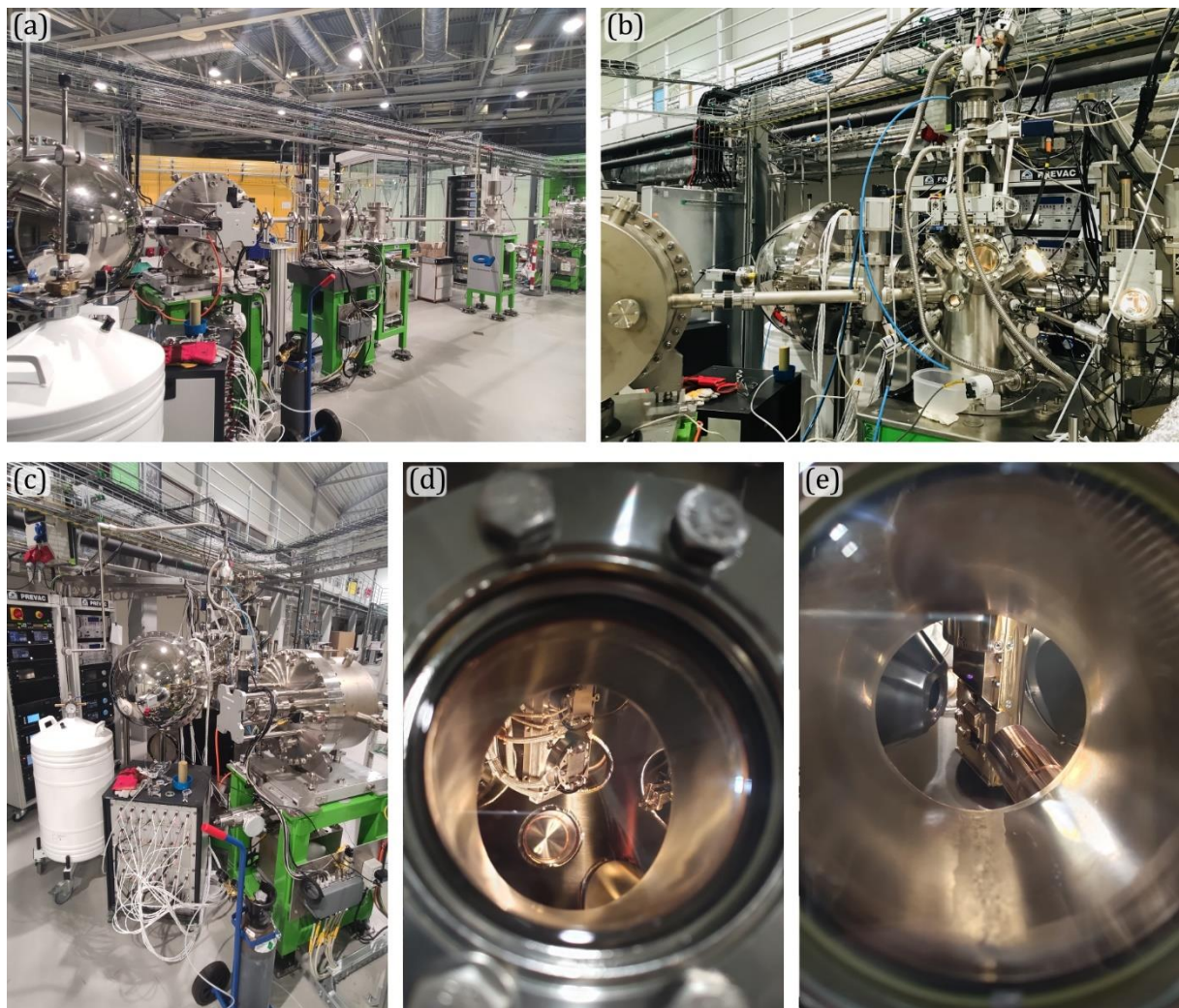
Appendix Figure A.1: Photos of the URANOS beamline. (a) Beamline. **(b)** and **(c)** End-station. **(d)** Sample stage in the Preparation Chamber. **(e)** Sample stage in the Analysis Chamber. Photos by M. Zięba and A. Wadge.
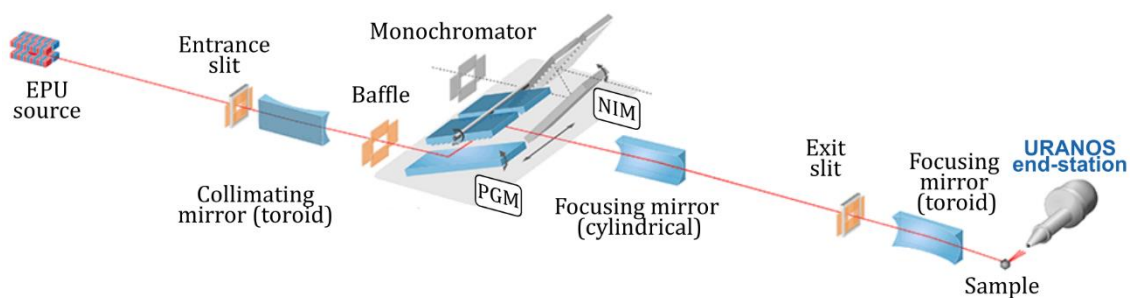
Appendix Figure A.2: URANOS beamline layout.
Image from https://synchrotron.uj.edu.pl/en_GB/linie-badawcze/uranos

Detailed information about the URANOS beamline can be found at:
https://synchrotron.uj.edu.pl/en_GB/linie-badawcze/uranos

PHELIX beamline

The PHELIX beamline in SOLARIS National Synchrotron Radiation Centre is an installation that enables experimental studies of the electronic structure of the solid surfaces by ARPES and spin-resolved ARPES, in addition to other types of measurements in the soft X-ray range. **Appendix Figures A.3** and **A.4** show layout, photos and the top view of the beamline.

Detailed information about the PHELIX beamline can be found at:
https://synchrotron.uj.edu.pl/en_GB/linie-badawcze/phelix
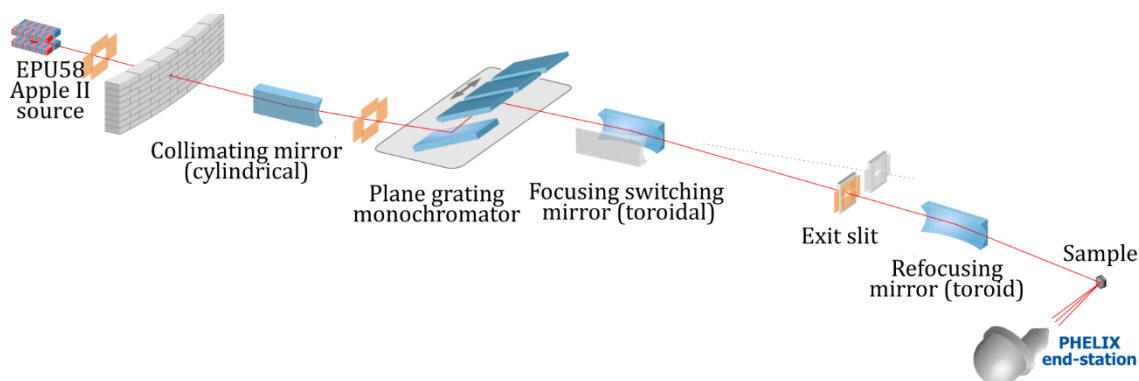
Appendix Figure A.3: PHELIX beamline layout.
Image from https://synchrotron.uj.edu.pl/en_GB/linie-badawcze/phelix
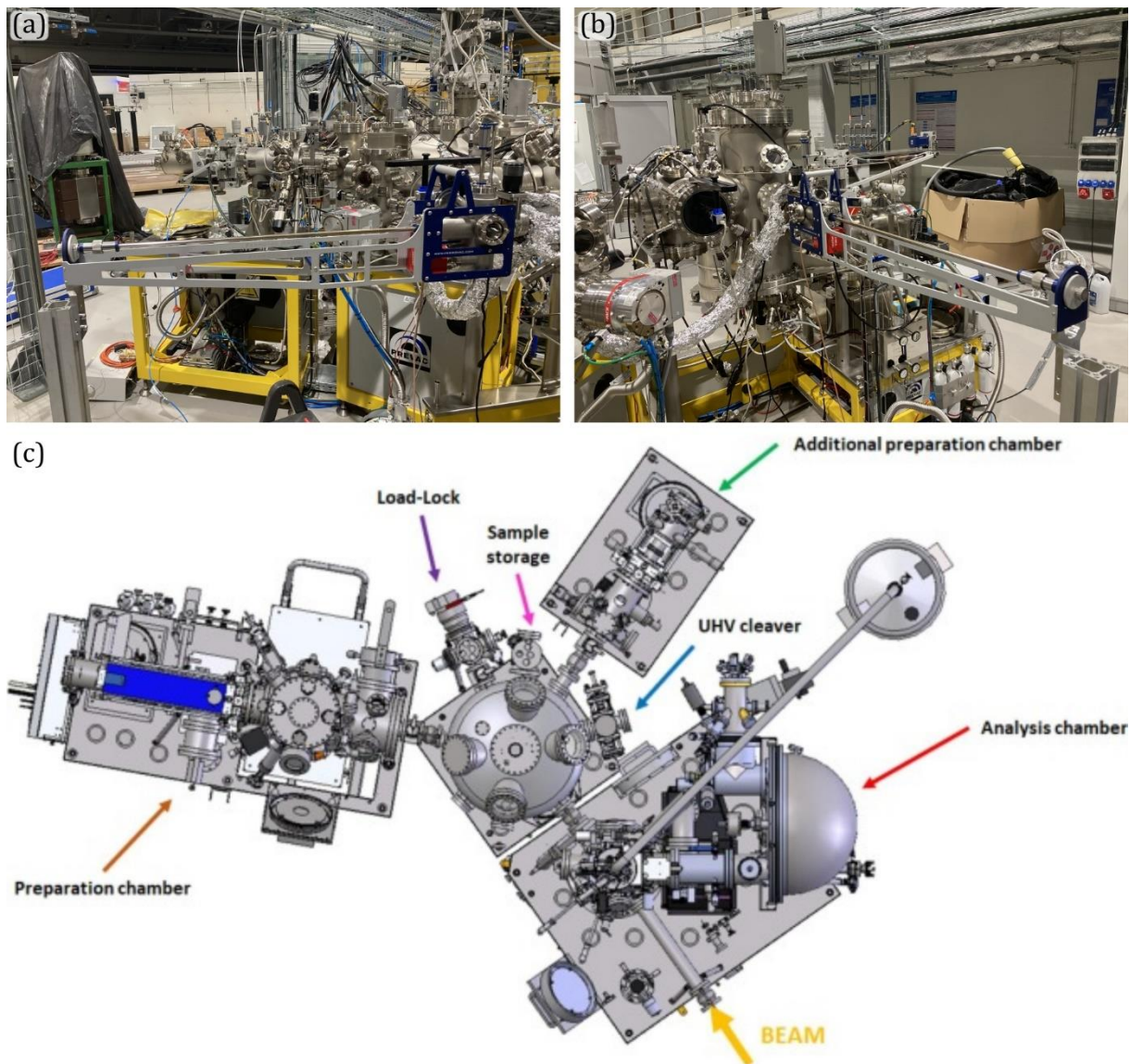
Appendix Figure A.4: PHELIX beamline. (a) Photo of the main part of the end station. **(b)** Photo of the Preparation chamber, with UHV suitcase attached. **(c)** Top view of the PHELIX end station model from Ref. **[128]**.

Appendix B

List of studied samples

Below, tables with samples relevant for this thesis are presented. I assisted the growth of the samples listed in **Appendix Table B.1** and grew the samples listed in **Appendix Table B.2** and **Appendix Table B.3**. The samples listed in **Appendix Table B.1**, **Appendix Table B.4** and **Appendix Table B.5** were grown dr by V. V. Volobuev.

The sample codes of the listed samples should be interpreted as follows: the first letter (P or G) denotes the PREVAC or GM#2 MBE chamber. Next, the date of the growth is given in US date format i.e. mmddyy. The following letter denotes if multiple samples were grown that day (A - first, B - second and so on). Due to the change in naming convention, some of the early GM#2 samples have names starting with "GM2_" followed by date of growth in ddmmyy format.

Appendix Table B.1: List of $Pb_{1-x}Sn_xSe$ samples grown in PREVAC 190 MBE system.

name	code	substrate	Sn content [%]	Thickness	Growth T [℃]	Studied by	Comments
P1	P121517B	BaF_2	19	1 μm	325	AFM, SEM	-
P2	P121617B	BaF_2	22	1 μm	325	AFM	-
P3	P011118A	BaF_2	24	50 nm	250	XRD	-
P4	P011118B	BaF_2	32	50 nm	250	AFM	-
P5	P011118C	BaF_2	16	50 nm	250	XRD	-
P6	P011218B	BaF_2	9	50 nm	250	XRD	-
P7	P032918B	BaF_2	19	1 μm	363	AFM	Se decap

Appendix Table B.2: List of $Pb_{1-x}Sn_xSe$ samples, thicker than 250 nm, grown in Veeco GENxplor GM#2 MBE system. (c) stands for cleaved and (p) for polished substrate.

name	code	substrate	Sn content [%]	Thickness	Growth T [℃]	Studied by	Bi [%]
G1	GM2_120220B	BaF_2	0	1 μm	340	XRD	-
G2	GM2_250220B	BaF_2	34	1 μm	340	AFM, XRD, EDS	-
G3	GM2_070920A	BaF_2	26	1 μm	355	ARPES, CL	0.06
G4	GM2_110920A	BaF_2	30	1 μm	330	ARPES	0.03
G5	GM2_140920A	BaF_2	30	1 μm	340	ARPES, CL	0.09
G6	G072621A	BaF_2	24	2.5 μm	350	XRD	-
G7	G100321B	BaF_2	31	1 μm	350	SR	0.08
G8	G102021A	BaF_2	0	1 μm	350	-	0.016
G9	G102121A	BaF_2	25	1 μm	365	XRD	0.067

G10	G102521A	BaF$_2$	10	1 µm	350	XRD	0.08
G11	G102621A	BaF$_2$	31	1 µm	350	XRD, RHEED	0.08
G12	G102821A	BaF$_2$	15	1 µm	360	XRD	0.08
G13	G102921A	BaF$_2$	0	260 nm	345	RHEED	-
G14	G110221A	BaF$_2$	0	1 µm	382	not measured	-
G15	G110321A	BaF$_2$	24	1 µm + 250nm	335	SR, Fe	0.068
G16	G110321B	BaF$_2$	31	1 µm	375	ARPES, SR	0.064
G17	G110421A	BaF$_2$	14	1 µm + 250nm	320	RHEED	0.082
G18	G110421B	BaF$_2$	10	1 µm	317	not measured	0.082
G19	G110821A	BaF$_2$	14	1 µm + 250nm	320	ARPES, Mn	0.078
G20	G110821B	BaF$_2$	24	1 µm + 250nm	325	RHEED	0.068
G21	G110921A	BaF$_2$	31	1 µm	330	SR	0.06
G22	G120621A	BaF$_2$	10	1 µm	370	not measured	0.082
G23	G120621B	G110421B	11	250 nm	317	see G110421B	0.082
G24	G120721A	G110321B	31	250 nm	336	see G110321B	0.064
G25	G120721B	G110921A	31	250 nm	300	see G110921A	0.066
G26	G120721C	G110221A	0	250 nm	340	see G110221A	0.098
G27	G120821A	BaF$_2$	31	1 µm	330	not measured	0.064
G28	G120921A	BaF$_2$	24	1 µm	370	SR (vs Fe)	0.072
G29	G011222B	BaF$_2$	23	1 µm	370	not measured	0.071
G30	G011222C	BaF$_2$	31	1 µm	370	not measured	0.061
G31	G011322A	BaF$_2$	12	1 µm	370	ARPES/SR, RHEED	0.079
G32	G011322B	BaF$_2$	30	1 µm	365		0.1
G33	G011422A	BaF$_2$	11	1 µm	366	not measured	0.132
G34	G011422B	BaF$_2$	15	1 µm	334	ARPES/SR	0.079
G35	G011522A	BaF$_2$	24	1 µm	342	ARPES/SR	0.066
G36	G011522B	BaF$_2$	30	1 µm	342	ARPES/SR	0.1
G37	G011522C	BaF$_2$	26	1 µm	340	ARPES/SR	0.069
G38	G042022A	G102021A	0	1 µm	160/350	XRD	-
G39	G070822Ap	BaF$_2$ (p)	27	1 µm	342	AFM	-
G40	G070822Ac	BaF$_2$ (c)	27	1 µm	342	AFM	-
G41	G092922A	BaF$_2$	27	1 µm	375	RHEED oscillations (Mn)	-
G42	G102622A	G092922A	28	10×10nm	353-96	RHEED oscillations	-

Appendix Table B.3: List of Pb$_{1-x}$Sn$_x$Se samples, thinner than 150 nm, grown in Veeco GENxplor GM#2 MBE system. (c) stands for cleaved and (p) for polished substrate.

name	code	substrate	Sn content [%]	Thickness	Growth T [°C]	Annealing T [°C]	Comments
G42	GM2_260220A	BaF2	30	50 nm	205	350	-
G43	GM2_120321A	BaF2	21	50 nm	180	340	-
G44	GM2_120321B	BaF2	31	50 nm	205	345	-
G45	GM2_120321C	BaF2	9	50 nm	185	340	-
G46	G121021A	BaF2 (c)	26	30 nm	200	380	-
G47	G071522A	BaF2 (c&p)	26	120 nm	360	-	100 nm Se

G48	G071822A	BaF2 (c&p)	26	80 nm	215	380	100 nm Se
G49	G072022A	BaF2 (c&p)	25	40 nm	225	390	100 nm Se
G50	G072522A	BaF2 (c&p)	25	20 nm	210	380	100 nm Se
G51	G072822A	BaF2 (c&p)	27	30 nm	205	380	100 nm Se
G52	G072922A	BaF2 (p)	27	-	295/335		Se removal
G53	G080222A	BaF2 (c)	27	60 nm	210	370	100 nm Se

Appendix Table B.4: List of Sn samples grown on hybrid (001) CdTe/GaAs substrate in Veeco GENxplor GM#1 and GM#2 MBE systems.

name	code	epilayer	Thickness [nm]	Growth T [°C]	Studied by/Comments
V1	GM2_290320A	α-Sn	50	5	XRD
V2	GM2_290320C	β-Sn	50	5	XRD
V3	GM2_200420A	α-Sn	30	5	XRD (fringes), RHEED
V4	GM2_130720A	α-Sn	150	0	-
V5	GM2_310820A	likely β-Sn	130	0	milky surface
V6	GM2_040920A	α-Sn	150	0	ARPES, CL
V7	GM2_060920A	α-Sn	150	0	ARPES not measured
V8	GM2_180920A	α-Sn	150	0	ARPES, CL
V9	GM2_220920A	α-Sn	46	0	ARPES, CL
V10	GM2_240920A	α-Sn	34	0	ARPES, CL
V11	GM2_240920B	α-Sn	150	0	ARPES, CL, Eph, 3D maps
V12	GM2_260920A	α-Sn	100	0	ARPES, 3D maps
V13	GM2_180221A	α-Sn	150	0	XRD (wide range)
V14	G061521A	α-Sn	50	0	AFM
V15	V020221B	CdTe	5000	300	AFM

Appendix Table B.5: List of Pb$_{1-x}$Sn$_x$Se samples from Riber 1000 system, studied by ARPES.

name	code	substrate	Sn content [%]	Thickness [μm]	Studied by	Comments
R1	MBE_3431B	KCl	26	1	ARPES, Mn deposition	Decap Se 15min at 330 ℃
R2	MBE_3440A	BaF2	30	1	ARPES, Mn deposition	Decap Se 10/15/15min 200/330/330 ℃
R3	MBE_3440B	BaF2	30	1	ARPES, Mn deposition	Decap Se 10/15/15min 200/330/330 ℃
R4	MBE_3426A	BaF2	25	1	ARPES, Fe deposition	Decap Se 15min at 330 ℃
R5	MBE_3426B	BaF2	25	1	ARPES, Fe deposition	Decap Se 15min at 330 ℃

Appendix C

RHEED patterns simulation script

Below code of RHEED patterns simulation Pyhon script is provided. This code was used to generate images of simulated RHEED patterns in this thesis. To run this code Python environment must be installed, as well as numpy, mathplotlib, and sympy modules must be installed. The script was written with Python 3.10. Comments provide instruction on how to run the script. The general flow of the script is as follows: an array of atoms is generated using a user-defined set of basis vectors. Based on this, the reciprocal space array is calculated. Each point of the calculated array corresponds to a top view of an infinite reciprocal space rod perpendicular to the surface of the material. At this point azimuthal rotation defined by a `theha_deg` angle is performed. A 2D Gaussian function (with user-defined broadening) is used at each point of the reciprocal space array to simulate finite thickness of the rods. The intensity of the points depends on the structure factor of the atoms. The resulting 2D image is a sum of the Gaussians at positions of reciprocal space rods. This image (called RLRP, reciprocal lattice rods projection, in the script) is then subjected to the transformation given by system of **Equations (3.5)** and **(3.6)**. In essence, this transformation is a geometrical transformation of 2D x, y image through a 3D sphere to a 2D x, z image. Generated RHEED image is then displayed and saved.

The code of the script is available at: https://github.com/turobart/RHEED-patterns.git

```python
import numpy as np
import matplotlib.pyplot as plt
import math
import sympy as sym
from sympy.utilities.lambdify import lambdify
import time

start_time = time.time()
# variables of the material
xSn = 0.3
# latticeConstant = (6.1240-xSn*0.1246) #in the given direction
latticeConstant = 6.490 #aSn
theta_deg = 0.
theta = np.deg2rad(theta_deg)

# broadening of the streaks to produce realistic RHEED image
sigma_x=0.1
sigma_y=0.1/3*2

# variables of the system
d = 32 #distance between sample and RHEED screen in cm. 32 cm in GM#2 VEECO GENxplor
MBE System
incAngle = np.deg2rad(3.2) # angle of incidence of the electron beam. Typical range:
2-5 degree
acceleratingV = 15000 #accelerating voltage of the electron beam source. Typical range
10,000-15,000 V
```

```python
electronWavelength = 12.247/math.sqrt(acceleratingV*(1+acceleratingV*0.000001))
k0=2*math.pi/electronWavelength # radius of the Ewald sphere

sampling_size = 500 # 500 is suggested for initial imageing; more than 1500 is
suggested for fine images

# size of G reciprocal array
N=10.
M=6.
# creation of the array of atoms
nv=(np.arange(-N,N+1))
mv=(np.arange(-N,M+1))

radius_shift = math.cos(incAngle)*k0 # shift of the Ewald sphere in the reciprocal
space

RotMatrix = np.array([[math.cos(theta), -math.sin(theta)], [math.sin(theta),
math.cos(theta)]])
# boundaries of the k-space calculations.
# calculated using
# x = k0*4//math.sqrt(d**2+4**2); y = k0*(-d/math.sqrt(d**2+5**2)+math.cos(incAngle))
# 4 and 5 correspond to the dimensions of the real RHEED screen
kxmin, kxmax =  -8, 8
kymin, kymax =  radius_shift-k0, 1.25

def defineLattice(latticeA1, latticeA2, latticeUnitCellFactor):
    latticeA1 = (latticeA1)*latticeConstant*latticeUnitCellFactor
    latticeA2 = (latticeA2)*latticeConstant*latticeUnitCellFactor

    # calculation of the reciprocal space distances
    latticeB1 = ((2*math.pi/np.cross(latticeA1, latticeA2))*np.array([latticeA2[1], -
latticeA2[0]])).round(5)
    latticeB2 = ((2*math.pi/np.cross(latticeA1, latticeA2))*np.array([-latticeA1[1],
latticeA1[0]])).round(5)

    # creation of the reciprocal space array
    latticeGxp=np.array([[i*latticeB1[0]+j*latticeB2[0] for i in nv] for j in
mv]).round(4)
    latticeGyp=np.array([[i*latticeB1[1]+j*latticeB2[1] for i in nv] for j in
mv]).round(4)

    electron_scattering_factor=[1,1] # array of the electron scattering factors. Must
have lengh of aM.
    atomPosition=[0,1] # array of the relative atoms positions in the unit cell. Must
have lengh of aM.
    aM=2

    # generation of grid for image calculation
    kx = np.linspace(kxmin, kxmax, sampling_size)
    ky = np.linspace(kymin, kymax, sampling_size)
    xx, yy = np.meshgrid(kx, ky)
    # rotation
    xxRot, yyRot = np.einsum('ij, mni -> jmn', RotMatrix, np.dstack([xx, yy]))

    # generation of the reciprocal lattice rods projected on 2D surface
    RLRP = np.zeros((sampling_size, sampling_size))
    for h in range(len(mv)):
        for k in range(len(nv)):
            structureFactor = sum((electron_scattering_factor[aM-
1]*np.exp(((latticeGxp[h][k]+latticeGyp[h][k])*atomPosition[aM-1])*1j)) for i in
range(1, aM + 1))
```

```python
            DiffIntensity = np.square(np.absolute(structureFactor))
            RLRP += DiffIntensity*np.exp(-((xxRot-latticeGxp[h][k])**2/(sigma_x**2) +
(yyRot-latticeGyp[h][k])**2/(sigma_y**2)))

    return RLRP

def calculateRHEEDarray(RLRP):
    x,y, xe, ye = sym.symbols('x,y, xe, ye', positive = True)
    dd, kk, aa = sym.symbols('dd kk aa', positive = True)

    kx_c = np.linspace(kxmin, kxmax, sampling_size, dtype=complex)
    ky_c = np.linspace(kymin, kymax, sampling_size, dtype=complex)
    xx, yy = (np.meshgrid(kx_c, ky_c))

#     # solution calculation with sympy
#     # ----------
#     Eq1 = sym.Eq(kk*x/sym.sqrt(dd**2+x**2+y**2), xe)
#     Eq2 = sym.Eq(kk*(-dd/sym.sqrt(dd**2+x**2+y**2)+sym.cos(aa)), ye)
#     sol = sym.solve([Eq1,Eq2],(x,y))
#     return sol
    # ----------
    eqs = (-sym.sqrt(dd**2*xe**2)/(kk*sym.cos(aa) - ye),
dd*sym.sqrt(kk**2*sym.sin(aa)**2 + 2*kk*ye*sym.cos(aa) - xe**2 -
ye**2)/(kk*sym.cos(aa) - ye))
    values = {kk: k0, dd: d, aa: incAngle}
    solsol = sym.Tuple(eqs).subs(values).simplify()

    func = lambdify((xe,ye), solsol,'numpy') # numpy-ready function for array
calculations

    numpy_array_of_results = np.real((func(xx, yy)))

    # generate RHEED image
    plot_name = 'Angle_%.2f' %theta_deg
    plot_numpy = plt.figure(plot_name)
    plt.axes().set_aspect('equal')
    plt.pcolormesh(numpy_array_of_results[0][0], numpy_array_of_results[0][1], RLRP,
cmap='gray')
    plt.ylim(0, 5) # in cm, should correspond to real size of RHEED screen
    plt.xlim(-4, 4) # in cm, should correspond to real size of RHEED screen
    # image saving
    if theta_deg%1>0:
        fig_name = 'Angle_%.2f' %theta_deg
        fig_name += '.png'
        print(fig_name)
    else:
        fig_name = 'Angle_%d' %theta_deg +'.png'
    plot_numpy.savefig(fig_name, bbox_inches='tight',transparent=True,format='png')

# definition of the basis vectors; uncomment as needed
#growth direction (111)
a11 = np.array([math.sqrt(3)/2, -1/2])
a12 = np.array([0., 1.])
# a21 = np.array([math.sqrt(3)/2, -1/2])
# a22 = np.array([0., 1.])
#growth direction (001)
# a11 = np.array([2., 0.])
# a12 = np.array([0., 1.])
# a21 = np.array([1., 0.])
# a22 = np.array([0., 2.])

# calculation of atoms distances in topmost layer
```

```python
UnitCellFactor = math.sqrt(2)/2 # used to take into account the distribution of atoms
on the topmost layer.
                                # Derived from geometrical properties of the unit cell
and desired growth orientation

RLRP1 = defineLattice(a11, a12, UnitCellFactor)
# RLRP2 = defineLattice(a21, a22, UnitCellFactor)

RLRP = RLRP1# + RLRP2

RLRP = RLRP /np.max(RLRP)
RLRP = np.array(RLRP * 255, dtype = np.uint8)

calculateRHEEDarray(RLRP)
print("--- %s seconds ---" % (time.time() - start_time))
plt.show()
```

Technical scripts

Parameters monitor script for GM#1 and GM#2:

(Python)

– Monitoring of flow and temperature of water in water enclosures of the effusion cells;
– Monitoring of turbo pumps parameters;
– Monitoring of cryo pumps temperature;
– Data logging and graph display of all monitored parameters.

Server deployed on Raspberry Pi computer:

(HTML, CSS, JavaScript, php, SQL and Python)

– Automatic and remote control over flow of liquid nitrogen to GM#1 and GM#2;
– SMS notifications in the case of the predefined emergency;
– Remote control of GM#1 RHEED shutter;
– Light control in the laboratory

I wrote both front-end (visual part) and back-end (communications, data transfer).

Portable temperature logging device, based on Raspberry Pi, for Edwards Cryo-Torr Cryopumps.

(Python)

– Data logging of the temperature;
– Remote access in local network.

Igor and Python **scripts for data analysis**:

The scrips are available at https://github.com/turobart/IgorPro-tools-ARPES.git

– plot 3D cube maps from 3D ARPES data;
– dynamically fit the band structure of the studied materials;
– generate spin polarization graphs form raw experimental data.

List of figures and tables

List of Figures

List of Tables

Bibliography

[1]   M. König, S. Wiedmann, C. Brüne, A. Roth, H. Buhmann, L.W. Molenkamp, X.-L. Qi, and S.-C. Zhang, ***Quantum Spin Hall Insulator State in HgTe Quantum Wells.*** Science **318**, 5851 (2007), https://doi.org/10.1126/science.1148047. **p. 1, 6, 7, 77**

[2]   B.A. Bernevig, C. Felser, and H. Beidenkopf, ***Progress and prospects in magnetic topological materials.*** Nature **603**, 7899 (2022), https://doi.org/10.1038/s41586-021-04105-x. **1**

[3]   J. Liu, T.H. Hsieh, P. Wei, W. Duan, J. Moodera, and L. Fu, ***Spin-filtered edge states with an electrically tunable gap in a two-dimensional topological crystalline insulator***. Nature Materials **13**, 2 (2014), https://doi.org/10.1038/nmat3828. **p. 1, 84**

[4]   Q.L. He, T.L. Hughes, N.P. Armitage, Y. Tokura, and K.L. Wang, ***Topological spintronics and magnetoelectronics.*** Nature Materials **21**, 1 (2022), https://doi.org/10.1038/s41563-021-01138-5. **p. 1**

[5]   J. Han and L. Liu, ***Topological insulators for efficient spin–orbit torques.*** APL Materials **9**, 6 (2021), https://doi.org/10.1063/5.0048619. **p. 1, 104**

[6]   R. Dey, A. Roy, L.F. Register, and S.K. Banerjee, ***Recent progress on measurement of spin–charge interconversion in topological insulators using ferromagnetic resonance***. APL Materials **9**, 6 (2021), https://doi.org/10.1063/5.0049887. **p. 1**

[7]   D.L. Mitchell and R.F. Wallis, ***Theoretical Energy-Band Parameters for the Lead Salts.*** Physical Review **151**, 2 (1966), https://doi.org/10.1103/PhysRev.151.581. **p. 1**

[8]   B.M. Wojek, R. Buczko, S. Safaei, P. Dziawa, B.J. Kowalski, M.H. Berntsen, T. Balasubramanian, M. Leandersson, A. Szczerbakow, P. Kacman, T. Story, and O. Tjernberg, ***Spin-polarized (001) surface states of the topological crystalline insulator $Pb_{0.73}Sn_{0.27}Se$.*** Physical Review B **87**, 11 (2013), https://doi.org/10.1103/PhysRevB.87.115106. **p. 1, 84, 104, 106, 107, 115**

[9]   P.S. Mandal, G. Springholz, V.V. Volobuev, O. Caha, A. Varykhalov, E. Golias, G. Bauer, O. Rader, and J. Sánchez-Barriga, ***Topological quantum phase transition from mirror to time reversal symmetry protected topological insulator.*** Nature Communications **8**, 1 (2017), https://doi.org/10.1038/s41467-017-01204-0. **p. 1, 15, 16, 19, 88, 104**

[10]   P. Dziawa, B.J. Kowalski, K. Dybko, R. Buczko, A. Szczerbakow, M. Szot, E. Łusakowska, T. Balasubramanian, B.M. Wojek, M.H. Berntsen, O. Tjernberg, and T. Story, ***Topological crystalline insulator states in $Pb_{1-x}Sn_xSe$.*** Nature Materials **11**, 12 (2012), https://doi.org/10.1038/nmat3449. **p. 1, 13, 15, 51, 83, 84, 104**

[11]   Z. Xiao, J. Wang, X. Liu, B.A. Assaf, and D. Burghoff, ***Optical-Pump Terahertz-Probe Spectroscopy of the Topological Crystalline Insulator Pb1−xSnxSe through the Topological Phase Transition***. ACS Photonics **9**, 3 (2022), https://doi.org/10.1021/acsphotonics.1c01717. **p. 1**

[12]   M.Z. Hasan, G. Chang, I. Belopolski, G. Bian, S.-Y. Xu, and J.-X. Yin, ***Weyl, Dirac and high-fold chiral fermions in topological quantum matter.*** Nature Reviews Materials **6**, 9 (2021), https://doi.org/10.1038/s41578-021-00301-3. **p. 1**

[13]   J. Polaczyński, G. Krizman, A. Kazakov, B. Turowski, J.B. Ortiz, R. Rudniewski, T. Wojciechowski, P. Dłużewski, M. Aleszkiewicz, W. Zaleszczyk, B. Kurowska, Z. Muhammad, M. Rosmus, N. Olszowska, L.-A. De Vaulchier, Y. Guldner, T. Wojtowicz, and V.V. Volobuev, ***3D Topological Semimetal Phases of Strained α-Sn on Insulating Substrate.*** submitted to Advanced Functional Materials, https://doi.org/10.48550/arXiv.2309.03951. **p. 2, 3, 119, 121, 123, 126**

[14]   B. Turowski, O. Caha, R. Rudniewski, N. Olszowska, J. Kołodziej, T. Wojtowicz, G. Springholz, and V.V. Volobuev, ***Surface States of Topological Crystalline Insulator Pb$_{1-x}$Sn$_x$Se with Ultrathin Transition Metal Adsorbate***. unpublished. **p. 3**

[15]   B. Turowski, A. Kazakov, R. Rudniewski, T. Sobol, E. Partyka-Jankowska, T. Wojciechowski, M. Aleszkiewicz, W. Zaleszczyk, M. Szczepanik, T. Wojtowicz, and V.V. Volobuev, ***Spin-polarization of topological crystalline and normal insulator Pb$_{1-x}$Sn$_x$Se (111) epilayers probed by photoelectron spectroscopy***. Applied Surface Science **610**, (2023), https://doi.org/10.1016/j.apsusc.2022.155434, https://arxiv.org/abs/2212.00816. **p. 3, 36, 64, 68, 105, 107 , 110, 114, 115, 125, 126**

[16]   C.L. Kane and E.J. Mele, ***Z$_2$ Topological Order and the Quantum Spin Hall Effect***. Physical Review Letters **95**, 14 (2005), https://doi.org/10.1103/PhysRevLett.95.146802. **p. 6**

[17]   C.L. Kane and E.J. Mele, ***Quantum Spin Hall Effect in Graphene***. Physical Review Letters **95**, 22 (2005), https://doi.org/10.1103/PhysRevLett.95.226801. **p. 6**

[18]   Y. Ando and L. Fu, ***Topological Crystalline Insulators and Topological Superconductors: From Concepts to Materials***. Annual Review of Condensed Matter Physics **6**, 1 (2015), https://doi.org/10.1146/annurev-conmatphys-031214-014501. **p. 6**

[19]   J. Maciejko, T.L. Hughes, and S.-C. Zhang, ***The Quantum Spin Hall Effect***. Annual Review of Condensed Matter Physics **2**, 1 (2011), https://doi.org/10.1146/annurev-conmatphys-062910-140538. **p. 6**

[20]   J. Chu and A. Sher, ***Band Structures***, in *Physics and Properties of Narrow Gap Semiconductors*, Editors: J. Chu and A. Sher. 2008, Springer New York: New York, NY. p. 151-237, https://doi.org/10.1007/978-0-387-74801-6_3. **p. 6,** Error! Bookmark not defined.**, 10**

[21]   M. König, H. Buhmann, L. W. Molenkamp, T. Hughes, C.-X. Liu, X.-L. Qi, and S.-C. Zhang, ***The Quantum Spin Hall Effect: Theory and Experiment***. Journal of the Physical Society of Japan **77**, 3 (2008), https://doi.org/10.1143/JPSJ.77.031007. **p. 6**

[22]   Y. Ando, ***Topological Insulator Materials***. Journal of the Physical Society of Japan **82**, 10 (2013), https://doi.org/10.7566/JPSJ.82.102001. **p. 6, 11**

[23]   J.C.Y. Teo, L. Fu, and C.L. Kane, ***Surface states and topological invariants in three-dimensional topological insulators: Application to Bi$_{1-x}$Sb$_x$***. Physical Review B **78**, 4 (2008), https://doi.org/10.1103/PhysRevB.78.045426. **p. 6**

[24]   T.H. Hsieh, H. Lin, J. Liu, W. Duan, A. Bansil, and L. Fu, ***Topological crystalline insulators in the SnTe material class***. Nature Communications **3**, 1 (2012), https://doi.org/10.1038/ncomms1969. **p. 6, 11, 12, 84, 87, 99**

[25]   B.A. Bernevig, T.L. Hughes, and S.-C. Zhang, ***Quantum Spin Hall Effect and Topological Phase Transition in HgTe Quantum Wells***. Science **314**, 5806 (2006), https://doi.org/10.1126/science.1133734. **p. 6**

[26]   L. Fu and C.L. Kane, ***Topological insulators with inversion symmetry***. Physical Review B **76**, 4 (2007), https://doi.org/10.1103/PhysRevB.76.045302. **p. 6**

[27]   R. Roy, ***Topological phases and the quantum spin Hall effect in three dimensions***. Physical Review B **79**, 19 (2009), https://doi.org/10.1103/PhysRevB.79.195322. **p. 6**

[28]   L. Fu, C.L. Kane, and E.J. Mele, ***Topological Insulators in Three Dimensions***. Physical Review Letters **98**, 10 (2007), https://doi.org/10.1103/PhysRevLett.98.106803. **p. 6**

[29]   S.M. Young, S. Zaheer, J.C.Y. Teo, C.L. Kane, E.J. Mele, and A.M. Rappe, *Dirac Semimetal in Three Dimensions*. Physical Review Letters **108**, 14 (2012), https://doi.org/10.1103/PhysRevLett.108.140405. **p. 7**

[30]   Z. Wang, Y. Sun, X.-Q. Chen, C. Franchini, G. Xu, H. Weng, X. Dai, and Z. Fang, *Dirac semimetal and topological phase transitions in A_3Bi (A = Na, K, Rb)*. Physical Review B **85**, 19 (2012), https://doi.org/10.1103/PhysRevB.85.195320. **p. 7**

[31]   A.A. Burkov, M.D. Hook, and L. Balents, *Topological nodal semimetals*. Physical Review B **84**, 23 (2011), https://doi.org/10.1103/PhysRevB.84.235126. **p. 7**

[32]   X. Wan, A.M. Turner, A. Vishwanath, and S.Y. Savrasov, *Topological semimetal and Fermi-arc surface states in the electronic structure of pyrochlore iridates*. Physical Review B **83**, 20 (2011), https://doi.org/10.1103/PhysRevB.83.205101. **p. 7, 14**

[33]   P. Narang, C.A.C. Garcia, and C. Felser, *The topology of electronic band structures*. Nature Materials **20**, 3 (2021), https://doi.org/10.1038/s41563-020-00820-4. **p. 7**

[34]   B.J. Wieder, B. Bradlyn, J. Cano, Z. Wang, M.G. Vergniory, L. Elcoro, A.A. Soluyanov, C. Felser, T. Neupert, N. Regnault, and B.A. Bernevig, *Topological materials discovery from crystal symmetry*. Nature Reviews Materials **7**, 3 (2022), https://doi.org/10.1038/s41578-021-00380-2. **p. 7**

[35]   L. Fu, *Topological Crystalline Insulators*. Physical Review Letters **106**, 10 (2011), https://doi.org/10.1103/PhysRevLett.106.106802. **p. 7, 15, 16, 83, 104**

[36]   G. Bihlmayer, Y.M. Koroteev, P.M. Echenique, E.V. Chulkov, and S. Blügel, *The Rashba-effect at metallic surfaces*. Surface Science **600**, 18 (2006), https://doi.org/10.1016/j.susc.2006.01.098. **p. 7**

[37]   E.O. Kane, *Chapter 3 The k•p Method*, in *Semiconductors and Semimetals*, Editors: R.K. Willardson and A.C. Beer. 1966, Elsevier. p. 75-100, https://doi.org/10.1016/S0080-8784(08)62376-5. **p.** Error! Bookmark not defined.

[38]   G. Dresselhaus, *Spin-Orbit Coupling Effects in Zinc Blende Structures*. Physical Review **100**, 2 (1955), https://doi.org/10.1103/PhysRev.100.580. **p.** Error! Bookmark not defined.

[39]   Y.A. Bychkov and É.I. Rashba, *Properties of a 2D electron gas with lifted spectral degeneracy*. Soviet Journal of Experimental and Theoretical Physics Letters **39**, (1984). **p.** Error! Bookmark not defined.**, 88, 89**

[40]   L. Petersen and P. Hedegård, *A simple tight-binding model of spin–orbit splitting of sp-derived surface states*. Surface Science **459**, 1 (2000), https://doi.org/10.1016/S0039-6028(00)00441-6. **p. 9**

[41]   L.W. Molenkamp, G. Schmidt, and G.E.W. Bauer, *Rashba Hamiltonian and electron transport*. Physical Review B **64**, 12 (2001), https://doi.org/10.1103/PhysRevB.64.121202. **p. 9**

[42]   Z.H. Zhu, G. Levy, B. Ludbrook, C.N. Veenstra, J.A. Rosen, R. Comin, D. Wong, P. Dosanjh, A. Ubaldini, P. Syers, N.P. Butch, J. Paglione, I.S. Elfimov, and A. Damascelli, *Rashba Spin-Splitting Control at the Surface of the Topological Insulator Bi_2Se_3*. Physical Review Letters **107**, 18 (2011), https://doi.org/10.1103/PhysRevLett.107.186405. **p. 9**

[43]   M.R. Scholz, J. Sánchez-Barriga, D. Marchenko, A. Varykhalov, A. Volykhov, L.V. Yashina, and O. Rader, *Tolerance of Topological Surface States towards Magnetic Moments: Fe on Bi_2Se_3*. Physical Review Letters **108**, 25 (2012), https://doi.org/10.1103/PhysRevLett.108.256810. **p. 9, 84, 85, 87, 88, 90,** Error! Bookmark not defined.**, 98, 102, 103, 104**

[44]   E. Wang, P. Tang, G. Wan, A.V. Fedorov, I. Miotkowski, Y.P. Chen, W. Duan, and S. Zhou, *Robust Gapless Surface State and Rashba-Splitting Bands upon Surface Deposition of Magnetic Cr on Bi_2Se_3.* Nano Letters **15**, 3 (2015), https://doi.org/10.1021/nl504900s. **p. 9, 84, 85, 87, 88, 90, 91, 98, 103**

[45]   J.M. Ziman, *Principles of the Theory of Solids*. 1972: Cambridge University Press. **p. 9**

[46]   S. LaShell, B.A. McDougall, and E. Jensen, *Spin Splitting of an Au(111) Surface State Band Observed with Angle Resolved Photoelectron Spectroscopy.* Physical Review Letters **77**, 16 (1996), https://doi.org/10.1103/PhysRevLett.77.3419. **p. 9, 11, 105**

[47]   A. Manchon, H.C. Koo, J. Nitta, S.M. Frolov, and R.A. Duine, *New perspectives for Rashba spin–orbit coupling.* Nature Materials **14**, 9 (2015), https://doi.org/10.1038/nmat4360. **p. 9**

[48]   F. Herman, C.D. Kuglin, K.F. Cuff, and R.L. Kortum, *Relativistic Corrections to the Band Structure of Tetrahedrally Bonded Semiconductors.* Physical Review Letters **11**, 12 (1963), https://doi.org/10.1103/PhysRevLett.11.541. **p. 10**

[49]   A.H. Castro Neto, F. Guinea, N.M.R. Peres, K.S. Novoselov, and A.K. Geim, *The electronic properties of graphene.* Reviews of Modern Physics **81**, 1 (2009), https://doi.org/10.1103/RevModPhys.81.109. **p. 11**

[50]   Y. Tanaka, Z. Ren, T. Sato, K. Nakayama, S. Souma, T. Takahashi, K. Segawa, and Y. Ando, *Experimental realization of a topological crystalline insulator in SnTe.* Nature Physics **8**, 11 (2012), https://doi.org/10.1038/nphys2442. **p. 11, 13, 59, 83**

[51]   J.O. Dimmock, I. Melngailis, and A.J. Strauss, *Band Structure and Laser Action in $Pb_xSn_{1-x}Te$.* Physical Review Letters **16**, 26 (1966), https://doi.org/10.1103/PhysRevLett.16.1193. **p. 12**

[52]   M.Y. Toriyama, M.K. Brod, L.C. Gomes, F.A. Bipasha, B.A. Assaf, E. Ertekin, and G.J. Snyder, *Tuning valley degeneracy with band inversion.* Journal of Materials Chemistry A **10**, 3 (2022), https://doi.org/10.1039/D1TA08379A. **p. 12**

[53]   S.Y. Xu, C. Liu, N. Alidoust, M. Neupane, D. Qian, I. Belopolski, J.D. Denlinger, Y.J. Wang, H. Lin, L.A. Wray, G. Landolt, B. Slomski, J.H. Dil, A. Marcinkova, E. Morosan, Q. Gibson, R. Sankar, F.C. Chou, R.J. Cava, A. Bansil, and M.Z. Hasan, *Observation of a topological crystalline insulator phase and topological phase transition in $Pb_{1-x}Sn_xTe$.* Nature Communications **3**, (2012), https://doi.org/10.1038/ncomms2191. **p. 12, 13, 83, 106**

[54]   S. Safaei, P. Kacman, and R. Buczko, *Topological crystalline insulator (Pb,Sn)Te: Surface states and their spin polarization.* Physical Review B **88**, 4 (2013), https://doi.org/10.1103/PhysRevB.88.045305. **p. 13, 87, 104**

[55]   P.B. Littlewood, B. Mihaila, R.K. Schulze, D.J. Safarik, J.E. Gubernatis, A. Bostwick, E. Rotenberg, C.P. Opeil, T. Durakiewicz, J.L. Smith, and J.C. Lashley, *Band Structure of SnTe Studied by Photoemission Spectroscopy.* Physical Review Letters **105**, 8 (2010), https://doi.org/10.1103/PhysRevLett.105.086404. **p. 13**

[56]   J.R. Burke, R.S. Allgaier, B.B. Houston, J. Babiskin, and P.G. Siebenmann, *Shubnikov-de Haas Effect in SnTe.* Physical Review Letters **14**, 10 (1965), https://doi.org/10.1103/PhysRevLett.14.360. **p. 13**

[57]   M. Iizumi, Y. Hamaguchi, K. F. Komatsubara, and Y. Kato, *Phase Transition in SnTe with Low Carrier Concentration.* Journal of the Physical Society of Japan **38**, 2 (1975), https://doi.org/10.1143/JPSJ.38.443. **p. 13**

[58]   N.P. Armitage, E.J. Mele, and A. Vishwanath, ***Weyl and Dirac semimetals in three-dimensional solids***. Reviews of Modern Physics **90**, 1 (2018), https://doi.org/10.1103/RevModPhys.90.015001. **p. 13, 14**

[59]   A.A. Burkov and L. Balents, ***Weyl Semimetal in a Topological Insulator Multilayer***. Physical Review Letters **107**, 12 (2011), https://doi.org/10.1103/PhysRevLett.107.127205. **p. 13, 14**

[60]   G.B. Halász and L. Balents, ***Time-reversal invariant realization of the Weyl semimetal phase***. Physical Review B **85**, 3 (2012), https://doi.org/10.1103/PhysRevB.85.035103. **p. 13**

[61]   T. Yu, Z. Luo, and G.E.W. Bauer, ***Chirality as generalized spin–orbit interaction in spintronics***. Physics Reports **1009**, (2023), https://doi.org/10.1016/j.physrep.2023.01.002. **p. 14**

[62]   H. Weyl, ***Gravitation and the electron***. Proceedings of the National Academy of Sciences **15**, 4 (1929), https://doi.org/10.1073/pnas.15.4.323. **p. 14**

[63]   D.T. Son and B.Z. Spivak, ***Chiral anomaly and classical negative magnetoresistance of Weyl metals***. Physical Review B **88**, 10 (2013), https://doi.org/10.1103/PhysRevB.88.104412. **p. 14**

[64]   H.B. Nielsen and M. Ninomiya, ***The Adler-Bell-Jackiw anomaly and Weyl fermions in a crystal***. Physics Letters B **130**, 6 (1983), https://doi.org/10.1016/0370-2693(83)91529-0. **p. 14**

[65]   J. Hu, S.-Y. Xu, N. Ni, and Z. Mao, ***Transport of Topological Semimetals***. Annual Review of Materials Research **49**, 1 (2019), https://doi.org/10.1146/annurev-matsci-070218-010023. **p. 14**

[66]   J. Chen, T. Zhang, J. Wang, N. Zhang, W. Ji, S. Zhou, and Y. Chai, ***Field-Effect Chiral Anomaly Devices with Dirac Semimetal***. Advanced Functional Materials **31**, 40 (2021), https://doi.org/10.1002/adfm.202104192. **p. 14**

[67]   A.J. Strauss, ***Inversion of Conduction and Valence Bands in Pb_{1-x}Sn_xSe Alloys***. Physical Review **157**, 3 (1967), https://doi.org/10.1103/PhysRev.157.608. **p. 15, 16, 106, 115**

[68]   H. Preier, ***Recent advances in lead-chalcogenide diode lasers***. Applied physics **20**, 3 (1979), https://doi.org/10.1007/BF00886018. **p. 15, 60, 89, 106, 114, 115**

[69]   R. Carter, M. Suyetin, S. Lister, M.A. Dyson, H. Trewhitt, S. Goel, Z. Liu, K. Suenaga, C. Giusca, R.J. Kashtiban, J.L. Hutchison, J.C. Dore, G.R. Bell, E. Bichoutskaia, and J. Sloan, ***Band gap expansion, shear inversion phase change behaviour and low-voltage induced crystal oscillation in low-dimensional tin selenide crystals***. Dalton Transactions **43**, 20 (2014), https://doi.org/10.1039/C4DT00185K. **p. 15**

[70]   R. Grisar, W. Riedel, and H. Preier, ***Properties of diffused PbSnSe homojunction diode lasers***. IEEE Journal of Quantum Electronics **17**, 5 (1981), https://doi.org/10.1109/JQE.1981.1071169. **p. 15**

[71]   M. Tacke, ***New developments and applications of tunable IR lead salt lasers***. Infrared Physics & Technology **36**, 1 (1995), https://doi.org/10.1016/1350-4495(94)00101-P. **p. 15**

[72]   M.M. Jaime, H. Jose Luis, A. Lucía, R. Acacio, and F. López, ***Arrays of thermally evaporated PbSe infrared photodetectors deposited on Si substrates operating at room temperature***. Semiconductor Science and Technology **11**, 11 (1996), https://doi.org/10.1088/0268-1242/11/11/017. **p. 15**

[73]   A. Muñoz, J. Meléndez, M.C. Torquemada, M.T. Rodrigo, J. Cebrián, A.J. de Castro, J. Meneses, M. Ugarte, F. López, G. Vergara, J.L. Hernández, J.M. Martín, L. Adell, and M.T. Montojo, ***PbSe photodetector arrays for IR sensors***. Thin Solid Films **317**, 1 (1998), https://doi.org/https://doi.org/10.1016/S0040-6090(97)00576-2. **p. 15**

[74] A.F. Ioffe, L.S. Stil'bans, E.K. Iordanishvili, T.S. Stavitskaya, A. Gelbtuch, and G. Vineyard, *Semiconductor Thermoelements and Thermoelectric Cooling*. Physics Today **12**, 5 (1959), https://doi.org/10.1063/1.3060810. **p. 15**

[75] L.-D. Zhao, C. Chang, G. Tan, and M.G. Kanatzidis, *SnSe: a remarkable new thermoelectric material*. Energy & Environmental Science **9**, 10 (2016), https://doi.org/10.1039/C6EE01755J. **p. 15**

[76] T.M. Tritt, *Thermoelectric Materials: Principles, Structure, Properties, and Applications*, in *Encyclopedia of Materials: Science and Technology*, Editors: K.H.J. Buschow, et al. 2002, Elsevier: Oxford. p. 1-11, https://doi.org/10.1016/B0-08-043152-6/01822-2. **p. 15**

[77] Q. Zhang, F. Cao, K. Lukas, W. Liu, K. Esfarjani, C. Opeil, D. Broido, D. Parker, D.J. Singh, G. Chen, and Z. Ren, *Study of the Thermoelectric Properties of Lead Selenide Doped with Boron, Gallium, Indium, or Thallium*. Journal of the American Chemical Society **134**, 42 (2012), https://doi.org/10.1021/ja307910u. **p. 15**

[78] C. Gayner, K.K. Kar, and W. Kim, *Recent progress and futuristic development of PbSe thermoelectric materials and devices*. Materials Today Energy **9**, (2018), https://doi.org/10.1016/j.mtener.2018.06.010. **p. 15**

[79] C.M. Polley, P. Dziawa, A. Reszka, A. Szczerbakow, R. Minikayev, J.Z. Domagala, S. Safaei, P. Kacman, R. Buczko, J. Adell, M.H. Berntsen, B.M. Wojek, O. Tjernberg, B.J. Kowalski, T. Story, and T. Balasubramanian, *Observation of topological crystalline insulator surface states on (111)-oriented $Pb_{1-x}Sn_xSe$ films*. Physical Review B **89**, 7 (2014), https://doi.org/10.1103/PhysRevB.89.075317. **p. 15, 87**

[80] P. Barone, T. Rauch, D. Di Sante, J. Henk, I. Mertig, and S. Picozzi, *Pressure-induced topological phase transitions in rocksalt chalcogenides*. Physical Review B **88**, 4 (2013), https://doi.org/10.1103/PhysRevB.88.045207. **p. 15**

[81] G. Springholz, *Chapter 11 - Molecular Beam Epitaxy of IV–VI Semiconductors: Fundamentals, Low-dimensional Structures, and Device Applications*, in *Molecular Beam Epitaxy (Second Edition)*, Editors: M. Henini. 2018, Elsevier. p. 211-276, https://doi.org/10.1016/B978-0-12-812136-8.00011-6. **p. 16**

[82] G. Nimtz and B. Schlicht, *Narrow-gap lead salts*, in *Narrow-Gap Semiconductors*, Editors: R. Dornhaus, G. Nimtz, and B. Schlicht. 1983, Springer Berlin Heidelberg: Berlin, Heidelberg. p. 1-117, https://doi.org/10.1007/BFb0044920. **p. 16, 60, 83**

[83] V.V. Volobuev, P.S. Mandal, M. Galicka, O. Caha, J. Sánchez-Barriga, D. Di Sante, A. Varykhalov, A. Khiar, S. Picozzi, G. Bauer, P. Kacman, R. Buczko, O. Rader, and G. Springholz, *Giant Rashba Splitting in $Pb_{1-x}Sn_xTe$ (111) Topological Crystalline Insulator Films Controlled by Bi Doping in the Bulk*. Advanced Materials **29**, 3 (2017), https://doi.org/10.1002/adma.201604185. **p. 16, 19, 38, 51, 89, 90, 100, 106, 107**

[84] D. Zhang, H. Wang, J. Ruan, G. Yao, and H. Zhang, *Engineering topological phases in the Luttinger semimetal α-Sn*. Physical Review B **97**, 19 (2018), https://doi.org/10.1103/PhysRevB.97.195139. **p. 16, 17, 116, 117, 121**

[85] M. Kharitonov, J.-B. Mayer, and E.M. Hankiewicz, *Evolution of the surface states of the Luttinger semimetal under strain and inversion-symmetry breaking: Dirac, line-node, and Weyl semimetals*. arxiv.org, (2022), https://doi.org/10.48550/arXiv.2212.00902. **p. 16, 17, 123**

[86] J.M. Luttinger, *Quantum Theory of Cyclotron Resonance in Semiconductors: General Theory*. Physical Review **102**, 4 (1956), https://doi.org/10.1103/PhysRev.102.1030. **p. 16, 123**

[87]   H. Huang and F. Liu, ***Tensile strained gray tin: Dirac semimetal for observing negative magnetoresistance with Shubnikov--de Haas oscillations***. Physical Review B **95**, 20 (2017), https://doi.org/10.1103/PhysRevB.95.201101. **p. 16, 17, 80, 116, 121**

[88]   F.H. Pollak, M. Cardona, C.W. Higginbotham, F. Herman, and J.P. Van Dyke, ***Energy-Band Structure and Optical Spectrum of Grey Tin***. Physical Review B **2**, 2 (1970), https://doi.org/10.1103/PhysRevB.2.352. **p. 16**

[89]   B.J. Roman and A.W. Ewald, ***Stress-Induced Band Gap and Related Phenomena in Gray Tin***. Physical Review B **5**, 10 (1972), https://doi.org/10.1103/PhysRevB.5.3914. **p. 17, 116**

[90]   R.F.C. Farrow, D.S. Robertson, G.M. Williams, A.G. Cullis, G.R. Jones, I.M. Young, and P.N.J. Dennis, ***The growth of metastable, heteroepitaxial films of α-Sn by metal beam epitaxy***. Journal of Crystal Growth **54**, 3 (1981), https://doi.org/10.1016/0022-0248(81)90506-6. **p. 18, 77, 80**

[91]   B. Cornelius, S. Treivish, Y. Rosenthal, and M. Pecht, ***The phenomenon of tin pest: A review***. Microelectronics Reliability **79**, (2017), https://doi.org/10.1016/j.microrel.2017.10.030. **p. 18**

[92]   K. Ojima, H. Matsumoto, and Y. Taneda, ***Differential scanning calorimetry study of the $\alpha \rightarrow \beta$ transition in tin***. Journal of the Less Common Metals **157**, 1 (1990), https://doi.org/10.1016/0022-5088(90)90422-G. **p. 18**

[93]   G. Springholz and G. Bauer, ***Systematic study of PbTe (111) molecular-beam epitaxy using reflection high-energy electron-diffraction intensity oscillations***. Journal of Applied Physics **77**, 2 (1995), https://doi.org/10.1063/1.359038. **p. 19**

[94]   M.A. Herman and H. Sitter, ***Introduction***, in *Molecular Beam Epitaxy: Fundamentals and Current Status*, Editors: M.A. Herman and H. Sitter. 1996, Springer Berlin Heidelberg: Berlin, Heidelberg. p. 1-31, https://doi.org/10.1007/978-3-642-80060-3_1. **p. 20**

[95]   C.K. O'Sullivan and G.G. Guilbault, ***Commercial quartz crystal microbalances – theory and applications***. Biosensors and Bioelectronics **14**, 8 (1999), https://doi.org/10.1016/S0956-5663(99)00040-8. **p. 21**

[96]   M.A. Herman and H. Sitter, ***Molecular Beam Epitaxy***. 1996: Springer Berlin, Heidelberg, https://doi.org/10.1007/978-3-642-80060-3. **p. 22, 40**

[97]   M.A. Herman and H. Sitter, ***MBE Growth Processes of Lattice-Matched Structures***, in *Molecular Beam Epitaxy: Fundamentals and Current Status*, Editors: M.A. Herman and H. Sitter. 1996, Springer Berlin Heidelberg: Berlin, Heidelberg. p. 229-288, https://doi.org/10.1007/978-3-642-80060-3_5. **p. 22**

[98]   T.F. Kuech, ***4.01 - Integration of Dissimilar Materials***, in *Comprehensive Semiconductor Science and Technology*, Editors: P. Bhattacharya, R. Fornari, and H. Kamimura. 2011, Elsevier: Amsterdam. p. 1-24, https://doi.org/10.1016/B978-0-44-453153-7.00106-1. **p. 23**

[99]   B.A. Assaf, T. Phuphachong, V.V. Volobuev, G. Bauer, G. Springholz, L.-A. de Vaulchier, and Y. Guldner, ***Magnetooptical determination of a topological index***. npj Quantum Materials **2**, 1 (2017), https://doi.org/10.1038/s41535-017-0028-5. **p. 36, 88, 104**

[100]   A. Kazakov, W. Brzezicki, T. Hyart, B. Turowski, J. Polaczyński, Z. Adamus, M. Aleszkiewicz, T. Wojciechowski, J.Z. Domagala, O. Caha, A. Varykhalov, G. Springholz, T. Wojtowicz, V.V. Volobuev, and T. Dietl, ***Signatures of dephasing by mirror-symmetry breaking in weak-antilocalization magnetoresistance across the topological transition in $Pb_{1-x}Sn_xSe$***. Physical Review B **103**, 24 (2021), https://doi.org/10.1103/PhysRevB.103.245307, https://arxiv.org/abs/2002.07622. **p. 3, 36, 59, 61, 74, 107, 114, 126**

[101]   A.J. SpringThorpe, S.J. Ingrey, B. Emmerstorfer, P. Mandeville, and W.T. Moore, ***Measurement of GaAs surface oxide desorption temperatures****.* Applied Physics Letters **50**, 2 (1987), https://doi.org/10.1063/1.97824. **p. 38**

[102]   H. Shtrikman, M. Oron, A. Raizman, and G. Cinader, ***Determining the [001] crystal orientation of CdTe layers grown on (001) GaAs****.* Journal of Electronic Materials **17**, 2 (1988), https://doi.org/10.1007/BF02652138. **p. 38**

[103]   H. Nishino, I. Sugiyama, and Y. Nishijima, ***Misfit stress relaxation mechanism in CdTe(100) and CdTe/ZnTe(100) on a GaAs(100) highly mismatched heteroepitaxial layer****.* Journal of Applied Physics **80**, 6 (1996), https://doi.org/10.1063/1.363265. **p. 38**

[104]   H. Tatsuoka, H. Kuwabara, Y. Nakanishi, and H. Fujiyasu, ***Strain relaxation of CdTe(100) layers grown by hot-wall epitaxy on GaAs(100) substrates****.* Journal of Applied Physics **67**, 11 (1990), https://doi.org/10.1063/1.346079. **p. 38**

[105]   Ferrovac GmbH, ***VSN40 NexGeneration Ultra High Vacuum Suitcase Instructıon manual***. Available from: https://ferrovac.com/?tool=SysFileFetch&file=VSN40S-MANUAL.pdf, **p. 38**

[106]   N. Masud and J.B. Pendry, ***Theory of RHEED****.* Journal of Physics C: Solid State Physics **9**, 10 (1976), https://doi.org/10.1088/0022-3719/9/10/004. **p. 40**

[107]   S. Hasegawa, ***Reflection High-Energy Electron Diffraction***, in *Characterization of Materials*. p. 1-14, https://doi.org/10.1002/0471266965.com139. **p. 42, 43**

[108]   M.G. Lagally, D.E. Savage, and M.C. Tringides, ***Diffraction from Disordered Surfaces: an Overview***, in *Reflection High Energy Electron Diffraction and Reflection Electron Imaging of Surfaces*, Editors: P.K. Larsen and P.J. Dobson. 1989, Springer New York, NY. p. 139-174, https://doi.org/10.1007/978-1-4684-5580-9. **p. 43, 67**

[109]   G. Koster, ***1 - Reflection high-energy electron diffraction (RHEED) for in situ characterization of thin film growth***, in *In Situ Characterization of Thin Film Growth*, Editors: G. Koster and G. Rijnders. 2011, Woodhead Publishing. p. 3-28, https://doi.org/10.1533/9780857094957.1.3. **p. 43**

[110]   C. Liu, K. Chang, and K. Zou, ***Realistic simulation of reflection high-energy electron diffraction patterns for two-dimensional lattices using Ewald construction****.* Journal of Vacuum Science & Technology B **40**, 5 (2022), https://doi.org/10.1116/6.0001899. **p. 43**

[111]   T. Sakamoto, ***Rheed Oscillations in MBE and Their Applications to Precisely Controlled Crystal Growth***, in *Physics, Fabrication, and Applications of Multilayered Structures*, Editors: P. Dhez and C. Weisbuch. 1988, Springer US: Boston, MA. p. 93-110, https://doi.org/10.1007/978-1-4757-0091-6_5. **p. 45**

[112]   Y. Waseda, E. Matsubara, and K. Shinoda, ***Scattering and Diffraction***, in *X-Ray Diffraction Crystallography: Introduction, Examples and Solved Problems*, Editors: Y. Waseda, E. Matsubara, and K. Shinoda. 2011, Springer Berlin Heidelberg: Berlin, Heidelberg. p. 67-106, https://doi.org/10.1007/978-3-642-16635-8_3. **p. 47**

[113]   A.R. Denton and N.W. Ashcroft, ***Vegard's law****.* Physical Review A **43**, 6 (1991), https://doi.org/10.1103/PhysRevA.43.3161. **p. 48**

[114]   D. Shindo and T. Oikawa, ***Energy Dispersive X-ray Spectroscopy***, in *Analytical Electron Microscopy for Materials Science*, Editors: D. Shindo and T. Oikawa. 2002, Springer Japan: Tokyo. p. 81-102, https://doi.org/10.1007/978-4-431-66988-3_4. **p. 50**

[115]   E. Meyer, ***Atomic force microscopy****.* Progress in Surface Science **41**, 1 (1992), https://doi.org/10.1016/0079-6816(92)90009-7. **p. 50**

[116]   D. Nečas and P. Klapetek, ***Gwyddion: an open-source software for SPM data analysis****.* Open
        Physics **10**, 1 (2012), https://doi.org/10.2478/s11534-011-0096-2. **p. 51**

[117]   Gwyddion developers. *Gwyddion.* 2023; Available from: http://gwyddion.net/. **p. 51**

[118]   T. Valla, Z.H. Pan, D. Gardner, Y.S. Lee, and S. Chu, ***Photoemission Spectroscopy of Magnetic and
        Nonmagnetic Impurities on the Surface of theBi₂Se₃ Topological Insulator****.* Physical Review
        Letters **108**, 11 (2012), https://doi.org/10.1103/PhysRevLett.108.117601. **p. 51, 84, 87, 88, 103**

[119]   A. Einstein, Annalen der Physik **322**, 132 (1905). **p. 51**

[120]   C.N. Berglund and W.E. Spicer, ***Photoemission Studies of Copper and Silver: Theory****.* Physical
        Review **136**, 4A (1964), https://doi.org/10.1103/PhysRev.136.A1030. **p. 51**

[121]   S. Suga and A. Sekiyama, ***Theoretical Background***, in *Photoelectron Spectroscopy: Bulk and
        Surface Electronic Structures*, Editors: S. Suga and A. Sekiyama. 2014, Springer Berlin Heidelberg:
        Berlin, Heidelberg. p. 7-31, https://doi.org/10.1007/978-3-642-37530-9_2. **p. 51**

[122]   S. Hüfner, ***Photoemission of Valence Electrons from Metallic Solids in the One-Electron
        Approximation***, in *Photoelectron Spectroscopy: Principles and Applications*, Editors: S. Hüfner.
        2003, Springer Berlin Heidelberg: Berlin, Heidelberg. p. 347-409, https://doi.org/10.1007/978-3-
        662-09280-4_6. **p. 51**

[123]   M.P. Seah and W.A. Dench, ***Quantitative electron spectroscopy of surfaces: A standard data
        base for electron inelastic mean free paths in solids****.* Surface and Interface Analysis **1**, 1 (1979),
        https://doi.org/10.1002/sia.740010103. **p. 53**

[124]   Tanuma, S., C.J. Powell, and D.R. Penn, ***Calculations of electron inelastic mean free paths. IX.
        Data for 41 elemental solids over the 50 eV to 30 keV range****.* Surface and Interface Analysis **43**,
        3 (2011), https://doi.org/10.1002/sia.3522. **p. 53, 100**

[125]   E. Lahoud, E. Maniv, M.S. Petrushevsky, M. Naamneh, A. Ribak, S. Wiedmann, L. Petaccia, Z.
        Salman, K.B. Chashka, Y. Dagan, and A. Kanigel, ***Evolution of the Fermi surface of a doped
        topological insulator with carrier concentration****.* Physical Review B **88**, 19 (2013),
        https://doi.org/10.1103/PhysRevB.88.195107. **p. 54**

[126]   E. Kisker, R. Clauberg, and W. Gudat, ***Electron spectrometer for spin-polarized angle- and
        energy-resolved photoemission from ferromagnets****.* Review of Scientific Instruments **53**, 8
        (1982), https://doi.org/10.1063/1.1137146. **p. 54**

[127]   D. Tillmann, R. Thiel, and E. Kisker, ***Very-low-energy spin-polarized electron diffraction from
        Fe(001)****.* Zeitschrift für Physik B Condensed Matter **77**, 1 (1989),
        https://doi.org/10.1007/BF01313611. **p. 54**

[128]   M. Szczepanik-Ciba, T. Sobol, and J. Szade, ***PHELIX – A new soft X-ray spectroscopy beamline at
        SOLARIS synchrotron****.* Nuclear Instruments and Methods in Physics Research Section B: Beam
        Interactions with Materials and Atoms **492**, (2021),
        https://doi.org/10.1016/j.nimb.2021.01.021. **p. 54**

[129]   M. Escher, N.B. Weber, M. Merkel, L. Plucinski, and C.M. Schneider, ***FERRUM: A new highly
        efficient spin detector for electron spectroscopy****.* e-Journal of Surface Science and
        Nanotechnology **9**, (2011), https://doi.org/10.1380/ejssnt.2011.340. **p. 54, 55**

[130]   N. Sherman, ***Coulomb Scattering of Relativistic Electrons by Point Nuclei****.* Physical Review **103**,
        6 (1956), https://doi.org/10.1103/PhysRev.103.1601. **p. 55**

[131] J. Osterwalder, ***Spin-Polarized Photoemission***, in *Magnetism: A Synchrotron Radiation Approach*, Editors: E. Beaurepaire, et al. 2006, Springer Berlin Heidelberg: Berlin, Heidelberg. p. 95-120, https://doi.org/10.1007/3-540-33242-1_5. **p. 55**

[132] C. Bigi, P.K. Das, D. Benedetti, F. Salvador, D. Krizmancic, R. Sergo, A. Martin, G. Panaccione, G. Rossi, J. Fujii, and I. Vobornik, ***Very efficient spin polarization analysis (VESPA): new exchange scattering-based setup for spin-resolved ARPES at APE-NFFA beamline at Elettra***. Journal of Synchrotron Radiation **24**, 4 (2017), https://doi.org/10.1107/S1600577517006907. **p. 55**

[133] A. Winkelmann, D. Hartung, H. Engelhard, C.T. Chiang, and J. Kirschner, ***High efficiency electron spin polarization analyzer based on exchange scattering at Fe/W(001)***. Review of Scientific Instruments **79**, 8 (2008), https://doi.org/10.1063/1.2949877. **p. 55**

[134] P. Zhang. *Curvature*. 2018; Available from: https://github.com/zhangpengphi/curvature. **p. 57, 59, 119**

[135] P. Marchand and L. Marmet, ***Binomial smoothing filter: A way to avoid some pitfalls of least-squares polynomial smoothing***. Review of Scientific Instruments **54**, 8 (1983), https://doi.org/10.1063/1.1137498. **p. 57**

[136] I. WaveMetrics, ***Igor Pro 8 Manual***. 2018, Available from: https://www.wavemetrics.net/doc/IgorMan8.pdf, **p. 57, 113**

[137] P. Zhang, P. Richard, T. Qian, Y.-M. Xu, X. Dai, and H. Ding, ***A precise method for visualizing dispersive features in image plots***. Review of Scientific Instruments **82**, 4 (2011), https://doi.org/10.1063/1.3585113. **p. 59, 119**

[138] A.S. Wadge, B.J. Kowalski, C. Autieri, P. Iwanowski, A. Hruban, N. Olszowska, M. Rosmus, J. Kołodziej, and A. Wiśniewski, ***Topological Lifshitz transition in Weyl semimetal NbP decorated with heavy elements***. Physical Review B **105**, 23 (2022), https://doi.org/10.1103/PhysRevB.105.235304. **p. 59, 100**

[139] Y. Tanaka, T. Shoman, K. Nakayama, S. Souma, T. Sato, T. Takahashi, M. Novak, K. Segawa, and Y. Ando, ***Two types of Dirac-cone surface states on the (111) surface of the topological crystalline insulator SnTe***. Physical Review B **88**, 23 (2013), https://doi.org/10.1103/PhysRevB.88.235126. **p. 59, 87, 88**

[140] H. Lohani, P. Mishra, A. Banerjee, K. Majhi, R. Ganesan, U. Manju, D. Topwal, P.S.A. Kumar, and B.R. Sekhar, ***Band Structure of Topological Insulator BiSbTe$_{1.25}$Se$_{1.75}$***. Scientific Reports **7**, 1 (2017), https://doi.org/10.1038/s41598-017-04985-y. **p. 59**

[141] K. Kuroda, M. Ye, A. Kimura, S.V. Eremeev, E.E. Krasovskii, E.V. Chulkov, Y. Ueda, K. Miyamoto, T. Okuda, K. Shimada, H. Namatame, and M. Taniguchi, ***Experimental Realization of a Three-Dimensional Topological Insulator Phase in Ternary Chalcogenide TlBiSe$_2$***. Physical Review Letters **105**, 14 (2010), https://doi.org/10.1103/PhysRevLett.105.146801. **p. 59**

[142] L. Fu, ***Hexagonal Warping Effects in the Surface States of the Topological Insulator Bi$_2$Te$_3$***. Physical Review Letters **103**, 26 (2009), https://doi.org/10.1103/PhysRevLett.103.266801. **p. 59**

[143] A. Soumyanarayanan and J.E. Hoffman, ***Momentum-resolved STM studies of Rashba-split surface states on the topological semimetal Sb***. Journal of Electron Spectroscopy and Related Phenomena **201**, (2015), https://doi.org/10.1016/j.elspec.2014.10.008. **p. 60**

[144] Y.A. Bychkov and E.I. Rashba, ***Oscillatory effects and the magnetic susceptibility of carriers in inversion layers***. Journal of Physics C: Solid State Physics **17**, 33 (1984), https://doi.org/10.1088/0022-3719/17/33/015. **p. 60**

[145] G. Springholz, A.Y. Ueta, N. Frank, and G. Bauer, *Spiral growth and threading dislocations for molecular beam epitaxy of PbTe on BaF2 (111) studied by scanning tunneling microscopy*. Applied Physics Letters **69**, 19 (1996), https://doi.org/10.1063/1.116855. **p. 62, 68**

[146] A.I. Nikiforov, V.A. Markov, V.A. Cherepanov, and O.P. Pchelyakov, *The influence of growth temperature on the period of RHEED oscillations during MBE of Si and Ge on Si(111) surface*. Thin Solid Films **336**, 1 (1998), https://doi.org/10.1016/S0040-6090(98)01235-8. **p. 67**

[147] G. Krizman, B.A. Assaf, T. Phuphachong, G. Bauer, G. Springholz, L.A. de Vaulchier, and Y. Guldner, *Dirac parameters and topological phase diagram of Pb$_{1-x}$Sn$_x$Se from magnetospectroscopy*. Physical Review B **98**, 24 (2018), https://doi.org/10.1103/PhysRevB.98.245202. **p. 70, 88, 115**

[148] S. Reja, H.A. Fertig, L. Brey, and S. Zhang, *Surface magnetism in topological crystalline insulators*. Physical Review B **96**, 20 (2017), https://doi.org/10.1103/PhysRevB.96.201111. **p. 71, 84, 87, 90, 103, 114**

[149] S. Reja, H.A. Fertig, and L. Brey, *Spin stiffness and domain walls in Dirac-electron mediated magnets*. Physical Review B **99**, 4 (2019), https://doi.org/10.1103/PhysRevB.99.045427. **p. 71, 87, 103**

[150] M. Gerloch and E.C. Constable, *An Introduction to Transition-Metal Chemistry*, in *Transition Metal Chemistry*. 1994. p. 1-19, https://doi.org/10.1002/3527604014.ch1. **p. 72**

[151] M. Gerloch and E.C. Constable, *Focus on the dn Configuration*, in *Transition Metal Chemistry*. 1994. p. 21-26, https://doi.org/10.1002/3527604014.ch2. **p. 72**

[152] M. Gerloch and E.C. Constable, *Transition Metal Chemistry*. 1994, https://doi.org/10.1002/3527604014. **p. 72**

[153] W.L. Winterbottom and J.P. Hirth, *Diffusional Contribution to the Total Flow from a Knudsen Cell*. The Journal of Chemical Physics **37**, 4 (1962), https://doi.org/10.1063/1.1733161. **p. 72**

[154] M. Knudsen, *Experimentelle Bestimmung des Druckes gesättigter Quecksilberdämpfe bei 0° und höheren Temperaturen*. Annalen der Physik **334**, 6 (1909), https://doi.org/10.1002/andp.19093340614. **p. 72**

[155] F. Wang and J. Wu, *Chapter 8 - Magnetron sputtering*, in *Modern Ion Plating Technology*, Editors: F. Wang and J. Wu. 2023, Elsevier. p. 189-228, https://doi.org/10.1016/B978-0-323-90833-7.00008-5. **p. 74**

[156] Y. Ding, H. Song, J. Huang, J. Yao, Y. Gu, L. Wei, Y.B. Chen, Y. Deng, H. Yuan, H. Lu, and Y.-F. Chen, *Wafer-Scale and Topologically Nontrivial α-Sn Films Grown on InSb (001) by Molecular-Beam Epitaxy*. Physical Review Applied **17**, 1 (2022), https://doi.org/10.1103/PhysRevApplied.17.014015. **p. 77**

[157] H. Song, J. Yao, Y. Ding, Y. Gu, Y. Deng, M.-H. Lu, H. Lu, and Y.-F. Chen, *Thermal Stability Enhancement in Epitaxial Alpha Tin Films by Strain Engineering*. Advanced Engineering Materials **21**, 10 (2019), https://doi.org/10.1002/adem.201900410. **p. 77**

[158] W.T. Yuen, W.K. Liu, B.A. Joyce, and R.A. Stradling, *RHEED studies of the surface morphology of α-Sn pseudomorphically grown on InSb(100) by MBE-a new kind of non-polar/polar system*. Semiconductor Science and Technology **5**, 5 (1990), https://doi.org/10.1088/0268-1242/5/5/001. **p. 77**

[159] D.A. Papaconstantopoulos and M.J. Mehl, *Tight-Binding Method in Electronic Structure*, in *Encyclopedia of Condensed Matter Physics*, Editors: F. Bassani, G.L. Liedl, and P. Wyder. 2005, Elsevier: Oxford. p. 194-206, https://doi.org/10.1016/B0-12-369401-9/00452-6. **p. 79**

[160] D.L. Price, J.M. Rowe, and R.M. Nicklow, *Lattice Dynamics of Grey Tin and Indium Antimonide*. Physical Review B **3**, 4 (1971), https://doi.org/10.1103/PhysRevB.3.1268. **p. 79**

[161] D. Iaia, C.-Y. Wang, Y. Maximenko, D. Walkup, R. Sankar, F. Chou, Y.-M. Lu, and V. Madhavan, ***Topological nature of step-edge states on the surface of the topological crystalline insulator*** ***$Pb_{0.7}Sn_{0.3}Se$***. Physical Review B **99**, 15 (2019), https://doi.org/10.1103/PhysRevB.99.155116. **p. 83, 84**

[162] Y. Okada, M. Serbyn, H. Lin, D. Walkup, W. Zhou, C. Dhital, M. Neupane, S. Xu, Y.J. Wang, R. Sankar, F. Chou, A. Bansil, M.Z. Hasan, S.D. Wilson, L. Fu, and V. Madhavan, ***Observation of Dirac Node Formation and Mass Acquisition in a Topological Crystalline Insulator***. Science **341**, 6153 (2013), https://doi.org/10.1126/science.1239451. **p. 83, 87**

[163] C.M. Polley, R. Buczko, A. Forsman, P. Dziawa, A. Szczerbakow, R. Rechciński, B.J. Kowalski, T. Story, M. Trzyna, M. Bianchi, A. Grubišić Čabo, P. Hofmann, O. Tjernberg, and T. Balasubramanian, ***Fragility of the Dirac Cone Splitting in Topological Crystalline Insulator Heterostructures***. ACS Nano **12**, 1 (2018), https://doi.org/10.1021/acsnano.7b07502. **p. 83, 84, 85, 87**

[164] Y. Ando, T. Hamasaki, T. Kurokawa, K. Ichiba, F. Yang, M. Novak, S. Sasaki, K. Segawa, Y. Ando, and M. Shiraishi, ***Electrical Detection of the Spin Polarization Due to Charge Flow in the Surface State of the Topological Insulator*** ***$Bi_{1.5}Sb_{0.5}Te_{1.7}Se_{1.3}$***. Nano Letters **14**, 11 (2014), https://doi.org/10.1021/nl502546c. **p. 84**

[165] J. Tang, L.-T. Chang, X. Kou, K. Murata, E.S. Choi, M. Lang, Y. Fan, Y. Jiang, M. Montazeri, W. Jiang, Y. Wang, L. He, and K.L. Wang, ***Electrical Detection of Spin-Polarized Surface States Conduction in*** ***$(Bi_{0.53}Sb_{0.47})2Te_3$ Topological Insulator***. Nano Letters **14**, 9 (2014), https://doi.org/10.1021/nl5026198. **p. 84**

[166] S. Zhang and A. Fert, ***Conversion between spin and charge currents with topological insulators***. Physical Review B **94**, 18 (2016), https://doi.org/10.1103/PhysRevB.94.184423. **p. 84**

[167] A.R. Mellnik, J.S. Lee, A. Richardella, J.L. Grab, P.J. Mintun, M.H. Fischer, A. Vaezi, A. Manchon, E.A. Kim, N. Samarth, and D.C. Ralph, ***Spin-transfer torque generated by a topological insulator***. Nature **511**, 7510 (2014), https://doi.org/10.1038/nature13534. **p. 84, 104**

[168] W. Han, Y. Otani, and S. Maekawa, ***Quantum materials for spin and charge conversion***. npj Quantum Materials **3**, 1 (2018), https://doi.org/10.1038/s41535-018-0100-9. **p. 84**

[169] Y. Fan, P. Upadhyaya, X. Kou, M. Lang, S. Takei, Z. Wang, J. Tang, L. He, L.-T. Chang, M. Montazeri, G. Yu, W. Jiang, T. Nie, R.N. Schwartz, Y. Tserkovnyak, and K.L. Wang, ***Magnetization switching through giant spin–orbit torque in a magnetically doped topological insulator heterostructure***. Nature Materials **13**, 7 (2014), https://doi.org/10.1038/nmat3973. **p. 84**

[170] Y. Fan, X. Kou, P. Upadhyaya, Q. Shao, L. Pan, M. Lang, X. Che, J. Tang, M. Montazeri, K. Murata, L.-T. Chang, M. Akyol, G. Yu, T. Nie, K.L. Wong, J. Liu, Y. Wang, Y. Tserkovnyak, and K.L. Wang, ***Electric-field control of spin–orbit torque in a magnetically doped topological insulator***. Nature Nanotechnology **11**, 4 (2016), https://doi.org/10.1038/nnano.2015.294. **p. 84**

[171] F. Bonell, M. Goto, G. Sauthier, J.F. Sierra, A.I. Figueroa, M.V. Costache, S. Miwa, Y. Suzuki, and S.O. Valenzuela, ***Control of Spin–Orbit Torques by Interface Engineering in Topological Insulator Heterostructures***. Nano Letters **20**, 8 (2020), https://doi.org/10.1021/acs.nanolett.0c01850. **p. 84**

[172] Y. Cao, G. Xing, H. Lin, N. Zhang, H. Zheng, and K. Wang, ***Prospect of Spin-Orbitronic Devices and Their Applications***. iScience **23**, 10 (2020), https://doi.org/10.1016/j.isci.2020.101614. **p. 84**

[173] G. Krizman, B.A. Assaf, M. Orlita, G. Bauer, G. Springholz, R. Ferreira, L.A. de Vaulchier, and Y. Guldner, *Interaction between interface and massive states in multivalley topological heterostructures*. Physical Review Research **4**, 1 (2022), https://doi.org/10.1103/PhysRevResearch.4.013179. **p. 84**

[174] R. Rechciński, M. Galicka, M. Simma, V.V. Volobuev, O. Caha, J. Sánchez-Barriga, P.S. Mandal, E. Golias, A. Varykhalov, O. Rader, G. Bauer, P. Kacman, R. Buczko, and G. Springholz, *Structure Inversion Asymmetry and Rashba Effect in Quantum Confined Topological Crystalline Insulator Heterostructures*. Advanced Functional Materials **31**, 23 (2021), https://doi.org/10.1002/adfm.202008885. **p. 84, 90, 99 , 106, 107**

[175] F. Zhang, X. Li, J. Feng, and C. Kane, *Zeeman Field-Tuned Transitions for Surface Chern Insulators*. arxiv.org, (2013), https://doi.org/10.48550/arXiv.1309.7682. **p. 84**

[176] M. Serbyn and L. Fu, *Symmetry breaking and Landau quantization in topological crystalline insulators*. Physical Review B **90**, 3 (2014), https://doi.org/10.1103/PhysRevB.90.035402. **p. 84, 114**

[177] P. Sessi, D. Di Sante, A. Szczerbakow, F. Glott, S. Wilfert, H. Schmidt, T. Bathon, P. Dziawa, M. Greiter, T. Neupert, G. Sangiovanni, T. Story, R. Thomale, and M. Bode, *Robust spin-polarized midgap states at step edges of topological crystalline insulators*. Science **354**, 6317 (2016), https://doi.org/10.1126/science.aah6233. **p. 84**

[178] Y. Tanaka, T. Sato, K. Nakayama, S. Souma, T. Takahashi, Z. Ren, M. Novak, K. Segawa, and Y. Ando, *Tunability of the k-space location of the Dirac cones in the topological crystalline insulator $Pb_{1-x}Sn_xTe$*. Physical Review B **87**, 15 (2013), https://doi.org/10.1103/PhysRevB.87.155105. **p. 85**

[179] I. Zeljkovic, Y. Okada, C.-Y. Huang, R. Sankar, D. Walkup, W. Zhou, M. Serbyn, F. Chou, W.-F. Tsai, H. Lin, A. Bansil, L. Fu, M.Z. Hasan, and V. Madhavan, *Mapping the unconventional orbital texture in topological crystalline insulators*. Nature Physics **10**, 8 (2014), https://doi.org/10.1038/nphys3012. **p. 87**

[180] J. Liu, W. Duan, and L. Fu, *Two types of surface states in topological crystalline insulators*. Physical Review B **88**, 24 (2013), https://doi.org/10.1103/PhysRevB.88.241303. **p. 87**

[181] I. Lifshitz, *Anomalies of electron characteristics of a metal in the high pressure region*. Sov. Phys. JETP **11**, 5 (1960). **p. 87**

[182] I. Pletikosić, G.D. Gu, and T. Valla, *Inducing a Lifshitz Transition by Extrinsic Doping of Surface Bands in the Topological Crystalline Insulator $Pb_{1-x}Sn_xSe$*. Physical Review Letters **112**, 14 (2014), https://doi.org/10.1103/PhysRevLett.112.146403. **p. 87**

[183] T. Sato, Y. Tanaka, K. Nakayama, S. Souma, T. Takahashi, S. Sasaki, Z. Ren, A.A. Taskin, K. Segawa, and Y. Ando, *Fermiology of the Strongly Spin-Orbit Coupled Superconductor $Sn_{1-x}In_xTe$: Implications for Topological Superconductivity*. Physical Review Letters **110**, 20 (2013), https://doi.org/10.1103/PhysRevLett.110.206804. **p. 88**

[184] H.M. Benia, C. Lin, K. Kern, and C.R. Ast, *Reactive Chemical Doping of the Bi_2Se_3 Topological Insulator*. Physical Review Letters **107**, 17 (2011), https://doi.org/10.1103/PhysRevLett.107.177602. **p. 90**

[185] M. Bianchi, R.C. Hatch, J. Mi, B.B. Iversen, and P. Hofmann, *Simultaneous Quantization of Bulk Conduction and Valence States through Adsorption of Nonmagnetic Impurities on Bi_2Se_3*. Physical Review Letters **107**, 8 (2011), https://doi.org/10.1103/PhysRevLett.107.086802. **p. 90**

[186]   P.D.C. King, R.C. Hatch, M. Bianchi, R. Ovsyannikov, C. Lupulescu, G. Landolt, B. Slomski, J.H. Dil, D. Guan, J.L. Mi, E.D.L. Rienks, J. Fink, A. Lindblad, S. Svensson, S. Bao, G. Balakrishnan, B.B. Iversen, J. Osterwalder, W. Eberhardt, F. Baumberger, and P. Hofmann, ***Large Tunable Rashba Spin Splitting of a Two-Dimensional Electron Gas in Bi$_2$Se$_3$.*** Physical Review Letters **107**, 9 (2011), https://doi.org/10.1103/PhysRevLett.107.096802. **p. 90**

[187]   L.A. Wray, S.-Y. Xu, Y. Xia, D. Hsieh, A.V. Fedorov, Y.S. Hor, R.J. Cava, A. Bansil, H. Lin, and M.Z. Hasan, ***A topological insulator surface under strong Coulomb, magnetic and disorder perturbations.*** Nature Physics **7**, 1 (2011), https://doi.org/10.1038/nphys1838. **p. 91**

[188]   S.G. Louie, P. Thiry, R. Pinchaux, Y. Pétroff, D. Chandesris, and J. Lecante, ***Periodic Oscillations of the Frequency-Dependent Photoelectric Cross Sections of Surface States: Theory and Experiment.*** Physical Review Letters **44**, 8 (1980), https://doi.org/10.1103/PhysRevLett.44.549. **p. 98, 121**

[189]   M. Bianchi, D. Guan, S. Bao, J. Mi, B.B. Iversen, P.D.C. King, and P. Hofmann, ***Coexistence of the topological state and a two-dimensional electron gas on the surface of Bi$_2$Se$_3$.*** Nature Communications **1**, 1 (2010), https://doi.org/10.1038/ncomms1131. **p. 99**

[190]   S. Kurth, M.A.L. Marques, and E.K.U. Gross, ***Density-Functional Theory***, in *Encyclopedia of Condensed Matter Physics*, Editors: F. Bassani, G.L. Liedl, and P. Wyder. 2005, Elsevier: Oxford. p. 395-402, https://doi.org/10.1016/B0-12-369401-9/00445-9. **p. 99**

[191]   K. Kuroda, M. Ye, E.F. Schwier, M. Nurmamat, K. Shirai, M. Nakatake, S. Ueda, K. Miyamoto, T. Okuda, H. Namatame, M. Taniguchi, Y. Ueda, and A. Kimura, ***Experimental verification of the surface termination in the topological insulator TlBiSe$_2$ using core-level photoelectron spectroscopy and scanning tunneling microscopy.*** Physical Review B **88**, 24 (2013), https://doi.org/10.1103/PhysRevB.88.245308. **p. 100**

[192]   G.P. Williams, ***X-Ray Properties of the Elements***, in *X-ray data booklet.* October 2009, Lawrence Berkeley National Laboratory, University of California, https://xdb.lbl.gov. **p. 102**

[193]   R.B. Shalvoy, G.B. Fisher, and P.J. Stiles, ***Bond ionicity and structural stability of some average-valence-five materials studied by x-ray photoemission.*** Physical Review B **15**, 4 (1977), https://doi.org/10.1103/PhysRevB.15.1680. **p. 102**

[194]   M. Cardona and L. Ley, ***Introduction***, in *Photoemission in Solids I: General Principles*, Editors: M. Cardona and L. Ley. 1978, Springer Berlin Heidelberg: Berlin, Heidelberg. p. 1-104, https://doi.org/10.1007/3540086854_1. **p. 102**

[195]   C.R. Ast, J. Henk, A. Ernst, L. Moreschini, M.C. Falub, D. Pacilé, P. Bruno, K. Kern, and M. Grioni, ***Giant Spin Splitting through Surface Alloying.*** Physical Review Letters **98**, 18 (2007), https://doi.org/10.1103/PhysRevLett.98.186807. **p. 103**

[196]   K. Ishizaka, M.S. Bahramy, H. Murakawa, M. Sakano, T. Shimojima, T. Sonobe, K. Koizumi, S. Shin, H. Miyahara, A. Kimura, K. Miyamoto, T. Okuda, H. Namatame, M. Taniguchi, R. Arita, N. Nagaosa, K. Kobayashi, Y. Murakami, R. Kumai, Y. Kaneko, Y. Onose, and Y. Tokura, ***Giant Rashba-type spin splitting in bulk BiTeI.*** Nature Materials **10**, 7 (2011), https://doi.org/10.1038/nmat3051. **p. 103**

[197]   C.H. Li, O.M.J. van 't Erve, J.T. Robinson, Y. Liu, L. Li, and B.T. Jonker, ***Electrical detection of charge-current-induced spin polarization due to spin-momentum locking in Bi2Se3.*** Nature Nanotechnology **9**, 3 (2014), https://doi.org/10.1038/nnano.2014.16. **p. 104**

[198]   H. Wang, J. Kally, J.S. Lee, T. Liu, H. Chang, D.R. Hickey, K.A. Mkhoyan, M. Wu, A. Richardella, and N. Samarth, ***Surface-State-Dominated Spin-Charge Current Conversion in Topological-Insulator--Ferromagnetic-Insulator Heterostructures.*** Physical Review Letters **117**, 7 (2016), https://doi.org/10.1103/PhysRevLett.117.076601. **p. 104**

[199] J. Ding, C. Liu, V. Kalappattil, Y. Zhang, O. Mosendz, U. Erugu, R. Yu, J. Tian, A. DeMann, S.B. Field, X. Yang, H. Ding, J. Tang, B. Terris, A. Fert, H. Chen, and M. Wu, *Switching of a Magnet by Spin-Orbit Torque from a Topological Dirac Semimetal*. Advanced Materials **33**, 23 (2021), https://doi.org/10.1002/adma.202005909. **p. 104**

[200] S.-Y. Xu, M. Neupane, I. Belopolski, C. Liu, N. Alidoust, G. Bian, S. Jia, G. Landolt, B. Slomski, J.H. Dil, P.P. Shibayev, S. Basak, T.-R. Chang, H.-T. Jeng, R.J. Cava, H. Lin, A. Bansil, and M.Z. Hasan, *Unconventional transformation of spin Dirac phase across a topological quantum phase transition*. Nature Communications **6**, 1 (2015), https://doi.org/10.1038/ncomms7870. **p. 104, 106, 110, 112, 115**

[201] O.V. Yazyev, J.E. Moore, and S.G. Louie, *Spin Polarization and Transport of Surface States in the Topological Insulators Bi_2Se_3 and Bi_2Te_3 from First Principles*. Physical Review Letters **105**, 26 (2010), https://doi.org/10.1103/PhysRevLett.105.266806. **p. 106**

[202] C. Jozwiak, J.A. Sobota, K. Gotlieb, A.F. Kemper, C.R. Rotundu, R.J. Birgeneau, Z. Hussain, D.H. Lee, Z.X. Shen, and A. Lanzara, *Spin-polarized surface resonances accompanying topological surface state formation*. Nature Communications **7**, (2016), https://doi.org/10.1038/ncomms13143. **p. 106, 107**

[203] J. Sánchez-Barriga, I. Aguilera, L.V. Yashina, D.Y. Tsukanova, F. Freyse, A.N. Chaika, C. Callaert, A.M. Abakumov, J. Hadermann, A. Varykhalov, E.D.L. Rienks, G. Bihlmayer, S. Blügel, and O. Rader, *Anomalous behavior of the electronic structure of $(Bi_{1-x}In_x)_2Se_3$ across the quantum phase transition from topological to trivial insulator*. Physical Review B **98**, 23 (2018), https://doi.org/10.1103/PhysRevB.98.235110. **p. 110, 112, 115**

[204] C. Fang, M.J. Gilbert, and B.A. Bernevig, *Large-Chern-Number Quantum Anomalous Hall Effect in Thin-Film Topological Crystalline Insulators*. Physical Review Letters **112**, 4 (2014), https://doi.org/10.1103/PhysRevLett.112.046801. **p. 114**

[205] H.A. Fertig, S. Reja, S. Zhang, and L. Brey, *Probing topology and symmetry in topological crystalline insulators with magnetism*. Physica E: Low-dimensional Systems and Nanostructures **114**, (2019), https://doi.org/10.1016/j.physe.2019.113623. **p. 114**

[206] J. Sánchez-Barriga, A. Varykhalov, G. Springholz, H. Steiner, R. Kirchschlager, G. Bauer, O. Caha, E. Schierle, E. Weschke, A.A. Ünal, S. Valencia, M. Dunst, J. Braun, H. Ebert, J. Minár, E. Golias, L.V. Yashina, A. Ney, V. Holý, and O. Rader, *Nonmagnetic band gap at the Dirac point of the magnetic topological insulator $(Bi_{1-x}Mn_x)_2Se_3$*. Nature Communications **7**, 1 (2016), https://doi.org/10.1038/ncomms10559. **p. 114**

[207] V.A. Rogalev, T. Rauch, M.R. Scholz, F. Reis, L. Dudy, A. Fleszar, M.-A. Husanu, V.N. Strocov, J. Henk, I. Mertig, J. Schäfer, and R. Claessen, *Double band inversion in α-Sn: Appearance of topological surface states and the role of orbital composition*. Physical Review B **95**, 16 (2017), https://doi.org/10.1103/PhysRevB.95.161117. **p. 116, 119, 121, 123**

[208] M.R. Scholz, V.A. Rogalev, L. Dudy, F. Reis, F. Adler, J. Aulbach, L.J. Collins-McIntyre, L.B. Duffy, H.F. Yang, Y.L. Chen, T. Hesjedal, Z.K. Liu, M. Hoesch, S. Muff, J.H. Dil, J. Schäfer, and R. Claessen, *Topological surface state of α-Sn on InSb(001) as studied by photoemission*. Physical Review B **97**, 7 (2018), https://doi.org/10.1103/PhysRevB.97.075101. **p. 116, 117 , 119, 121**

[209] I. Madarevic, U. Thupakula, G. Lippertz, N. Claessens, P.-C. Lin, H. Bana, S. Gonzalez, G.D. Santo, L. Petaccia, M.N. Nair, L.M.C. Pereira, C.V. Haesendonck, and M.J.V. Bael, *Structural and electronic properties of the pure and stable elemental 3D topological Dirac semimetal α-Sn*. APL Materials **8**, 3 (2020), https://doi.org/10.1063/1.5142841. **p. 117**

[210] K.H.M. Chen, K.Y. Lin, S.W. Lien, S.W. Huang, C.K. Cheng, H.Y. Lin, C.H. Hsu, T.R. Chang, C.M. Cheng, M. Hong, and J. Kwo, *Thickness-dependent topological phase transition and Rashba-like preformed topological surface states of α-Sn(001) thin films on InSb(001)*. Physical Review B **105**, 7 (2022), https://doi.org/10.1103/PhysRevB.105.075109. **p. 117 , 119, 121, 123**

[211] A. Barfuss, L. Dudy, M.R. Scholz, H. Roth, P. Höpfner, C. Blumenstein, G. Landolt, J.H. Dil, N.C. Plumb, M. Radovic, A. Bostwick, E. Rotenberg, A. Fleszar, G. Bihlmayer, D. Wortmann, G. Li, W. Hanke, R. Claessen, and J. Schäfer, *Elemental Topological Insulator with Tunable Fermi Level: Strained α-Sn on InSb(001)*. Physical Review Letters **111**, 15 (2013), https://doi.org/10.1103/PhysRevLett.111.157205. **p. 117**

[212] J. Ren, L. Fu, G. Bian, M. Wong, T. Wang, G. Zha, W. Jie, T. Miller, M.Z. Hasan, and T.C. Chiang, *Spectroscopic studies of CdTe(111) bulk and surface electronic structure*. Physical Review B **91**, 23 (2015), https://doi.org/10.1103/PhysRevB.91.235303. **p. 117**

[213] B. Voigtländer, A. Zinner, T. Weber, and H.P. Bonzel, *Modification of growth kinetics in surfactant-mediated epitaxy*. Physical Review B **51**, 12 (1995), https://doi.org/10.1103/PhysRevB.51.7583. **p. 117**

[214] R.A. Carrasco, C.M. Zamarripa, S. Zollner, J. Menéndez, S.A. Chastang, J. Duan, G.J. Grzybowski, B.B. Claflin, and A.M. Kiefer, *The direct bandgap of gray α-tin investigated by infrared ellipsometry*. Applied Physics Letters **113**, 23 (2018), https://doi.org/10.1063/1.5053884. **p. 119, 121**

[215] C.-Z. Xu, Y.-H. Chan, Y. Chen, P. Chen, X. Wang, C. Dejoie, M.-H. Wong, J.A. Hlevyack, H. Ryu, H.-Y. Kee, N. Tamura, M.-Y. Chou, Z. Hussain, S.-K. Mo, and T.-C. Chiang, *Elemental Topological Dirac Semimetal: α-Sn on InSb(111)*. Physical Review Letters **118**, 14 (2017), https://doi.org/10.1103/PhysRevLett.118.146402. **p. 121, 123**

[216] S. Moser, *An experimentalist's guide to the matrix element in angle resolved photoemission*. Journal of Electron Spectroscopy and Related Phenomena **214**, (2017), https://doi.org/10.1016/j.elspec.2016.11.007. **p. 121**

[217] S. Hüfner, *Introduction and Basic Principles*, in *Photoelectron Spectroscopy: Principles and Applications*, Editors: S. Hüfner. 2003, Springer Berlin Heidelberg: Berlin, Heidelberg. p. 1-60, https://doi.org/10.1007/978-3-662-09280-4_1. **p. 121**

[218] Y. Ohtsubo, P. Le Fèvre, F. Bertran, and A. Taleb-Ibrahimi, *Dirac Cone with Helical Spin Polarization in Ultrathin α-Sn(001) Films*. Physical Review Letters **111**, 21 (2013), https://doi.org/10.1103/PhysRevLett.111.216401. **p. 123**

[219] O.A. Pankratov, S.V. Pakhomov, and B.A. Volkov, *Supersymmetry in heterojunctions: Band-inverting contact on the basis of $Pb_{1-x}Sn_xTe$ and $Hg_{1-x}Cd_xTe$*. Solid State Communications **61**, 2 (1987), https://doi.org/10.1016/0038-1098(87)90934-3. **p. 123**

[220] M. Dyakonov and A. Khaetskl, *Size quantization of the holes in a semiconductor with a complicated valence band and of the carriers in a gapless semiconductor*. Journal of Experimental and Theoretical Physics **82**, (1982). **p. 123**

[221] A. Khaetskii, V. Golovach, and A. Kiefer, *Revisiting the physical origin and nature of surface states in inverted-band semiconductors*. Physical Review B **105**, 3 (2022), https://doi.org/10.1103/PhysRevB.105.035305. **p. 123**

[222] D.M. Mahler, J.-B. Mayer, P. Leubner, L. Lunczer, D. Di Sante, G. Sangiovanni, R. Thomale, E.M. Hankiewicz, H. Buhmann, C. Gould, and L.W. Molenkamp, *Interplay of Dirac Nodes and Volkov-Pankratov Surface States in Compressively Strained HgTe*. Physical Review X **9**, 3 (2019), https://doi.org/10.1103/PhysRevX.9.031034. **p. 123**

[223] J. Bermejo-Ortiz, G. Krizman, R. Jakiela, Z. Khosravizadeh, M. Hajlaoui, G. Bauer, G. Springholz, L.A. de Vaulchier, and Y. Guldner, *Observation of Weyl and Dirac fermions at smooth topological Volkov-Pankratov heterojunctions*. Physical Review B **107**, 7 (2023), https://doi.org/10.1103/PhysRevB.107.075129. **p. 123**